ABSTRACT

Title of dissertation: COHERENCE IN DC SQUID PHASE QUBITS

Hanhee Paik, Doctor of Philosophy, 2007

Dissertation directed by: Professors Chris Lobb and Fred Wellstood
Department of Physics

I report measurements of energy relaxation and quantum coherence times in an aluminum dc SQUID phase qubit and a niobium dc SQUID phase qubit at 80 mK. In a dc SQUID phase qubit, the energy levels of one Josephson junction are used as qubit states and the rest of the SQUID forms an inductive network to isolate the qubit junction. Noise current from the SQUID's current bias leads is filtered by the network, with the amount of filtering depending on the ratio of the loop inductance to the Josephson inductance of the isolation junction. The isolation junction inductance can be tuned by adjusting the current, and this allows the isolation to be varied *in situ*. I quantify the isolation by the isolation factor r_I which is the ratio of the current noise power in the qubit junction to the total noise current power on its bias leads.

I measured the energy relaxation time T_1, the spectroscopic coherence time T_2^* and the decay time constant T' of Rabi oscillations in the Al dc SQUID phase qubit AL1 and the Nb dc SQUID phase qubit NBG, which had a gradiometer loop. In particular, I investigated the dependence of T_1 on the isolation r_I. T_1 from the relaxation measurements did not reveal any dependance on the isolation factor r_I. For comparison, I found T_1 by fitting to the thermally induced background escape rate and found that it depended on r_I. However, further investigation suggests that

this apparent dependence may be due to a small-noise induced population in $|2\rangle$ so I cannot draw any firm conclusion.

I also measured the spectroscopic coherence time T_2^*, Rabi oscillations and the decay constant T' at significantly different isolation factors. Again, I did not observe any dependence of T_2^* and T' on r_I, suggesting that the main decoherence source in the qubit AL1 was not the noise from the bias current. Similar results were found previously in our group's Nb devices.

I compared T_1, T_2^* and T' for the qubit AL1 with those for NBG and a niobium dc SQUID phase qubit NB1 and found significant differences in T_2^* and T' among the devices but similar T_1 values. If flux noise was dominant, NBG which has a gradiometer loop would have the longest Rabi decay time T'. However, T' for NBG was similar to NB1, a Nb dc SQUID phase qubit without a gradiometer. I found that $T' = 28$ ns for AL1, the Al dc SQUID phase qubit, and this was more than twice as long as in NBG ($T' \simeq 15$ ns) or NB1 ($T' \simeq 15$ ns). This suggests that materials played an important role in determining the coherence times of the different devices.

Finally, I discuss the possibility of using a Cooper pair box to produce variable coupling between phase qubits. I calculated the effective capacitance of a Cooper pair box as a function of gate voltage. I also calculated the energy levels of a Josephson phase qubit coupled to a Cooper pair box and showed that the energy levels of the phase qubit can be tuned with the coupled Cooper pair box.

COHERENCE IN dc SQUID PHASE QUBITS

by

Hanhee Paik

Dissertation submitted to the Faculty of the Graduate School of the
University of Maryland, College Park in partial fulfillment
of the requirements for the degree of
Doctor of Philosophy
2007

Advisory Committee:
Professor Christopher J. Lobb, Co-Chair/Advisor
Professor Frederick C. Wellstood, Co-Chair/Advisor
Professor Alex J. Dragt
Professor Michael S. Fuhrer
Professor John Melngailis

Acknowledgements

I always think graduate students are like rice crops (it can be wheats depending on where you are from). Growing them requires lots of effort, care and time, especially if you want them to be good ones when you harvest, i.e. when they graduate with PhD degrees. Not to mention that the crops have to endure tough times, overcome unexpected obstacles and work hard to be full-grown crops.

Whether I was a good rice crop, I don't know. One thing I can say for sure is I received incredible amount of supports and helps from many people while I was in the graduate school. I certainly know that the space here in "Acknowledgements" is not enough to show what they did for me during all those years and how much I appreciate them. First I thank my dissertation committee members, Prof. Chris Lobb, Prof. Fred Wellstood, Prof. Alex Dragt, Prof. Michael Fuhrer and Prof. John Melngailis for giving me good advice on my thesis and their good suggestions.

I owe great debts to my advisors, Professors Chris Lobb, Fred Wellstood and Bob Anderson. I just cannot imagine myself being in the United States, studying physics without them. They are my academic parents who taught me everything I need to know including how to be a good physicist. Also they showed me how to be a good advisor through themselves as the example. They became the reason that I want to be a good physicist and the motivation that kept me going during the troubled time in the graduate school. I find sometimes a little bit of Chrisness or Fredness or Dr. Andersonness inside myself and I feel proud of that.

Chris taught me how important it is in physics to think deeply and ask questions. Chris is like a physicist that I always imagine to be when I grow up. When I was about to give up after two failed projects, he didn't give up on me, believed in me and encouraged me to try again. While I was struggling in communication (probably still I am), he was very patient and always willing to listen to me on any subject as a physicist and mentor. I will never be able to say thanks enough to him and I wish I will be able to become one his students that he is proud of.

Dr. Anderson always gave me warm advice, was very supportive and most of all, he inspired me in every way through his restless will to learn and try new things as a physicist. He showed me joy of learning, and I was able to discover the fun part of quantum computation through him. I admire his young heart and mind. And I hope I will become like him in the future.

Fred is my academic "mom". I won't exist as a physicist without him. I look up to his incredible strength and momentum as well as his intuition and studiousness. He taught me the joy of studying physics. He always encouraged me and listened to me about anything. He helped me to discover myself that I enjoy research in physics and motivated me to pursue physics as a career.

I thank Dr. Alex Dragt for giving me good insight in physics in terms of theory. Also I will never forget his warm encouragement during the group meetings for many years and thesis defense. I thank Dr. Michael Fuhrer for introducing me new physics of carbon, giving me good discussions, encouragement and advice.

It would have been impossible for me to finish Ph.D if Dr. Sudeep K. Dutta wasn't there. He taught me many things such as cryogenic skills, created MATLAB codes which are essential part in analysis in this thesis, and most of all, taught me how to do experiment right. If I didn't meet him and didn't have a chance to work together with him, I would have become a bad student (seriously!). I thank Sudeep also for LaTex thesis templates and sharing his bibliography. Having Sudeep in the subbasement was one of the best parts being in the subbasement for me.

Dr. Rupert Lewis is like my academic uncle. I owe him for so many things that to describe those, I have to write a thick book about all those years of my life in the subbasement lab; not only he was always encouraging me and being supportive, but also he gave me priceless advice and discussions. He helped me out all those trouble I've had during the experiment and the analysis, and still he will be the first one that I would ask if I get stuck in research in the future. He is a good advisor and mentor. I thank Rupert for good discussions and for his teaching in physics, experiment and how to be a good physicist.

I thank Dr. Roberto Ramos who taught me the beauty of a dilution fridge; he taught me how to deal with the dilution refrigerator. He taught me how to set up the experiment from the scratch that I did in this thesis. He put lots of work on

the dilution fridge wiring which I also learned from him, setting up the electronics and measurement. He is also naturally good teacher and good friend of mine who gave me lots of advice in physics as well as in life.

I thank Tauno Palomaki, a.k.a. "Face of Angel". He is a working- hard graduate student who I learned a lot about how to be a good student. I enjoyed discussions about decoherence with him which inspired me in my T_1 analysis in this thesis. I also thank Ben Coooper, a.k.a. "Cooop" or "Beeeeeen" for sharing his deep thoughts on our research with me and good discussions, and sometimes, theoretical supports. I thank Tony Przybysz, a.k.a. "Yo! Toni!" for good discussions and I enjoyed very much working on the small fridge project together. I thank Hyeokshin Kwon, a.k.a. "Hyeokster" for good discussions and I liked exchanging ideas on physics with him.

We have incredible members of experimentalists in the subbasement but I shouldn't forget that we also have incredible theorists working with those experimentalists. I thank Dr. Fred Strauch for his theoretical support, calculations on the coupled Cooper pair box, and helping me out for many other physics questions that I've asked whenever I got stuck. I thank Kaushik for his calculation on a dc SQUID phase qubit and many good discussions. I also thank Dr. Phil Johnson for his theoretical support and his good notes on Caldeira-Leggett model.

All the glory we have in the subbasement started from our starting members, Huizhing Xu, Andrew Berkley, and Mark Gubrud. The legendary Dr. Huizhong Xu; I thank him, who basically set up the subbasement, for his noise theory and his contributions on my experiment setup. He was a good physicist from whom I learned how to be a good physicist. I thank Dr. Andrew Berkley for helping me setting up the small fridge. I also thank Mark Gubrud for the electronics and fridge setup.

I thank our "SQUID neighbors", Gus Vlahacos and Dr. John Matthews for good discussions and conversation. I thank John also for the discussions on how to calculate a dc SQUID current-flux map and I-V curves. I thank Ben Palmer for useful comments and discussions at the group meetings.

I used to work on a SET microscope project and I thank Dave Tobias and Matt Kenyon for teaching me the basics of device fabrication and good discussions on the

SET project. Especially I thank David for many things in my life in graduate school; Dave is one of my best friends in the US, and while talking to him, my English skill improved 300 % (this is true!!). I thank Su-Young Lee, who was like my sister, for helping me out to settle down when I came to the US and many good advice on physics and life. I thank Dr. Zhengli Li and Dr. Hua Xu for good discussions. I enjoyed their company as a fellow graduate student in GLG (great Lobb group).

I thank Dr. Paola Barbara and Yanfei Yang at Georgetown University for good discussions. Paola was my role model as a women physicist and Yanfei was one of those few fellow women physicists that I really enjoyed talking to about physics as well as our life.

The Center for Superconductivity Research is where I spent seven years of the best part of my life. I thank Dr. Richard Greene for many things, especially the superconductivity seminar. I got a job because I gave a good talk at the conference and this is all because I was able to practice a lot for many years through the superconductivity seminar. Dr. Greene - actually he said I could call him Rick, which I really wanted to try, but I was too shy to do so. However, I'm going to try here now - or Rick was such a cheerful person that it was fun to talk to him. I thank people in Greene group; Dr. Pengcheng Li and Dr. Weiqiang Yu for their help on liquid helium and good discussions. I thank Dr. Steve Anlage, Dr. Dragos Mircea, Dr. Sameer Hemmady, Dr. Mike Ricci and Nate Orloff for good discussions on microwave physics and their company. I thank Dr. Ichiro Takeuchi and his group members for useful discussions. I'm looking forward to playing the famous annual baseball game with Takeuchi group at the center picnic this year.

The Center for Superconductivity Research won't be able to run at all if we didn't have Belta Pollard, Cleopatra White, Grace Sewlall and Brian Barnaby, and I thank them for everything. I thank Doug Bensen and Brian Straughn for their incredible help on my experiments. All of them are like my family and I enjoyed very much their company.

I have to thank the members of Michael's Nanotechnology lab, Dr. Michael Fuhrer, Dr. Anthony Ayari, Dr. Todd Brintlinger, Dr. Tobias Dürkop, Enrique Cobas, Dr. Yung-Fu Chen and others for their help and discussions on nanotube transistors. I learned a lot from them. They are also good friends of mine who

enriched my life in graduate school.

In the Physics department, I thank Dr. Nicholas Chant who was a great person and the graduate chair that I owe him for many things in my life at school. I won't be able to go through the graduate school if I didn't get help from Jane Hessing. I thank Jane for so much help and encouragement that I received during the graduate school years. I thank Linda O'Hara for her incredible help when I started the graduate school and for her encouragement. I thank Bernie Kozlowski for many things including physics tea. I thank Jesse Anderson, Al Godinez, George Butler and Bob Dahms for, first of all, being such a caring person, all those warmth they gave me, as well as their professional help on liquid helium and equipments which are essential part in my research. I thank Dr. Kim who is one of my best friends in physics for nice stories on Korean history and for his advice. I thank Dr. Ho Jung Paik (big Dr. Paik) for his good advice and conversation. I thank Dr. Michael Dreyer for useful discussions and his friendship. I should thank Dr. Kevin D. Osborn for good discussions on fabrications and his patience to wait for me to finish as well.

I have buddies that I went through the graduate school together with; Dr. Yung-Fu Chen, Dr. Micwah Ng and Dr. Narupon "Tor" Chattrapiban. I appreciate their friendship which brought joy in my life in the graduate school and even though we are apart in Illinois, Japan and Thailand and Maryland, I hope our friendship will last forever.

I thank my Korean fellow physicists; Dr. Junghwan Kim, Dr. Seok-Hwan Chung, Young Soo Youn, Bora Sul, Young-Noh Youn, Zaeil Kim, Hyeokshin Kwon, Chaun Jang and others for their help and friendship. I especially thank Jonghee Lee for his help and friendship. He saved me from many troubles so many times.

I have to thank Dr. Jae Hoon Kim who first introduced the world of superconductivity to me for his support for studying abroad. I thank Dr. Kibum Kim for his help and giving me insight to look into physics problems when I was studying at Yonsei University, in Korea. I thank Dr. Mi-Ock Mun, Young Sup Roh and other members of Yonsei Spectroscopy Lab for their help. I thank the professors at the physics department at Yonsei University for their support and teaching that eventually led me to pursue further steps in studying physics.

I thank Dr. Seunghee Son and Sejin Han who are my college classmates from Korea for their friendship and support. I also thank my year-94 Yonsei Physics classmates for their friendship and support. I should thank Dr. Kiwoong Kim for useful discussions on NMR.

Finally I deeply thank my parents-in-law for their incredible support and love, and my brother-in-law Sangbong Jeong and my brother Tae-jong Paik. My parents, Dr. Sunbok Paik and Jeongja Kim who convinced me to study physics instead of electrical engineering 13 years ago when I went to college, I thank them for their good insight on me as well as, not to mention, their endless support and love. I also thank my husband Jae Kwang Jeong who took care of the household jobs for me, cooking, cleaning, etc during my time writing my thesis, for his support and love. I was able to get my PhD because I had his support and I am honestly looking forward to his time writing thesis (I'm not being sadist!) so that I could be supportive for him like he did for me.

Table of Contents

List of Tables

List of Figures

Chapter 1

Introduction

1.1 Quantum computers and qubits

A quantum computer is a device that employs physical mechanisms described by quantum mechanics to perform computations [1]. The idea of quantum computation was first proposed by Richard Feynman in 1982 [2]. He showed that only simple quantum systems could be efficiently simulated on a classical computer, while one quantum system could, in principle, efficiently simulate another. In 1985, David Deutsch published his description of a quantum Turing machine, showing how to use "quantum parallelism" [3]. The quantum-bit or qubit is the basic unit of a quantum computer and the term "qubit" was first used by Benjamin Schumacher, who developed a coding theorem for quantum information theory [4].

Superposition and entanglement are two key quantum properties that are required for quantum computation. The main difference between a bit and a qubit is that only the qubit is allowed to be in a superposition of $|0\rangle$ and $|1\rangle$, enabling it to span a 2-dimensional Hilbert space. In addition, the qubit state can be entangled with other qubits. Entanglement can be used to store, exchange or read out information. In principle, because of superposition and entanglement, N qubits can be placed into of order 2^{2^N} states while N classical bits only have available 2^N distinct states. Moreover, operations can be done on all registers at the same time in a quantum computer. In this sense, an N-qubit quantum register is like a 2^N-classical bit register.

One of the main motivations to build a quantum computer is that a quantum computer would be able to break RSA encryption [5]. RSA encryption uses multiplication of two large prime numbers to produce a public key. If the key could

be factored, then messages that were encrypted could be deciphered. Enormous interest in quantum computation developed after Peter Shor developed an algorithm (Shor's algorithm) for factoring numbers very efficiently on a quantum computer [6].

With Shor's algorithm, the difference in the speed of computation for a classical computer and a quantum computer gets bigger as the size of the number to be factored grows. For example, to factor an integer with k digits, the classical computer would take on the order of $2^{k^{1/3}}$ operations while a quantum computer would take on the order of k^3 operations [7]. If both computers could factor a 130-digit number in one month, then the classical computer would require 10^{10} years to factor a 400-digit number, while the quantum computer would take only three years [8]. At present, however, no quantum computer exists that can factor such large numbers. In 2001, Vandersypen *et al.* used Shor's algorithm to factor 15 using a solution of molecules that each had five ^{19}F and two ^{13}C spin-1/2 nuclei qubits in liquid state NMR at room temperature [7], and even this result has been questioned as to whether it was true quantum computation.

To be able to perform useful computation, the qubits and their interconnections in a quantum computer must satisfy the DiVincenzo criteria [9]:

1. Be a scalable physical system with well-defined qubits
2. Be initializable to a simple fiducial state such as $|000...\rangle$
3. Have long coherence times
4. Have a universal set of quantum gates
5. Permit high quantum efficiency, qubit-specific measurements

The coherence time is the time scale that characterizes how long the qubit can remain in a well-defined superposition of states. Since the qubit needs to occupy

superposition states to perform quantum operations, the coherence time is a measure of the time available for a computation, and long coherence time is important. To obtain a long coherence time, the qubit must be isolated from dissipation and all external disturbance [10, 11].

There are many types of qubits that have been proposed and may one day satisfy the DiVincenzo criteria. Table 1.1 summarizes some of the main types of qubits being built and studied currently. I note that the same physical system can provide various types of qubits. For example, photons can use polarization, number or photon time-bin encoding to construct distinct types of qubits. Similarly, superconducting devices with Josephson junctions can be used to construct three main classes of qubits - charge, phase and flux qubits.

Each qubit has advantages and disadvantages. Neutral atom qubits (two atomic states as a qubit) and hyperfine qubits (two hyperfine states of a trapped ion) tend to be well-isolated, and in consequence they can have long coherence times. However, they do not interact strongly, making it challenging to control and couple them together. Superconducting qubits are easily controlled and coupled, but they have been plagued by relatively short coherence times. For the superconducting quantum computing community, finding and removing the causes of decoherence is a major challenge. Since superconducting qubits consist of large numbers of atoms and electrons, they can easily interact with many other unwanted quantum states. As a result, superconducting qubits require more elaborate isolation scheme than naturally well-isolated qubits such as atoms or photons. The basic approach to isolating superconducting qubits involves placing a large impedance between the qubit and the environment or noise, so that the qubit does not interact with external degrees of freedom.

Table 1.1: Types of qubits.

Name of qubit	qubit states	$\|0\rangle$	$\|1\rangle$
photon	polarization	horizontal	vertical
	number	vacuum	single photon
	time of arrival	early	late
coherent light (wave)	squeezed quadrature	amplitude	phase
electron	spin	up	down
	charge	0	e
nuclear spin (NMR)	spin	up	down
neutral atom	atomic spin	up	down
trapped ion	hyperfine states		
	atomic energy	ground state	excited state
Cooper pair box	charge	zero 2e	one 2e
three junction SQUID	flux (current)	clockwise	counterclockwise
phase qubit	energy (phase)	ground state	1st excited state
Quantum dot	charge	e on left dot	e on right dot

1.2 What is this thesis about

In this thesis, I focus on isolation and coherence in large capacitance Josephson-junctions or phase qubits [12]. In particular, I built Al/AlO_x/Al Josephson junction with on-chip inductive isolation networks which act as current noise isolation filters. Because the inductive isolation network and the Josephson junction phase qubit form a dc SQUID, our group calls this type of qubit the "dc SQUID phase qubit". In Chapters 2 and 3, I review essential background material on superconductivity, superconducting qubits and qubit dynamics. In Chapter 4, I describe the experimental setup and device fabrication techniques that I used. Chapters 5 and 6 show my experimental results for the relaxation time and coherence time, and I discuss possible causes of decoherence in my qubits. In Chapter 7, I compare the coherence time of an Al dc SQUID qubit to those of Nb dc SQUID qubits. I also discuss how the design and material choices could influence the coherence times. Chapter 8 discusses the Cooper pair box and how it can be coupled to a dc SQUID phase qubit. Finally in Chapter 9, I provide a summary of the thesis.

Chapter 2

Josephson junctions, SQUIDs and superconducting qubits

2.1 Superconductivity

Following his success in liquifying helium, superconductivity was first discovered in mercury by Kamerlingh Onnes in 1911 [13] (also see the Nobel Lecture by Kamerlingh Onnes [14]). Soon after, Meissner and his colleagues found that superconductors were perfect diamagnets (the Meissner effect) [13]. However, the microscopic origin of superconductivity wasn't revealed until the Bardeen-Cooper-Schrieffer (BCS) theory was introduced in 1957 [15]. The conventional BCS superconducting state is a thermodynamic phase in which the electrons in a conducting material form pairs and condense into a state with perfect diamagnetism and zero resistivity below a critical temperature T_c [13].

Before the BCS theory was developed, Ginzburg and Landau proposed a phenomenological theory that describes superconductivity as a phase transition from the normal to superconducting state [13]. The Ginzburg-Landau (GL) theory does surprisingly well at defining and explaining the behavior of important parameters such as the coherence length, the penetration depth, and the condensation energy. Later, Gor'kov proved that the GL theory can be derived from the BCS formalism [13]. In this chapter, I use the GL approach to discuss a few important phenomena related to Josephson junctions [13, 16, 17].

2.2 Superconducting wave function and flux quantization

The superconducting state is thermodynamically more ordered than the normal state. In particular, for temperature T less than the critical temparature T_c, the free energy is a minimum in the superconducting state. In the GL theory, the superconductor is described by a complex "order parameter" ψ

$$\psi(\mathbf{r}) = \sqrt{n_s(\mathbf{r})}\exp[i\theta(\mathbf{r})] \tag{2.1}$$

where $|\psi|^2 = n_s(\mathbf{r})$ is the density of the "superconducting electrons" that have condensed into the superconducting state and θ is a phase factor that depends on position $\mathbf{r}$. The "superconducting electrons" were later revealed by the BCS theory to be pairs of electrons that were attracted to each other by the exchange of phonons; they are called "Cooper pairs" [15].

The order parameter ψ satisfies the first Ginzburg-Landau equation

$$\frac{(-i\hbar\nabla - q\mathbf{A})^2}{2m^*}\psi + \alpha\psi + \beta|\psi|^2\psi = 0. \tag{2.2}$$

where q is the charge of the Cooper pair and m^* is its mass. Ginzburg and Landau found this equation by minimizing the Gibb's free energy with respect to ψ [13]. Eq. 2.2 resembles the Schrödinger equation of a particle with charge q and mass m^* except for the nonlinear $|\psi|^2\psi$ term. Keeping the similarity in mind, we treat $\psi(\mathbf{r})$ as a wavefunction for the Cooper pairs. ψ can be normalized to the total number N of Cooper pairs:

$$\int \psi^*(\mathbf{r})\psi(\mathbf{r})dV = N. \tag{2.3}$$

where the integral is taken over the volume V of superconductor.

The current density **J** due to the Cooper pairs is given by

$$\mathbf{J} = Re[q\langle\hat{\mathbf{v}}\rangle] \tag{2.4}$$

where q = − 2e = − 2 × (1.6 ×10^{-19} C) is the charge of a Cooper pair. Here

$$\hat{\mathbf{v}} = \left(\frac{\mathbf{p} - q\mathbf{A}}{m^*}\right) = \frac{1}{m^*}\left(-i\hbar\nabla - q\mathbf{A}\right) \tag{2.5}$$

is the velocity operator of a Cooper pair in the superconductor and **A** is the vector potential of any magnetic field that is present. Since

$$\nabla\psi = i\psi\nabla\theta(\mathbf{r}) + \exp[i\theta(\mathbf{r})]\nabla\sqrt{n_s(\mathbf{r})}, \tag{2.6}$$

the current density in Eq. 2.4 can be written as

$$\begin{aligned} \mathbf{J} &= Re[q\langle\psi|\frac{\mathbf{p} - q\mathbf{A}}{m^*}|\psi\rangle] & (2.7)\\ &= \frac{qn_s(\mathbf{r})}{m^*}[\hbar\nabla\theta(\mathbf{r}) - q\mathbf{A}]. & (2.8) \end{aligned}$$

Some of the most interesting features of Cooper pairs comes from the phase factor $\theta(\mathbf{r})$ and its connection to current. For example, the phase $\theta(\mathbf{r})$ has to produce a single-valued wavefunction. If we consider a superconducting ring, this gives a quantization rule

$$\oint \nabla\theta(\mathbf{r}) \cdot d\mathbf{l} = 2\pi n \tag{2.9}$$

where $d\mathbf{l}$ is a line element and the integration is taken along any path in the superconductor. Thus in a closed-loop of superconductor, the super current must flow so as to satisfy Eq. 2.9. Taking a line integral over both sides of Eq. 2.8, one finds:

$$\oint \mathbf{J} \cdot d\mathbf{l} = \frac{qn_s}{m^*}\left[\hbar\oint \nabla\theta(\mathbf{r}) \cdot d\mathbf{l} - q\oint \mathbf{A} \cdot d\mathbf{l}\right] \tag{2.10}$$

where I have assumed n_s is constant so that it can be taken out of the integral. Using Eq. 2.9 and Stokes' theorem, Eq. 2.10 becomes

$$\oint \mathbf{J} \cdot d\mathbf{l} = \frac{q^2 n_s}{m^*} \left[2\pi \frac{\hbar}{q} n - \int \mathbf{B} \cdot d\mathbf{a} \right] \tag{2.11}$$

$$= \frac{q^2 n_s}{m^*} \left[\frac{nh}{q} - \int \mathbf{B} \cdot d\mathbf{a} \right] \tag{2.12}$$

where $d\mathbf{a}$ is an infinitesimal area element and $\mathbf{B}$ is the total magnetic field. The integral over $\mathbf{B}$ is done over the area enclosed by the contour for the line integral, and

$$\int \mathbf{B} \cdot d\mathbf{a} = \Phi \tag{2.13}$$

is the total magnetic flux in the superconducting ring. The first term in the brackets in Eq. 2.12 yields

$$\frac{nh}{q} \equiv \frac{nh}{2e} \equiv n\Phi_0 \tag{2.14}$$

where $\Phi_0 = h/2e$ is the flux quantum. Using Eq. 2.13 and 2.14, Eq. 2.12 becomes

$$\frac{m_e}{2e^2 n_s(\mathbf{r})} \oint \mathbf{J} \cdot d\mathbf{l} + \Phi = n\Phi_0. \tag{2.15}$$

Here I have taken $m^* = 2m_e$ and m_e is the mass of an electron. This equation describes fluxoid quantization. Deep inside a superconductor, we expect $\mathbf{J} = 0$. In this case, Eq. 2.15 implies that the total flux inside a closed path in a superconductor should be an integer multiple of a flux quantum.

An important fact to keep in mind is that although the vector potential $\mathbf{A}$ is not unique, any physical quantities that involves $\mathbf{A}$ must be gauge invariant. For example, suppose we choose a vector potential that satisfies

$$\mathbf{A}' = \mathbf{A} + \nabla\chi \tag{2.16}$$

instead of $\mathbf{A} = 0$. Since Eq. 2.8 must yield the same $\mathbf{J}$ for either choice of $\mathbf{A}$ or $\mathbf{A}'$, it is necessary to define a new gauge invariant phase difference γ_{12} by [13]

$$\gamma_{12} = \theta_1 - \theta_2 - \frac{2\pi}{\Phi_0}\int_1^2 \mathbf{A}\cdot d\mathbf{l}. \tag{2.17}$$

2.3 Josephson junctions

Josephson junctions are formed from superconductor-insulator-superconductor structures (SIS), superconductor-normal-superconductor junction (SNS) or even by creating a small constriction between two superconducting banks (weak links). In this section, I discuss the basic properties of SIS Josephson junctions and show how the Josephson junction Hamiltonian is found from the Josephson equations.

2.3.1 dc and ac Josephson effects

In 1962, Brian Josephson predicted that for two superconducting electrodes separated by a very thin insulator (see Fig. 2.1), current can flow via tunneling without any voltage drop [18]. He found that the tunneling current flowing from superconductor 1 to superconductor 2 across the junction is given by

$$\begin{aligned} I &= I_0 \sin(\theta_1 - \theta_2 - \frac{2\pi}{\Phi_0}(\chi_1 - \chi_2)) && (2.18)\\ &= I_0 \sin\gamma && (2.19) \end{aligned}$$

where γ is the gauge invariant phase difference between superconductor 1 and superconductor 2 (defined in Eq. 2.17) and I_0 is the critical current. Equation 2.18 is called the "dc Josephson effect". Josephson also found that if the phase changes with respect to time, then a voltage develops across the junction, given by:

$$V = \frac{\hbar}{2e}\frac{d\gamma}{dt}. \tag{2.20}$$

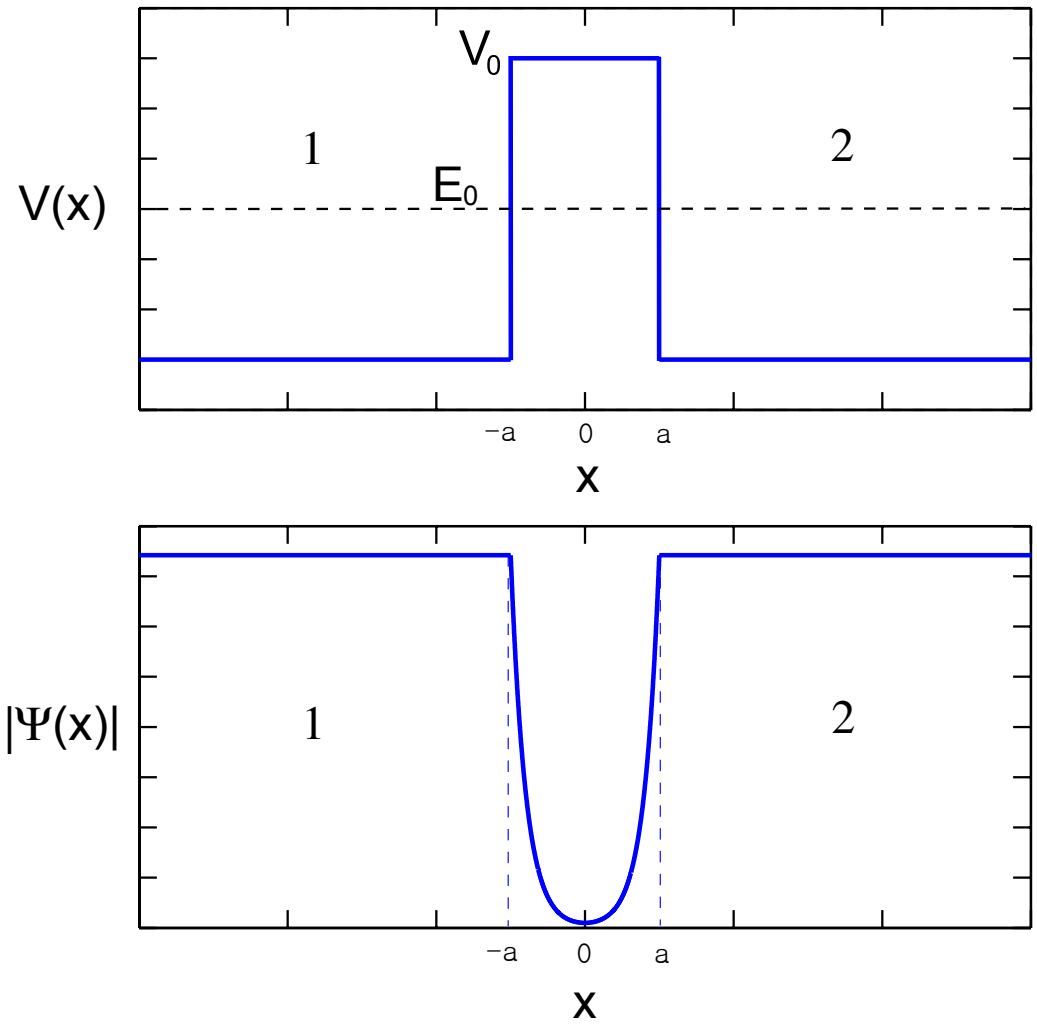

Figure 2.1: Schematic diagram of the potential energy and the magnitude of the wave function for pairs in a Josephson junction with a thin insulating barrier. The thickness of the barrier is 2a.

Equation 2.20 is called the "ac Josephson effect". The dc and ac Josephson effects were experimentally confirmed by Anderson and Rowell in 1963 [19]. For historical background to the discoveries of the Josephson junction, see "Foundations of Applied Superconductivity" by Orlando and Delin [16] and the Nobel lectures by B. Josephson and I. Giaever [20].

The dc and ac Josephson effects provide the basis for the international voltage standard. The essential physics of the technique is that if a constant voltage V is applied to the Josephson junction, the phase across the junction becomes

$$\gamma = \int_0^t \frac{d\gamma}{dt} dt = \frac{2eV}{\hbar} t. \tag{2.21}$$

Substituting γ from Eq. 2.21 into Eq. 2.18, one finds an oscillating current,

$$I(t) = I_0 \sin\left(\frac{2eV}{\hbar} t\right) \tag{2.22}$$

at frequency $f = 2eV/h$. In practice, a microwave current that is oscillating at an accurately known frequency f is applied and a voltage step is produced at V = hf/2e.

2.3.2 Properties of Josephson tunnel junctions

Cooper pairs flowing through a Josephson junction are naturally described with two variables: the superconducting phase γ and the number N of the Cooper pairs that have passed through the junction. They are connected classically by the ac Josephson equation

$$V = \frac{\Phi_0}{2\pi} \frac{d\gamma}{dt} = \frac{Q}{C} = \frac{2eN}{C} \tag{2.23}$$

where C is the junction capacitance.

In fact, we need both N and γ to obtain the Hamiltonian of the Cooper pairs involved in Josephson tunneling, but we can choose either one as the independent

coordinate (see sec. 2.3.6). If the tunneling is very small (small junction), the tunneling process can be strongly affected by the Coulomb energy associated with the junction capacitance. In this small capacitance limit, the tunneling is suppressed unless we apply enough energy for the Cooper pairs to overcome the Coulomb charging energy $Q^2/2C = 2e^2/C$. This is called the Coulomb blockade effect [21]. In this limit the pair number N is the natural choice for the independent variable in the Hamiltonian.

However, if the junction has a large area, its capacitance is large and the Coulomb energy stored in the junction capacitor becomes less important. In this limit, the device behavior is dominated by the dc and ac Josephson effects and γ is a more convenient choice to use in the Hamiltonian. In this thesis, I mainly focus on large-area Josephson junctions, where the Josephson effect dominates and the dynamics of Cooper pairs is best described using the phase variable. The exception is in Chapter 9, where I discuss some aspects of the Cooper pair box.

2.3.3 Equation of motion and Lagrangian

In a real Josephson junction, the junction electrodes form a capacitor and quasiparticles can tunnel as well as pairs. In addition, there can be other normal resistive shunts across the junction. Therefore, displacement current through the capacitor, quasiparticle current and current associated with any normal shunt will flow as well as the Josephson supercurrent. Taking those into account, the total current that flows through a junction can be written as

$$I = I_0 \sin\gamma + C\frac{dV}{dt} + \frac{V}{R}. \tag{2.24}$$

Here I is the bias current, C is the junction capacitance and R is the effective resistance due to any normal shunt and quasiparticle tunneling [13]. Substituting

Eq. 2.20 into Eq. 2.24, we obtain the equation of motion for the phase difference

$$I = I_0 \sin\gamma + \frac{\Phi_0 C}{2\pi}\frac{d^2\gamma}{dt^2} + \frac{\Phi_0}{2\pi R}\frac{d\gamma}{dt}. \tag{2.25}$$

This equation of motion is identical to that of a damped driven pendulum with the angular displacement γ. In this pendulum analog, the current I becomes a torque, the capacitance term $\Phi_0 C/2\pi$ is the moment of inertia of the pendulum, and the term $\Phi_0/2\pi R$ is a damping term [17, 22]. Note in particular that the shunting conductance 1/R is related to dissipation in the Josephson junction, i.e. large R yields small dissipation.

The Lagrangian for a Josephson junction can be guessed by comparing Eq. 2.25 to Lagrange's equation

$$\frac{d}{dt}\frac{\partial\mathcal{L}}{\partial\dot{\gamma}} - \frac{\partial\mathcal{L}}{\partial\gamma} = 0. \tag{2.26}$$

Ignoring the dissipation, the equation of motion becomes

$$I = I_0 \sin\gamma + \frac{\Phi_0 C}{2\pi}\frac{d^2\gamma}{dt^2}. \tag{2.27}$$

and comparing Eq. 2.27 to Eq. 2.26, we obtain

$$\mathcal{L} = \frac{1}{2}\left(\frac{\Phi_0}{2\pi}\right)^2 C\dot{\gamma}^2 + \frac{\Phi_0}{2\pi}(I_0\cos\gamma + I\gamma). \tag{2.28}$$

Notice that I multiplied Eq. 2.27 by a factor $\Phi_0/2\pi$ to make $\mathcal{L}$ have dimensions of energy.

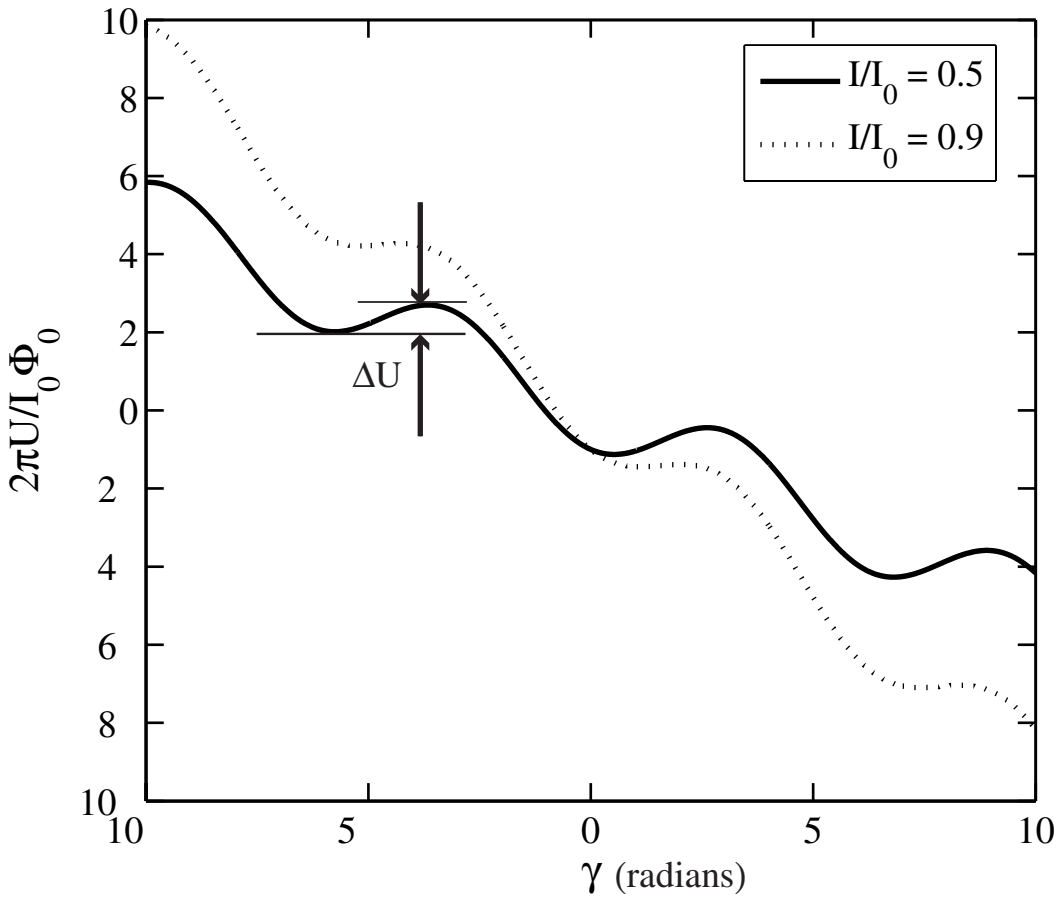

Figure 2.2: Graph of tilted washboard potential U (normalized by $\Phi_0 I_0/2\pi$) versus phase difference γ. The solid curve is for I = $0.5I_0$ and the dotted curve for I = $0.9I_0$.

2.3.4 Hamiltonian of a Josephson junction

Choosing the phase γ as a generalized position coordinate, the conjugate momentum p_γ is then

$$p_\gamma = \frac{\partial \mathcal{L}}{\partial \dot{\gamma}} = \left(\frac{\Phi_0}{2\pi}\right)^2 C\dot{\gamma} \tag{2.29}$$

Then the Hamiltonian H can be found from

$$\begin{aligned} H(p,\gamma) &= p_\gamma \dot{\gamma} - \mathcal{L}(\gamma,\dot{\gamma}) & (2.30)\\ &= \frac{1}{2C}\left(\frac{2\pi}{\Phi_0}\right)^2 p_\gamma^2 - \frac{\Phi_0}{2\pi}(I_0\cos\gamma + I\gamma). & (2.31) \end{aligned}$$

The Josephson junction Hamiltonian given by Eq. 2.31 is analogous to a ball of mass $m = C(\Phi_0/2\pi)^2$ moving in a tilted washboard potential

$$U(\gamma) = -\frac{\Phi_0}{\pi}(I_0\cos\gamma + I\gamma). \tag{2.32}$$

Figure 2.2 shows the tilted washboard potential in γ space. For small bias, we can approximate $\cos\gamma \approx 1 - \frac{1}{2}\gamma^2$. Thus for small γ the potential looks harmonic and the phase will oscillate at the minimum of the potential with angular frequency ω_{p0} where

$$\omega_{p0} \equiv \sqrt{\frac{2\pi I_0}{\Phi_0 C}}. \tag{2.33}$$

Examination of Fig. 2.2 reveals that the potential U has local minima that are separated by a barrier of height ΔU. Increasing the bias current causes the barrier height to decrease and one finds in general [23]:

$$\Delta U = -\frac{\Phi_0}{2\pi} I_0 \left(\sqrt{1 - \frac{I^2}{I_0^2}} - \frac{I}{I_0}\cos^{-1}\frac{I}{I_0}\right). \tag{2.34}$$

The location of the extrema can be found by setting the first derivative of the potential to zero. The second derivative of the potential at the potential minimum

gives the spring constant k of the effective harmonic potential. Using a cubic approximation [24], we then obtain the plasma frequency

$$\omega_p = \sqrt{\frac{k}{m}} = \sqrt{\frac{2\pi I_0}{\Phi_0 C}} \left(1 - \left(\frac{I}{I_0}\right)^2\right)^{1/4} = \omega_{p0} \left(1 - \left(\frac{I}{I_0}\right)^2\right)^{1/4}. \tag{2.35}$$

where ω_{p0} is the frequency of a small oscillation (harmonic approximation) at the bottom of the washboard potential.

2.3.5 Solution of the Josephson junction Hamiltonian

With the Hamiltonian given by Eq. 2.31, one can substitute $p_\gamma = -i\hbar\partial_\gamma$ and write the Schrödinger equation $H\Psi = E\Psi$. This equation can be solved for Ψ using a numerical method [24] or a WKB approximation [23, 25]. F. W. Strauch's thesis contains a discussion of several methods to solve Schrödinger equation for the Josephson junction and the accuracy of the different approaches [24]. The Josephson junction simulation I used in this thesis is based on a numerical simulation code written by H. Xu and S. K. Dutta [23].

If we cool a large-area Josephson junction and isolate it enough [11], well-defined metastable resonant energy states [24] will exist, as shown in Fig. 2.3. Inside a well, the discrete resonant states can be labeled as $|0\rangle$, $|1\rangle$, $|2\rangle$, etc. Energy states also exist above the well and form a continuum. Each metastable state in the well is distinguishable spectroscopically because the level spacings are anharmonic. The anharmonicity in the potential increases as we increase the current bias [24]. For $T \ll \Delta E/k_B$ where ΔE is the energy level spacing, the system will tend to relax to the ground state. We can control the state by applying microwave current to the Josephson junction. When $f = \Delta E/h$ where f is microwave frequency, the corresponding energy level resonates with the microwave drive and the system can make transitions to higher levels.

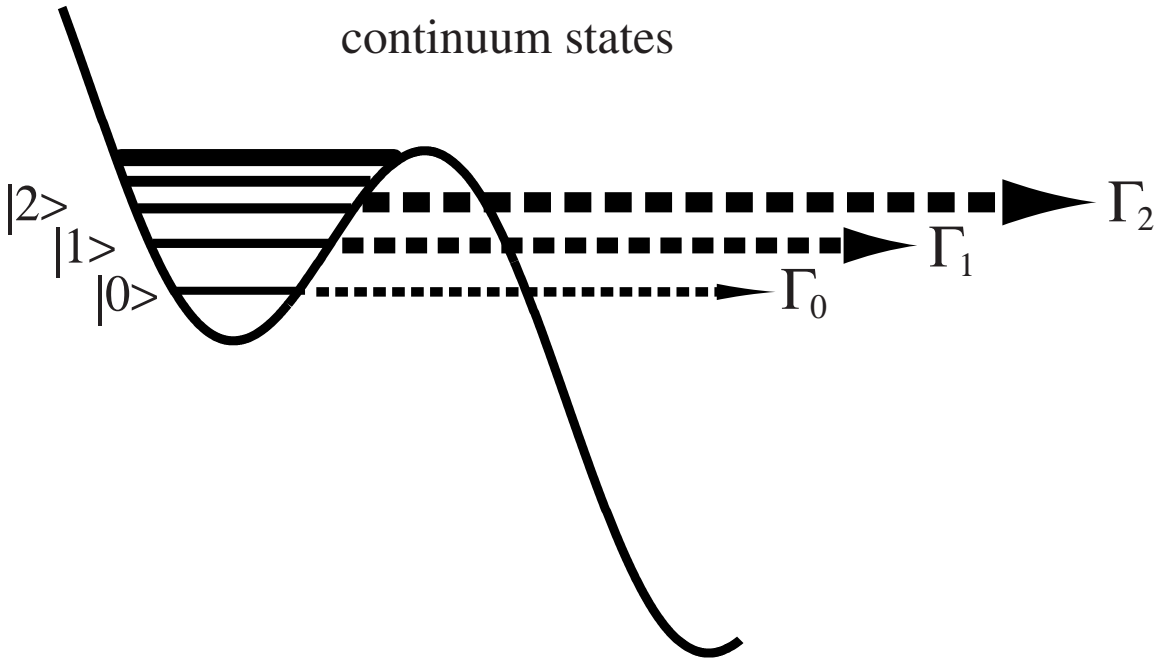

Figure 2.3: Metastable states in a well of the tilted washboard potential. Close to the top of the barrier, the energy levels form a continuous energy band. The depth of the well is exaggerated. Γ_0, Γ_1 and Γ_2 are the escape rates from the energy level $|0\rangle$, $|1\rangle$ and $|2\rangle$, respectively.

The occupancy of a state can be measured from the escape rate. As we increase the bias current, the energy barrier gets lower and eventually the Josephson junction phase tunnels through the barrier to a running state that produces a voltage across the junction. This phenomena is called macroscopic quantum tunneling [26, 27] since the tunneling involves macroscopic numbers of electrons (also see sec.2.3.6). The escape rate for tunneling depends on the barrier height. For example, the escape rate at zero temperature is given as [28]

$$\Gamma_0 = \sqrt{120\pi \frac{7.2\Delta U}{\hbar\omega_p}} \frac{\omega_p}{2\pi} exp\left[-\frac{7.2\Delta U}{\hbar\omega_p}\left(1 + \frac{0.87}{\omega_p R_{eff} C_{eff}} + \cdots\right)\right] \tag{2.36}$$

where R_{eff} is the effective resistance, and C_{eff} is the effective capacitance, both of which are in parallel to the junction. Equation 2.36 includes the effect of dissipation in R_{eff} and C_{eff}.

More rigorously, escape rates from each levels can be calculated by solving Schrödinger's equation for the Hamiltonian in Eq. 2.31 with a full washboard potential and a decaying boundary condition [23, 24]. The'escape rate Γ_n from level n is given by

$$\Gamma_n = (7.2\, N_s)^{n+1/2} \ \frac{\omega_p}{2\pi} \ \exp\left[-7.2\, N_s + f_\Gamma^n\left(N_s\right)\right] \tag{2.37}$$

where

$$N_s \equiv \frac{\Delta U}{\hbar\omega_p} = \frac{1}{\sqrt{2}}\left(\frac{E_J}{E_C}\right)^{1/2}\left[\left(1 - I_r^2\right)^{1/4} - I_r\left(1 - I_r^2\right)^{-1/4}\cos^{-1} I_r\right] \tag{2.38}$$

is the number of energy levels in the well obtained from a full tilted washboard potential and f_Γ^n is a correction term [23, 24]. Appendix A shows a MATLAB code to solve the Schrödinger's equation for a single Josephson junction to obtain the escape rates. In my experiment, I measure the total escape rate from all energy levels. Since escape rates from the various energy levels differ by a factor of ~ 500

to 1000 we are able to distinguish which levels the Josephson junction phase tunnels from. The procedure to distinguish levels is described in detail in chapter 4.

The energy level spacings can also be obtained by solving Schrödinger's equation for the Hamiltonian in Eq. 2.31 with a full washboard potential and a decaying boundary condition [23, 24]. The calculated energy level spacing between level $|n\rangle$ and $|n+1\rangle$ can be written as

$$\omega_{n,n+1} = \omega_p \; f_\omega^n \left(N_s\right). \tag{2.39}$$

where f_ω^n is a correction term and N_s is the number of energy levels in the well shown in Eq. 2.38. Appendix A gives the code I used to calculate this factor and Strauch's thesis [24] contains a detailed discussion.

2.3.6 $\hat{\gamma}$ and $\hat{n}$ uncertainty relation

While the underlying physics of the Josephson effects is quantum mechanical, it was not apparent that the dynamics of the phase difference would require quantum mechanics as well until the discovery of Macroscopic quantum tunneling (MQT) [26]. Although it is known from the BCS theory that the Cooper pairs are in a coherent state (the condensate), the discovery of MQT was surprising because the Josephson junction itself is a macroscopic object that is directly coupled to the rest of the world through leads to the current bias source. Observation of MQT proved that if a macroscopic object like a Josephson junction is reasonably well-isolated [10, 11], it can show quantum mechanical behavior.

In a quantum mechanical treatment, the two conjugate variables γ and p_γ are conjugate operators similar to $\hat{x}$ and $\hat{p}$ where the relationship is $\hat{\gamma} \leftrightarrow \hat{x}$ and $\hat{p_\gamma} \leftrightarrow \hat{p}$.

Thus one expects the commutation relation of $\hat{\gamma}$ and $\hat{p_\gamma}$ is [13]

$$[\hat{\gamma}, \hat{p_\gamma}] = i\hbar. \tag{2.40}$$

I note that $\hat{p_\gamma}$ is related to the voltage V across the junction because V is related to the time derivative of $\hat{\gamma}$. From Eq. 2.29, $\hat{p_\gamma}$ is given by

$$\hat{p_\gamma} = \left(\frac{\Phi_0}{2\pi}\right)^2 C\dot{\hat{\gamma}} = \frac{\Phi_0}{2\pi} CV = \frac{\Phi_0}{2\pi}\hat{Q} \tag{2.41}$$

where $\hat{Q}$ is the charge on one plate of the capacitor C of the Josephson junction. If there are N Cooper pairs on the capacitor, then $\hat{Q}$ = - 2e$\hat{N}$; $\hat{N}$ is the number operator for the number of Cooper pairs on the capacitor. Therefore,

$$\hat{p_\gamma} = \frac{\Phi_0}{2\pi}\hat{Q} = -\frac{\hbar}{2e} 2e\hat{N} = -\hbar\hat{N} \tag{2.42}$$

and the commutation relation, Eq. 2.40 becomes

$$[\hat{\gamma}, \hbar\hat{N}] = -i\hbar \tag{2.43}$$

or

$$[\hat{\gamma}, \hat{N}] = -i. \tag{2.44}$$

This result implies that $\hat{\gamma}$ and $\hat{N}$ obey an uncertainty relation $\Delta\gamma\Delta N \geq 1/2$ where $\Delta\gamma$ is the uncertainty in $\hat{\gamma}$ and ΔN is the uncertainty in $\hat{N}$. If we know exactly how many Cooper pairs exist on the Josephson junction, we lose information on γ and the amount of supercurrent flowing through the junction. This phenomena can be interpreted as electrostatic energy causing the phase to delocalize [29].

We can choose either the phase representation or the number (charge) represen-

tation for the Hamiltonian. In the phase representation, the Hamiltonian becomes

$$\hat{H} = \frac{1}{2}\left(\frac{\Phi_0}{2\pi}\right)^2 C\dot{\hat{\gamma}}^2 - \frac{\Phi_0}{2\pi} I_0 \cos\gamma \tag{2.45}$$

where I = 0. The Josephson coupling energy is

$$\frac{\Phi_0}{2\pi}\cos\hat{\gamma} = \frac{\Phi_0}{2\pi}\frac{e^{i\hat{\gamma}} + e^{-i\hat{\gamma}}}{2}. \tag{2.46}$$

and $e^{\pm i\hat{\gamma}}$ is the translation operator which satisfies

$$e^{\pm i\hat{\gamma}}|N\rangle = |N \mp 1\rangle. \tag{2.47}$$

In the same manner as a translation operator for $\hat{x}$ [30], $e^{\pm i\hat{\gamma}}$ changes a number state by ± 1. Thus $e^{\pm i\hat{\gamma}}$ can be written as

$$e^{\pm i\hat{\gamma}} = \sum_N e^{\pm i\hat{\gamma}}|N\rangle\langle N| = \sum_N |N \mp 1\rangle\langle N|. \tag{2.48}$$

Therefore, in number representation, the Hamiltonian becomes

$$\hat{H} = \frac{2e^2}{C}(\hat{N})^2 - \frac{\Phi_0}{4\pi} I_0 \sum_N \left(|N-1\rangle\langle N| + |N+1\rangle\langle N|\right). \tag{2.49}$$

Examination of Eq. 2.49 reveals that the Hamiltonian does not commute with either $\hat{\gamma}$ or $\hat{N}$. The kinetic energy part is associated with charge ($\hat{N}$) and gives the "charging energy". The potential energy is associated with phase ($\hat{\gamma}$) and is the source of the "Josephson coupling energy". In many cases, either $\hat{N}$ or γ is much more sharply defined. Which operator is sharper determines which representation we choose for the Hamiltonian. For the Josephson junction phase qubit, γ is relatively well-defined, so it is the natural coordinate (phase representation). The number representation is in Ch. 9, where I discuss the Cooper pair box.

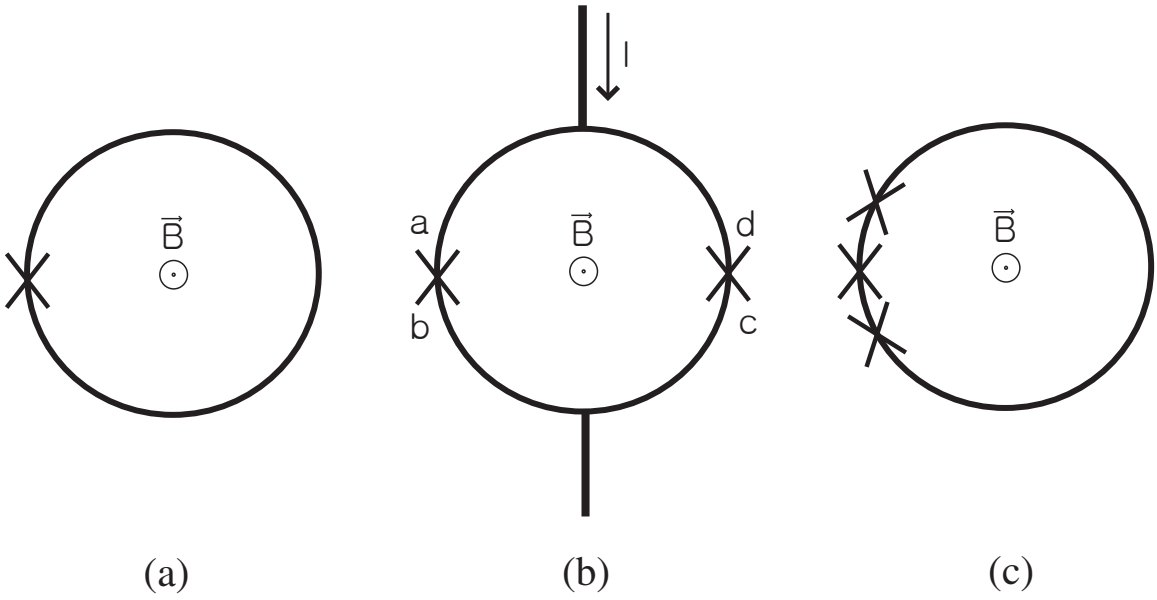

Figure 2.4: Types of SQUIDs. (a) Schematic of an rf SQUID, (b) a dc SQUID and (c) a three junction SQUID.

2.4 Classical properties of SQUIDs

2.4.1 What is a SQUID?

SQUID is an acronym for **S**uperconducting **QU**antum **I**nterference **D**evice. There are three main types of SQUIDs (see Fig. 2.4). The rf SQUID is formed by placing one Josephson junction in a superconducting loop and uses only a flux bias [see Fig 2.4(a)]. The dc SQUID is formed by placing two Josephson junctions in a loop and uses a current bias and a flux bias [see Fig 2.4(b)]. Three junction SQUIDs are formed by placing three small or ultrasmall junctions in a loop [see Fig 2.4(c)]. The dc SQUID was invented in 1964 by Jaklevic, Lambe, Silver, and Mercereau from Ford Research Labs [31]. A year later, Zimmerman and Silver from Ford Research Labs invented the rf SQUID [32]. As the most sensitive known devices for detecting magnetic flux, SQUIDS have been used as a magnetic field detector in many applications [33, 34]. In this thesis I am mainly interested in the dc SQUID since it forms the basis for the dc SQUID phase qubit. Here I review some basic classical properties of the dc SQUID [35, 16].

2.4.2 Flux-phase relation: fluxoid quantization rule revisited

In Eq. 2.15, I showed the fluxoid quantization rule, which I can write as:

$$\frac{m_e}{2e^2 n_s} \oint \mathbf{J} \cdot d\mathbf{l} + \int \mathbf{B} \cdot d\mathbf{a} = n\Phi_0. \tag{2.50}$$

This result can be generalized to describe current and flux in a dc SQUID even though the SQUID is not a full superconducting ring. For a SQUID, the phase differences across each junction must be taken into account. Consider the diagram of a SQUID shown in Fig. 2.5. The points a, b, c and d indicate points on the

SQUID loop. First, from Eq. 2.10 I can write

$$\oint \mathbf{J} \cdot d\mathbf{l} = \frac{-2en_s}{m_e} \left[\hbar \oint \nabla\theta(\mathbf{r}) \cdot d\mathbf{l} + 2e \oint \mathbf{A} \cdot d\mathbf{l} \right]. \tag{2.51}$$

By integrating along the lower half of the SQUID loop from b to c, we obtain [16]

$$\int_b^c \mathbf{J} \cdot d\mathbf{l} = \frac{-2en_s}{m_e} \left[\hbar \int_b^c \nabla\theta(\mathbf{r}) \cdot d\mathbf{l} + 2e \int_b^c \mathbf{A} \cdot d\mathbf{l} \right], \tag{2.52}$$

and then by integrating along the upper half of the SQUID loop from d to a, we obtain

$$\int_d^a \mathbf{J} \cdot d\mathbf{l} = \frac{-2en_s}{m} \left[\hbar \int_d^a \nabla\theta(\mathbf{r}) \cdot d\mathbf{l} + 2e \int_d^a \mathbf{A} \cdot d\mathbf{l} \right]. \tag{2.53}$$

If the superconductor that forms the SQUID is thick enough, we can choose a path inside the superconductor such that integration over the current density is negligible, that is:

$$\int_d^a \mathbf{J} \cdot d\mathbf{l} \approx 0 \tag{2.54}$$

and since

$$\theta_2 - \theta_1 = \int_1^2 \nabla\theta \cdot d\mathbf{l}, \tag{2.55}$$

Eqs. 2.52 and 2.53 become

$$-\frac{m_e}{2e\hbar n_s} \int_b^c \mathbf{J} \cdot d\mathbf{l} = \theta_c - \theta_b + \frac{2\pi}{\Phi_0} \int_b^c \mathbf{A} \cdot d\mathbf{l} = 0, \tag{2.56}$$

$$-\frac{m_e}{2e\hbar n_s} \int_d^a \mathbf{J} \cdot d\mathbf{l} = \theta_a - \theta_d + \frac{2\pi}{\Phi_0} \int_d^a \mathbf{A} \cdot d\mathbf{l} = 0 \tag{2.57}$$

where I used $2e/\hbar = 2\pi/\Phi_0$. From the definition of the gauge invariance phase differences γ_{ij},

$$\gamma_{ij} = \theta_i - \theta_j - \frac{2\pi}{\Phi_0} \int_i^j \mathbf{A} \cdot d\mathbf{l}, \tag{2.58}$$

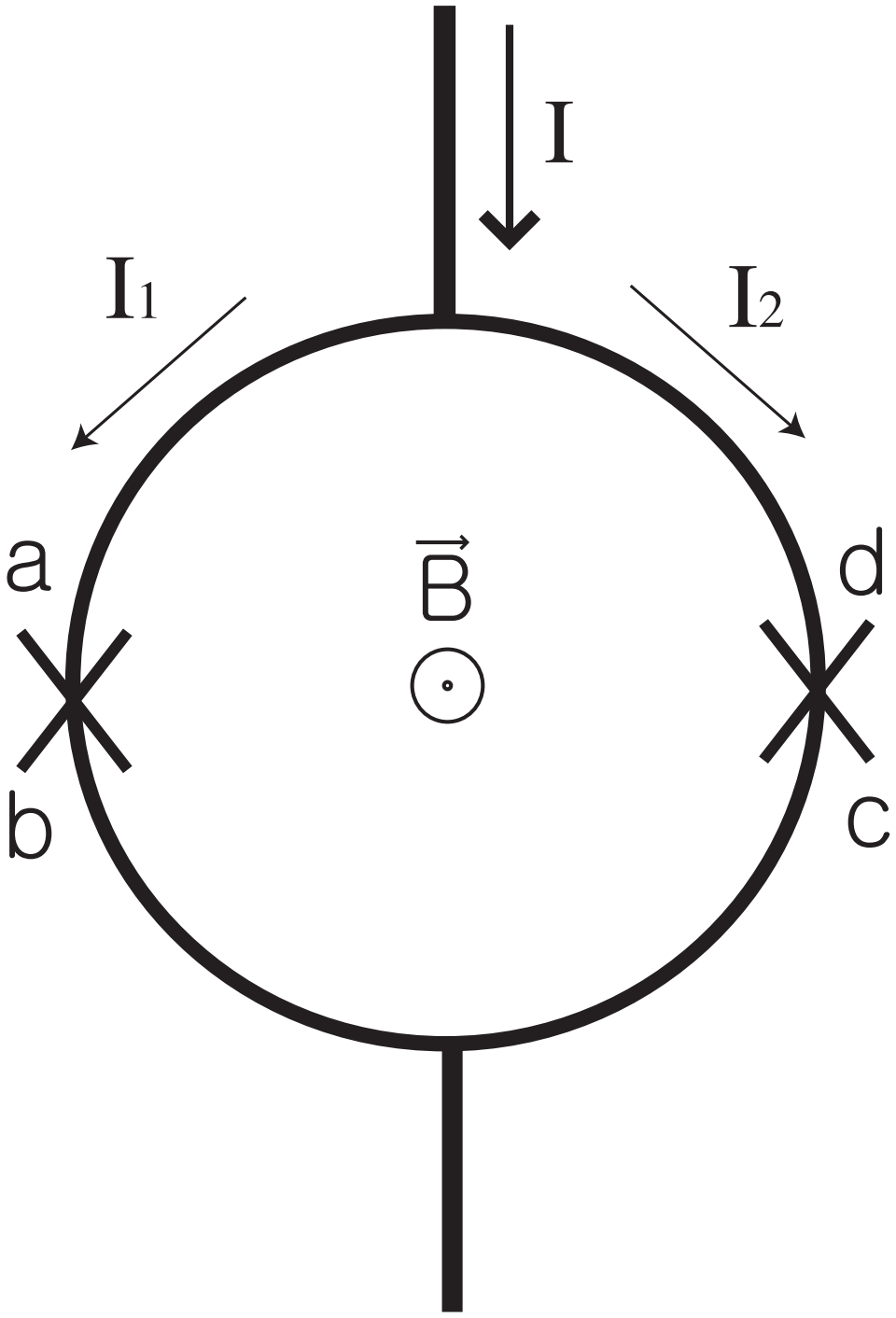

Figure 2.5: Schematic of a dc SQUID.

the phase difference of the left junction (γ_{ab}) and the right junction (γ_{dc}) is defined by

$$\gamma_{ab} = \theta_a - \theta_b - \frac{2\pi}{\Phi_0}\int_a^b \mathbf{A}\cdot d\mathbf{l} \tag{2.59}$$

$$\gamma_{dc} = \theta_d - \theta_c - \frac{2\pi}{\Phi_0}\int_d^c \mathbf{A}\cdot d\mathbf{l}. \tag{2.60}$$

where $\hbar/2e = \Phi_0/2\pi$ and the line integrals are taken through the left and right junction, respectively, from top to bottom in Figure 2.5.

The superconducting phase around the SQUID loop must be single-valued, i.e. the sum of the phase differences around the loop must satisfy

$$\oint \nabla\theta(\mathbf{r})\cdot d\mathbf{l} = 2\pi n \tag{2.61}$$

where n is an integer. Substituting Eqs. 2.56, 2.57, 2.59 and 2.60 into Eq. 2.61 yields

$$\begin{aligned}
\oint \nabla\theta(\mathbf{r})\cdot d\mathbf{l} &= \int_a^b \nabla\theta(\mathbf{r})\cdot d\mathbf{l} + \int_b^c \nabla\theta(\mathbf{r})\cdot d\mathbf{l} + \int_c^d \nabla\theta(\mathbf{r})\cdot d\mathbf{l} + \int_d^a \nabla\theta(\mathbf{r})\cdot d\mathbf{l} \\
&= (\theta_b - \theta_a) + (\theta_c - \theta_b) + (\theta_d - \theta_c) + (\theta_a - \theta_d) \\
&= -\gamma_{ab} - \frac{2\pi}{\Phi_0}\int_a^b \mathbf{A}\cdot d\mathbf{l} - \frac{2\pi}{\Phi_0}\int_b^c \mathbf{A}\cdot d\mathbf{l} + \gamma_{dc} + \frac{2\pi}{\Phi_0}\int_d^c \mathbf{A}\cdot d\mathbf{l} - \frac{2\pi}{\Phi_0}\int_d^a \mathbf{A}\cdot d\mathbf{l} \\
&= -\gamma_{ab} - \frac{2\pi}{\Phi_0}\int_a^b \mathbf{A}\cdot d\mathbf{l} - \frac{2\pi}{\Phi_0}\int_b^c \mathbf{A}\cdot d\mathbf{l} + \gamma_{dc} - \frac{2\pi}{\Phi_0}\int_c^d \mathbf{A}\cdot d\mathbf{l} - \frac{2\pi}{\Phi_0}\int_d^a \mathbf{A}\cdot d\mathbf{l} \\
&= -\frac{2\pi}{\Phi_0}\oint \mathbf{A}\cdot d\mathbf{l} + \gamma_{dc} - \gamma_{ab} \\
&= 2\pi n.
\end{aligned} \tag{2.62}$$

Since

$$\oint \mathbf{A}\cdot d\mathbf{l} = \int \mathbf{B}\cdot d\mathbf{a} = \Phi \tag{2.63}$$

where Φ is the total flux in the SQUID loop. I can then write Eq. 2.62 as [16]:

$$\gamma_{dc} - \gamma_{ab} = \gamma_2 - \gamma_1 = 2\pi n + \frac{2\pi\Phi}{\Phi_0}. \tag{2.64}$$

I set $\gamma_{dc} = -\gamma_{cd} = \gamma_2$ and $\gamma_{ab} = \gamma_1$ so that the current through each junction flows from the top to the bottom. Here γ_1 is the phase difference of the junction 1 (ab) where the current I_1 going through the junction 1 flows from a to b, and γ_2 is the phase difference of the junction 2 (dc) where the current I_2 going through the junction 2 flows from d to c.

The total flux Φ includes any external applied flux Φ_a and any flux generated by the current J circulating around the loop. Including these explicitly gives the flux-phase relation:

$$\gamma_2 - \gamma_1 = 2\pi n + \frac{2\pi(\Phi_a + LJ)}{\Phi_0} \tag{2.65}$$

where L is the loop inductance of the SQUID.

2.4.3 SQUID potential energy function

In this section I find the equations of motion and derive the potential energy function of the dc SQUID [35, 36]. Figure 2.6 shows a more detailed circuit diagram of the dc SQUID. In this diagram, J1 is junction 1 and J2 is junction 2, and C_1 and C_2 are the junction capacitances of J1 and J2. J1 and J2 are connected through two inductors L_1 and L_2 that form the SQUID loop. M is the mutual inductance between the SQUID loop and a flux bias current source I_f which produces an applied flux Φ_a. Finally, I is the current bias source.

Ignoring any normal shunting paths through the junction from current conservation, we can write

$$I = I_1 + I_2 = I_{01}\sin\gamma_1 + I_{02}\sin\gamma_2 + C_1\frac{\Phi_0}{2\pi}\ddot{\gamma}_1 + C_2\frac{\Phi_0}{2\pi}\ddot{\gamma}_2 \tag{2.66}$$

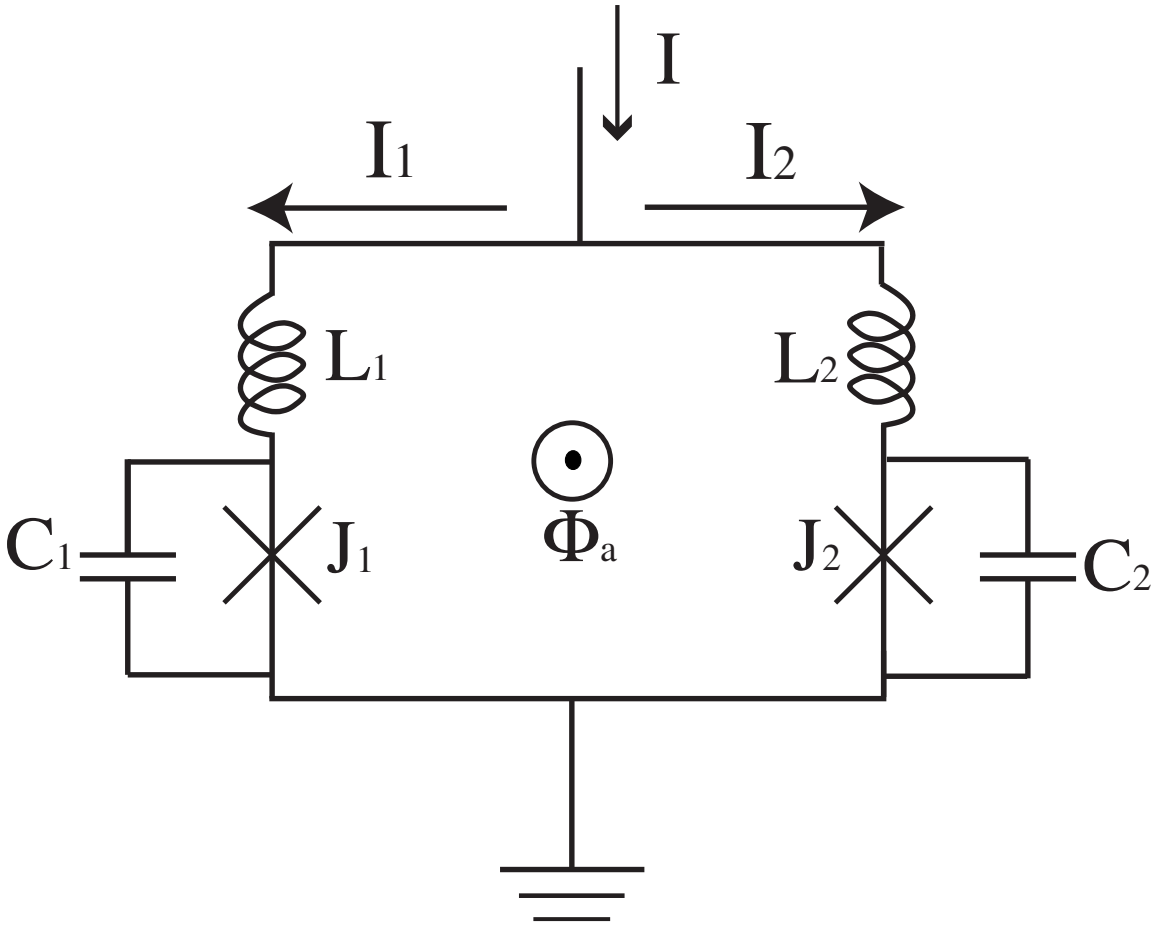

Figure 2.6: Schematic of a dc SQUID. J1 is junction 1 and J2 is junction 2. C_1 and C_2 are junction capacitances of J1 and J2. J1 and J2 are connected through two inductors on the SQUID loop, L_1 and L_2 and we will assume the total inductance is $L = L_1 + L_2$. Φ_a is the applied flux. I is the current bias source.

where I_1 is the current in the left arm of the SQUID and I_2 is the current in the right arm which are given by

$$I_1 = I_{01} \sin \gamma_1 + C_1 \frac{\Phi_0}{2\pi} \ddot{\gamma_1} \tag{2.67}$$

$$I_2 = I_{02} \sin \gamma_2 + C_2 \frac{\Phi_0}{2\pi} \ddot{\gamma_2}. \tag{2.68}$$

The flux-phase relation, as given by Eq. 2.65, can be written as:

$$\gamma_2 - \gamma_1 = 2\pi\phi_a + \frac{2\pi L_1}{\Phi_0} I_1 - \frac{2\pi L_2}{\Phi_0} I_2. \tag{2.69}$$

$\phi_a = \Phi_a/\Phi_0$ is a dimensionless applied flux, and I_{01} and I_{02} are the critical currents of junction 1 and junction 2, respectively. [1].

Here, the current I and dimensionless flux ϕ_a are external control parameters. Substituting Eq. 2.67 into Eq. 2.69 gives

$$\gamma_2 - \gamma_1 = 2\pi\phi_a + \frac{2\pi L_1}{\Phi_0} I_1 - \frac{2\pi L_2}{\Phi_0} (I - I_1) \tag{2.70}$$

$$= 2\pi\phi_a + \frac{2\pi(L_1 + L_2)}{\Phi_0} (I_{01} \sin \gamma_1 + C_1 \frac{\Phi_0}{2\pi} \ddot{\gamma_1}) - \frac{2\pi L_2 I}{\Phi_0}. \tag{2.71}$$

and substituting Eq. 2.68 into Eq. 2.69 gives

$$\gamma_2 - \gamma_1 = 2\pi\phi_a + \frac{2\pi L_1}{\Phi_0} (I - I_2) - \frac{2\pi L_2}{\Phi_0} I_2,$$

$$= 2\pi\phi_a + \frac{2\pi L_1}{\Phi_0} I - \frac{2\pi(L_1 + L_2)}{\Phi_0} (I_{02} \sin \gamma_2 + C_2 \frac{\Phi_0}{2\pi} \ddot{\gamma_2}). \tag{2.72}$$

[1] I assume that a flux Φ_1 generated from the inductance L_1 and current I_1, is calculated with respect to the area of the SQUID loop and so as Φ_2

Thus the equations of motion for γ_1 and γ_2 become

$$\frac{\Phi_0}{2\pi(L_1+L_2)}(\gamma_2-\gamma_1)=\frac{\Phi_0}{(L_1+L_2)}\phi_a+I_{01}\sin\gamma_1+C_1\frac{\Phi_0}{2\pi}\ddot{\gamma_1}-\frac{L_2}{L_1+L_2}I \quad (2.73)$$

$$\frac{\Phi_0}{2\pi(L_1+L_2)}(\gamma_2-\gamma_1)=\frac{\Phi_0}{(L_1+L_2)}\phi_a-I_{02}\sin\gamma_2-C_2\frac{\Phi_0}{2\pi}\ddot{\gamma_2}+\frac{L_1}{L_1+L_2}I \quad (2.74)$$

Now if we had the Lagrangian $\mathcal{L}$, the equations of motion could be found from,

$$\frac{d}{dt}\frac{\partial\mathcal{L}}{\partial\dot{\gamma_1}}-\frac{\partial\mathcal{L}}{\partial\gamma_1}=0 \quad (2.75)$$

$$\frac{d}{dt}\frac{\partial\mathcal{L}}{\partial\dot{\gamma_2}}-\frac{\partial\mathcal{L}}{\partial\gamma_2}=0. \quad (2.76)$$

Comparing Eqs. 2.73 and 2.74 to Eqs. 2.75 and 2.76, we find the following Lagrangian as

$$\mathcal{L}=\frac{\Phi_0^2}{4\pi^2}\Bigg[(C_1\dot{\gamma_1}^2+C_2\dot{\gamma_2}^2)+\frac{2\pi(I_{01}\cos\gamma_1+I_{02}\cos\gamma_2)}{\Phi_0}-\frac{(\gamma_2-\gamma_1)^2}{2L} \quad (2.77)$$
$$-\frac{2\pi\phi_a(\gamma_2-\gamma_1)}{L}+\frac{2\pi I}{\Phi_0}\left(\frac{L_2\gamma_1+L_1\gamma_2}{L}\right)\Bigg]$$

where the total loop inductance $L\simeq L_1+L_2$. Here a constant $\Phi_0/2\pi$ is multiplied to $\mathcal{L}$ to give the Lagrangian the dimension of energy. The potential energy U for the dc SQUID phase qubit is then obtained by inspection from Eq. 2.77

$$U=\frac{\Phi_0}{2\pi}\left[-I_{01}\cos\gamma_1-I_{02}\cos\gamma_2+\frac{\Phi_0}{4\pi L}(\gamma_2-\gamma_1)^2+\frac{\Phi_0}{L}\phi_a(\gamma_2-\gamma_1)-I\left(\frac{L_2\gamma_1+L_1\gamma_2}{L}\right)\right]. \quad (2.78)$$

It is convenient to normalize U with respect to the total critical current I_0 and define a dimensionless potential:

$$u=\frac{2\pi U}{\Phi_0 I_0}=-\frac{I_{01}}{I_0}\cos\gamma_1-\frac{I_{02}}{I_0}\cos\gamma_2+\frac{\Phi_0}{4\pi LI_0}(\gamma_2-\gamma_1+2\pi\phi_a)^2+4\pi^2\phi_a^2-\frac{I}{I_0}\left(\frac{L_2\gamma_1+L_1\gamma_2}{L}\right). \quad (2.79)$$

where $2I_0 = I_{01} + I_{02}$. The first and the second terms in Eq. 2.79 are due to the Josephson coupling energies of junction 1 and 2 respectively (see fig. 2.5). The third and the fourth terms can be combined and yields a quadratic term in $\gamma_2 - \gamma_1 - 2\pi\phi_a$ which causes coupling between the two junction phases. This term accounts for the magnetic energy stored in the SQUID inductances. The last term is the energy due to the bias current.

2.4.4 Current-flux map

In a dc SQUID, the critical current I_c is the maximum current that can flow through the SQUID loop with zero voltage drop. Many key properties of the SQUID arise from the fact that the critical current changes as a function of the applied magnetic flux (see Fig. 2.6). Moreover, depending on the inductances and the critical currents of each junction, the SQUID can have a single critical current or multiple critical currents at a given applied flux. Multiple critical currents typically occur in our dc SQUID qubit because we choose $\beta = \pi L(I_{01} + I_{02})/\Phi_0 \gg 1$ for isolation purposes and this allows the loop to trap a persistent circulating current.

The relation between critical current and applied flux is best visualized by plotting the switching current vs. flux; *i.e.* I versus Φ_a. In practice, I determine SQUID parameters such as the total loop inductance L, the critical currents of each junction, and the mutual inductance between the SQUID loop and the feedback coil from the measurements of the current-flux map.

We can calculate the current-flux map classically from the equations of motion. In the classical model, the critical current is the maximum static current that can flow through the SQUID with constant phase across the junctions. To calculate the critical current as a function of the applied flux, I use an approach described by

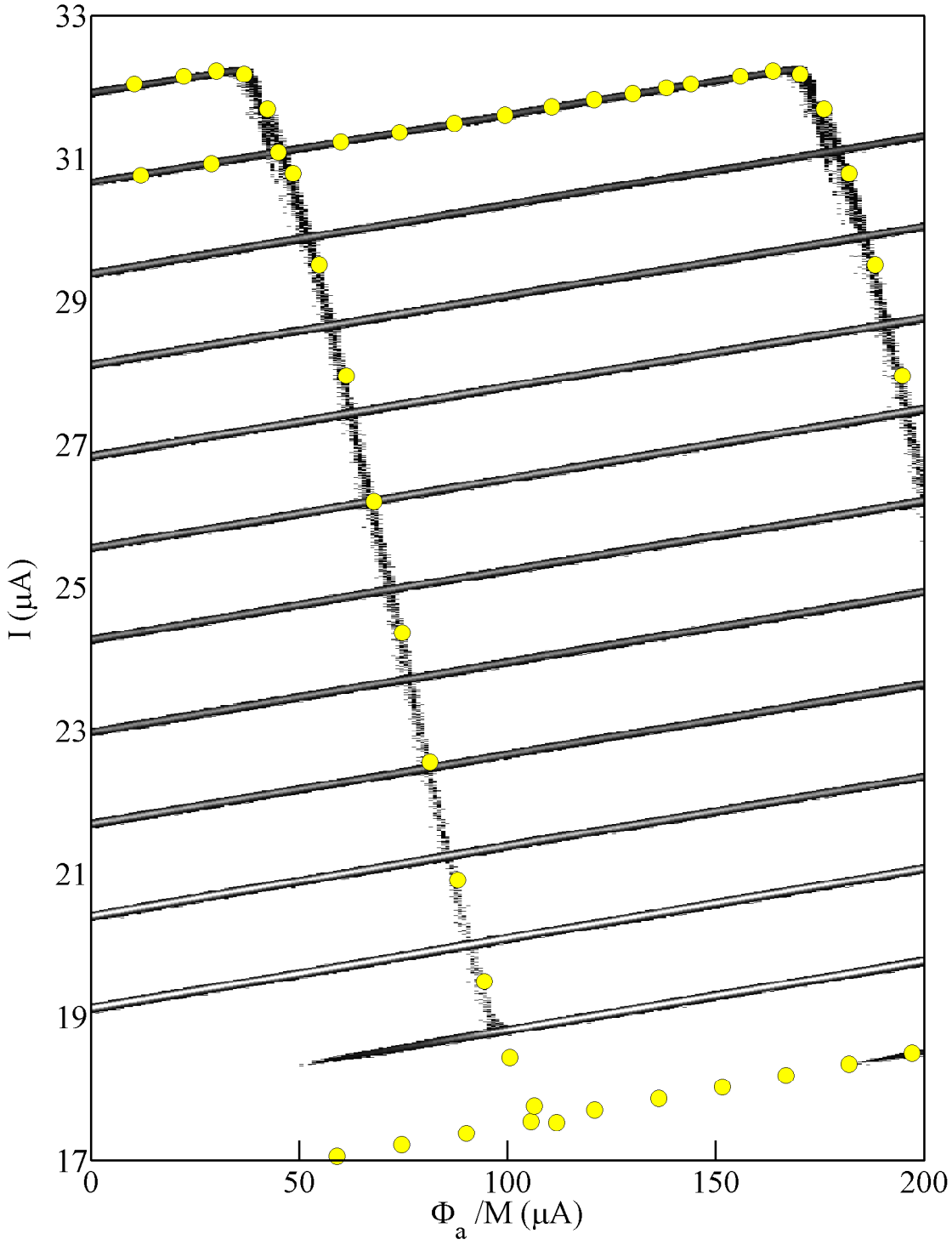

Figure 2.7: Critical current versus flux curve. Yellow dots show results from the calculation of the critical current using a method of Tsang *et al.* [37]. Solid curves (which are made from small dashes) are measured switching currents for the dc SQUID phase qubit AL1 at 80 mK.

Tsang *et al.* [37]. They start from the static current conservation equation,

$$I = I_{01} \sin \gamma_1 + I_{02} \sin \gamma_2 \tag{2.80}$$

and use the flux-phase relation as a constraint:

$$\gamma_1 - \gamma_2 = 2\pi\phi_a + \frac{2\pi L_1}{\Phi_0} I_1 - \frac{2\pi L_2}{\Phi_0} I_2 \tag{2.81}$$

where

$$I_1 = I_{01} \sin \gamma_1 \tag{2.82}$$

$$I_2 = I_{02} \sin \gamma_2 \tag{2.83}$$

are the static currents through junctions 1 and 2, respectively. Here any normal shunts across the junctions are ignored, since no current flows through at V = 0. Also the displacement currents from the capacitances do not contribute because we are dealing with the static, zero-voltage, situation before switching.

Our goal is to find the maximum of I subject to the constraint given by Eq. 2.81. The Euler-Lagrange equation is a convenient tool to find extrema functions that are subject to constraints. The goal is to find a function F of γ_1 and γ_2 which satisfies

$$\frac{\partial F}{\partial \gamma_1} = 0 \tag{2.84}$$

$$\frac{\partial F}{\partial \gamma_2} = 0 \tag{2.85}$$

$$\frac{\partial F}{\partial \gamma_2} = 0 \tag{2.86}$$

when $I(\gamma_1, \gamma_2)$ is maximized and the constraint given by Eq. 2.81 is also satisfied.

The appropriate F is

$$F(\gamma_1(t), \gamma_2(t)) = I_{01} \sin \gamma_1 + I_{02} \sin \gamma_2 + \lambda \left(\gamma_1 - \gamma_2 - 2\pi\phi_a - \frac{2\pi L_1}{\Phi_0} I_1 + \frac{2\pi L_2}{\Phi_0} I_2 \right) \tag{2.87}$$

where λ is the Lagrange multiplier. From the solutions γ_1 and γ_2 of Eqs. 2.84 to 2.86, we find the currents $I_1(\gamma_1)$ and $I_2(\gamma_2)$ which maximize or minimize I. The equations can not be solved analytically but the numerical solution is straightforward.

Figure 2.7 shows a plot of a best fit calculation of the critical currents vs. applied flux (circles) compared to experimental data (solid curves). The data was collected for an Al/AlO_x/Al dc SQUID, device AL1. AL1 is an asymmetric dc SQUID with$L_1 \gg L_2$. In the current-flux map, this results in switching events from each junction being distinguishable [37, 23]. The section of the I-Φ_a curves with higher slope with respect to the applied flux is due to junction 1 switching first, and the section with lower slope with respect to the applied flux is due to junction 2 switching first.

For the best fit, I find good agreement between the data and the simulation. The maximum of the curve gives the sum of the critical currents of J1 and J2 and the minimum of the line with higher slope gives the difference of the critical currents of J1 and J2, although this was not resolved in the data. Any two adjacent curves in this figure are separated along the current axis by almost exactly Φ_0/L, so I can get a good estimate for the total loop inductance L. Also the switchings curves are strictly periodic with period of Φ_0/M along the x-axis, so I can also obtain the mutual inductance M between the SQUID loop and the flux bias. In this case, the best fit was for $I_{01} = 21.401\ \mu A$, $I_{02} = 9.445\ \mu A$, $L_1 = 1.236$ nH, $L_2 = 5$ pH, and M = 15 pH.

2.5 Application of Josephson junctions to quantum computation

This thesis concerns the potential application of Josephson junctions to quantum computation. In this section, I review the types of superconducting qubits and summarize progress on them. I also introduce our dc SQUID phase qubit.

2.5.1 Superconducting qubits

Superconducting qubits are classified into three main types: charge qubits, flux qubits and phase qubits.

Charge qubits are based on ultra-small Josephson junctions in which the charging energy ($Q^2/2C$) is dominant (see Fig. 2.8). Charge qubits use the two lowest energy states, represented in charge basis, as qubit states. For charge qubit, the Hamiltonian is dominated by the charging energy stored in the junction capacitor. The state can be manipulated by applying a gate voltage. The Cooper pair box is the best-known type of charge qubit [38]. The Hamiltonian of the Cooper pair box can essentially be obtained from Eq. 2.31 by changing from the phase basis into the charge (number) basis. Although the charge (number) states are not the exact eigenstates of the Hamiltonian [29], the energy eigenstates can be found from superpositions of a few number states by treating the Josephson energy term in Eq. 2.31 as a perturbation. An in-depth discussion of the Cooper pair box is given in chapter 9. The first experimental demonstration of coherent oscillations in a superconducting qubit was performed on a Cooper pair box by Nakamura *et al.* in 1999 [38]. The longest coherence time in charge qubit has been obtained by the Yale group [39, 40]; using a non-demolition readout [41, 42] they recently reported finding $T_2 \sim 2$ μs in a hybrid charge/phase qubit called the "transmon" [43].

Flux qubits are SQUIDs with one, two or three junctions. The basis states correspond to different amounts of flux in the SQUID loop or superpositions of such

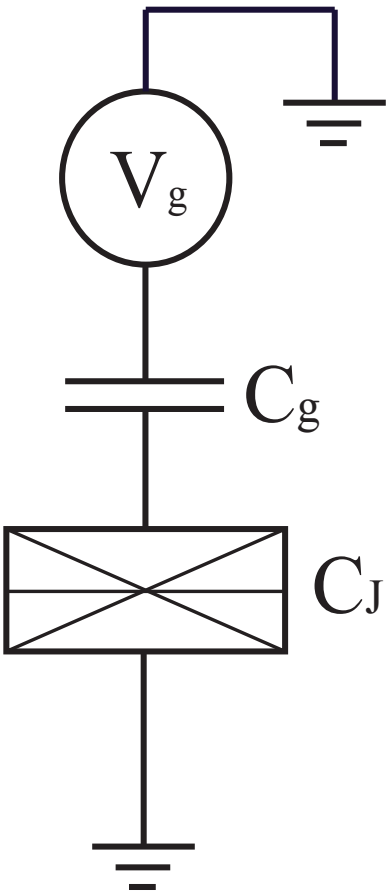

Figure 2.8: a Cooper-pair box with a single ultra small junction. C_J is the capacitance of the superconducting ultra small junction and C_g is the gate capacitance. V_g is the gate voltage.

states. An rf-SQUID with appropriate flux bias and choice of parameters is one example of a flux qubit. In flux qubits, the scale of the charging energy is comparable to the Josephson energy. The control variable is applied flux [13]. The flux qubit has a double-welled potential where the two flux states correspond to being trapped in one well or the other. The most popular form of the qubit has three junctions [44]. The Hamiltonian can be truncated and the reduced state space spanned by two flux states, similar to the two level approximation to the Hamiltonian of the Cooper pair box. Friedman *et al.* first observed avoided crossings of two flux states in their rf SQUID energy spectrum in 2000 [45]. The longest coherence time reported in the flux qubit so far is $T_2 \sim 4$ μs [46].

Phase qubits are based on large-area Josephson junctions where the Josephson energy is dominant and the phase is relatively well-defined. Phase qubits can be constructed from rf or dc SQUIDs so they share some similarities to flux qubits. However, the phase qubit states are the two lowest energy states of the washboard potential in a given well, not flux states in different wells. Ramos *et al.* first proposed that the two lowest energy levels from a single large-capacitance Josephson junction can be used as a phase qubit [12], but the isolation scheme for a single Josephson junction was not trivial. The first coherent oscillation in a phase qubit was observed in 2002 by Martinis *et al.* [47] in their dc SQUID phase qubit and the entanglement of two coupled phase qubits was reported in 2002 by Berkley *et al.* [48]. The longest coherence time reported on the phase qubit is $T_2 \sim 500$ ns [49].

2.5.2 dc SQUID phase qubit: design and basic idea, inductive isolation

In this section, I discuss in some detail the dc SQUID phase qubit and the idea behind its design.

Superconducting qubits are macroscopic devices that can readily couple to

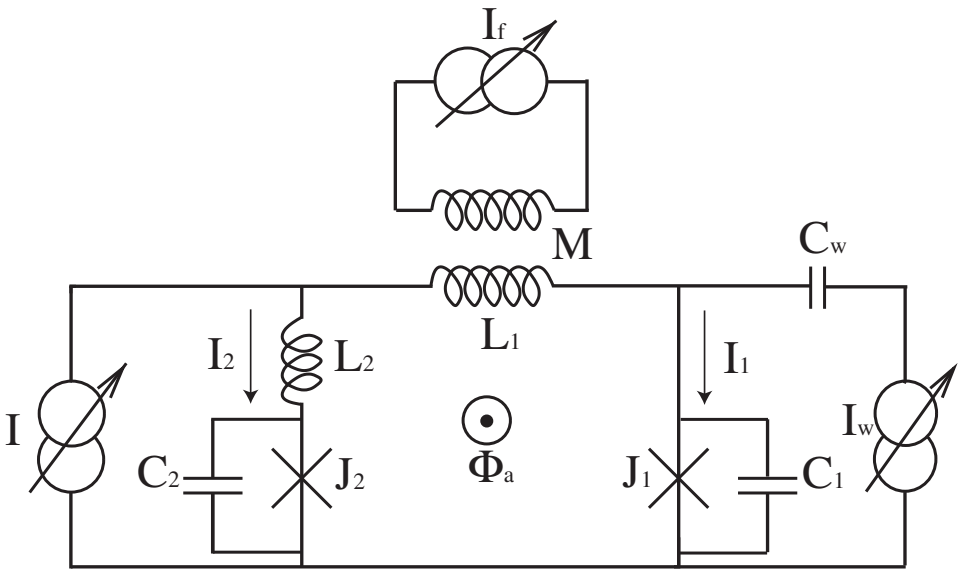

Figure 2.9: Schematic of a dc SQUID phase qubit. J1 is the qubit junction and J2 is the isolation junction. C_1 and C_2 are the capacitances of J1 and J2. J1 and J2 are connected through two inductors on the SQUID loop, L_1 and L_2. M is a mutual inductance between the SQUID loop and the current source I_f supplies the applied flux Φ_a. I is the current bias source. The microwave source I_w is coupled to the qubit junction J1 by capacitor C_w

many degrees of freedom in the environment. This undesirable coupling between a qubit and its environment can be reduced by good isolation and biasing schemes. Finding an optimal design for the qubit isolation is challenging because the state of the qubit still has to be manipulated and measured.

Inductive isolation for Josephson junction phase qubits was first introduced by Martinis *et al.* [47]. In this scheme, a qubit junction is shunted by a relatively large inductor in series with a Josephson junction (see Fig. 2.9). The second junction is called the "isolation junction" because it helps to isolate the qubit junction from current noise. In Fig. 2.9, junction J1 acts as a phase qubit and the rest of the SQUID serves as an inductive isolation network that filters out noise from the current bias leads; The inductive isolation network consists of a fixed inductance L_1, an isolation junction J2 and a parasitic inductance L_2. The junction J2 has an associated Josephson inductance L_{J2}.

When noise current is introduced into the bias leads, $L_1 + L_{J1}$ and $L_2 + L_{J2}$ work as an inductive current divider and only a fraction of the current noise will pass through the qubit junction J1. If there is a small fluctuations ΔI in the current bias, then we can write

$$\frac{\Delta I_1}{\Delta I_2} = \frac{L_2 + L_{J2}}{L_1 + L_{J1}} \tag{2.88}$$

where ΔI_1 is the corresponding current fluctuation going through the qubit junction J1, ΔI_2 is the current fluctuation going through the isolation junction and $\Delta I = \Delta I_1 + \Delta I_2$. By choosing $L_1 + L_{j1} \gg L_2 + L_{j2}$, we can reduce ΔI_1 with respect to ΔI_2. Typical inductances in my devices are $L_1 = 1$ nH, $L_{j1} = 20$ pH, $L_2 = 5$ pH and $L_{j2} = 40$ pH, which yields $\Delta I_1/\Delta I_2 \simeq 0.044$.

The inductive current divider also reduces the bias current that reaches the qubit. To compensate, we use a secondary current source, a flux bias Φ_a supplied by a current I_f that couples to the SQUID loop via a mutual inductance M (see Fig. 2.9). Noise ΔI_f on the flux bias line will also induce a noise current through

the qubit junction, where

$$\frac{\Delta I_1}{\Delta I_f} = \frac{M}{L_1 + L_{J1} + L_2 + L_{J2}}. \tag{2.89}$$

In qubit AL1, I found M $\approx$ 10 pH, $L_1 \approx 1$ nH and $L_1 \gg L_{j1} + L_2 + L_{j2}$. Equation 2.89 then gives $\Delta I_1/\Delta I_f \approx 0.01$.

In order to use a static flux bias to current-bias the qubit junction, the inductive isolation network must be superconducting. In practice, we detect the qubit states by monitoring when the qubit junction switches to the voltage state. For this voltage to be measurable, the isolation element must present some impedance when the qubit switches. If L_{J2} were just a small superconducting inductor, it would prevent a static voltage from appearing across the output leads and we would not be able to detect the junction switching voltage (See Fiq. 2.6). This is why the dc SQUID pase qubit has the isolation junction in the isolation network.

By placing a second Josephson junction into the inductive current divider we can achieve two purposes; a small inductor for isolation and a non-linear element that allows detection. The idea is that the isolation junction remains superconducting until the qubit junction switches. When the qubit switches, the bias current is shunted to the isolation junction which triggers the isolation junction to switch and leads to a voltage across the output leads. It also turns out that by using a Josephson inductor, we can tune the inductance ratio between the qubit branch and the isolation network. A detailed analysis of the isolation circuit is given in Chapter 5.

Chapter 3

Dynamics of a two-level quantum system

3.1 Introduction

Nuclear magnetic resonance (NMR) was first seen by Rabi in 1938 [50]. Later, Bloch *et al.* and Purcell *et al.* individually developed methods to measure nuclear magnetic resonance in solids (paraffin) [51] and liquids (water) [52, 53]. In 1946, Bloch introduced the equation of motion for nuclear magnetization in a magnetic field; these are the now well-known Bloch equations [52].

Atomic physicists soon adapted Bloch's theory to explain radiation phenomena in atoms. They modified the Bloch equations to obtain the optical Bloch equations, which describe how atoms interact with light [54]. The resulting models are now widely used to describe quantum behavior in two-level systems, as well as systems with more than two levels, such as the Cooper pair box or Josephson junction phase qubit.

In this chapter, I briefly review the quantum dynamics of two-level systems. I discuss the density matrix formalism and construct the optical Bloch equations. Next I discuss the density matrix formalism with dissipation and decoherence. Finally, I connect the optical Bloch equation to the density matrix description and show how to construct the Bloch vector for the Josephson phase qubit.

The main references of this chapter are an unpublished note by Dr. Wellstood [55], the book "Optical Resonance and Two Level Atoms" by Allen and Eberly [54] and "The Principles of Nuclear Magnetism" by Abragam [56].

3.2 Density matrix formalism for a two-level system

In general, a qubit is not necessarily in a pure state, but can be in an incoherent superposition of states or "mixed state". Such mixed states naturally form because of entanglement with the environment, and it is impossible to measure everything about the state of the system and the entangled environment. The density operator, $\hat{\rho}$, is an operator that gives the probabilities of the system being in certain states which can be measured by the experiment. Using the density operator, we can describe the evolution without knowing the complete wavefunction of the system and the environment.

I start by considering an isolated two-state system being driven by a periodic external force. Choosing the basis as the two qubit states of the qubit; $|0\rangle$ and $|1\rangle$, the density operator, $\hat{\rho}$ can be written as a 2 by 2 matrix,

$$\hat{\rho} = \begin{pmatrix} \langle 0|\hat{\rho}|0\rangle & \langle 0|\hat{\rho}|1\rangle \\ \langle 1|\hat{\rho}|0\rangle & \langle 1|\hat{\rho}|1\rangle \end{pmatrix} = \begin{pmatrix} \rho_{00} & \rho_{01} \\ \rho_{10} & \rho_{11} \end{pmatrix}. \tag{3.1}$$

where

$$|0\rangle = \begin{pmatrix} 1 \\ 0 \end{pmatrix} \tag{3.2}$$

and

$$|0\rangle = \begin{pmatrix} 0 \\ 1 \end{pmatrix}. \tag{3.3}$$

Two important properties of $\hat{\rho}$ are

$$Tr(\hat{\rho}) = \rho_{00} + \rho_{11} = 1 \tag{3.4}$$

and

$$\rho_{01} = \rho_{10}^{*}. \tag{3.5}$$

Also $\hat{\rho}$ satisfies the equation of motion,

$$i\hbar\frac{d\hat{\rho}}{dt} = [H, \hat{\rho}]. \tag{3.6}$$

Here I will consider the Hamiltonian

$$\hat{H} = \begin{pmatrix} E_0 & F_0\langle 0|\hat{x}|1\rangle \cos\omega t \\ F_0\langle 1|\hat{x}|0\rangle \cos\omega t & E_1 \end{pmatrix} = \hat{H}_0 + \hat{H}' \tag{3.7}$$

where

$$\hat{H}_0 = \begin{pmatrix} E_0 & 0 \\ 0 & E_1 \end{pmatrix} \tag{3.8}$$

is the unperturbed 2-level Hamiltonian and

$$H' = \begin{pmatrix} 0 & F_0\langle 0|\hat{x}|1\rangle \cos(\omega t) \\ F_0\langle 1|\hat{x}|0\rangle \cos(\omega t) & 0 \end{pmatrix} \tag{3.9}$$

describes a periodic drive field for exciting the two-level system. For convenience, I define $a_0 = F_0\langle 0|\hat{x}|1\rangle$ where $\hat{x}$ is a conjugate position operator (coordinate) for the two-level system that couples to the drive and I will assume a_0 is real. Equation 3.6 then gives four equations of motion,

$$i\hbar\frac{d\rho_{00}}{dt} = a_0(\rho_{10} - \rho_{01})\cos\omega t \tag{3.10a}$$

$$i\hbar\frac{d\rho_{01}}{dt} = a_0(\rho_{11} - \rho_{00})\cos\omega t - \Delta E\rho_{01} \tag{3.10b}$$

$$i\hbar\frac{d\rho_{10}}{dt} = -a_0(\rho_{11} - \rho_{00})\cos\omega t + \Delta E\rho_{10} \tag{3.10c}$$

$$i\hbar\frac{d\rho_{11}}{dt} = -a_0(\rho_{10} - \rho_{01})\cos\omega t. \tag{3.10d}$$

where $\Delta E = E_1 - E_0$, $\hat{H}_0|0\rangle = E_0|0\rangle$ and $\hat{H}_0|1\rangle = E_1|1\rangle$. Note that Eqs. 3.10 imply $d\rho_{11}/dt = -d\rho_{00}/dt$, which is essential for maintaining $Tr(\hat{\rho}) = 1$, and allows

ρ_{00} and ρ_{11} to be interpreted as the probabilities to find the system in $|0\rangle$ and $|1\rangle$ respectively.

3.3 Optical Bloch equations: two-level systems and magnetic spin

A spin-1/2 system is the proto-typical two-level system; we can define $|0\rangle$ as spin-down and $|1\rangle$ as spin-up. Due to its pictorial convenience, the language of magnetic spins and NMR is widely used to describe the behavior of two level systems, including qubits. In this section, I discuss the optical Bloch equations, which is a version of the Bloch equations [52, 53] for two-level systems. This section is largely based on Ch. 2 in "Optical resonance and two-level atoms" by Allen and Eberly [54].

3.3.1 Representing the Hamiltonian of a two-level system with Pauli matrices

Consider an atom interacting with an electric field $\hat{E}$ which drives transitions between two-levels, $|+\rangle$ and $|-\rangle$ of the atom. I can write the Hamiltonian as

$$\hat{H} = \hat{H}_0 - \hat{d} \cdot \hat{E}. \tag{3.11}$$

I will assume that the interaction energy $\hat{d} \cdot \hat{E}$ can be treated as a small perturbation. Here $\hat{H}_0$ is the unperturbed Hamiltonian and $\hat{d}$ is the electric dipole moment of the atom,

$$\hat{d} = -e\hat{r} \tag{3.12}$$

where $\hat{r}$ is the position vector of the electron with respect to the nucleus. Since our interest is only in two-levels, we can span the Hamiltonian with the basis $|+\rangle$ and $|-\rangle$, which are eigenstates of $\hat{H}_0$. In this case, $\hat{H}_0$ can be written as a 2 by 2 matrix

of the form:form

$$\hat{H}_0 = \begin{pmatrix} E_+ & 0 \\ 0 & E_- \end{pmatrix} \tag{3.13}$$

and the perturbation term becomes

$$\langle d \rangle \cdot \hat{E} = \begin{pmatrix} \langle + | \hat{d} | + \rangle & \langle + | \hat{d} | - \rangle \\ \langle - | \hat{d} | + \rangle & \langle - | \hat{d} | - \rangle \end{pmatrix} \cdot \hat{E} = \begin{pmatrix} 0 & \mathbf{d_R} + i\mathbf{d_I} \\ \mathbf{d_R} - i\mathbf{d_I} & 0 \end{pmatrix} \cdot \hat{E} \tag{3.14}$$

where only the off-diagonal terms are non-zero because of the spatial symmetry of $|+\rangle$ and $|-\rangle$ states in atomic systems. Here $\mathbf{d_R}$ and $\mathbf{d_I}$ are the real and imaginary parts of $\langle + | \hat{d} | - \rangle$.

It is useful to recall that any 2 by 2 matrix equation can be expressed in terms of the Pauli spin matrices and the identity matrix $\hat{I}$ [54]. In this case, Eq. 3.11 can be written as

$$\hat{H} = \frac{1}{2}(E_+ + E_-)\hat{I} + \frac{1}{2}(E_+ - E_-)\hat{\sigma_3} - (\mathbf{d_R} \cdot \hat{E})\hat{\sigma_1} + (\mathbf{d_I} \cdot \hat{E})\hat{\sigma_2}. \tag{3.15}$$

where

$$\hat{\sigma_1} \equiv \begin{pmatrix} 0 & 1 \\ 1 & 0 \end{pmatrix}, \hat{\sigma_2} \equiv \begin{pmatrix} 0 & -i \\ i & 0 \end{pmatrix}, \hat{\sigma_3} \equiv \begin{pmatrix} 1 & 0 \\ 0 & -1 \end{pmatrix} \tag{3.16}$$

are the Pauli spin matrices.

3.3.2 Equation of motion for a two-level system

To obtain the equation of motion of a two-level system, I note that the time evolution of Pauli operators obey the equation;

$$i\hbar\dot{\hat{\sigma}_n} = [\hat{\sigma_n}, \hat{H}] \tag{3.17}$$

for n = 1, 2, 3. Substituting Eq. 3.15 for $\hat{H}$, one finds

$$\dot{\hat{\sigma_1}}(t) = -\omega_0\hat{\sigma_2}(t) + \frac{2}{\hbar}[\mathbf{d_I}\cdot\hat{E}(t)]\hat{\sigma_3}(t) \tag{3.18a}$$

$$\dot{\hat{\sigma_2}}(t) = \omega_0\hat{\sigma_1}(t) + \frac{2}{\hbar}[\mathbf{d_R}\cdot\hat{E}(t)]\hat{\sigma_3}(t) \tag{3.18b}$$

$$\dot{\hat{\sigma_3}}(t) = -\frac{2}{\hbar}[\mathbf{d_R}\cdot\hat{E}(t)]\hat{\sigma_2}(t) - \frac{2}{\hbar}[\mathbf{d_I}\cdot\hat{E}(t)]\hat{\sigma_1}(t). \tag{3.18c}$$

where

$$\omega_0 = \frac{E_+ - E_-}{\hbar}. \tag{3.19}$$

Taking an expectation value of both sides of Eq. 3.18 and defining $s_n(t) = \langle\sigma_n(t)\hat{\sigma_n}\rangle$ [57], then I can write

$$\dot{s_1}(t) = -\omega_0 s_2(t) \tag{3.20a}$$

$$\dot{s_2}(t) = \omega_0 s_1(t) + \kappa E(t) s_3(t) \tag{3.20b}$$

$$\dot{s_3}(t) = -\kappa E(t) s_2(t). \tag{3.20c}$$

where $\kappa = 2|\mathbf{d_R}|/\hbar$ and E(t) = $E_0(t)[e^{i\omega t} + e^{-i\omega t}]$, is the electric field component parallel to $\mathbf{d_R}$. There are two additional assumptions I used to derive Eqs. 3.20(a - c); (i) the dipole matrix $\hat{d}$ is real so that $\mathbf{d_I}\cdot\hat{E}(t) = 0$ [54] and (ii) the correlation between the electric field and the atom can be ignored. The second condition implies that

$$\langle\hat{E}(t)\hat{\sigma_n}(t)\rangle \approx \langle\hat{E}(t)\rangle\langle\hat{\sigma_n}(t)\rangle. \tag{3.21}$$

Eqs. 3.20(a - c) are the optical Bloch equations [54] and equivalent to Bloch equations for describing the interactions between atoms and light. The solution $s_1(t), s_2(t), s_3(t)$ of the optical Bloch equations can be drawn as a vector that lies on the unit sphere (see Fig. 3.3.2). Eqs. 3.20 can be put into an equivalent vector

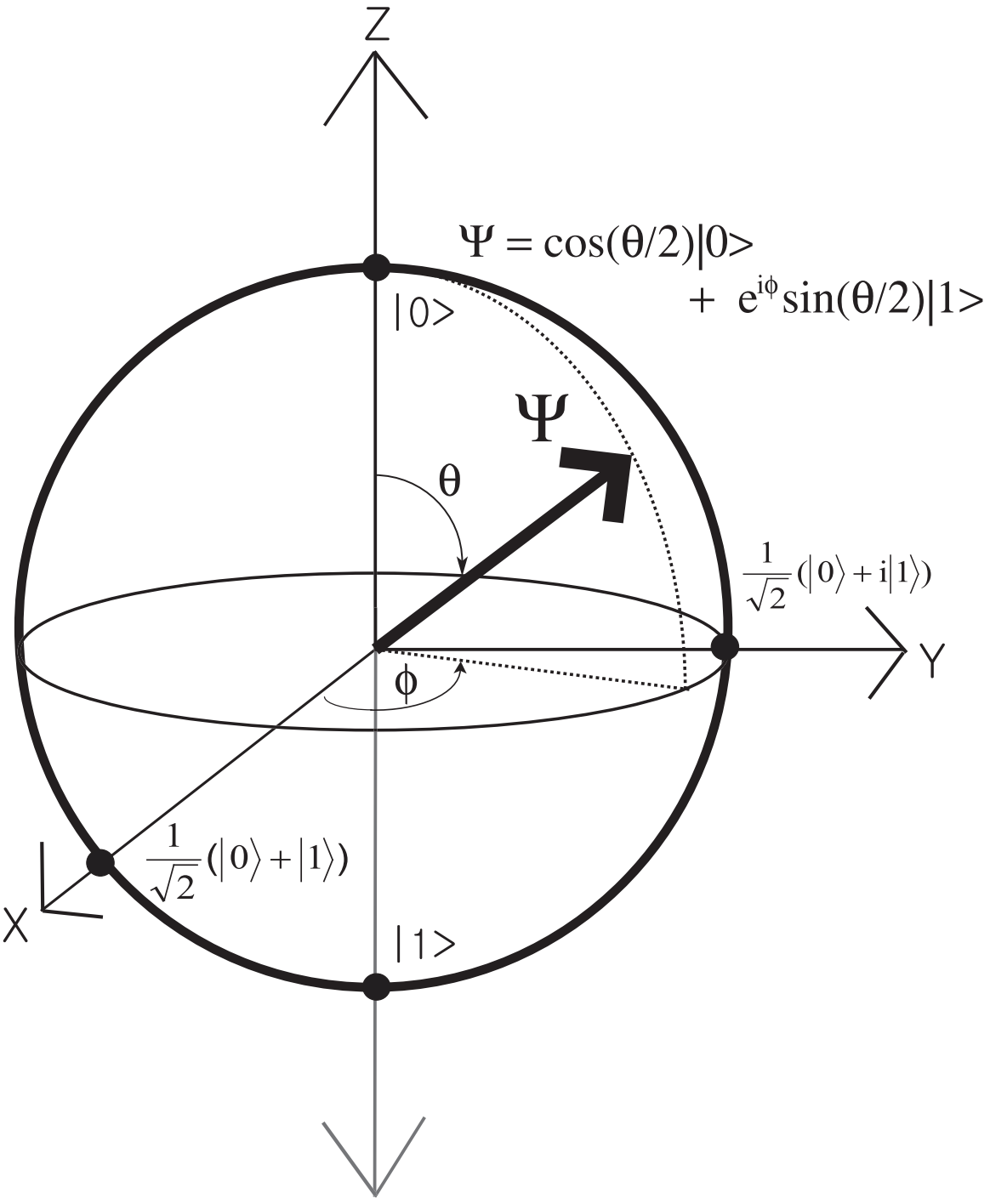

Figure 3.1: Two-level system represented as a vector on the Bloch sphere.

form for $\mathbf{s}(t) = [s_1(t), s_2(t), s_3(t)]$ as

$$\frac{d}{dt}\mathbf{s}(t) = \mathbf{\Omega}(t) \times \mathbf{s}(t) \tag{3.22}$$

where $\mathbf{\Omega}(t) = [-\kappa E_0(t)[e^{i\omega t} + e^{-i\omega t}], 0, \omega_0]$. The resulting behavior resembles the motion of a rotating rigid body or a classical spin vector where $\mathbf{\Omega}(t)$ is the torque applied to the spin vector $\mathbf{s}(t)$. In general, $\mathbf{\Omega}(t)$ can oscillate at frequency $\omega \sim \omega_0$ when E(t) is in resonance with the atom.

Our main interest is in the behavior of $\mathbf{s}(t)$. However, due to the moving $\mathbf{\Omega}(t)$, the motion of $\mathbf{s}(t)$ is not so simple. It is most convenient to describe $\mathbf{s}(t)$ in a frame which rotates at an angular frequency ω about the z axis. To proceed, we need to change from the fixed frame basis we have been using into the basis of a rotating frame. To change bases, we use the rotation matrix $\hat{U}$

$$\hat{U} = \begin{pmatrix} \cos(\omega t) & \sin(\omega t) & 0 \\ -\sin(\omega t) & \cos(\omega t) & 0 \\ 0 & 0 & 1 \end{pmatrix}. \tag{3.23}$$

In the rotating frame basis, $\mathbf{s}$ is transformed to $\mathbf{s_r}$ via;

$$\mathbf{s_r} = \hat{U}\mathbf{s} \tag{3.24}$$

$$= \begin{pmatrix} \cos(\omega t) & \sin(\omega t) & 0 \\ -\sin(\omega t) & \cos(\omega t) & 0 \\ 0 & 0 & 1 \end{pmatrix} \begin{pmatrix} s_1 \\ s_2 \\ s_3 \end{pmatrix} \tag{3.25}$$

$$= \begin{pmatrix} s_1\cos(\omega t) + s_2\sin(\omega t) \\ s_2\cos(\omega t) - s_1\sin(\omega t) \\ s_3 \end{pmatrix} = \begin{pmatrix} u \\ v \\ w \end{pmatrix} \tag{3.26}$$

and $\dot{\mathbf{s}}$ is transformed into

$$\frac{d\mathbf{s_r}}{dt} = \begin{pmatrix} \dot{u} \\ \dot{v} \\ \dot{w} \end{pmatrix}. \tag{3.27}$$

Similarly, the vector $\mathbf{\Omega}$ is transformed to $\mathbf{\Omega_r}$ in the rotating basis as

$$\begin{aligned}
\mathbf{\Omega_r} &= \hat{U}\mathbf{\Omega} && (3.28)\\
&= \begin{pmatrix} \cos(\omega t) & \sin(\omega t) & 0 \\ -\sin(\omega t) & \cos(\omega t) & 0 \\ 0 & 0 & 1 \end{pmatrix} \begin{pmatrix} -2\kappa E_0 \cos\omega t \\ 0 \\ \omega_0 \end{pmatrix} && (3.29)\\
&= \begin{pmatrix} -2\kappa E_0 \cos^2 \omega t \\ -2\kappa E_0 \cos\omega t \sin\omega t \\ \omega_0 \end{pmatrix} && (3.30)\\
&= \begin{pmatrix} -\kappa E_0 - \kappa E_0 \cos 2\omega t \\ -\kappa E_0 \sin 2\omega t \\ \omega_0 \end{pmatrix} && (3.31)
\end{aligned}$$

The dynamics should be the same no matter what basis I use. This implies that $\mathbf{s_r}$ observed in the fixed frame should be expressed in the same way even though I changed the basis into the basis of the rotating frame. Thus from Eq. 3.22, $\mathbf{s_r}$ observed in the fixed frame is written as

$$\left(\frac{d}{dt}\mathbf{s_r}(t)\right)_{fixed} = \mathbf{\Omega_r}(t) \times \mathbf{s_r}(t) \tag{3.32}$$

But in the rotating frame, $\mathbf{s_r}(t)$ will experience a fictitious torque due to rotation.

Thus the behavior of $\mathbf{s_r}(t)$ in the rotating frame is given by [58]

$$\left(\frac{d}{dt}\mathbf{s_r}(t)\right)_{rotating} = \left(\frac{d}{dt}\mathbf{s_r}(t)\right)_{fixed} - \vec{\omega}(t) \times \mathbf{s_r}(t) \tag{3.33}$$

$$= \mathbf{\Omega_r}(t) \times \mathbf{s_r}(t) - \vec{\omega} \times \mathbf{s_r}(t) \tag{3.34}$$

$$= (\mathbf{\Omega_r}(t) - \vec{\omega}) \times \mathbf{s_r}(t). \tag{3.35}$$

where $\tilde{\omega} = \omega\hat{z}$.

Examination of Eq. 3.31 shows that $\mathbf{\Omega_r}$ has a fixed component along the z-axis and x-axis and a component that rotates in the x-y plane at frequency 2ω with a small amplitude. Typically $\omega \approx \omega_{01}$, and the 2ω components are not important because they are not in resonance. To simplify the analysis, we ignore the 2ω components. This is called the rotating wave approximation [59]. With the rotating wave approximation, $\mathbf{\Omega_r}$ becomes simply:

$$\Omega_r = \begin{pmatrix} -\kappa E_0 \\ -0 \\ \omega_0 \end{pmatrix}. \tag{3.36}$$

We can then write Eq. 3.35 in the rotating basis as

$$\begin{pmatrix} \dot{u} \\ \dot{v} \\ \dot{w} \end{pmatrix} = \begin{pmatrix} -\kappa E_0 \\ -0 \\ \omega_0 - \omega \end{pmatrix} \times \begin{pmatrix} u \\ v \\ w \end{pmatrix} \tag{3.37}$$

or equivalently

$$\dot{u} = -(\omega_0 - \omega)v \tag{3.38a}$$

$$\dot{v} = (\omega_0 - \omega)u + \kappa E_0(t)w \tag{3.38b}$$

$$\dot{w} = -\kappa E_0(t)v. \tag{3.38c}$$

Equations 3.38(a - c) are just another version of the Bloch equations.

3.4 Including decoherence and dissipation

Up to this point, I ignored dissipation and decoherence. Even if we do not know the microscopic mechanism that causes decoherence and relaxation in our qubit, we can still describe their effects phenomenologically by adding some terms to the equation of motion. In NMR, the sample magnetization decays due to interactions with the lattice and other spins. These interactions can change or preserve the energy of the spin. In practice, two-level systems experience analogous effects.

When a qubit interacts with a dissipative thermal reservoir, it can decay from the excited state to the ground state. The time constant T_1 for this decay from $|1\rangle$ to $|0\rangle$ is called the relaxation time or the energy dissipation time.

For a Josephson junction qubit, T_1 can be calculated by modeling the dissipation source admittance $Y(\omega)$ as a bath of Harmonic oscillators [60, 61, 25]. If the coupling between the qubit and the harmonic oscillator bath is linear in a coordinate of the qubit, then T_1 will be proportional to the real part of $Y(\omega)$. One finds

$$T_1 = \frac{C}{Re[Y(\omega_{01})]} \tag{3.39}$$

where C is the total capacitance in parallel with the qubit junction, including the qubit junction capacitance [25].

Elastic scattering processes cause decoherence even though no energy is dissipated. Decoherence involves a loss of information in the phase ϕ in the Bloch representation (see Fig 3.3.2). In a spin system, decoherence happens when spins that are initially in phase (coherent), evolve to have different phases (incoherent). Elastic scattering can act homogeneously or randomly on each spin, and this leads to different effects on a system.

The coherence time T_2 is the characteristic lifetime for a qubit to retain its phase and it is used in the Bloch equations [54]. T_2 is also called the transverse relaxation time in NMR [56]. T_1 and T_2 are connected to the decay time constant T' of Rabi oscillations by [54]

$$\frac{1}{T'} = \frac{1}{2T_1} + \frac{1}{2T_2}. \tag{3.40}$$

Thus by measuring T_1 from relaxation and T' from Rabi oscillations, T_2 can be obtained experimentally. One expects $T_2 = 2T_1$ if only dissipation is present as a decoherence source [62]. In practice, however, T_2 is often found to be shorter than T_1 [56] due to the presence of a pure dephasing source.

There are other important time constants that can be obtained from spectroscopic measurements. The half-width at half-maximum Δf of the resonance obeys [56]

$$\Delta f \equiv \frac{1}{2\pi T_2^*} \tag{3.41}$$

where T_2^* is the spectroscopic coherence time. T_2^* includes broadening of a resonance due to T_2, and also inhomogeneous (random) scattering (for example, from low frequency noise) represented by the inhomogeneous coherence time $T_2^\dagger$ [54]. If microwave power broadening is also present,

$$\frac{1}{T_2^*} = \frac{1}{T_2}\sqrt{1 + \Omega^2 T_1 T_2} + \frac{1}{T_2^\dagger} \tag{3.42}$$

Table 3.1: Notation for time constants used here and Ref. [54].

	Relaxation time	coherence time	spectroscopic coherence time	inhomogeneous coherence time
In this thesis	T_1	T_2	T_2^*	$T_2^\dagger$
Ref. [54]	T_1	T_2'	T_2	T_2^*

where Ω is the Rabi frequency. Ideally, the resonance width is only limited by dissipation [30, 54] in which $T_2^* = 2T_1 = T_2$. However, inhomogeneous broadening can create situations where the resonance frequency varies randomly from one measurement to the next, and as a result, the resonance peak broadens. Basically any effect that makes a measurement non-identical, can cause inhomogeneous broadening and a short T_2^* in the system. In a dc SQUID phase qubit, fluctuations in current, flux or critical current can cause inhomogeneous broadening.

Unfortunately, there is no universal agreement upon notations for the various time constants of the qubit. For example, in Allen and Eberly [54], T_2 is denoted as T_2', $T_2^\dagger$ as T_2^* and T_2^* as T_2 (see Table. 3.1). In this thesis, I followed the notation from Refs. [55, 56].

3.5 Solutions of the density matrix equation with T_1 and T_2

The time constants T_1 and T_2 associated with dissipation and decoherence, can be added to the density matrix equation of motion in the following *ad hoc*

manner [63]. Starting from Eqs 3.10 (a - d), I can write:

$$i\hbar\frac{d\rho_{00}}{dt} = a_0(\rho_{10} - \rho_{01})\cos\omega t + i\hbar\frac{\rho_{11}}{T_1} \tag{3.43a}$$

$$i\hbar\frac{d\rho_{01}}{dt} = a_0(\rho_{11} - \rho_{00})\cos\omega t - \Delta E\rho_{01} - i\hbar\frac{\rho_{01}}{T_2} \tag{3.43b}$$

$$i\hbar\frac{d\rho_{10}}{dt} = -a_0(\rho_{11} - \rho_{00})\cos\omega t + \Delta E\rho_{10} - i\hbar\frac{\rho_{10}}{T_2} \tag{3.43c}$$

$$i\hbar\frac{d\rho_{11}}{dt} = -a_0(\rho_{10} - \rho_{01})\cos\omega t - i\hbar\frac{\rho_{11}}{T_1}. \tag{3.43d}$$

Notice that T_1 and T_2 enter differently; T_2 goes into the off-diagonal equations, while T_1 goes into the diagonal equations. To solve Eqs. 3.43, we try the test solution [63]

$$\rho_{00} = Ae^{\lambda t} \tag{3.44a}$$

$$\rho_{01} = Be^{i\omega t}e^{\lambda t} \tag{3.44b}$$

$$\rho_{10} = Ce^{-i\omega t}e^{\lambda t} \tag{3.44c}$$

$$\rho_{11} = De^{\lambda t}. \tag{3.44d}$$

The possible values for the exponent λ are found by substituting Eqs. 3.48(a - d) into Eqs. 3.43(a - d) and finding the roots of the resulting characteristic equation. After using the rotating wave approximation to eliminate $2\omega t$ terms, we get four roots of λ [63, 64, 55]

$$\lambda_0 = 0 \tag{3.45a}$$

$$\lambda_1 = -\frac{1}{T'} + i\Omega \tag{3.45b}$$

$$\lambda_2 = -\frac{1}{T'} - i\Omega \tag{3.45c}$$

$$\lambda_3 = -\frac{1}{T_2} \tag{3.45d}$$

where

$$\frac{1}{T'} = \frac{1}{2T_1} + \frac{1}{2T_2} \tag{3.46}$$

and

$$\Omega = \sqrt{{\Omega_0}^2 - \left(\frac{1}{2T_2} - \frac{1}{2T_1}\right)^2}. \tag{3.47}$$

Here $\Omega_0 = a_0/\hbar$ is the bare Rabi frequency which depends only on the microwave power and the matrix elements of $\hat{x}$ (see Eq. 3.9).

We now consider the case when $\rho_{00} = 1$ at t = 0, and resonant microwave power is applied at $\omega = \omega_0$. For sufficiently high power, Ω from Eq. 3.47 is real and the solutions are given by; [63]

$$\rho_{00} = 1 - \rho_{11} \tag{3.48a}$$

$$\rho_{01} = i\frac{\rho_{eq}e^{i\omega t}}{\Omega_0}\left\{\frac{e^{-t/T'}}{T_1} + \frac{1}{\Omega}\left[\cos(\Omega t)\left(\Omega^2 - \frac{1}{(2T_1)^2} + \frac{1}{(2T_2)^2}\right) + \frac{\sin(\Omega t)}{T_1}\right]\right\} \tag{3.48b}$$

$$\rho_{10} = \rho_{01}^* \tag{3.48c}$$

$$\rho_{11} = \rho_{eq} - \rho_{eq}\left[1 - \cos(\Omega t) + \frac{\sin(\Omega t)}{\Omega T'}\right]\exp(-t/T') \tag{3.48d}$$

where

$$\rho_{eq} = \frac{\Omega_0^2 T_1 T_2}{2[1 + \Omega_0^2 T_1 T_2]} \tag{3.49}$$

is the probability of the qubit being in $|1\rangle$ if the power is left on for an arbitrarily long time. From Eq. 3.49, we see that ρ_{eq} is determined by the microwave power (related to Ω_0^2), T_1 and T_2. The high power limit occurs for $\Omega_0 \gg (T_1T_2)^{-1/2}$ where $\rho_{eq} \cong 1/2$. This is called "saturation".

To measure Rabi oscillations, we need to use a sufficiently high microwave power, so that $\Omega_0 \gg (T_1T_2)^{-1/2}$. In this limit, ρ_{eq} becomes close to 1/2 and Eq. 3.48(d) for ρ_{11} then gives decaying oscillations with the Rabi frequency Ω. The decay time constant T' of these oscillations is given in Eq. 3.46 and involves both

T_1 and T_2.

3.6 From the density matrix to the Bloch vector

While the density matrix provides a good way to describe Rabi oscillations and the state of the qubit, the Bloch sphere provides a more intuitive picture of the time-dependent behavior. The three components u, v, and w of a Bloch vector can be related to the components of the density matrix by [55]

$$u = \rho_{01}\exp(-i\omega t) + \rho_{10}\exp(i\omega t) \tag{3.50a}$$

$$v = -i[\rho_{01}\exp(-i\omega t) - \rho_{10}\exp(i\omega t)] \tag{3.50b}$$

$$w = \rho_{00} - \rho_{11}. \tag{3.50c}$$

In matrix form, I can write

$$\hat{\rho} = \begin{pmatrix} \rho_{00} & \rho_{01} \\ \rho_{10} & \rho_{11} \end{pmatrix} = \frac{1}{2}\begin{pmatrix} 1+w & (u+iv)\exp(i\omega t) \\ (u-iv)\exp(-i\omega t) & 1-w \end{pmatrix}. \tag{3.51}$$

Finally, I note that if the qubit is prepared in a superposition of pure states, the density matrix can be written as

$$\hat{\rho} = \begin{pmatrix} |a_0|^2 & a_0^* a_1 \\ a_0 a_1^* & |a_1|^2 \end{pmatrix} = \begin{pmatrix} \cos^2\theta/2 & e^{i\phi}\sin\theta/2 \\ e^{-i\phi}\sin\theta/2 & \sin^2\theta/2 \end{pmatrix}. \tag{3.52}$$

where the qubit state $|\Psi\rangle$ is [55]

$$|\Psi\rangle = a_0|0\rangle + a_1|1\rangle \tag{3.53}$$

$$= \cos\left(\frac{\theta}{2}\right)|0\rangle + e^{i\phi}\sin\left(\frac{\theta}{2}\right)|1\rangle. \tag{3.54}$$

We can interpret θ and ϕ as angles (see fig. 3.3.2) allowing us to represent each point on the Bloch sphere as a state. This representation shows more clearly how the qubit state evolves as we apply external field (microwaves), and the meaning of the different components of the density matrix.

3.7 Bloch vector of the Josephson junction phase qubit

Here I discuss explicitly how to construct a Bloch vector for the Josephson junction phase qubit. The derivation was published by Martinis *et al.* in Ref. [47]. As I showed in Ch. 2, the Hamiltonian of the phase qubit is

$$\hat{H} = \frac{\hat{Q}^2}{2C} - \frac{\Phi_0}{2\pi}(I_0 \cos\hat{\gamma} + I\hat{\gamma}) \tag{3.55}$$

where $\hat{Q} = -2e\hat{N}$ is the charge operator, e = 1.6 $\times 10^{-19}$, $\hat{\gamma}$ is the phase operator, I_0 is the critical current of the qubit junction, and I is the bias current. The bias current can include dc and microwave components [61]. Making this explicit, I can write

$$I(t) = I_{dc} + I_{rfz}(t) + I_{rfx}(t)\cos\omega_{01}t + I_{rfy}(t)\sin\omega_{01}t = I_{dc} + I_{rf}(t). \tag{3.56}$$

where I_{dc} is the dc current, $I_{rfz}(t)$ is a "dc" pulse, $I_{rfx}(t)\cos\omega t$ and $I_{rfy}(t)\sin\omega t$ are microwave currents at frequency ω. The time dependent terms in the Hamiltonian can be treated as a time-dependent perturbation so that

$$\hat{H} = \frac{\hat{Q}^2}{2C} - \frac{\Phi_0}{2\pi}(I_0\cos\hat{\gamma} + I(t)\hat{\gamma}) = \hat{H}_0 - \frac{\Phi_0}{2\pi}I_{rf}(t)\hat{\gamma} \tag{3.57}$$

where the unperturbed Hamiltonian is

$$\hat{H}_0 = \frac{\hat{Q}^2}{2C} - \frac{\Phi_0}{2\pi}(I_0\cos\hat{\gamma} + I_{dc}\hat{\gamma}). \tag{3.58}$$

If we assume that the Josephson phase qubit can be approximated as a two-level system with the two lowest energy states, then the Hamiltonian becomes

$$\hat{H} = \begin{pmatrix} E_0 & 0 \\ 0 & E_1 \end{pmatrix} + \frac{\Phi_0}{2\pi} \begin{pmatrix} \gamma_{00} I_{rf}(t) & \gamma_{01} I_{rf}(t) \\ \gamma_{10} I_{rf}(t) & \gamma_{11} I_{rf}(t) \end{pmatrix} \tag{3.59}$$

where E_0 and E_1 are the energy of $|0\rangle$ and $|1\rangle$ at $I = I_{dc}$, the second term is the time-dependent perturbation due to microwave driving which is responsible for the energy level transitions, the matrix element $\gamma_{ij} = \langle i|\hat{\gamma}|j\rangle = \gamma_{ji}$.

As shown in the previous section, it is convenient to use a rotating frame for a system which is oscillating. In a frame that is rotating with frequency ω_{01}, $\hat{H}$ becomes [24]

$$\hat{H}_r = \exp\left(\frac{i\hat{H}_0 t}{\hbar}\right) \hat{H} \exp\left(\frac{-i\hat{H}_0 t}{\hbar}\right) \tag{3.60}$$

and in the basis of unperturbed energy eigenstates,

$$\exp\left(\frac{-i\hat{H}_0 t}{\hbar}\right) = \exp(i\omega_0 t) \begin{pmatrix} 1 & 0 \\ 0 & \exp(i\omega_{01} t) \end{pmatrix} \tag{3.61}$$

where $\hbar\omega_0 = E_0$. The Hamiltonian in the rotating frame then becomes

$$\hat{H}_r = \begin{pmatrix} 1 & 0 \\ 0 & e^{i\omega_{01} t} \end{pmatrix} \hat{H} \begin{pmatrix} 1 & 0 \\ 0 & e^{-i\omega_{01} t} \end{pmatrix} \tag{3.62}$$

and I obtain

$$\hat{H}_r = \begin{pmatrix} E_0 & 0 \\ 0 & E_1 \end{pmatrix} + \frac{\Phi_0}{2\pi} \begin{pmatrix} \gamma_{00} I_{rf}(t) & \gamma_{01} I_{rf}(t) e^{-i\omega_{01} t} \\ \gamma_{10} I_{rf}(t) e^{i\omega_{01} t} & +\gamma_{11} I_{rf}(t) \end{pmatrix}. \tag{3.63}$$

Since

$$
\begin{aligned}
I_{rf}(t)e^{\pm i\omega_{01}t} &= I_{rfz}(t)e^{\pm i\omega_{01}t} + \frac{I_{rfx}(t)}{2}(\pm 1 + \cos 2\omega_{01}t \pm i\sin 2\omega_{01}t) \\
&\quad + \frac{I_{rfy}(t)}{2}(\sin 2\omega_{01}t \mp i \pm i\cos 2\omega_{01}t) \qquad (3.64) \\
&\approx \pm\frac{I_{rfx}(t)}{2} \mp i\frac{I_{rfy}(t)}{2} \qquad (3.65)
\end{aligned}
$$

where in the last step I have applied the rotating wave approximation and dropped all the 2ω terms as well as terms oscillating at ω. Equation 3.63 then becomes

$$
\hat{H}_r = \begin{pmatrix} E_0 & 0 \\ 0 & E_1 \end{pmatrix} + \frac{\Phi_0}{2\pi}\begin{pmatrix} \gamma_{00}I_{rfz}(t) & \gamma_{01}(\frac{I_{rfx}(t)}{2} - i\frac{I_{rfy}(t)}{2}) \\ \gamma_{01}(\frac{I_{rfx}(t)}{2} + i\frac{I_{rfy}(t)}{2}) & \gamma_{11}I_{rfz}(t) \end{pmatrix}. \qquad (3.66)
$$

If we apply a constant amplitude microwave current of $I_{rfx}(t) = I_{rfx}$, $I_{rfy}(t) = I_{rfy}$, and a constant current pulse $I_{rfz}(t) = I_{rfz}$ over time Δt, the diagonal terms can be expressed as

$$
E_0 + \frac{\Phi_0}{2\pi}\gamma_{00}I_{rfz} = E_0(I(t)) \qquad (3.67)
$$

$$
E_1 + \frac{\Phi_0}{2\pi}\gamma_{11}I_{rfz} = E_1(I(t)). \qquad (3.68)
$$

Rearranging terms, I find

$$\begin{aligned}
\begin{pmatrix} E_0(I) & 0 \\ 0 & E_1(I) \end{pmatrix} &= \frac{1}{2}\begin{pmatrix} -(E_1(I)-E_0(I)) & 0 \\ 0 & E_1(I)-E_0(I) \end{pmatrix} + \frac{(E_0(I)+E_1(I))}{2}\hat{\mathbf{I}} \\
&= \frac{1}{2}\begin{pmatrix} -E_{01}(I) & 0 \\ 0 & E_{01}(I) \end{pmatrix} + \frac{(E_0(I)+E_1(I))}{2}\hat{\mathbf{I}} \\
&= \frac{1}{2}\begin{pmatrix} -(E_{01}(I)-E_{01}(I_{dc})) & 0 \\ 0 & E_{01}(I)-E_{01}(I_{dc}) \end{pmatrix} + \mathbb{C} \\
&= -\frac{1}{2}\begin{pmatrix} I_{rfz}\partial E_{01}/\partial I & 0 \\ 0 & -(I_{rfz}\partial E_{01}/\partial I) \end{pmatrix} + \mathbb{C}. \qquad (3.69)
\end{aligned}$$

Here $\hat{\mathbf{I}}$ is the identity matrix and $\mathbb{C}$ is

$$\mathbb{C} = \frac{(E_0(I)+E_1(I))}{2} + \begin{pmatrix} -E_{01}(I_{dc}) & 0 \\ 0 & E_{01}(I_{dc}) \end{pmatrix}. \qquad (3.70)$$

Also I assume $I - I_{dc} \approx I_{rfz}$ which implies that the oscillating current $e^{\pm i\omega_{01}t}$ will not tilt the washboard potential on average.

Recalling the definition of the Pauli matrices, $\hat{H}_r$ can be written as [61]

$$\hat{H_r} = \frac{\Phi_0}{2\pi}\frac{\gamma_{01}I_{rfx}}{2}\hat{\sigma_{\mathbf{x}}} + \frac{\Phi_0}{2\pi}\frac{\gamma_{01}I_{rfy}}{2}\hat{\sigma_{\mathbf{y}}} + \frac{I_{rfz}}{2}\left(-\frac{\partial E_{01}}{\partial I}\right)\hat{\sigma_{\mathbf{z}}} + \mathcal{C} \qquad (3.71)$$

where the Pauli matrices are

$$\hat{\sigma_{\mathbf{x}}} = \hat{\sigma_{\mathbf{1}}} = \begin{pmatrix} 0 & 1 \\ 1 & 0 \end{pmatrix}, \hat{\sigma_{\mathbf{y}}} = \hat{\sigma_{\mathbf{2}}} = \begin{pmatrix} 0 & -i \\ i & 0 \end{pmatrix}, \hat{\sigma_{\mathbf{z}}} = \hat{\sigma_{\mathbf{3}}} = \begin{pmatrix} 1 & 0 \\ 0 & -1 \end{pmatrix}. \qquad (3.72)$$

The idea behind Eq. 3.71 is that when we apply I_{rf}, it rotates the state of the

qubit on the Bloch sphere according to the unitary transformation given by

$$\Psi \longrightarrow \hat{U}\Psi \tag{3.73}$$

$$\hat{U} = \exp\left[\frac{-i\hat{H}_r\Delta t}{\hbar}\right]\Psi \tag{3.74}$$

$$= \exp\left[\frac{-i\vec{\sigma}\cdot(\vec{c})}{2}\right]\Psi \tag{3.75}$$

where $\vec{c}$ is a "control vector" defined as

$$\vec{c} = \left(\frac{\Phi_0}{2\pi}\gamma_{01}\Delta I_{rfx}, \frac{\Phi_0}{2\pi}\gamma_{01}\Delta I_{rfy}, -\frac{\Delta I_{rfz}}{2}\frac{\partial E_0 1}{\partial I}\right)\frac{\Delta t}{\hbar}. \tag{3.76}$$

Comparing with the rotation operator

$$R[\varphi] = \exp\left[-i\frac{\varphi}{2}\hat{n}\cdot\vec{\sigma}\right] \tag{3.77}$$

that rotates the system by angle φ in the direction of $\hat{n}$, one sees that $\hat{U}$ rotates the qubit by angle $|\vec{c}|$ about the $\vec{c}$ axis. For example, if a pulsed bias current $\vec{c} = (0, 0, \pi)$ is applied, this operation rotates the qubit 180∘ about the z-axis; this is a π_z operation or a phase qubit. Using $\vec{c}$ makes it easier to understand gate operations and follow the motion of the qubit on the Bloch sphere in applications such as state tomography [65].

Chapter 4

Qubit fabrication, experimental techniques and analysis

This chapter describes how I made aluminum dc SQUID phase qubits and the apparatus and techniques I used to measure them.

4.1 Fabrication recipe for aluminum dc SQUID phase qubits

In this section I explain the photolithographic technique that I used to make aluminum dc SQUID phase qubits, including device AL1 (see Fig. 4.1 to 4.5). I made device AL1 in our laboratory using photolithography followed by double-angle evaporation of approximately 50 nm thick Al films on an oxidized Si substrate. The oxide was thermally grown with a thickness of about 1.5 μm and the wafer was P-doped (boron) with an orientation (100) and a resistivity of about 10 Ωcm. The 40 μm x 2 μm Al/AlO_x/Al qubit junction had a zero-field critical current I_{01} = 21.28 μA and the device had a single-turn square loop with a 3 μm line-width and a 300 μm diameter (see Fig. 4.1).

The reason why I used photolithography rather than e-beam lithography was that photolithography could generate large-area junctions easily and more efficiently than e-beam lithography.

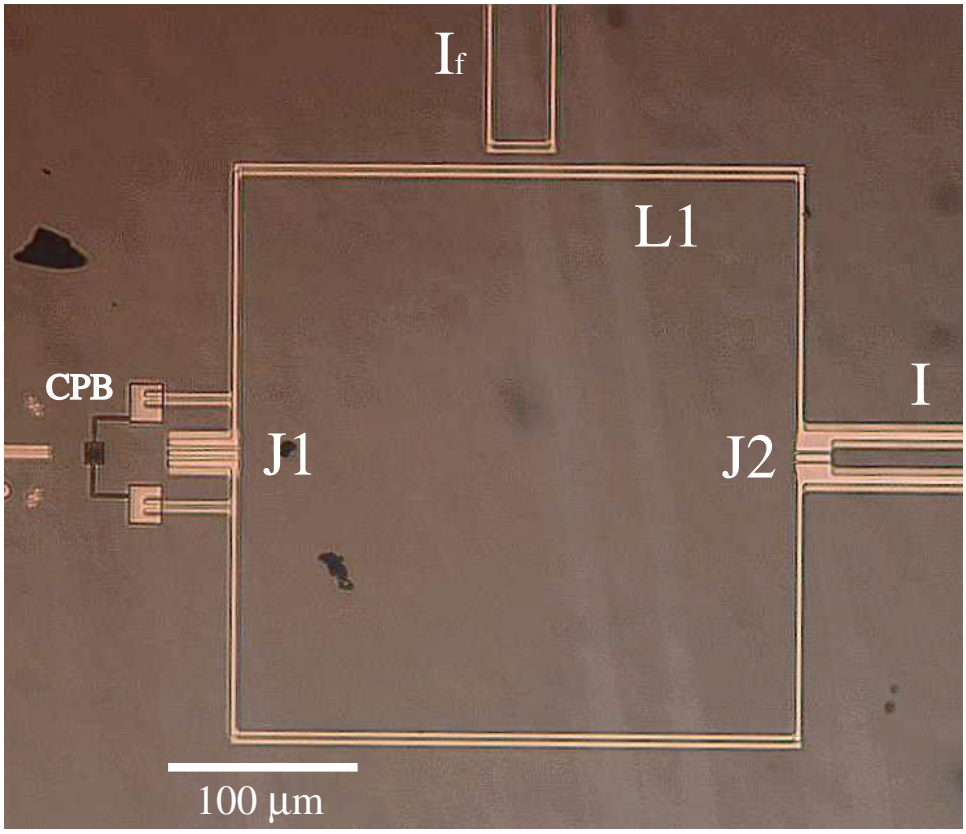

Figure 4.1: Photo of an Al/AlO_x/Al dc SQUID phase qubit made on a Si substrate with thermally grown SiO_2. The qubit junction J1 was designed to be coupled to a Cooper pair box (CPB) on the left. The device was made using photolithography and double-angle deposition.

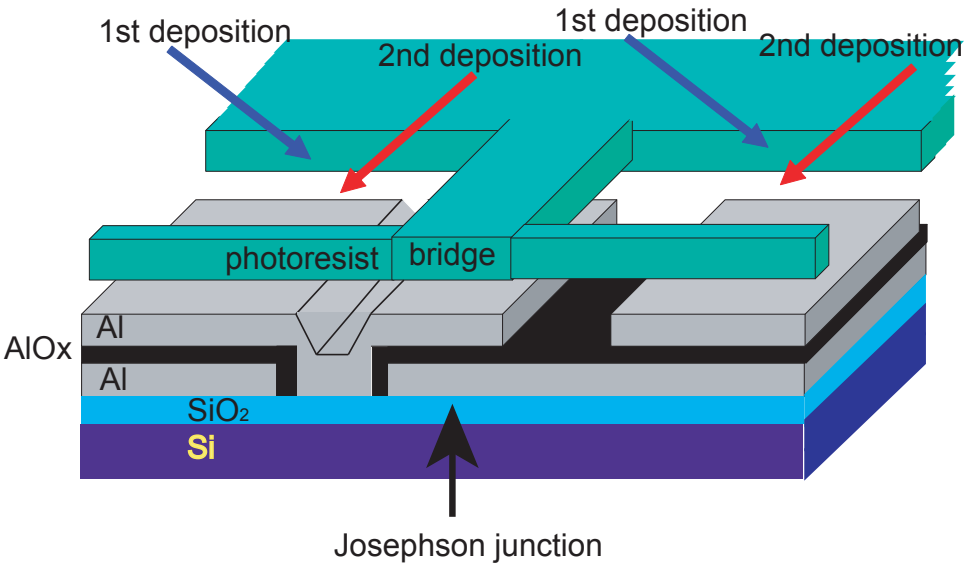

Figure 4.2: Schematic of double angle deposition after photolithography.

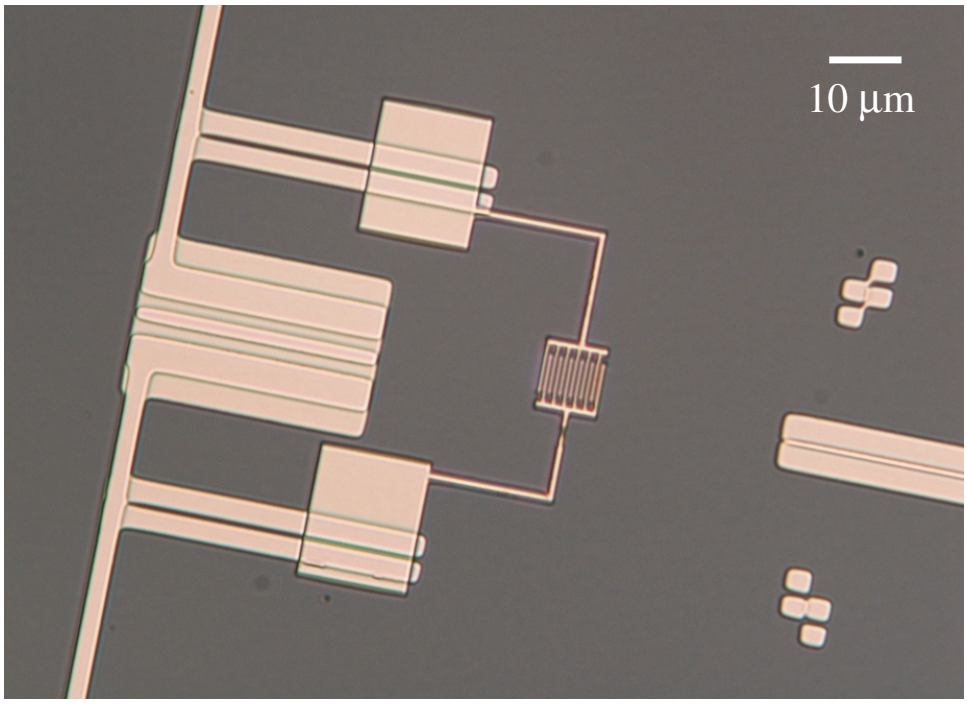

Figure 4.3: Photograph of qubit junction (left) with a coupled Cooper pair box (right) in device AL1.

4.1.1 Photolithography: Introduction

Lithography is a printing process that uses chemicals to create an image. In photolithography, a chemical "photoresist" is used to coat a flat substrate. The photoresist is exposed to UV light through a photomask, and then immersed in a developer to create the desired pattern on the substrate. Processes in photolithography are similar to conventional photographic film processing. There are two basic types of photoresist: positive and negative. Exposed positive photoresist will be washed away by the developer, while exposed negative photoresist will remain on the substrate after developing, and the unexposed area will be removed. "Novolac" with DNQ (diazonapthoquinone) photosensitizers is one of the most common types of photoresists. Novolac resin is soluble in water-based base solutions such as TMAH (Tetramethylammonium hydroxide, $(CH_3)_4NOH$) or NaOH, but when mixed with DNQ in the correct ratio, the resulting resist solution is not soluble in base solutions. When exposed to UV, DNQ is destroyed and the photoresist regains its solubility to bases which can serve as a developer.

Modern projection photolithography enables patterning of sub-micron features. Typical stepper machines use optical lenses to scale down the mask patterns for projection onto a photoresist layer. In contrast, I used contact lithography, where the photomask makes direct contact with the photoresist layer. The following recipe was what I used for making aluminum SQUID qubits including device AL1.

4.1.2 Preparation for photolithography

Before beginning fabrication of a new chip, there were several things that needed to be taken care of. I first made sure that I had all the materials, chemicals and supplies I needed, including;

3 inch SiO_2/Si wafer with thermally grown SiO_2 with 1.5 μm thickness.

LOR30B undercut resist [66]

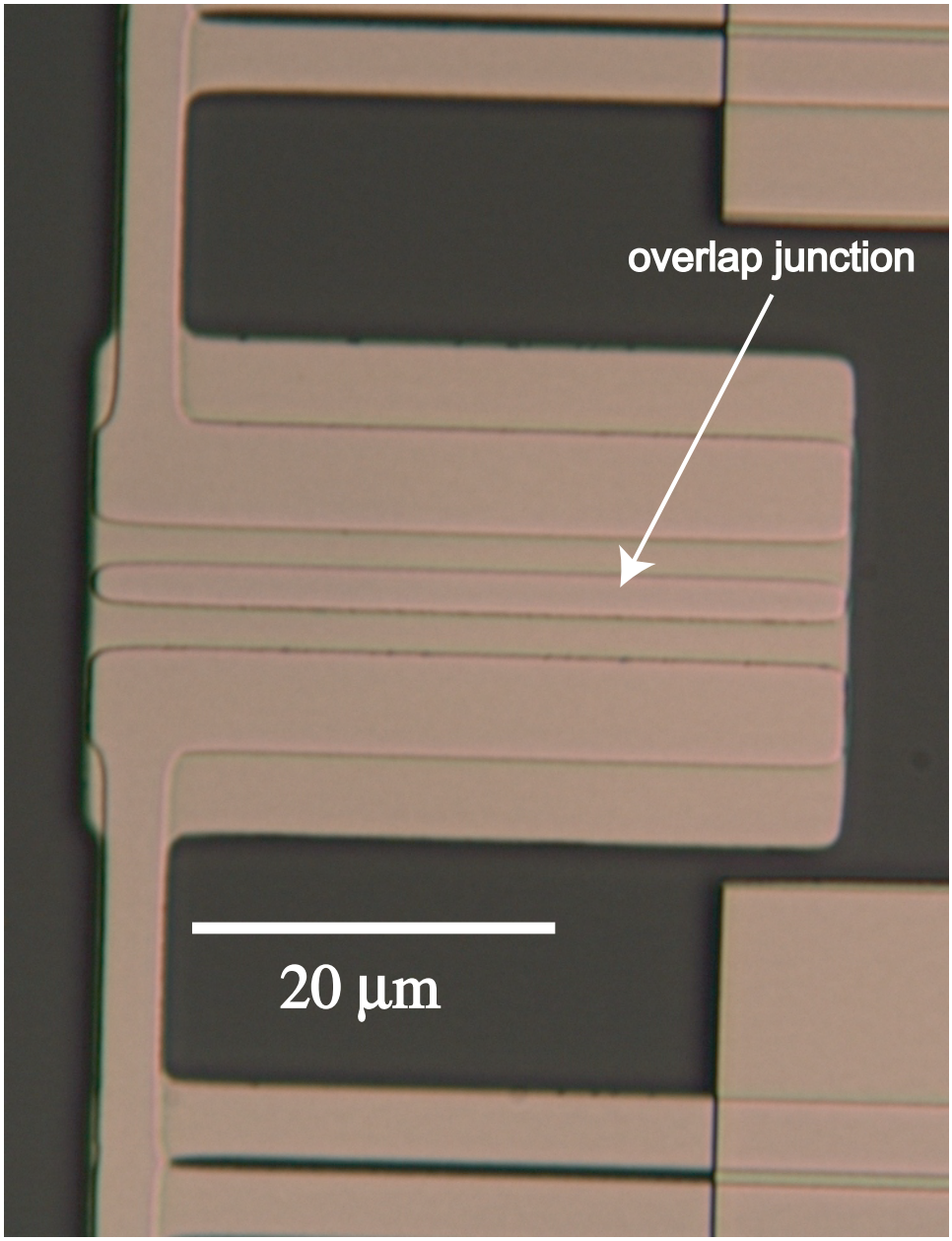

Figure 4.4: A zoomed-in photograph of qubit junction in device AL1 from Fig. 4.3 The junction is in the center overlapped section.

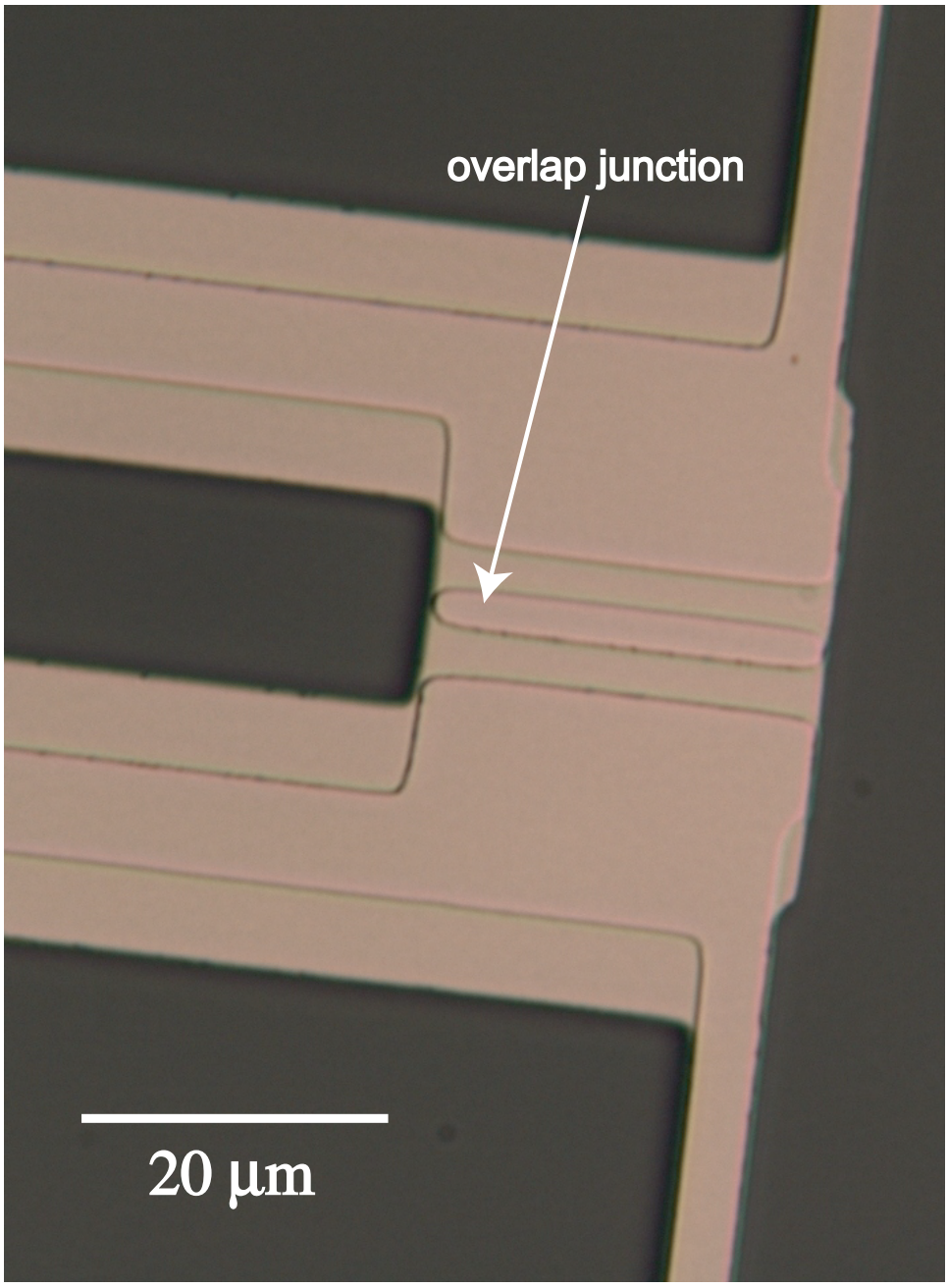

Figure 4.5: Photograph of isolation junction in device AL1.

S1813 photoresist [66]

Photomask [67]

Microchem MF319 (developer for LOR30B and S1813) [66]

Microchem PG resist stripper [66]

Al shot (purity 99.999% or above) [68]

Two spiral tungsten boats for evapoarating aluminum [69].

Creating a photomask

I designed the device patterns for the photomask using the 2-D circuit CAD program called ICED [70]. The photomasks were then printed at the U.C. Berkeley Microlab [67]. I used soda-lime glass plates with chromium film patterns. For AL1, I used a 2.5-inch mask.

Cleaning the wafer

I soaked the wafer in RBS35 detergent [71] for about 30 min and rinsed in DI water. I then sprayed acetone, methanol and isopropanol on the wafer for a minute each and rinsed in DI water. It is important to blow dry the wafer with (high purity, filtered) nitrogen gas to remove any water remaining on the wafer. I used an O_2 plasma etch at 400 mtorr, 200 W for 30 sec as a final degreasing step. I also used the O_3 etch station in the cleanroom in the Kim Engineering building for cleaning solvent residue.

Cleaning the Mask

Before photolithography, I used the following procedure to clean the masks:

1. Spray acetone, methanol and isopropanol on the mask for a minute each and rinse in DI water. Blow dry the mask.

2. Use O_3 etch for 10 min to remove solvent residue.

3. Use dry nitrogen gas to blow dry the mask.

4.1.3 Spinning and baking photoresist

I coated the wafer with photoresist by pouring a small quantity of resist solution onto the wafer when it was mounted at rest on the spinner. The wafer is then spun at a high RPM to produce a thin layer. I then baked the wafer on a hot plate to harden the resist and remove the resist solvent. After baking, the photoresist remains as a thin glass-like layer on the substrate.

The baking temperature and baking time determines the solubility of the photoresist in the developer. Baking at high temperature or baking for a long time makes the resist more hardened than baking at low temperature for a short time. This initial baking process is called a "soft bake". If the resist is to be used in a process that involves etching (for example, of SiO_2 on Si) then a "hard bake" is done after soft-baking. A hard bake literally hardens the resist by increasing cross-linking in the polymer so that the resist can survive chemical etching.

The developing speed of baked resist also depends on the temperature of the developer. For example, I baked S1813 at 110°C for 1 min when the cleanroom was at 85 °F (the temperature controller in the cleanroom was broken) and developing required 43 sec. Later with the cleanroom at 65 °F, I used the same recipe and I ended up overdeveloping the resist. The final recipe below was based on a room temperature of 70 °F.

To make a junction, I used two resist layers to create a suspended bridge over an undercut pattern. If there is too much undercut, the top bridge layer may collapse, and if the undercut is too small, junctions can not be formed using double angle evaporation. Developing time controls the amount of undercut and for some resists, developing for 1 more second can make a big difference. It can be very sensitive. To achieve a reproducible undercut, it is important to bake the resist at

the right temperature under the same conditions each time.

I used LOR30B [66] as an undercut resist. LOR30B is the thickest of all resists in the LOR (Lift-Off Resist) series. We put Shipley 1813 (S1813) [66] photosensitive resist on top for patterning.

Spin and bake of LOR30B

To spin a layer of LOR30B on a substrate, I used the following method:

1. Pour LOR30B in a small 10 mL beaker. For 3 inch wafers, 4 mL of LOR30B is enough to cover the wafer.

2. Slowly pour LOR30B resist on the center of a wafer spinning at 30 RPM. Once the resist covers the wafer, increase the speed to 3300 RPM within 5 sec. The total spin time should be 45 sec.

3. Bake the wafer at 150 C° for 5 min on a hot plate.

The LOR30B photoresist is a dense liquid and tends to harden quickly after exposure to air. I prepare the LOR30B about 10 to 20 minutes before spinning by letting it warm up to room temperature. LOR30B does not dissolve in common solvents such as acetone, isopropanol, methanol, ethanol or water. Those solvents (as well as water) tend to harden LOR30B. To remove LOR30B from a substrate, I use MF319 [66] or PG [66].

Spin and bake a layer of S1813

I used a similar method for spinning the S1813 resist on top of the coated LOR30 resist:

1. Spin the resist at 4500 RPM for 45 sec. Start spinning at low speed and increase to 4500 RPM to make the resist layer have uniform thickness.

2. Bake at 110 °C for 1 min on a hot plate.

Technical sheets for resists are available from the manufacturer [66]. These sheets contain the recommended baking time, baking temperature and developing time for different procedures.

4.1.4 Expose and develop photoresist

I used the following procedure for exposing photoresist bilayers of LOR30B and S1813 on the Karl-Suss MJB3 [72] contact mask aligner at "Fablab" in the Kim Engineering Building..

1. Set the UV exposure to 8 mW/cm^2 for 10 sec.

2. Develop for 30 sec in MF319 with agitation and, immediately after, rinse in DI water (the developing time can vary according to the conditions). I then check with an optical microscope with a red filter to see if the pattern has developed properly. If it has not developed, I develop for 5 sec and recheck on the optical microscope. I repeated 5 second-developing steps until the pattern developed to the desired undercut.

4.1.5 Deposition of aluminum

I used the following procedure for depositing Al/AlO_x/Al films for qubit junctions (see Fig. 4.2):

1. Double angle (45°) deposition. I used the cryopumped deposition chamber in room 0219 in the CSR, and put Al basket boats on electrodes #1 and #3. The sample was mounted on the rotating stage on the ion mill top. Before pumping, I set the sample stage to 45° to the vertical for each AL source and make a mark on the control knob so that I would be able to correctly tilt the sample for each evaporation.

2. Rough pumping. I purged the O_2 line for 1 min by flowing oxygen through the line at 1000 mTorr. I then closed the O_2 valve and rough pumped the chamber to 500 mTorr.

3. Once the pressure reached 500 mTorr, I started cryopumping by opening "hivac" valve. I continued pumping until the chamber pressure was below 10^{-6} Torr.

4. I rotated the sample holder to 45°, closed the evaporation shutter and slowly heated the boat until Al was evaporating at 1 nm/s. When Al started evaporating, the evaporation rate increased and I was able to observe sudden disturbance in pressure through the ion gauge. I observed the evaporation rate using the crystal thickness monitor. I deposited 50 nm of Al for the first layer, waited 5 to 10 minutes and then closed the hivac valve and oxidized the deposited Al film in 18 Torr of O_2 for 10 min.

5. I closed the O_2 valve, pumped the chamber to 10^{-6} Torr, rotated the sample holder to -45° and deposited 50 nm of Al to form the second Al layer.

With these oxidation parameters, I got a critical current density of 22 μA/80 μm^2 = 27 A/cm^2 and a capacitance of about 4 pF/80 μm^2 = 50 fF/$(\mu m)^2$. The oxidation step is critical because the thickness of the oxide determines the critical current density. I usually waited for 5 to 10 minutes to allow time for the substrate to cool before opening the O_2 valve, but I did not make a systematic study on how the temperature of the substrate affects the oxide. This temperature may also be important for determining defect density and ultimately the coherence time, so a systematic investigation of the grouwth procedure is of considerable current interest.

4.1.6 Lift-off

After deposition, I did a lift off to remove Al from everywhere it was deposited on undeveloped resist. I put the Al-deposited wafer in PG remover [66] and heated it to 60 °C on a hot plate. After 1 to 2 hours, I replaced the remover with a fresh PG remover and resumed lift-off for another 1 to 2 hours.

4.2 Fabrication recipe for a Cooper pair box: E-beam lithography

E-beam lithography provides an easy way to fabricate sub-micron devices. I used the following recipe to fabricate a Cooper pair box. The Cooper pair box was deposited on a dc SQUID phase qubit that I had built using photolithography.

4.2.1 Preparation

The materials and chemicals I needed for e-beam lithography are as follows:

950 PMMA C2 [66]

Copolymer (MMA) EL11 or EL9. EL9 is thinner [66].

PG remover [66] or acetone

Al shot (purity 99.999% or above) [68]

Two spiral tungsten boats [69]

Cleaning the wafer

To clean the wafer after finishing lifting off photoresist to make a phase qubit, I used nitrogen gas to blow dry the surface.

4.2.2 Spinning resist

I spun resist immediately after cleaning the wafer. Depending on the desired pattern, PMMA and MMA of different coating thicknesses can be used. For "nano"

fabrication, thin resists are suitable. For my work, I used the thinnest PMMA and MMA so that I could build junctions of about $\sim$ 100 nm $\times$100 nm. The procedure I used was as follows:

1. Spin copolymer (MMA) on the chip at 4000 RPM for 45 sec.
2. Bake the chip at 150 °C for 10 min on a hot plate. During this step, I covered the substrate with a beaker because MMA collects dust easily.
3. Spin PMMA at 6000 RPM (or maximum speed of the spinner) for 45 sec.
4. Bake at 150 °C for 10 min on a hot plate.

The technical sheets of PMMA and MMA can be downloaded from the MicroChem website [66] which provides information on the parameters for spinning speed versus thickness.

4.2.3 E-beam writing

DesignCad file and set-up

I used a Philips XL30 SEM located in Physics 2215 for e-beam writing. The SEM has the Nabity e-beam lithography system - NPGS [73]. For pattern designing, I used DesignCAD [74]. The pattern I used for a Cooper pair box was saved in c:/pg/pat/HPCP1.dc2 on the SEM writing computer. For lines with width less than 100 nm, I used a line dose of 0.5 nC/cm to 2 nC/cm. For fine lines that were close together, I decreased the dose. There is not a universal dose for a given substrate and line width, so I had to use trial and error. For patterns larger than 1 μm, I used an area dose of 170 μC/cm^2 to 200 μC/cm^2. The recommended e-beam setting for writing small features is 30 kV with spot size 1. For large patterns, a larger spot size can be used.

(a)

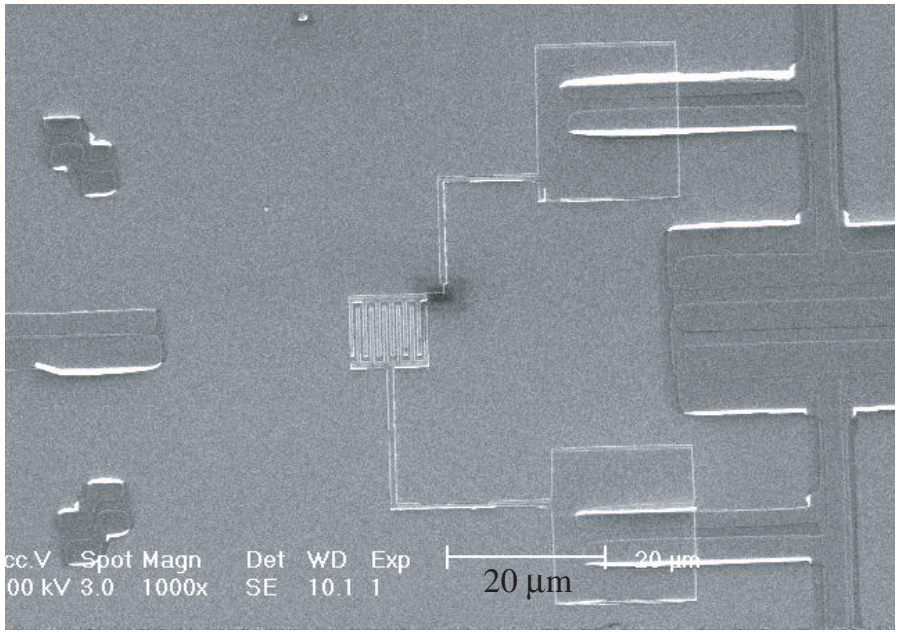

(b)

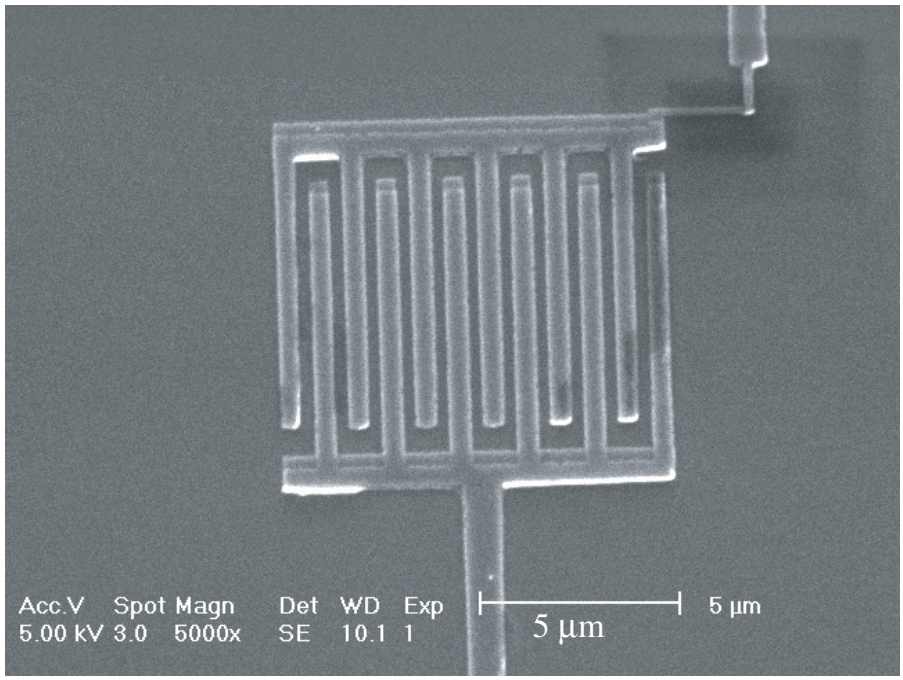

Figure 4.6: (a) A Cooper pair box coupled to a Josephson junction phase qubit. The phase qubit was fabricated by photolithography and the Cooper pair box was made by e-beam lithography. They are coupled through an interdigitated capacitor shown at the center. (b) The interdigitated capacitor of the Cooper pair box.

(a)

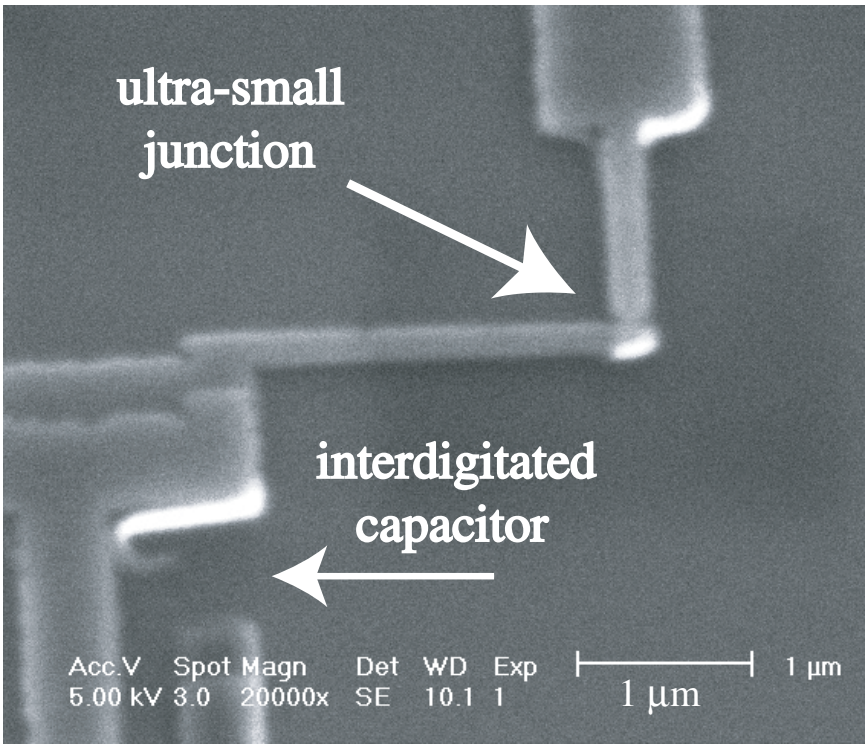

(b)

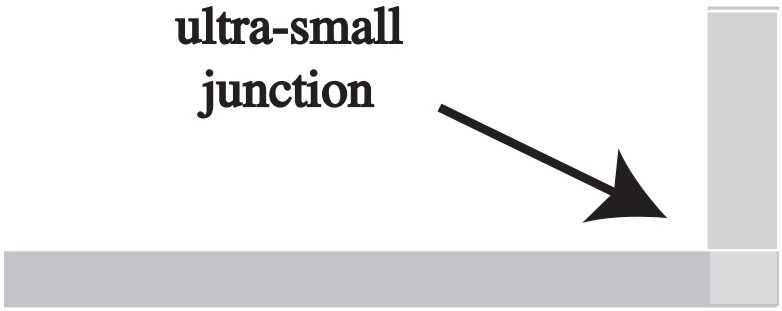

Figure 4.7: (a) Ultra-small junction of Cooper pair box fabricated by e-beam lithography. (b) Diagram showing layout of ultra-small junction.

Alignment

For putting the Cooper pair box on a phase qubit, alignment with underlying layers is important. However, Al is not easy to see with the SEM, especially on an SiO_2 coated surface. I found it was much easier to see the Al pattern if I first charged up the designated writing area with the beam set to 3 kV acceleration voltage, spot size 2. I then re-imaged with a 30 kV beam and spot size 1. Because of charging, the area will look brighter than other parts of the chip. However, this method also caused overexposure in some of the e-beam patterns I created. I also found it useful to make a scratch near the place I was writing.

4.2.4 Develop

To develop the pattern, I used 1 part of MIBK (Methyl Isobutyl Ketone) diluted with 3 parts IPA (Isopropyl alcohol) developer (conventionally known as "MIBK:IPA 1:3") [66] for PMMA and MMA. I dipped the chip in the "MIBK:IPA 1:3" solution and mildly agitated horizontally in line with the junction. Afterward, I dipped the chip in IPA to provide the undercut. I then dried the chip using nitrogen. MIBK is a more aggressive developer than IPA. The developing time depends on dose and I typically developed for 30 sec for PMMA and 60 sec for MMA. I used an optical microscope to check how much undercut was created and developed the MMA more in IPA if there was not enough undercut.

4.2.5 Ion milling and Al deposition

Before depositing Al for the Cooper pair box (see sec. 4.1), I had to use an ion-mill to remove AlO_x from the connection pads in the phase qubit so that I could make good electrical contact. I did this step just before doing the double-angle deposition of Al in the same chamber.

1. The deposition method is the same as discussed in sec. 4.1. The Ar ion gun [75, 76, 77] is mounted on the chamber top. I made sure that the sample holder was under the center of the ion mill chamber, set the sample stage facing each AL source at 45° to the vertical and made a mark. Also I made a mark when the sample stage faced upward to the ion mill (180°). After marking, I set the sample stage facing downward, toward the deposition electrodes (0°).

2. I purged the O_2 line for 1 min at a pressure of 1000 mTorr. Then I closed the O_2 valve on the top of the evaporation chamber; the Ar and O_2 share the same gas line to the evaporation chamber.

3. I purged the Ar line for 1 min.

4. I pumped the chamber below 10^{-6} Torr and degassed the ion gauge for more than 10 min at 10^{-6} torr before measuring the pressure.

5. I then throttled the cryopump valve (half open). Using the electronic Ar/O_2 valve, I set the deposition chamber pressure at 3×10^{-4} Torr by adjusting the Ar flow.

6. To ion mill the sample, I turned on the Ar ionization source and beam. I set the acceleration voltage to 100 V, the discharge voltage to 40 V, and the beam voltage to 600 V. I adjusted the cathode current until the beam current was 5 mA, and set the neutralizer current the same as the cathode current.

7. With a beam current of 5 mA, I turned the sample stage so that the sample holder faced the ion mill and milled for 1 min. From Ref. [75, 76, 77], this should result in the removal of about 1 nm of Al_2O_3.

8. I closed the electronic valve controlling the Ar gas and opened the hivac valve. I next switched the gas line from Ar to O_2 and pumped down the chamber to 10^{-6} Torr.

Table 4.1: Ar Ion beam etching rate at normal incidence for a beam current density of 1.0 mA/cm^2 and 500 V acceleration voltage as given by refs. [72 - 74].

Material	Etching rate (nm /min)
Al_2O_3	8.3
Al (bulk)	30
SiO_2 (crystal)	33
SiO_2 (evaporated film)	28
Shipley AZ1350 photo resist	20

9. I rotated the sample holder to 45° facing the electrodes and made sure the shutter was closed. I turned on the electrode and slowly increased the current in the electrode to preheat the Al boat. When Al started evaporating, I opened the shutter, deposited about 50 nm of first Al at 1 nm/s and closed the shutter. I turned off the power of the electrode and oxidized the Al film in 18 Torr O_2 for 10 min.

10. I then closed the valve for the oxygen and rough pumped the chamber to 500 mTorr using the mechanical pump and opened the hivac to pump the chamber to 10^{-6} Torr.

11. I rotated the sample holder to -45° and repeated the same procedure used in step 9 to deposit about 50 nm of Al at 1 nm/s.

4.2.6 Lift-off

I used acetone for lift-off of the e-beam patterns. I put the chip in a pyrex beaker filled with acetone at room temperature. The lift-off takes 3 to 4 hours. I checked the pattern using the optical microscope to see if lift-off was successful. If a small part did not lift off, I tried sonication for 10 to 20 sec. Since too much

Table 4.2: Parameters of some dc SQUID phase qubits measured by the UMD group. NB1, NB2 and NBG were made by Hypres, Inc. [78]. Index 1 indicates a qubit junction and index 2 indicates an isolation junction.

Device	$A_1(\mu m^2)$	$I_{01}(\mu A)$	$A_2(\mu m^2)$	$I_{02}(\mu A)$	L_1(nH)
AL1	80	21.2	40	9.5	1.2
NBG [79]	120	23	60	3.8	4.5
DS_1(NB1) [23]	100	107.9 (33.8)	49	51.7 (4.8)	3.5
DS_2(NB2) [23]	100	24, 20	49	3, 6	3.4
AL2 [80]	16	1.23	160	9.19	1.05

sonication can ruin the pattern, the sonication should be performed carefully and only for few seconds.

4.3 Table of dc SQUID phase qubits measured in UMD SQC group

Table 4.2 summarizes parameters of some of the dc SQUID phase qubits measured in our lab as of July 2007. In this table, A_1 is the area of the qubit junction, A_2 is the area of the isolation junction, I_{01} and I_{02} are the critical currents of the qubit and isolation junction, respectively, and L_1 is the inductance on the qubit junction arm of the SQUID loop.

4.4 Dilution refrigerator setup

Our phase qubits must be cooled to milli-Kelvin temperatures to operate properly [27]. I used an Oxford Instruments Kelvinox 25 dilution refrigerator [81] in a shielded room in the basement of the Physics building. With wiring attached, the refrigerator had a base temperature of 80 to 100 mK. Figures 4.8 to 4.12 show photographs of the refrigerator and its wiring.

For measuring qubits, the Kelvinox 25 is wired with six UT34 coaxes from the

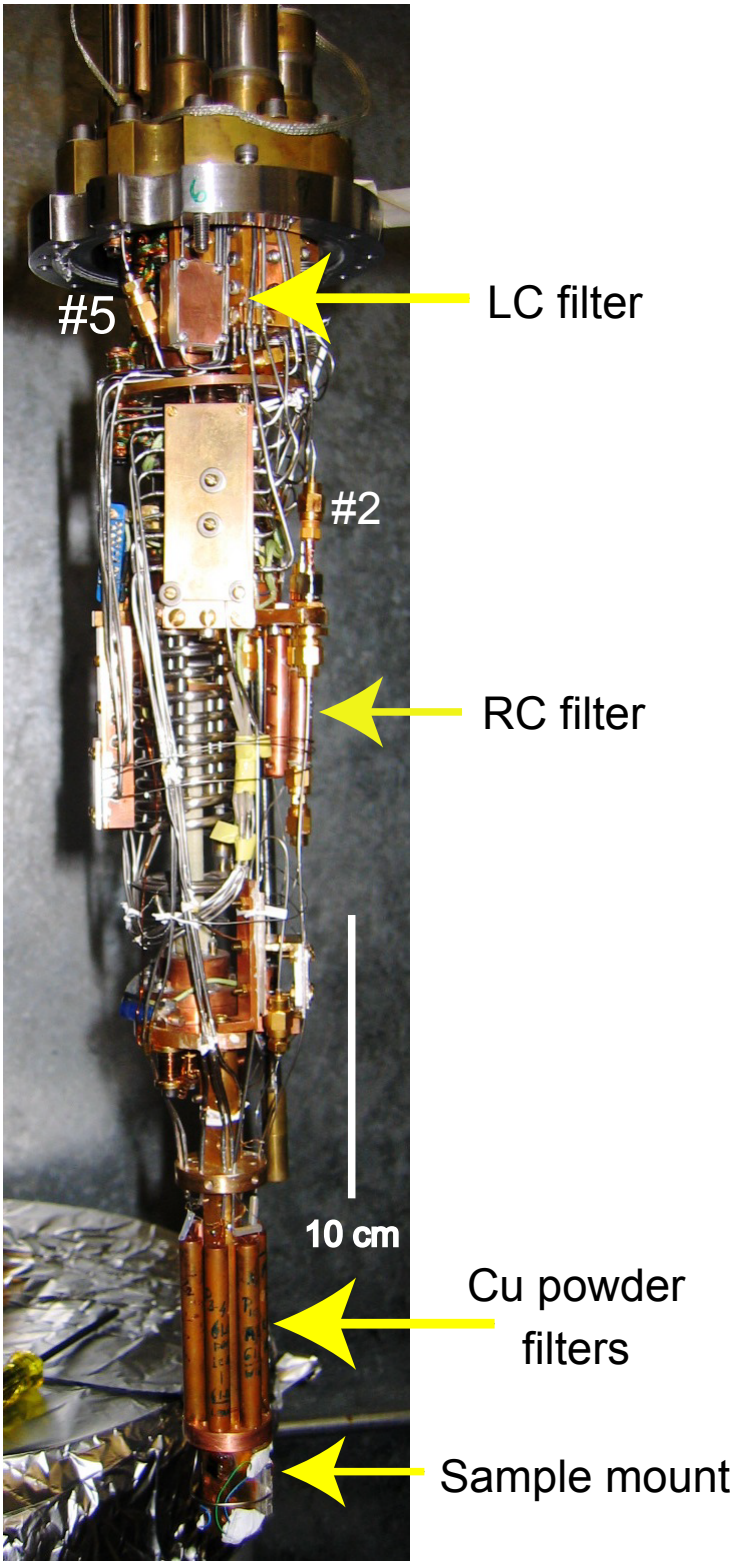

Figure 4.8: Oxford Instruments Kelvinox 25 dilution refrigerator and sample mount.

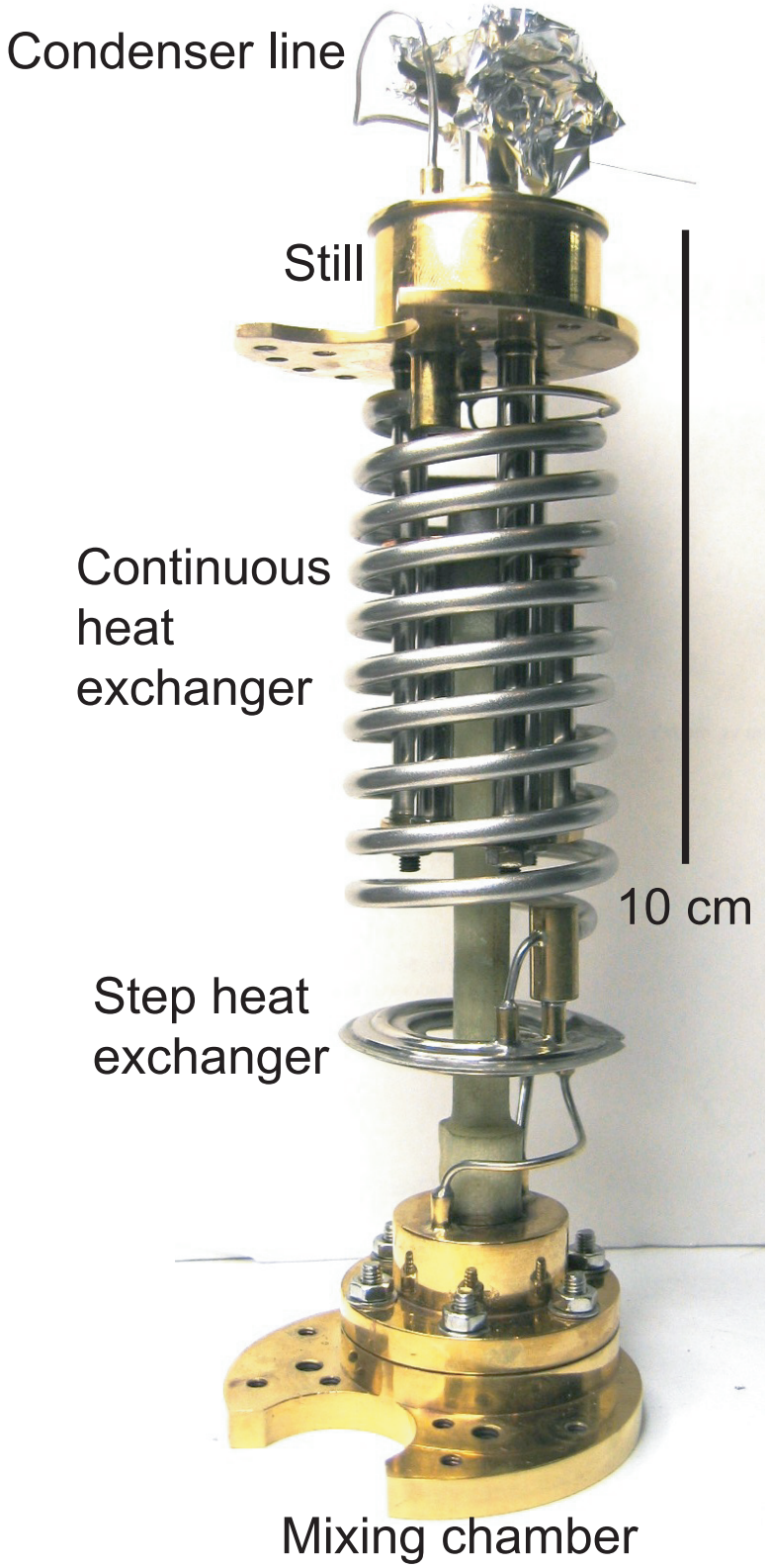

Figure 4.9: Oxford Instruments Kelvinox 25 dilution refrigerator unit.

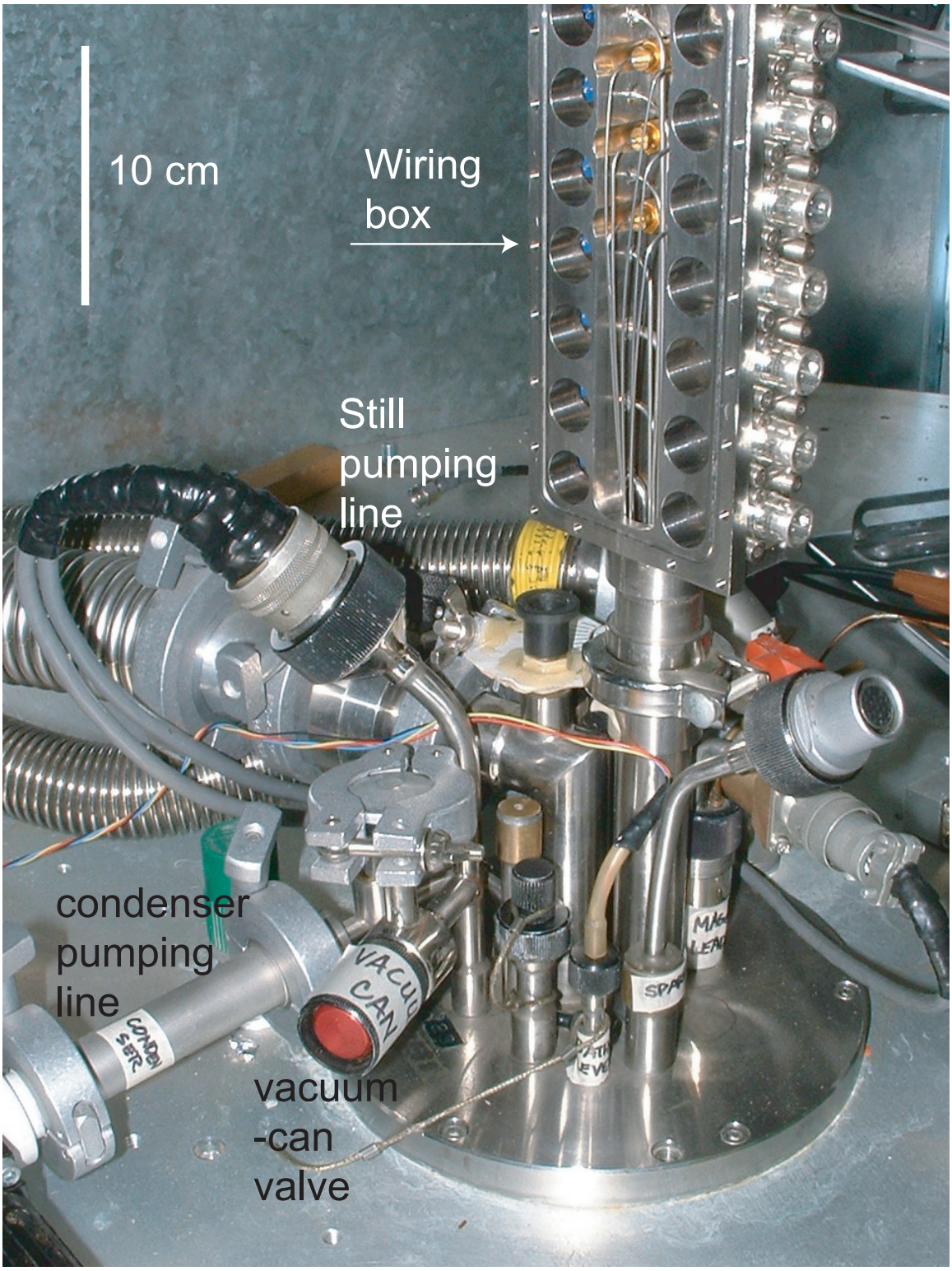

Figure 4.10: 300 K flange showing ports for wiring, gas and vacuum. The stainless steel box on the right side accommodates six coaxial cables as well as twisted-pair manganin lines.

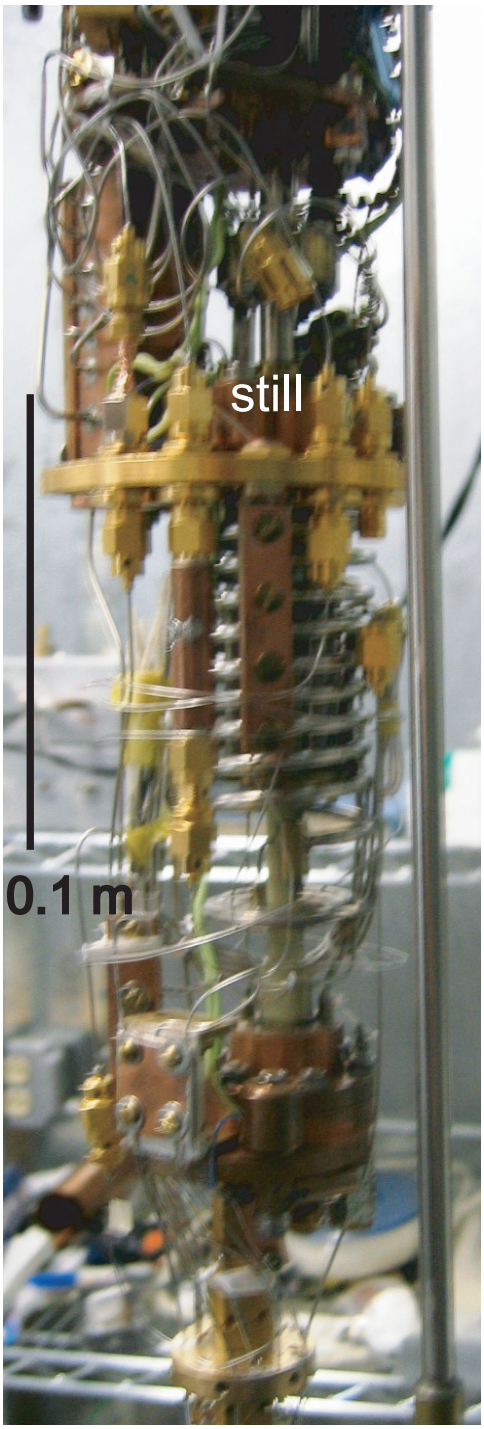

Figure 4.11: Wiring on the Oxford Instruments Kelvinox 25 dilution refrigerator. All coaxial lines are thermally anchored at the 4 K flange and still.

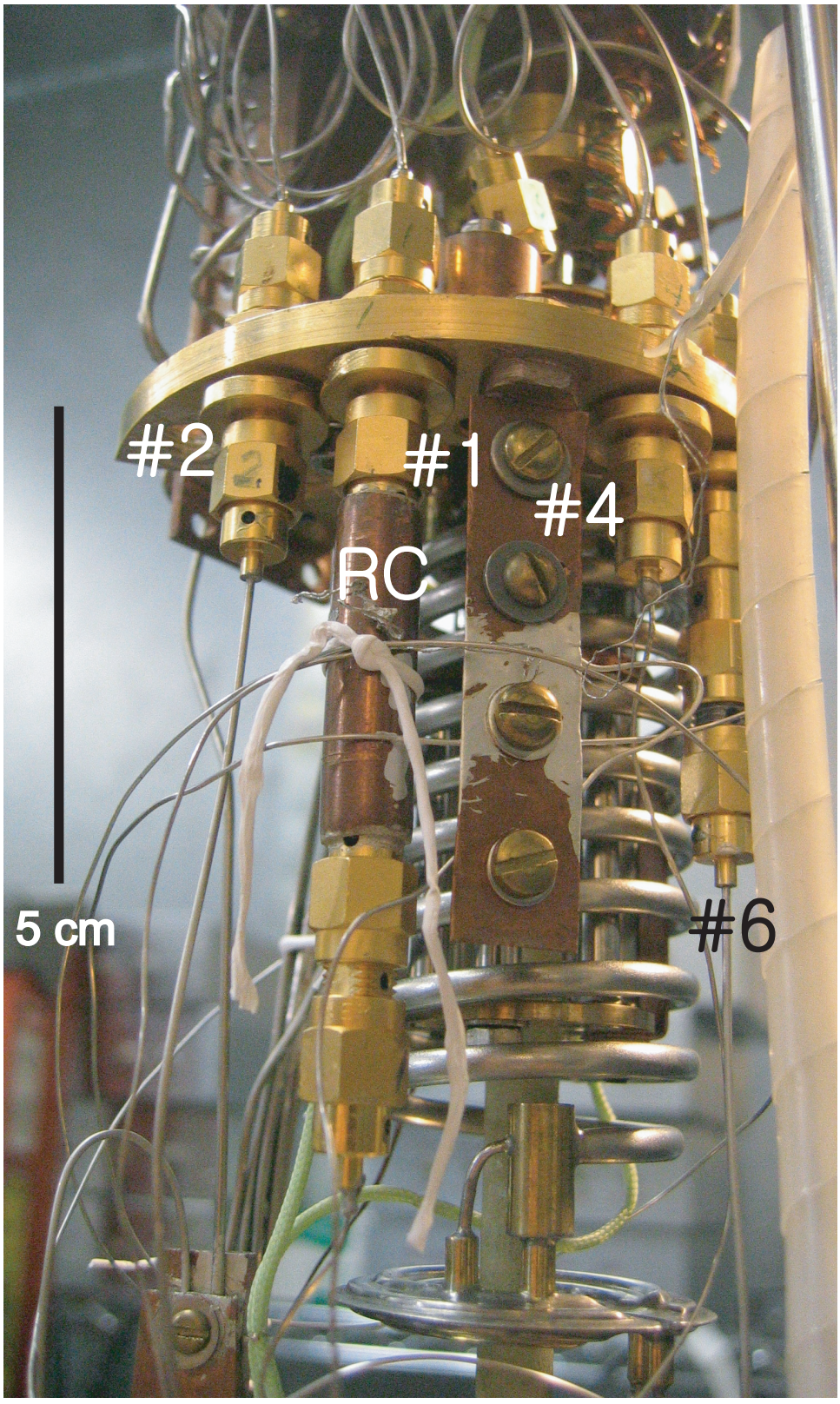

Figure 4.12: Photograph of the heat exchanger and still showing where the coaxial lines are thermally anchored.

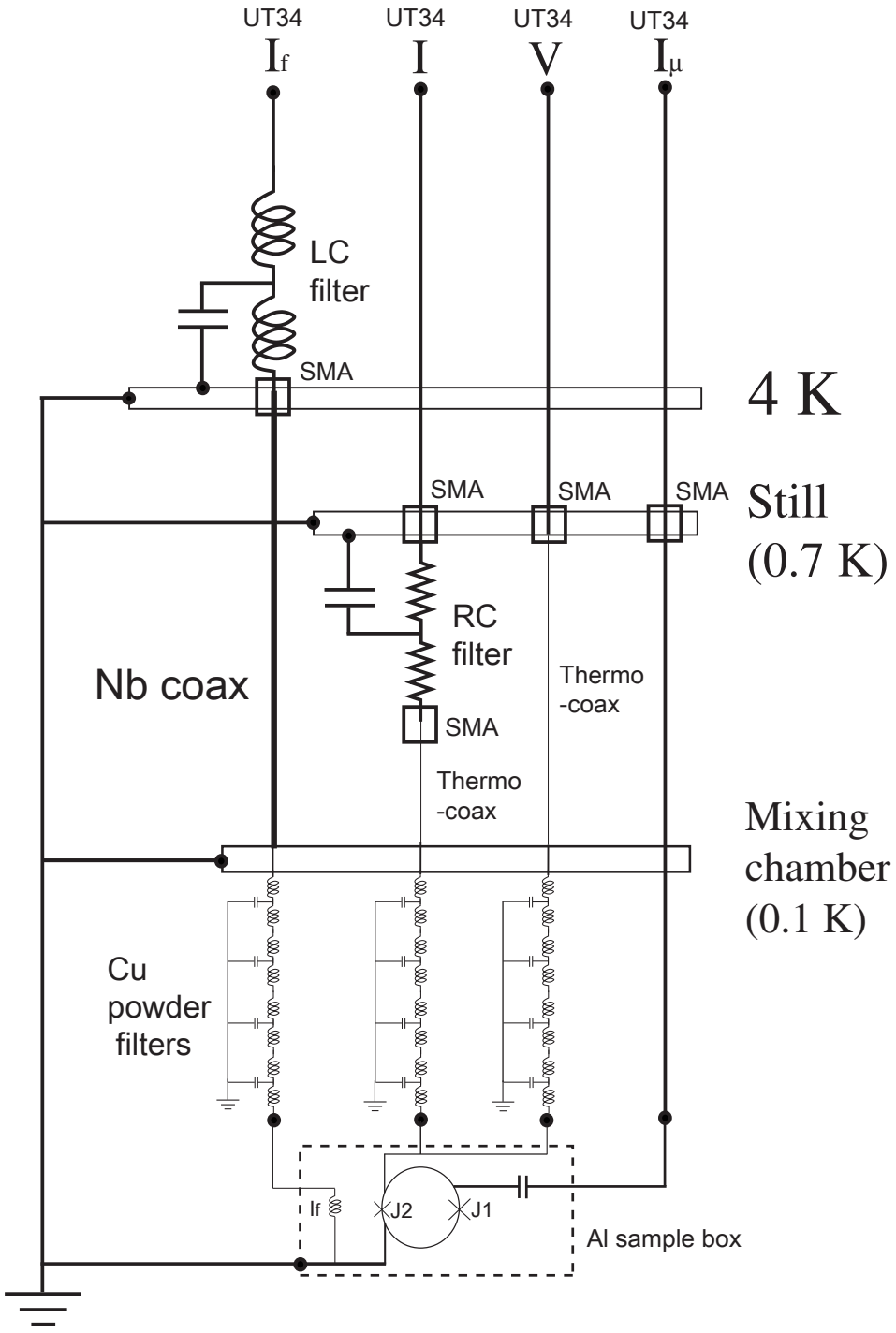

Figure 4.13: Wiring schematic for Oxford Instruments Kelvinox 25 dilution refrigerator. I_f is the flux bias current, I is the current bias, V is the voltage measurement lead and I_μ is the microwave line. Coaxial lines are thermally anchored at the 4 K stage and the still. The flux bias line I_f uses a superconducting Nb coax from 4 K to the mixing chamber and has an LC low pass filter. The current bias line I has an RC low pass filter. For V and I, Thermalcoaxes are used from the still to the mixing chamber where the coaxes are connected to copper power filters.

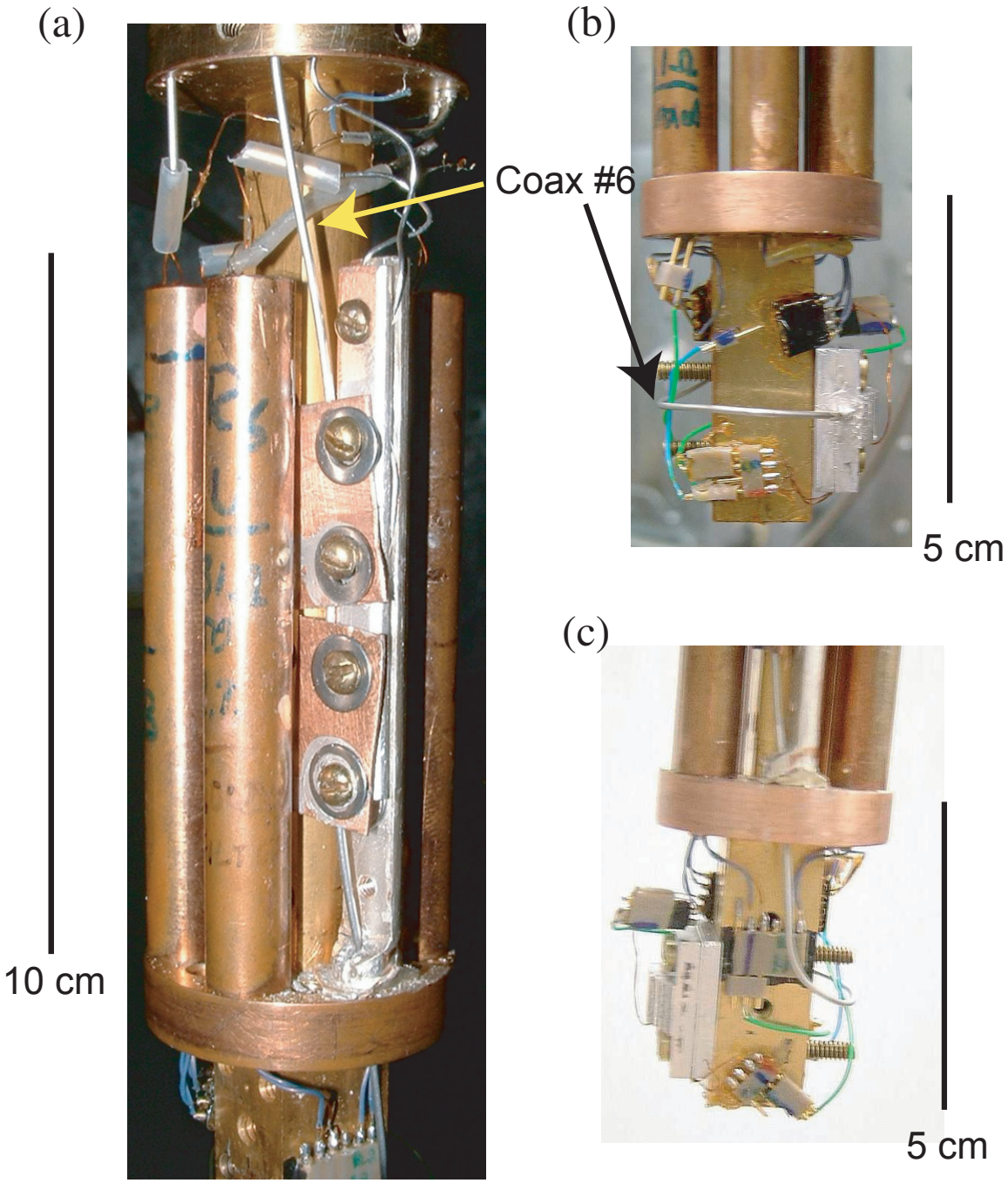

Figure 4.14: Copper powder filters and qubit sample holder box at the mixing chamber (MXC) of the refrigerator. (a) Copper power filters at MXC. (b) Side view of Aluminum box - sample holder mounted on the MXC. The sample holder aluminum box is located below the copper power filters. (c) Opposite view of the aluminum sample holder box.

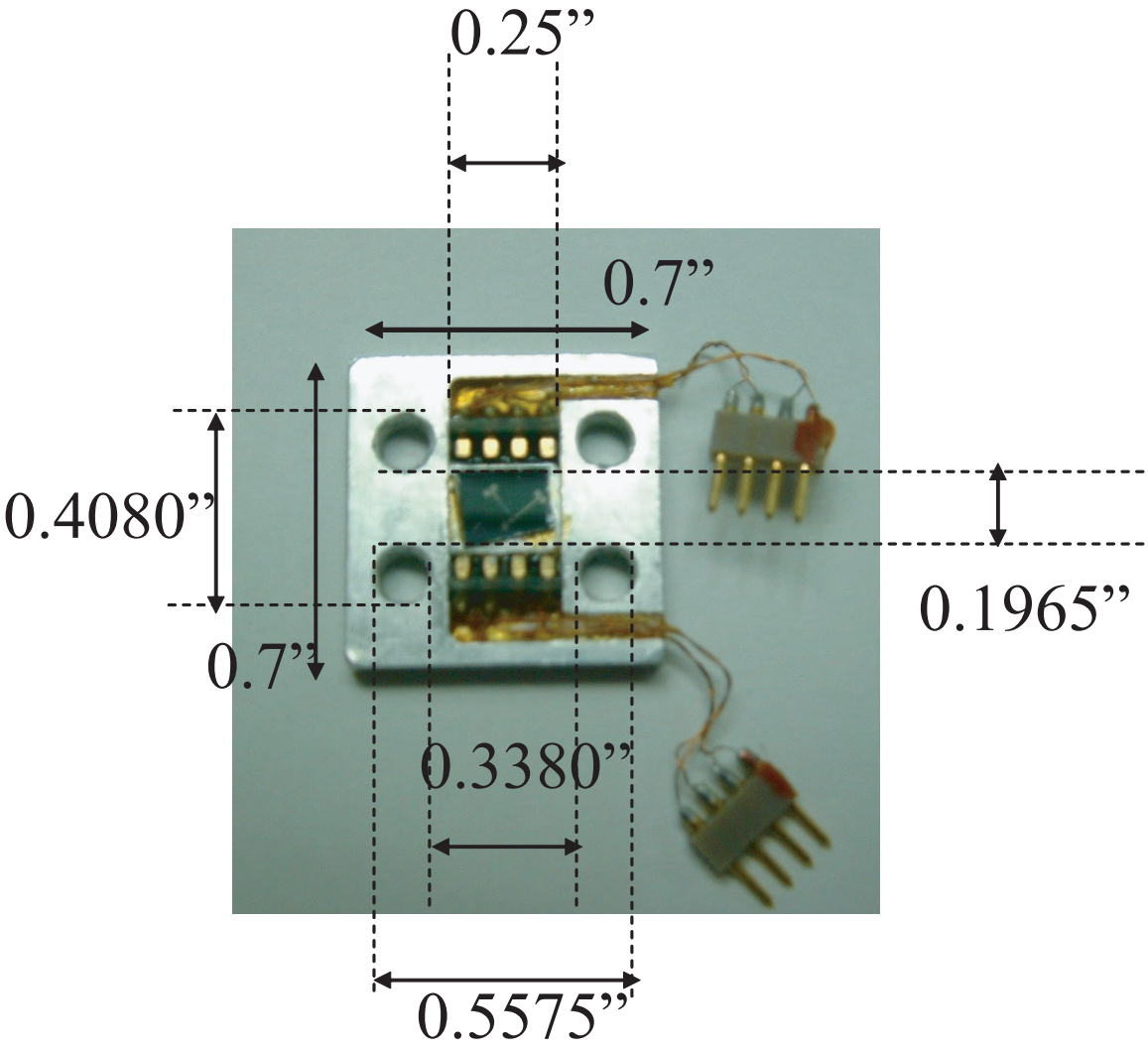

Figure 4.15: Aluminum sample holder shown without the top. The box thickness is 0.099”.

300 K flange to the still (see Fig. 4.10 to Fig. 4.12). The wiring schematic for the refrigerator is shown in Fig. 4.13. All six coaxes are thermally grounded at the still (see Fig. 4.12) and connect to copper power filters at the mixing chamber, except for Coax #6 which is used to supply microwave current to the devices. I used only #1, #4, #5 and #6 for the measurements in this thesis.

Coax #1 is made from stainless steel semi-rigid UT34 coaxial cable [25]; I used this line for the current bias. At the still (600 mK), Coax #1 is connected through a low-pass RC filter with a cutoff frequency of about 300 MHz (see Fig. 4.13). After the RC filter, Coax #1 is wired with a Thermocoax® cable [82], which works as a microwave filter [83, 84], and connects to a copper powder filter mounted on the mixing chamber. I used type 1 NcAc Thermocoax® [82] which has a NiCr center wire, a stainless steel outer conductor and an MgO dielectric layer.

Coax #4 is used as a voltage detection line and from 300 K to the still, it is made from UT34. From the still to the mixing chamber, I used a Thermocoax® cable. I used Coax #5 as a flux bias line. Coax #5 is wired with a UT34 coaxial cable from 300 K to 4 K. It is connected to a low-pass LC filter with a cutoff frequency of 100 MHz at the 4 K stage. From the 4 K flange to the copper powder filters in the mixing chamber, I used a superconducting Nb coax. Coax #6 uses UT34 cable continuously all the way to the sample box. The electrical characteristics of the UT34 coax, the Thermocoax® and the Nb coax are discussed in H. Xu's thesis [25].

At the mixing chamber, the copper powder filters are connected to the center pins of the coaxes, except for coax #6. After the copper powder filters, the copper wires from the filters have Microstrip connectors that plug into the aluminum sample box. Coax #6 passes straight through the top of the aluminum sample box (see Fig. 4.14), to serve as a microwave antenna. The qubit sample was mounted in a closed superconducting aluminum box to shield out magnetic fields (see Fig. 4.15). The sample was attached using GE varnish on the bottom and a Ag paint along the

Table 4.3: Commercial electronics used in the experiment.

Purpose	model number
Current bias I	Agilent 33120A Arbitrary waveform generator
Flux bias I_f	Agilent 33120A Arbitrary waveform generator
Microwaves	HP (Agilent) 83731B Synthesized signal generator
Gating microwave	SRS DG535 Pulse generator
Frequency counter	SRS SR620 Frequency counter
Calibration Voltage amp	SRS SR560 Low-noise voltage amp

sides for good thermal conduction. In addition, the refrigerator was surrounded by a copper radiation shield, a stainless steel vacuum can, an aluminum dewar, a room-temperature mu-metal shield and finally enclosed in an rf-shielded room.

4.5 Measurements and analysis

In my experiments, the qubit typically has to be initialized to a unique state, the state is then manipulated with microwaves, and measured. In this section, I discuss the initialization procedure and my measurement technique.

Figure 4.16 shows a schematic of the measurement setup I used. Tables 4.3 and 4.4 summarize the commercial and the homemade electronics that I used for my measurements.

4.5.1 Initialization of the flux state of the dc SQUID phase qubit

The flux state of the SQUID needs to be initialized before each measurement. The problem is that the dc SQUID phase qubit has multiple flux states due to a high value of $\beta = 2L(I_{01} + I_{02})/\Phi_0$ [85, 86]. Each flux state has different energy levels so I need to choose a unique flux state each time. To do this, I used a flux shaking

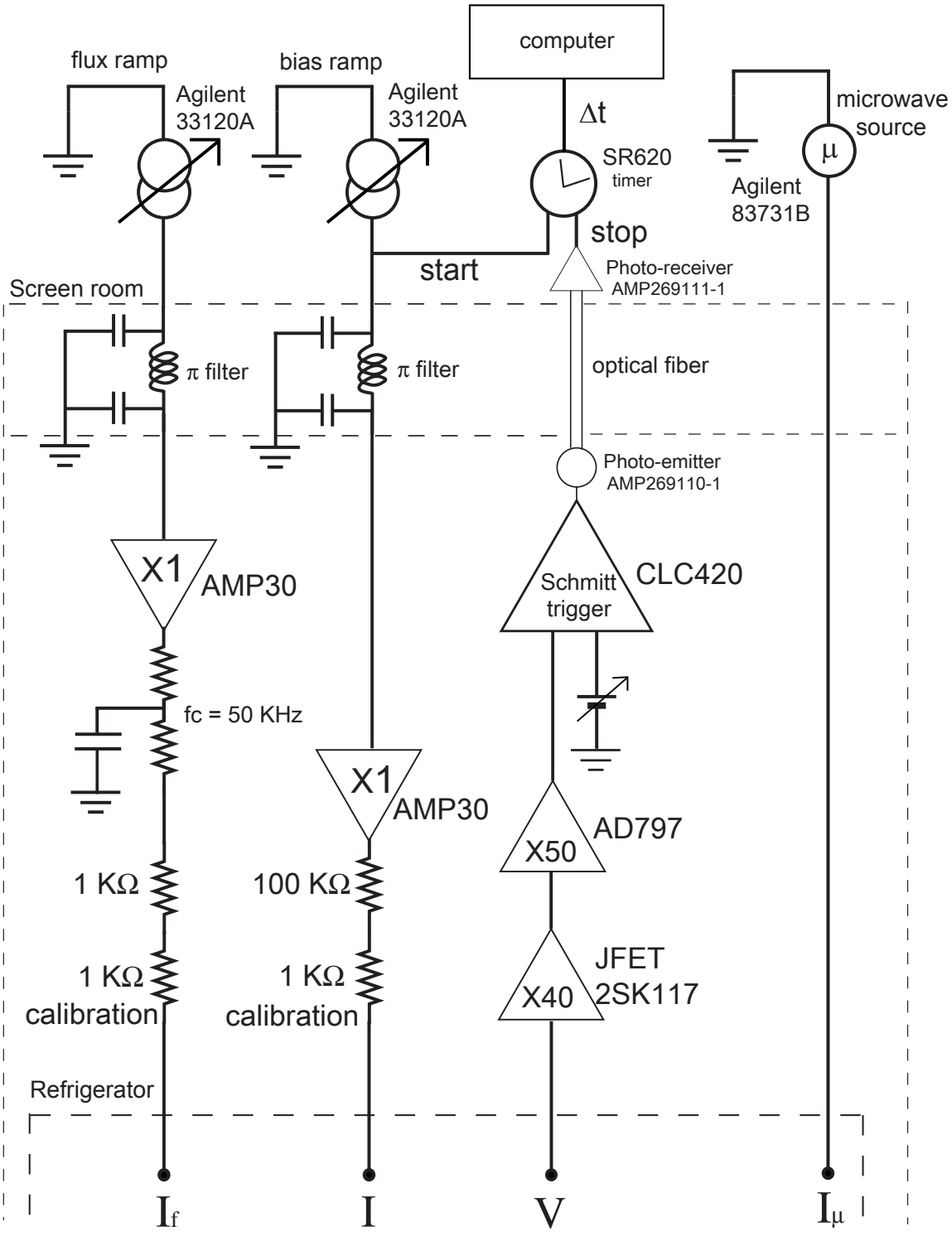

Figure 4.16: Schematic of the measurement setup.

Table 4.4: List of homemade electronics used in the experiment. Diagrams are in Ref. [25].

Purpose	chipset
Switching voltage detection Schmitt trigger	CLC420
Unity buffer after Schmitt trigger	LMH6624
1st stage switching voltage amplifier	JFET 2SK117
2nd stage switching voltage amplifier	AD797 or AD829
Unity gain buffer	AMP03

technique [86]. This technique involves applying a 20 to 30 kHz sinusoidal flux with a carefully chosen amplitude. Different flux states can be chosen by applying an appropriate dc flux offset for the sinusoidal flux. The detailed procedure is described in Ref. [86]. After shaking for about 50 flux oscillations, I was able to place the SQUID in the desired flux state with a 99 % or greater probability. S. K. Dutta's thesis also has discussion on flux shaking technique [23].

4.5.2 Biasing the qubit junction

To bias the qubit junction in the dc SQUID phase qubit [86], I used a simultaneous current and flux ramp [47] generated by two function generators. When the current bias ramp (I) started, its function generator sent out a TTL signal that was then used to trigger the second function generator to start the flux ramp (I_f). The idea of simultaneous biasing is to arrange the two ramps so that there is no change in the current going through the isolation junction, *i.e.* $\Delta I_2 = 0$, by keeping the ratio $I/I_f \simeq -M/L$ where L is the total loop inductance of the SQUID and M is the mutual inductance between the SQUID and the flux line. Figure 4.18 shows typical waveforms for the ramps. I used Agilent 33120A function generators (see Fig. Table 4.3 and Fig. 4.16) and a detailed discussion of the double ramping procedure is

given in Ref. [23].

4.5.3 Measurement of the qubit state via the escape rate

I read out the qubit state by measuring the total escape rate. Fig. 4.17 shows a sketch of the potential energy and energy levels of a Josephson junction qubit in a metastable well of the washboard potential. Because of the shape of the potential, higher-energy states are more likely to escape by tunneling than lower-energy states; each successive level tunnels about 500 times faster. In addition, when the current through the junction is increased, the tilt of the washboard potential increases and the potential barrier is lowered, causing the tunneling rates from all of the states to increase. The escape event is analogous to radioactive decay; the decay is exponential. What we measure in the experiment is the total escape rate, which is give by

$$\Gamma_{tot} = \rho_0\Gamma_0 + \rho_1\Gamma_1 + \rho_2\Gamma_2 + \rho_3\Gamma_3... = \sum_i \rho_i\Gamma_i \tag{4.1}$$

where ρ_i and Γ_i are the occupation probability (or population) and escape rate of level i. Since the escape rate increases by two or three orders of magnitude when i is increased by 1, the total escape rate is very sensitive to even small populations in the upper levels.

For an escape rate measurement, the qubit junction current is ramped linearly with time by simultaneously ramping the flux and bias current as described above, and the voltage across the SQUID is monitored. When the qubit junction tunnels, a relatively large voltage ($2\Delta/e \simeq 400\mu V$ for an Al Josephson junction) appears across the SQUID bias. This voltage is amplified to trigger a low-noise Schmitt trigger. The SR620 timer is used to measure the time interval between the start of the ramp (at t_I in Fig. 4.18) and the appearance of the switching voltage (at t_F in

Fig. 4.18). To detect the the switching voltage, I used a homemade Schmitt trigger [25] (see Table. 4.4 and Fig. 4.14) followed by a unity buffer. I set the threshold voltage for the Schmitt trigger so that it triggers at the point where the rise time of the switching voltage changes most rapidly in time. After each switching event, the time interval t_F - t_I is recorded on a computer.

This switching measurement is repeated $N \sim 10^5$ times at a repetition rate of 950 Hz. The resulting switching times are used to construct a histogram of switching events as a function of the switching time interval. The number of switching events $h(t_i)$ at time t_i in interval Δt is converted to the total escape rate $\Gamma(t_i)$ at time t_i using [23]

$$\Gamma(t_i) = \frac{1}{\Delta t} \ln \left[\frac{N(t_i)}{N(t_{i+1})} \right] = \frac{1}{\Delta t} \ln \left[\frac{\sum_{j \geq i} h(t_j)}{\sum_{j \geq i+1} h(t_j)} \right]. \tag{4.2}$$

where Δt is the time bin, typically of order 1 ns, and $N(t_i) = \sum_{j \geq i} h(t_j)$ is the number of measured switching events where the switching occurred after time time t_i. The uncertainty in the escape rate is [23]

$$\sigma_{\Gamma_i}(t_i) = \frac{1}{\Delta t} \sqrt{\left[\frac{1}{N(t_i)} \right]^2 h(t_i) + \left[\frac{1}{N(t_{i+1})} - \frac{1}{N(t_i)} \right]^2 N(t_{i+1})}. \tag{4.3}$$

The timer starts when it receives a TTL trigger signal from the current ramp. However, there could be an offset with respect to the time when the ramp starts because the TTL signal has a finite rise time. This would lead to an effective offset in current. To calibrate the current at any time on the ramp, I placed 1 kΩ resistors at 300 K on the current bias and the flux bias lines. The voltage across the resistor was amplified using a commercial low-noise amplifier SR560 and I then measured the voltage across the resistors versus time to get a calibration curve for the current ramps. For example, the calibration that I got for my measurements of AL1 was

$$I(t) = a \times t - b \tag{4.4}$$

where a = 3.482074 $\times 10^{-2}$ A/s and b = 2.493 μA. With the range calibrated as a function of time, I could readily convert $\Gamma(t)$ to $\Gamma(I)$.

The measured total escape rate $\Gamma(I)$ then can be fit to the calculated total escape rate. For the escape rate fit in Chapter 5, I assumed the populations from each levels was thermal and obtained the escape rates Γ_n from each level n using

$$\Gamma_n = (7.2\, N_s)^{n+1/2}\ \frac{\omega_p}{2\pi}\ \exp\left[-7.2\, N_s + f_\Gamma^n\,(N_s)\right] \tag{4.5}$$

as shown in Chapter 2. Then I was able to construct a calculated total escape rate according to Eq. 4.1. This requires just two fitting parameters, T_1 and temperature T.

4.5.4 Spectroscopy and T_2^*

When the microwaves are in resonance with an energy level spacing, microwaves can drive the qubit junction from one state to another state, producing an enhancement in the total escape rate. I measured the resonance peaks while sweeping the bias current; As I sweep the bias current, the energy level spacings decrease and resonance occur at multiple points on the current axis, wherever an energy level spacing is resonant with the microwaves.

Figure 4.19 shows microwave resonance peaks in the escape rate of AL1 measured at 80 mK. Here I applied a 6.9 GHz microwave drive. Two resonance peaks appear in the escape rate, corresponding to the $|0\rangle$ to $|1\rangle$ (at about I = 21.61 μA) and $|1\rangle$ to $|2\rangle$ (at about I = 21.67 μA) transitions. For spectroscopy, I used microwaves of relatively low power so the bare Rabi frequency satisfies $\Omega_0 \ll (T_1 T_2)^{-1/2}$.

For spectroscopy, I used an HP (Agilent) 83731B Synthesized signal generator for microwave source (see Fig. 4.14). I first fixed the microwave frequency and power, and then swept the qubit junction current. I then measured the time driving

the ramp at which the junction switched. After that, I did the same measurement without microwaves. I typically repeated this process 10^5 times; with and without microwaves were measured alternatively in the time sequence. After I finished the escape rate measurements for one microwave frequency, I changed the microwave frequency and repeated the whole procedure. For devices AL1 and NBG, I measured the spectra from about 6 GHz to 8 GHz.

For each escape rate curve, I obtained the microwave enhancement, $\Delta\Gamma/\Gamma$ given by

$$\frac{\Delta\Gamma}{\Gamma} = \frac{\Gamma_\mu - \Gamma_b}{\Gamma_b} \tag{4.6}$$

where Γ_μ is the escape rate with microwaves and Γ_b is the background escape rate without microwaves. Figure 4.20 shows the microwave enhancement $\Delta\Gamma/\Gamma$ versus current in device AL1 when 6.6 GHz microwaves are applied. This curve was extracted from the escape rate shown in Fig. 4.19. By fitting each peak in $\Delta\Gamma/\Gamma$ to a Lorentzian, I found the resonant current at which each peak was centered and the plotted the spectrum as points of microwave frequency versus resonance current. Figure 4.21 shows the Lorentzian fitting for the resonance peak of $|0\rangle \rightarrow |1\rangle$ transition in Fig. 4.20. Dots are the data and the dashed line is the Lorentzian fit. From the fitting, I obtained the center of the peak I = 22.017 μA with full width half maximum 3.5 nA. I performed the Lorentzian fitting to $\Delta\Gamma/\Gamma$ resonance peaks for each frequency and obtained the spectrum given as microwave frequency versus current.

A plot of a spectrum is shown in Fig. 5.9 in Chapter 5. The measured spectrum can be fit to the energy levels of a current biased junction. The calculated energy level spacing between level $|n\rangle$ and $|n+1\rangle$ is (see Chapter 2)

$$\omega_{n,n+1} = \omega_p \; f_\omega^n \left(N_s\right). \tag{4.7}$$

where f_ω^n is a correction term and N_s is the number of energy levels in the well (see Eq. 2.38). The free parameters are the critical current I_{01} of the qubit junction and the qubit junction capacitance C_1. Appendix A shows the MATLAB code that I used to solve Schrödinger equation for a single Josephson junction to obtain the energy level spacings.

The half-width at half maximum ΔI_{HWHM} of the $|0\rangle$ to $|1\rangle$ resonance peaks from the Lorentzian fits were used to obtain T_2^* through the equation :

$$T_2^* \equiv \frac{1}{2\pi\Delta f_{HWHM}} = \frac{dI}{df}\frac{1}{2\pi\Delta I_{HWHM}}. \tag{4.8}$$

where dI/df can be obtained by fitting from the measured spectrum.

4.5.5 Measurement of relaxation

To obtain T_1 from a relaxation measurement, I used the following procedure. First I took switching data for about 10^4 events with microwaves and used this to construct the escape rate versus time. I then recorded the position of the $|0\rangle$ to $|1\rangle$ resonance peak on the time axis. My microwave source, an HP (Agilent) 83731B synthesized signal generator can be triggered with an external TTL pulse (see Fig. 4.14). Using a DG535 pulse generator, I programmed a trigger pulse to turn off the microwaves at the time where the resonance peak was centered. When the microwaves were turned off, the qubit junction relaxed from the excited state to the ground state with the time constant T_1. Figure 4.18 shows the microwave sequence for the relaxation measurement with respect to the biasing currents and the switching voltage. The current bias, the flux bias and microwaves were programmed with respect to the start of the bias ramp. I used an internal clock in the SR620 frequency counter as the master clock for the all sources. (Clocks can be synchronized if they are connected by GPIB cables.)

The escape rate from a relaxation measurement shows a decay that can be fit to an exponential function (see Fig. 4.22) Detailed analysis of my T_1 data is discussed in Chapter 5.

4.5.6 Measurement of Rabi oscillations

The Rabi oscillation measurement was done similarly to the relaxation measurement but the microwaves were turned on at the center of the resonance peak with a high power (where the bare Rabi frequency $\Omega_0 \gg (T_1 T_2)^{-1/2}$). Figure 4.18 shows the measurements sequence for Rabi oscillations with respect to the biasing currents and the switching voltage. The escape rates from the Rabi oscillation measurements show an oscillating escape rate that I fit to a decaying oscillating function. Detailed analysis of my Rabi oscillation data is discussed in Chapter 6.

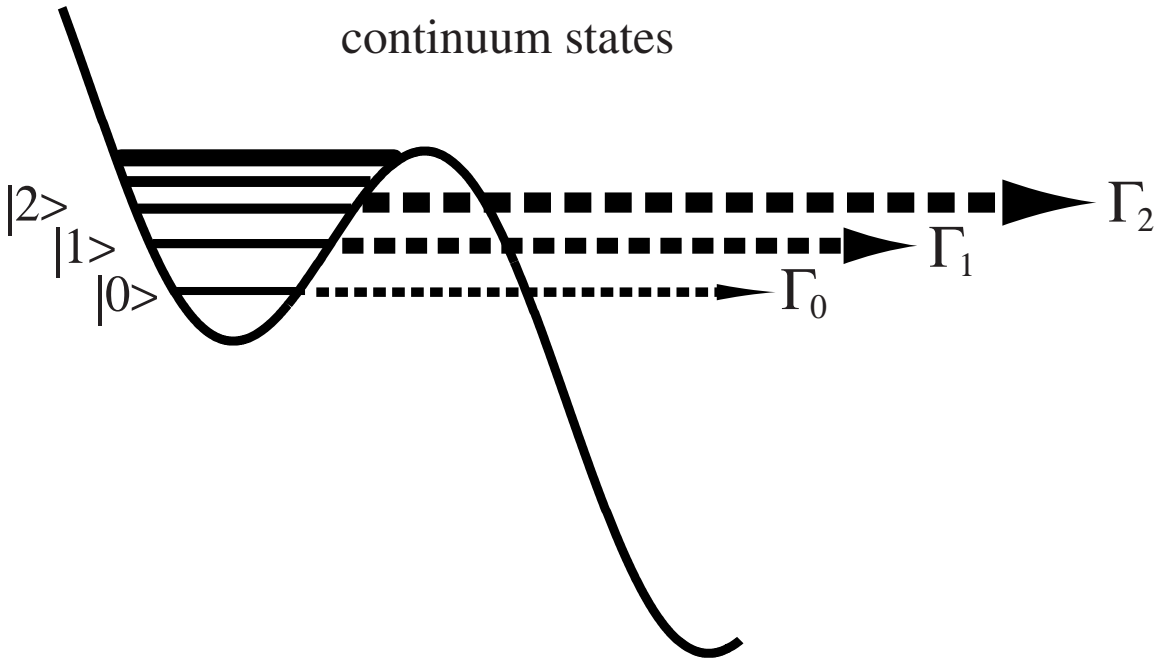

Figure 4.17: Metastable states in a well of the tilted washboard potential. Over the top of the barrier, the energy levels form a continuous energy band. Γ_0, Γ_1 and Γ_2 are the escape rates from the energy levels $|0\rangle$, $|1\rangle$ and $|2\rangle$, respectively.

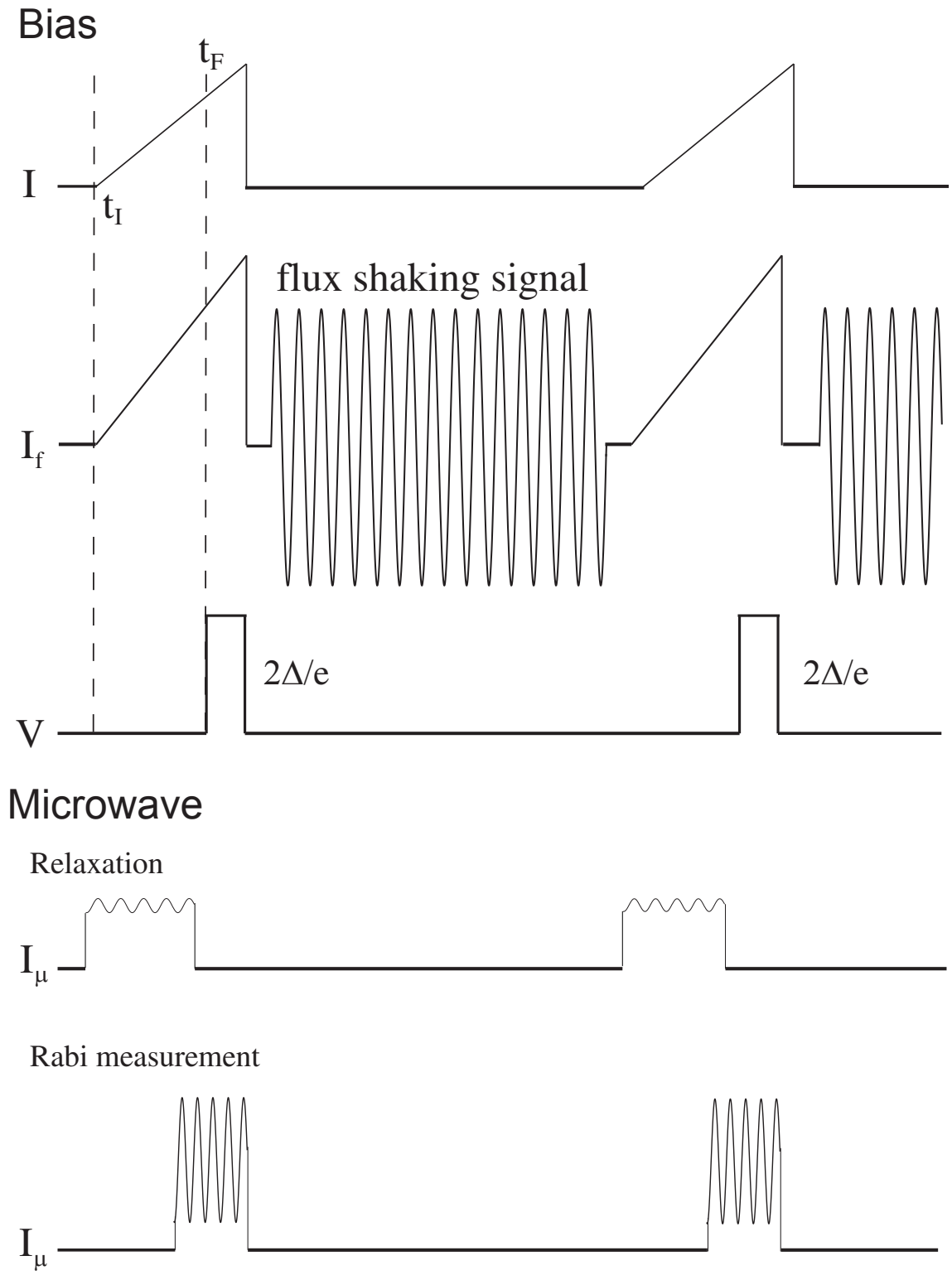

Figure 4.18: Biasing scheme for the dc SQUID phase qubit and microwave sequence. The time interval between t_I that the ramping starts and t_F when the qubit junction switching voltage V appears is recorded by the frequency counter SR620.

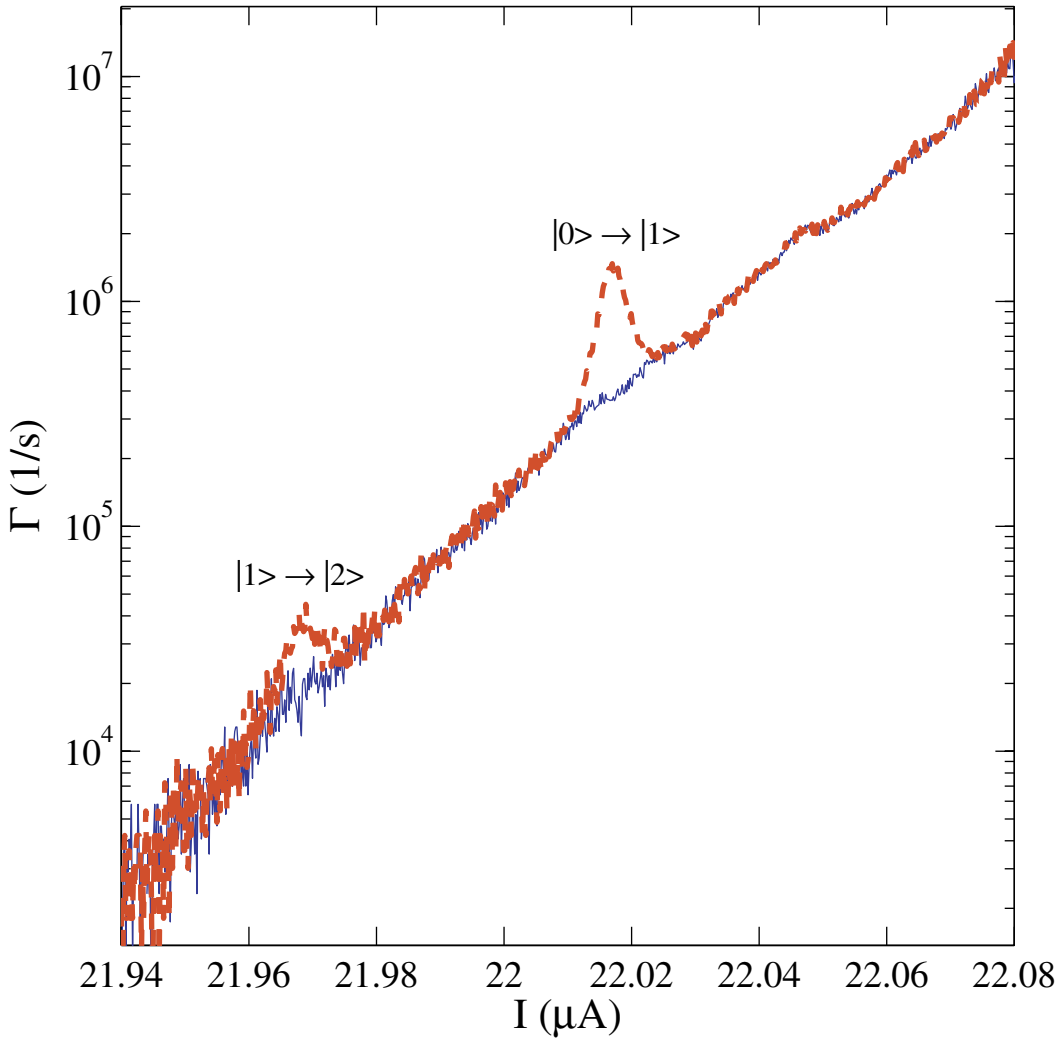

Figure 4.19: Total escape rate vs. current for qubit AL1 at 80 mK. Dashed line is when 6.9 GHz microwaves are applied to the qubit junction and solid line is without microwaves. Two prominent peaks are seen when microwaves are applied, corresponding to $|0\rangle$ to $|1\rangle$ and $|1\rangle$ to $|2\rangle$ transitions.

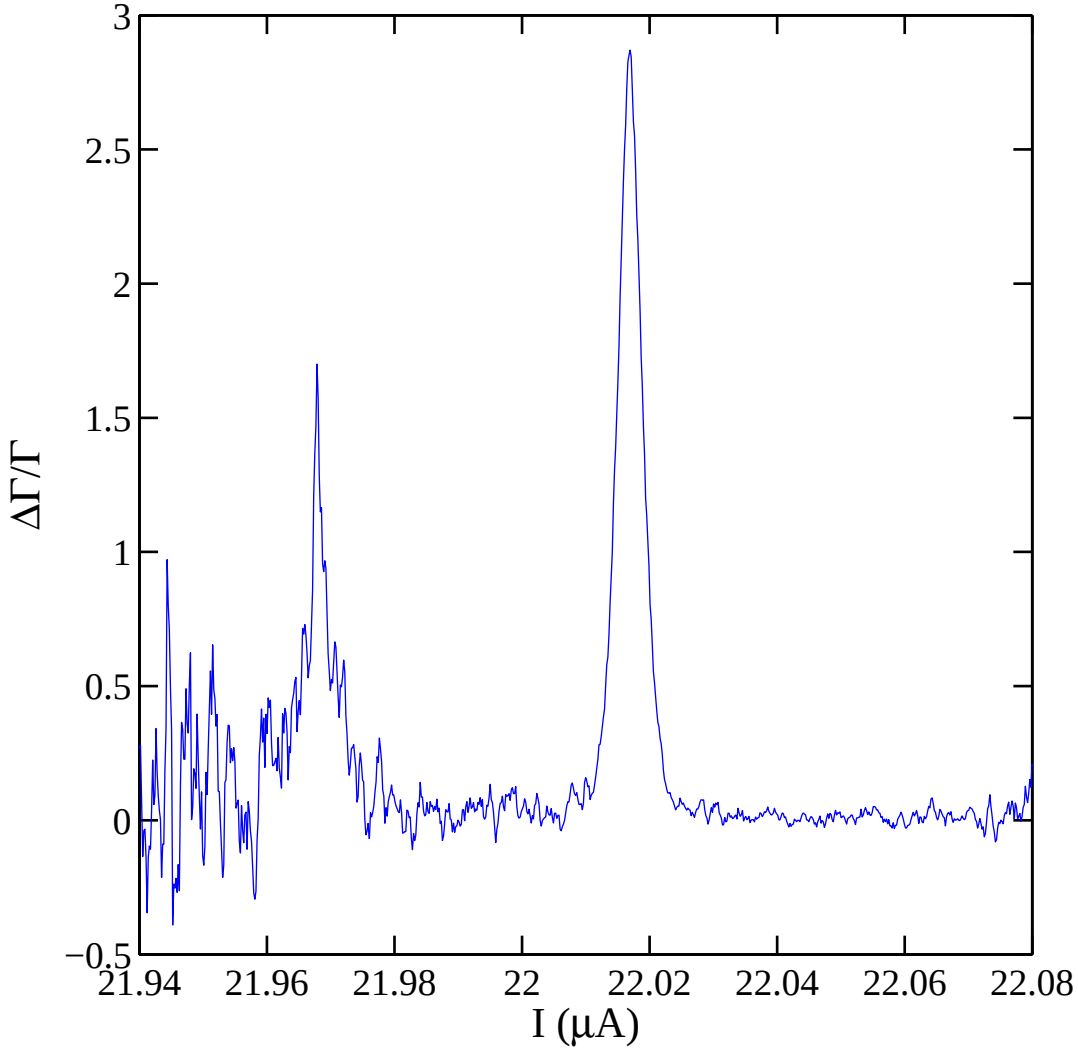

Figure 4.20: Microwave enhancement of the escape rate for AL1 at 80 mK when 6.9 GHz microwaves are applied to the qubit junction. The two peaks correspond to the $|0\rangle$ to $|1\rangle$ transition at about I = 22.18 μA and the $|1\rangle$ to $|2\rangle$ transition at I = 21.97 μA.

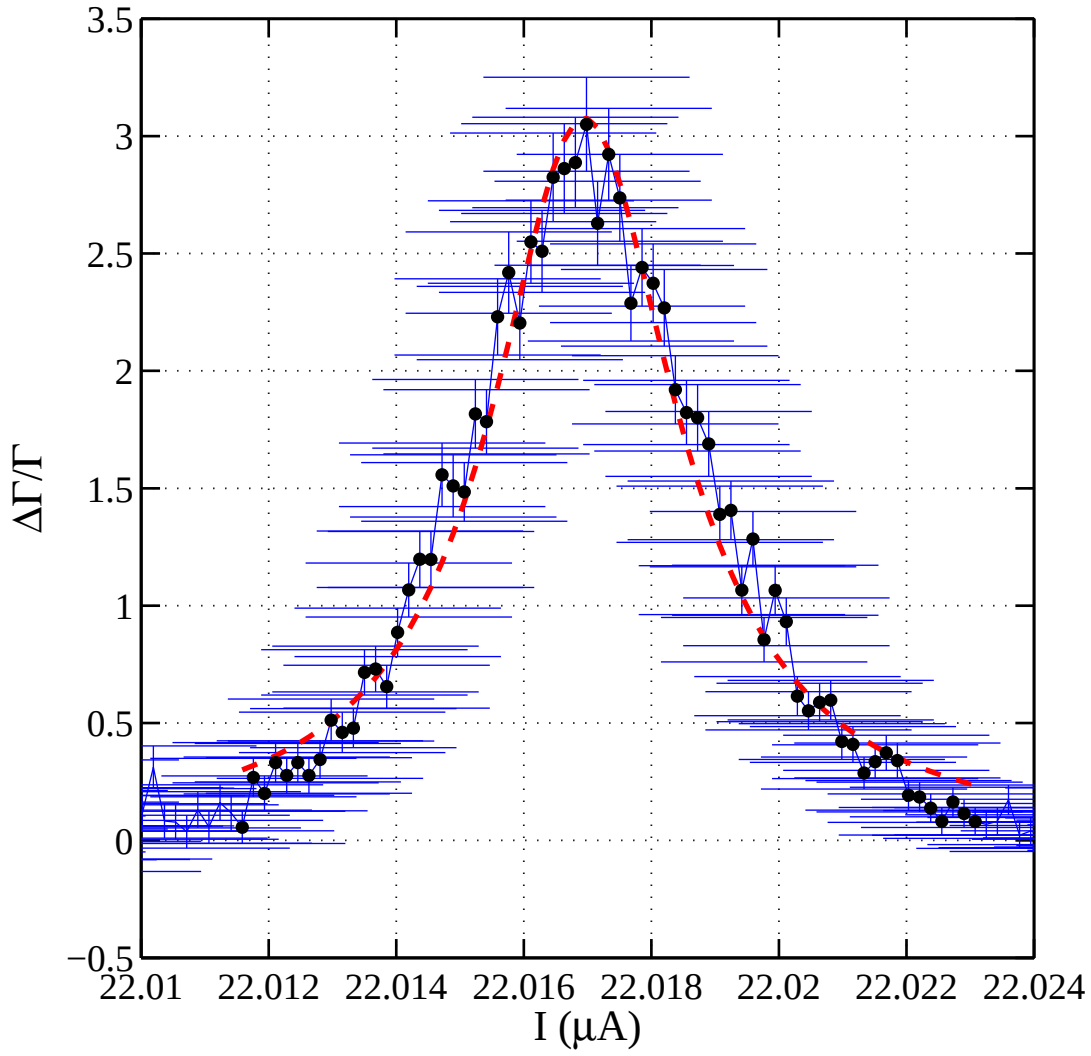

Figure 4.21: Lorentzian fit to the microwave enhancement of the escape rate for AL1 at 80 mK when 6.9 GHz microwaves are applied to the qubit junction. The peak is the $|0\rangle$ to $|1\rangle$ transition.

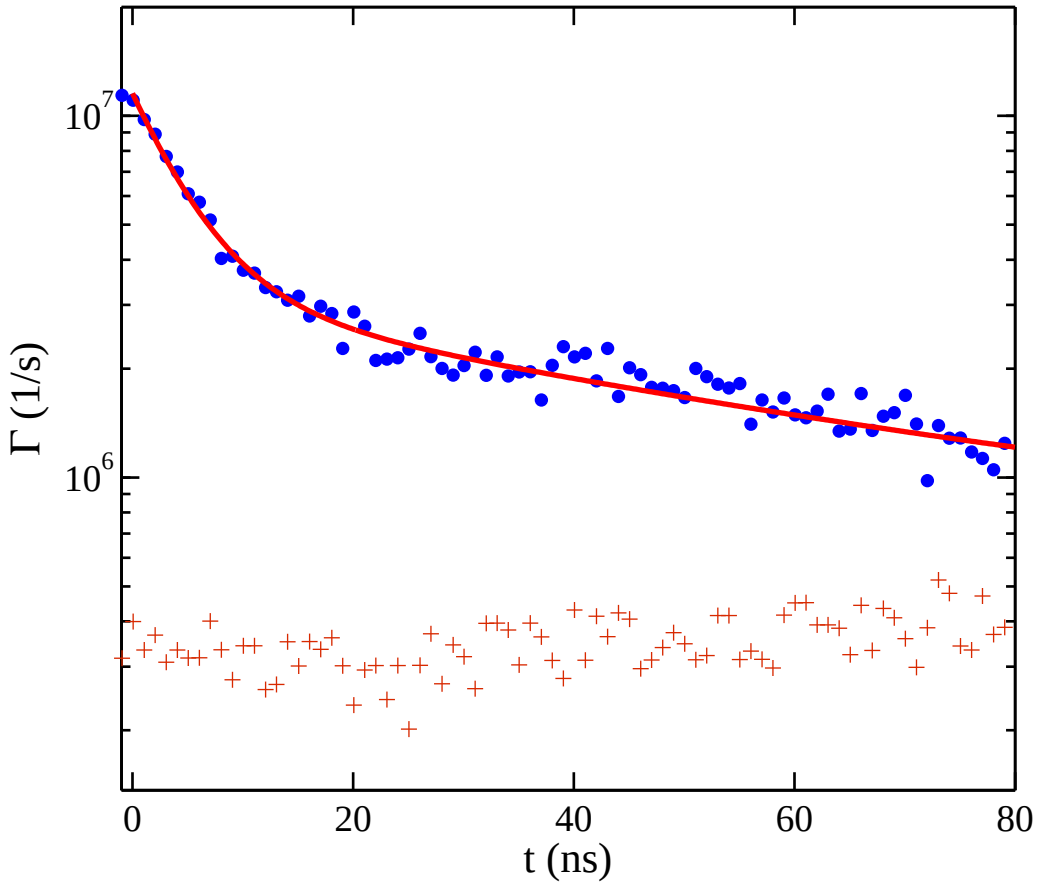

Figure 4.22: Observed relaxation in the escape rate at 80 mK in device AL1. Solid points are measured escape rates and the solid curve is the χ^2 fits to Eq. 5.40. Crosses are the background escape rate (without microwaves).

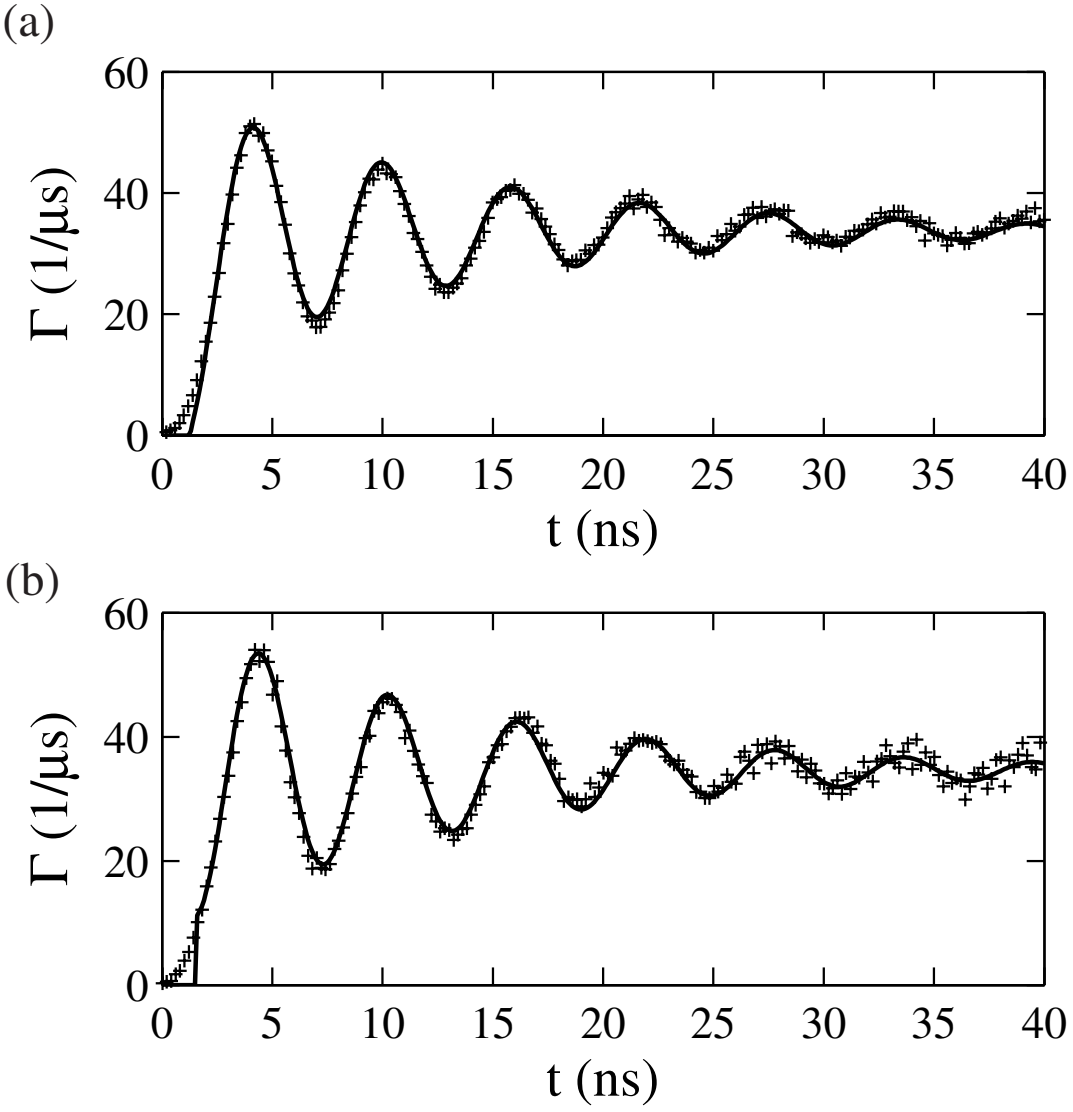

Figure 4.23: Examples of (a) Rabi oscillations in the escape rate Γ in device NB1 at 25 mK for (a) $r_I = 1300$ and (b) for $r_I = 450$ [23]. An 7.6 GHz drive was used.

Chapter 5

Effects of variable isolation on high frequency noise and T_1 in the dc SQUID phase qubit

5.1 Overview

In this chapter I show how the isolation of a qubit junction from the bias line can be varied in the dc SQUID phase qubit. Also, I discuss the frequency dependence of the inductive isolation and what effects this produces on the qubit junction. In particular, I will show that the inductive network provides good isolation for low-frequency current noise on the bias leads, but significant noise passes through at the plasma frequency of the isolation junction.

5.2 Variable current isolation and isolation factor

In the dc SQUID phase qubit, noise current in the bias leads is shunted away from the qubit junction and instead flows through the isolation junction. Figure 5.1(a) shows a schematic of the dc SQUID phase qubit. The qubit junction J1 is connected in series with inductor L_1, parasitic inductor L_2, and the isolation junction J2. The bias leads are then connected across L_2 and J2. At low frequencies, the capacitance C_2 of the isolation junction can be neglected and the isolation junction J2 acts as an inductor with inductance L_{J2}. For L_1 much larger than L_2+ L_{J2} only a small fraction of the current noise coming down the leads will reach the qubit junction (see Eq. 2.88).

One interesting feature of this scheme is that the noise division ratio depends on the current going through the isolation junction. This happens because the inductance of the isolation junction varies with the current; a Josephson junction

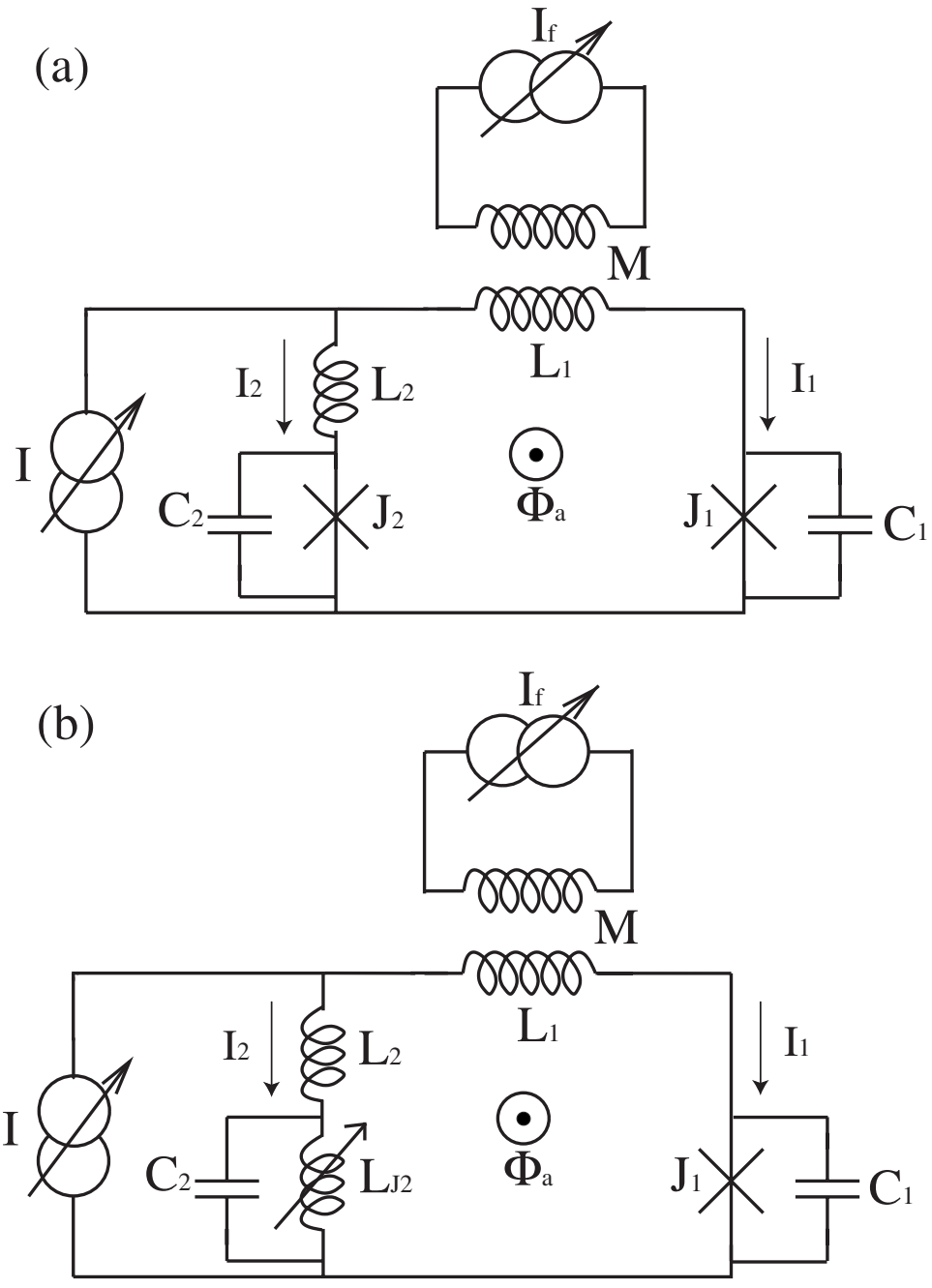

Figure 5.1: (a) dc SQUID phase qubit circuit diagram. (b) Effective circuit of dc SQUID phase qubit with isolation junction J2 replaced by an effective variable inductor L_{J2}.

can be described as a current-dependent inductor. The Josephson inductance for the qubit junction J1 is

$$\begin{aligned} L_{J1} &= \frac{\Phi_0}{2\pi}\frac{1}{I_{01}\cos\gamma_1} \\ &= \frac{\Phi_0}{2\pi}\frac{1}{I_{01}\sqrt{1-(I_1/I_{01})^2}} \qquad (5.1) \\ &= \frac{L_{J1}(0)}{\sqrt{1-(I_1/I_{01})^2}} \qquad (5.2) \end{aligned}$$

and for the isolation junction J2,

$$\begin{aligned} L_{J2} &= \frac{\Phi_0}{2\pi}\frac{1}{I_{02}\cos\gamma_2} \\ &= \frac{\Phi_0}{2\pi}\frac{1}{I_{02}\sqrt{1-(I_2/I_{02})^2}} \qquad (5.3) \\ &= \frac{L_{J2}(0)}{\sqrt{1-(I_1/I_{02})^2}} \qquad (5.4) \end{aligned}$$

where I_1 and I_2 are the currents going through the qubit and isolation junction, I_{01} and I_{02} are the critical currents of the qubit and the isolation junction, and $\Phi_0 = h/2e$ is the flux quantum. Notice also, for example, that L_{J2} has the minimum value,

$$L_{J2}(0) = \frac{\Phi_0}{2\pi I_{02}} \qquad (5.5)$$

at $I_2 = 0$.

Equation 5.4 implies that we can vary L_{J2} from $L_{J2}(0)$ to infinity by varying I_2 from 0 to I_{02}. This means that large *in situ* changes in the current isolation can be made by simply adjusting I_2. It is convenient to define an isolation factor,

$$r_I = \left(\frac{\Delta I}{\Delta I_1}\right)^2, \qquad (5.6)$$

as the ratio of the current noise power in the current bias leads (proportional to

the mean square current noise ΔI^2 in the leads) to the current noise power in the qubit junction (proportional to the mean square current noise ΔI_1^2). Consideration of Fig. 5.1(b) shows that r can be written:

$$r_I = \left(\frac{\Delta I}{\Delta I_1}\right)^2 = \left(\frac{L_1 + L_{J1} + L_2 + L_{J2}}{L_{J2} + L_2}\right)^2 \approx \left(\frac{L_1 + L_2 + L_{J2}}{L_{J2} + L_2}\right)^2 \qquad (5.7)$$

where in the last step I assumed that $L_{J1} \ll (L_1 + L_{J2} + L_2)$. Note that r shows how much the current noise power is reduced; for example, $r_I = 300$ means that the noise power reaching the qubit junction is reduced by a factor of 300. The bigger r_I is, the more the qubit is isolated.

From Eq. 5.4 and 5.7, we see that if I_2 is increased, L_{J2} increases and r_I decreases. The qubit is most isolated when $I_2 = 0$, since then L_{J2} is a minimum so r_I is a maximum.

I can also define an isolation factor r_f for the flux bias source. At low frequency, one finds

$$r_f = \left(\frac{\Delta I_f}{\Delta J}\right)^2 = \left(\frac{L_1 + L_{J1} + L_2 + L_{J2}}{M}\right)^2 \qquad (5.8)$$

where ΔI_f is noise current from the flux source and ΔJ is the circulating noise current induced in the SQUID loop by ΔI_f. Examination of Eq. 5.8 reveals that as we increase L_{J2}, the isolation from the flux bias source increases. This happens because increasing I_2 produces a larger L_{J2} which leads to a larger total effective loop inductance. For our devices, typically $L_1 \gg L_2 + L_{J2}$, and $L_1 \gg M$ so that $r_I \gg 1$ and $r_f \gg 1$, as required for good isolation.

Figure 5.2 shows an example where I have calculated r_I and r_f at zero frequency as a function of I_2/I_{02}. The device parameters I used for this calculation are are those of device AL1 (see Table 5.1). As we increase I_2, r_I varies from 1200 (max) to 0 (min) while r_f varies from 9000 to infinity. I note that r_f is always at least 8 times larger than r_I; dc current noise power from the flux bias source is 8 times

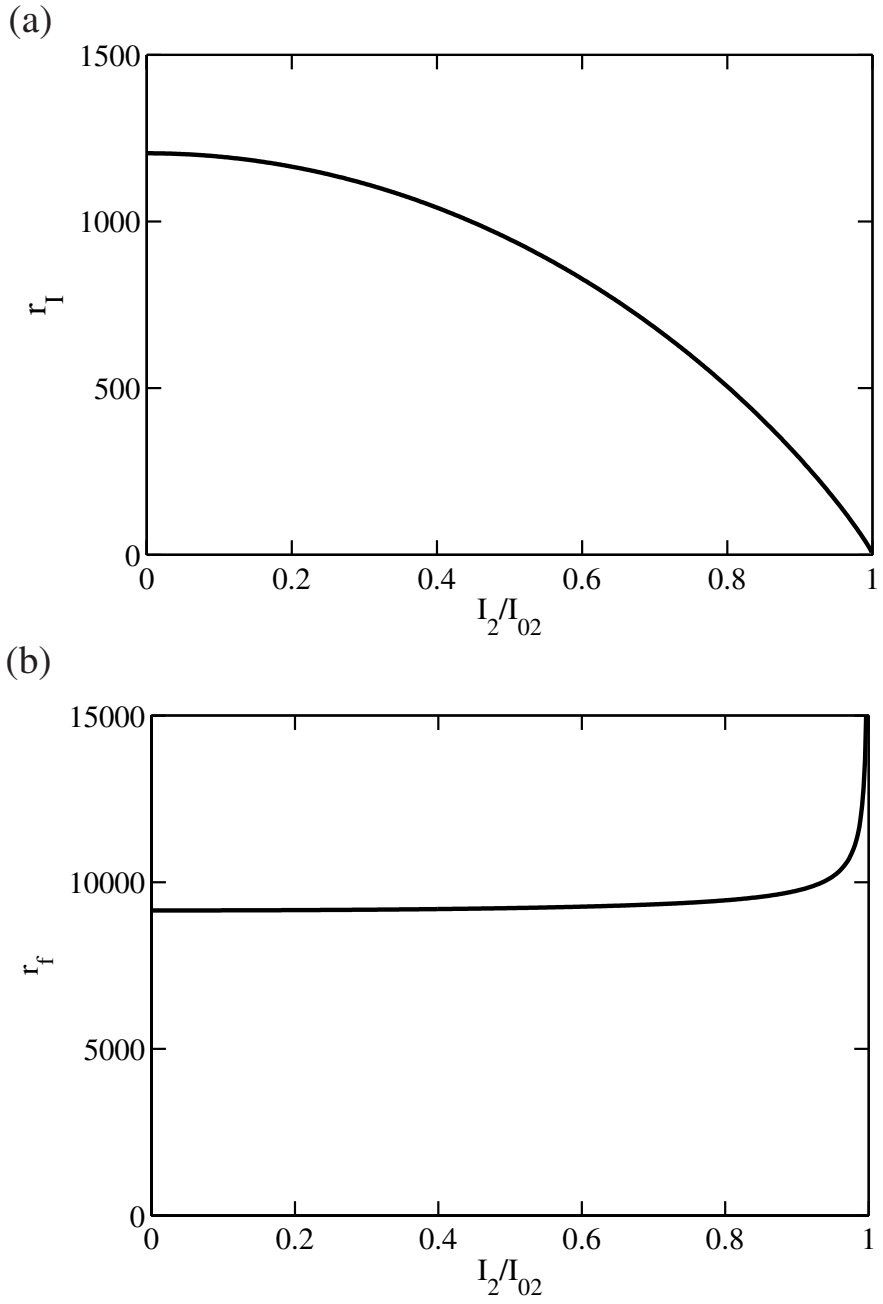

Figure 5.2: (a) Current power isolation factor r_I vs I_2/I_{02}. (b) Flux isolation factor r_f vs I_2/I_{02}. r_f is at least 8 times bigger than r_I.

more reduced than dc current noise power from the current bias source. From this, one can see that bias current noise will tend to have more impact on the device than noise on the flux line.

Equations 5.7 and 5.8 also imply that the effective impedance that the current bias leads and flux bias leads present to the qubit junction are stepped up by factors of r_I and r_f respectively. For device AL1 with a $Z_0 = 50\ \Omega$ and $\mathrm{I}_2 = 0$, the effective resistance across the junction due to the current bias leads will be $r_I Z_0 \simeq 50\ k\Omega$.

5.3 Arbitrary dissipation model for the dc SQUID phase qubit

Equations. 5.7 and 5.8 are valid only for current fluctuations that are sufficiently slow. However, in general, current noise occurs at all frequencies. Since the inductances and capacitances in the phase qubit have frequency-dependent impedances, the isolation will depend on frequency as well.

The impact of high frequency noise can be understood quantitatively by constructing a circuit model of the system. We model the noise as being produced by a source with a dissipative admittance $\mathrm{Y}_{eff}(\omega)$ connected in parallel with the qubit junction. The admittance can have a real and imaginary part, and we can write explicitly:

$$Y_{eff}(\omega) = \frac{1}{R_{eff}(\omega)} + i\omega C_{eff}(\omega) \tag{5.9}$$

where $R_{eff}(\omega)$ is the effective resistance and $C_{eff}(\omega)$ is the effective capacitance, and both can depend on frequency.

The energy relaxation time T_1 discussed in Ch. 3 for the $|1\rangle$ state to decay to $|0\rangle$ is

$$T_1 = C/Re[Y(\omega_{01})] = R_{eff}(\omega_{01})C_1 \tag{5.10}$$

and this is directly related to the dissipation [28, 60]. If the dc SQUID phase qubit is limited by dissipation from its leads, then T_1 will vary as a function of the isolation

Table 5.1: Parameters of dc SQUID qubit AL1 obtained form the current-flux map.

Device	I_{01} (μA)	I_{02} (μA)	L_1 (pH)	L_2 (pH)	Z_0 (Ω)	T (K)
AL1	21.401	9.445	1236	5	50	0.1

because $R_{eff} \simeq r_I Z_0$ will vary.

5.3.1 Calculation of effective admittance and T_1

To calculate Y_{eff}, I divide the dc SQUID phase qubit into two parts (see Fig. 5.3(a)).

(i) One part is any intrinsic resistance R_1 from the qubit junction itself, resistance R_2 from the isolation junction, inductance L_{J2} and capacitance C_2 of the isolation junction, the stray inductance L_2 on the isolation junction branch, the inductance L_1 of the SQUID loop and the impedance Z_0 of the current bias leads.

(ii) The other part is the qubit junction J1 with the junction capacitance C_1.

I found it easier to first calculate the effective impedance Z_{eff} of the first part and then get the admittance Y_{eff} using

$$Y_{eff} = \frac{1}{Z_{eff}}. \tag{5.11}$$

Z_{eff} includes all the circuit elements inside the dashed box in Fig. 5.3(a) as well as Z_0, which is the impedance of the current bias leads. I note that intrinsic dissipation associated with the qubit junction R_1 is included in Z_{eff} but C_1 is not included.

To proceed, I find the impedance Z_{iso} of the isolation network as viewed from the qubit junction. Z_{iso} includes the isolation junction, L_1, L_2 and Z_0 but not R_1,

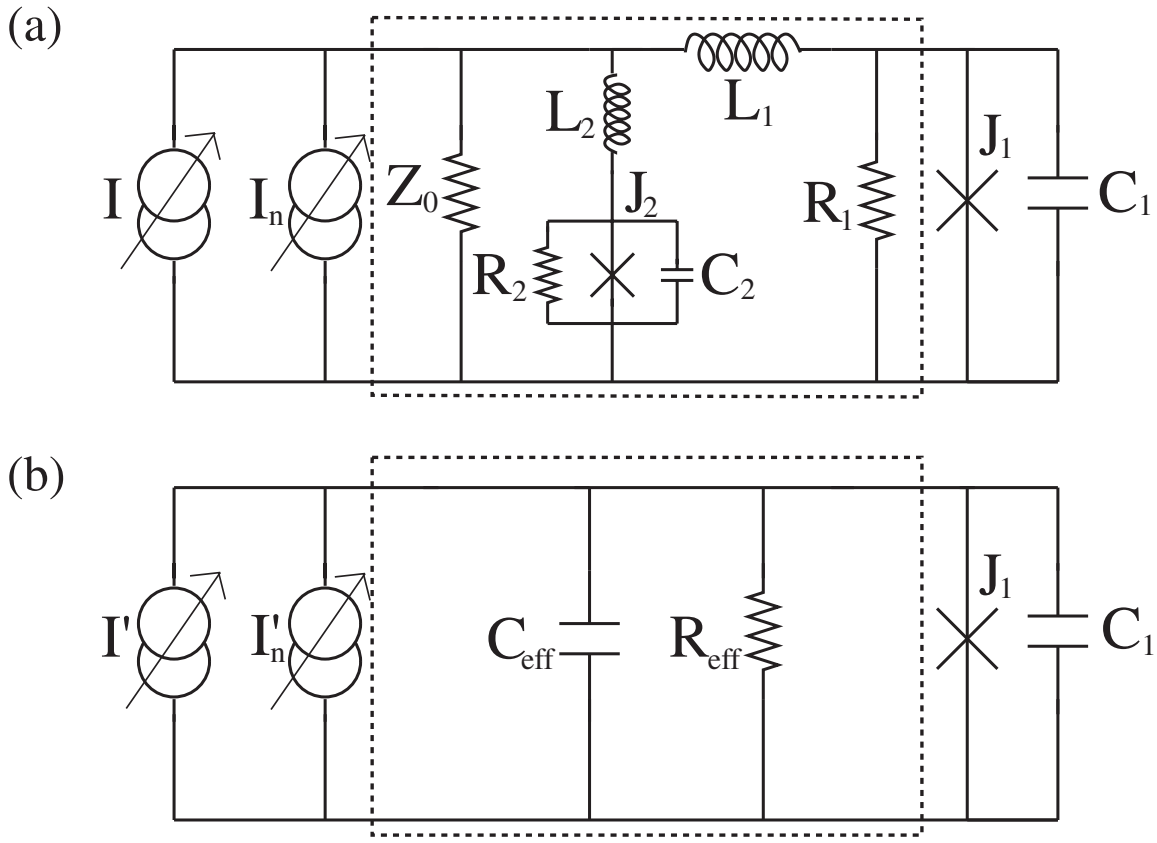

Figure 5.3: (a) Schematic of dc SQUID qubit. The isolation network and lead impedance Z_0 are inside the dashed box. (b) Equivalent circuit for the isolation network and leads used to calculate the effective admittance $Y_{eff}(\omega) = 1/R_{eff}(\omega) + i\omega C_{eff}(\omega)$. Notice that the current bias and current noise source must also be replaced by effective sources I' and I'_n.

and is given by

$$Z_{iso} = i\omega L_1 + \frac{Z_2 R_L}{Z_2 + R_L}. \tag{5.12}$$

where

$$Z_2 = i\omega L_2 + Z_{J2} \tag{5.13}$$

is the isolation branch impedance. In this expression, Z_{J2} is the impedance of the isolation junction:

$$\begin{aligned} Z_{J2} &= \left(iwC_2 + \frac{1}{iwL_{J2}} \right)^{-1} && (5.14) \\ &= \frac{i\omega L_{J2}}{1 - \omega^2 L_{J2} C_2}. && (5.15) \end{aligned}$$

where for simplicity I have neglected R_2. Here and elsewhere in this thesis ω is the angular frequency and I use index 1 for the qubit and 2 for the isolation junction. In Eq. 5.15, I have treated the isolation junction as a classical parallel LCR circuit with a resonance at the isolation junction plasma frequency ω_{p2},

$$\omega_{p2} = (L_{J2} C_2)^{-1/2}. \tag{5.16}$$

Substituting Eq. 5.15 into Eq. 5.13, and Eq. 5.13 into Eq. 5.12, I obtain

$$Z_{iso}(\omega) = i\omega L_1 + i\omega \left[\frac{Z_0[(L_2 + L_{J2}) - (\omega/\omega_{p2})^2 L_2]}{Z_0(1 - (\omega/\omega_{p2})^2) + i\omega[(L_2 + L_{J2}) - (\omega/\omega_{p2})^2 L_2]} \right]. \tag{5.17}$$

I can now write R_{iso}, the real part of Z_{iso} as

$$R_{iso}(\omega) = \frac{\omega^2 L_1^2}{Z_0} + \frac{Z_0[(L_1 + L_2 + L_{J2}) - (\omega/\omega_{p2})^2 (L_1 + L_2)]^2}{[(L_2 + L_{J2}) - (\omega/\omega_{p2})^2 L_2]^2}. \tag{5.18}$$

The real part of $1/Z_{eff}$ is the real part of Y_{eff} which is obtained by adding $1/R_1$

and $1/R_{iso}$

$$Re(Y_{eff}(\omega)) = Re\left(\frac{1}{Z_{eff}}\right) = \frac{1}{R_1} + \frac{1}{R_{iso}(\omega)} = \frac{1}{R_{eff}(\omega)} \tag{5.19}$$

where R_{eff} is the effective resistance in parallel with the qubit junction [see Fig. 5.3(b)].

The effective resistance R_{eff} is a function of the isolation factor and naturally changes as we change L_{J2} by applying current I_2. In the low frequency limit, this dependence of R_{eff} on L_{J2} is more apparent. Taking the limit $\omega \to 0$ in Eq. 5.18, $R_{iso}(0)$ becomes

$$R_{iso}(0) = Z_0\left(\frac{L_1 + L_2 + L_{J2}}{L_2 + L_{J2}}\right)^2 = rZ_0 \tag{5.20}$$

as expected. Thus $R_{eff}(0)$ is

$$R_{eff}(0) = \left(\frac{1}{R_1} + \frac{1}{rZ_0}\right)^{-1} = \frac{rR_1Z_0}{R_1 + rZ_0}. \tag{5.21}$$

The relaxation time T_1 is approximately a product of R_{eff} and C_{eff} where C_{eff} is

$$C_{tot} = C_1 + C_{iso} \tag{5.22}$$

and

$$C_{iso}(\omega) = -\frac{\omega^2A^2L_1 - B[Z_0A + L_1B]}{\omega^4A^2L_1^2 + \omega^2[Z_0A + L_1B]^2} \tag{5.23}$$

where

$$A = (L_2 + L_{J2}) - \omega^2\omega_{p2}^2L_2 \tag{5.24}$$

$$B = Z_0(1 - \omega^2\omega_{p2}^2). \tag{5.25}$$

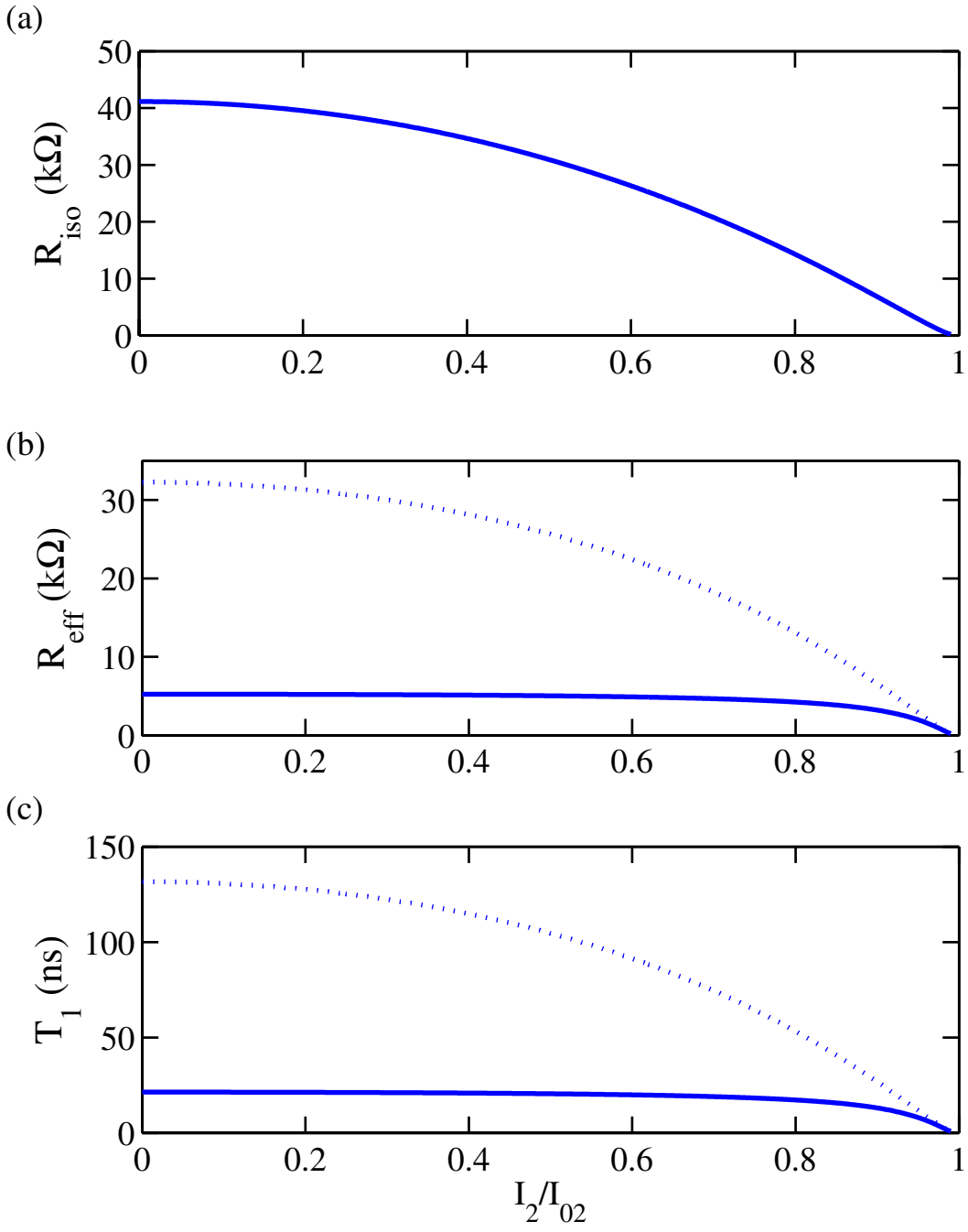

Figure 5.4: Simulation of (a) R_{iso}, (b) R_{eff} and (c) T_1 at 7 GHz for $Z_0 = 50\ \Omega$ and C = 4 pF. The dashed line is when $R_1 = 150$ kΩ and the solid line is when $R_1 = 6$ kΩ.

For our device, C_{iso} is typically only a few fF while $C_1 \sim 4$ pF, so C_{tot} is dominated by the qubit junction capacitance C_1 and $T_1 \simeq R_{eff}C_1$.

Figure 5.4 shows plots of R_{iso} [Fig 5.4(a)], R_{eff} [Fig 5.4(b)] and T_1 [Fig 5.4(c)] as a function of I_2 for two different values of R_1 (dotted and solid curves). For these plots, I used the parameters for AL1 listed in Table 5.1 and assumed $Z_0 = 50\ \Omega$ and $\omega/2\pi = 7$ GHz.

In Fig. 5.4(a), R_{iso} shows a clear dependence on I_2. At 7 GHz, the maximum $R_{iso} = 41$ kΩ occurs at $I_2/I_{02} = 0$ when the qubit is most isolated. R_{iso} drops to zero when $I_2/I_{02} = 1$, where the qubit has the poorest isolation from the current noise.

In my device the dissipation element R_1 (a resistance in parallel to the qubit which represents any kind of dissipation linked to the qubit junction itself) appears to be much smaller than R_{iso}. In this limit, R_{eff} is dominated by R_1. Fig. 5.4(b) shows R_{eff} when $R_1 = 150$ k Ω (dotted curve) and $R_1 = 6$ kΩ (solid curve). When R_1 is 150 kΩ, R_{eff} changes more dramatically with respect to I_2, varying from 32 kΩ to 0. In contrast, when $R_1 = 6$ kΩ, R_{eff} stays at around 6 kΩ until I_2/I_{02} approaches close to 1.

Figure 5.4(c) shows $T_1 = R_{eff}C_1$ which changes in the same fashion as R_{eff}; T_1 with $R_1 = 150$ kΩ shows a dramatic change as a function of I_2. In contrast, $T_1 \simeq 24$ ns with $R_1 = 6$ kΩ is almost independent of I_2.

The main point of this simulation is that if there is a local dissipation source R_1 that has a smaller resistance than that of the isolation network R_{iso}, the dissipation process is dominated by the local dissipation source and this fact can be investigated by measuring T_1 with respect to I_2.

5.3.2 Current noise power spectrum $S_{I1}(f)$ and noise induced transitions

Dissipation sources that are at non zero temperature T generate thermal noise. The thermal current noise power spectrum produced by $Y_{eff}(\omega)$ is given by

$$S_{I1}(f) = \frac{4\hbar\omega}{e^{\hbar\omega/k_BT} - 1} Re(Y_{eff}) \tag{5.26}$$

where $f = \omega/2\pi$ is the frequency. Here $S_{I1}(f)$ is the conventional current noise spectra defined for $f \geq 0$ and satisfies

$$\langle I_1^2 \rangle = \int_0^\infty S_{I1}(f) df \tag{5.27}$$

where $\langle I_1^2 \rangle$ is the mean square current fluctuation.

In general, the thermal current noise power spectrum $S_{I1}(f)$ is a function of L_{J2} and frequency ω. Figure 5.5 shows simulated plots of S_{I1} versus frequency for different values of L_{J2} assuming $Z_0 = 50\ \Omega$ and $R_1 = 6\ \text{k}\Omega$ at T = 100 mK (other qubit simulation parameters are those given in Table 5.1). I note that the noise spectrum is flat at low frequencies (below 1 GHz) and the current noise power for $I_2/I_{02} = 0$ (dotted curve in Fig. 5.5) is lower by a factor of 4 than the poorly isolated case $I_2/I_{02} = 0.99$ (thick solid curve in Fig. 5.5). The most striking feature in each curve is a large peak at $f = \omega_{p2}/2\pi$. This occurs because the impedance of a parallel LC circuit (the isolation junction) is infinite at resonance, leading to a breakdown of the isolation. Since ω_{p2} is a function of $L_{J2}(I_2)$, we can tune this noise peak by varying I_2. In Fig. 5.5, the noise peak moves from 20 GHz for the most isolated case (dotted curve, I_2/I_{02}=0) to $\sim$ 7 GHz for the least isolated case shown (thick solid curve, $I_2 = 0.99 I_{02}$).

Current noise at high frequencies is important because it can induce transitions

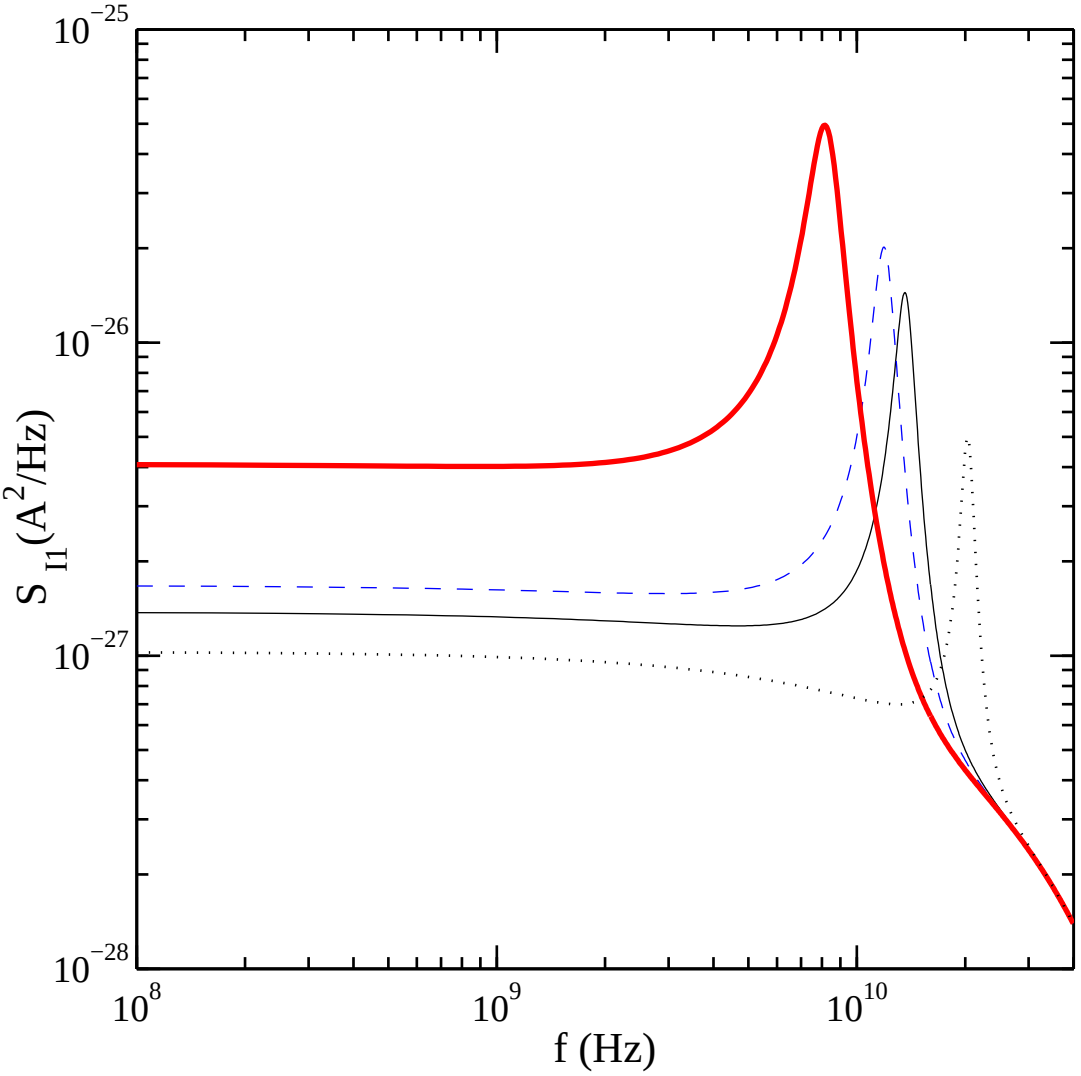

Figure 5.5: Plot of simulated thermal current noise power spectral density S_{I1}(f) at 100 mK for $Z_0 = 50\ \Omega$ and $R_1 = 6\ \text{k}\Omega$. Dotted line is for $I_2/I_{02} = 0$. Thin solid line is when $I_2/I_{02} = 0.9$, the dashed line is when $I_2/I_{02} = 0.95$ and thick solid line is when $I_2/I_{02} = 0.99$.

between the energy levels of the qubit. Since the tunneling rate out of higher energy levels is much greater than the tunneling rate out of the ground state, typically about a factor of 500 times greater for each successive level [87], even a relatively small probability of occupying an excited state leads to a significant enhancement in the average rate at which the system escapes. Using a two-level optical Bloch equation with the current noise being treated as a stochastic perturbation, Xu *et al.* [88] found that high frequency noise causes pumping from $|0\rangle$ to $|1\rangle$ at a rate which we can write here as

$$\Gamma_+ \approx \frac{S_{I1}(f_{01})}{8e^2}|\langle 0|\gamma|1\rangle|^2 \tag{5.28}$$

where $S_{I1}(f_{01})$ is the current noise spectrum at the $|0\rangle$ to $|1\rangle$ transition frequency f_{01} of the qubit junction. Equation 5.28 holds provided that $S(f_{01})$ does not diverge faster than $1/\omega^2$, which should be a good assumption for our system (see Fig. 5.5).

Transitions from $|0\rangle$ to $|1\rangle$ create an average occupancy of the first excited state $|1\rangle$ given by

$$\rho_{11} = \frac{\Gamma_+}{1/T_1 + \Gamma_1 + 2\Gamma_+} \tag{5.29}$$

where T_1 is the energy relaxation rate and Γ_1 is the tunneling escape rate from $|1\rangle$ [55]. Occupancy of $|1\rangle$ causes an increase in the escape rate compared to that from the ground state given by

$$G = \frac{\Gamma_{tot} - \Gamma_0}{\Gamma_0} \approx \rho_{11}\frac{\Gamma_1}{\Gamma_0} \tag{5.30}$$

where Γ_{tot} is the measured total escape rate, Γ_0 is the escape rate out of the ground state, and in the last expression we have used $\Gamma_1 \gg \Gamma_0$ and assumed that the population in the upper level is small compared to 1. Substituting Eq. 5.28 into Eq. 5.29, and taking the limit $\Gamma_+ \ll \Gamma_1 \ll 1/T_1$ we find

$$G \approx \frac{T_1 S_{I1}(f_{01})\Gamma_1}{8e^2\Gamma_0}|\langle 0|\gamma|1\rangle|^2. \tag{5.31}$$

Since ω_{01} can be varied by changing the current I_1 through the qubit, Eq. 5.31 implies that the spectrum of high frequency current noise can be mapped out by measuring the escape rate enhancement versus the qubit current.

As we will see below, in our system even quite small noise-induced occupancy in $|2\rangle$ and $|3\rangle$ are important, and one must generalize Eqs. 5.28 - 5.31 accordingly. In this case, the interpretation of G is not so straight-forward as suggested by Eq. 5.31 in that the enhancement at any current I_1 will generally contain contributions from noise at several frequencies, corresponding to the frequencies of different allowed transitions that produce transitions between different levels.

5.3.3 Determination of T_1 using thermal escape rate

When the timescale of interest is much longer than the coherence time T_2 [23], the off-diagonal terms in the density matrix equation (in Eq. 3.43) vanish and one finds a master equation:

$$\frac{d\rho_i(t)}{dt} = \sum_{j \neq i} \left[-W_{ij}\, \rho_i(t) + W_{ji}\, \rho_j(t) \right] - \Gamma_i\, \rho_i(t)\,, \tag{5.32}$$

where $\rho_i = \rho_{ii}$ is the population at i-th level. Note that this master equation is when temperature T is greater than zero and it includes tunneling process without microwave. If I set T = 0 and remove the tunneling from each level, Eq. 5.32 reduces to Eqs. 3.43(a) or 3.43(d) with microwave power $a_0 = 0$. Here W_{nm} is the transition rate from $|n\rangle$ and $|m\rangle$. W_{nm} includes transitions due to thermal emission/absorption, microwave pumping and any dissipation. In the thermal model, I assume that no microwaves are applied. In this case, W_{ji} and W_{ij} $(i < j)$ are given by [23][1]

$$W_{ji} = W_{ji}^{st} + \Gamma_{ji} = \frac{\Gamma_{ji}}{1 - \exp\left(-\hbar\omega_{ij}/k_B T\right)} \tag{5.33}$$

[1]Notation for W_{ij} here is from i to j, which is different from Ref. [23].

and

$$W_{ij} = W_{ji} \exp\left(-\hbar\omega_{ij}/k_B T\right) = \frac{\Gamma_{ji}}{\exp\left(\hbar\omega_{ij}/k_B T\right) - 1} = W_{ij}^{st}, \tag{5.34}$$

where

$$W_{ij}^{st} = W_{ji}^{st} = \frac{\hbar\omega_{ij}}{2R_{eff}e^2} \frac{\left|\langle i \,|\, \hat{\gamma} \,|\, j\rangle\right|^2}{\exp\left(\hbar\omega_{ij}/k_B T\right) - 1} \tag{5.35}$$

is the thermally stimulated emission and absorption rate due to R_{eff} between levels i and j, Γ_{ij} is

$$\Gamma_{ji} = \frac{\hbar\omega_{ij}}{2R_{eff}e^2} \left|\langle i \,|\, \hat{\gamma} \,|\, j\rangle\right|^2 \tag{5.36}$$

the spontaneous emission rate from j to i and ω_{ij} is the angular frequency spacing between two levels i and j.

Equations 5.32 - 5.36 have four free parameters: temperature T, the relaxation rate $T_1 = R_{eff}C_1$, the qubit critical current I_{01} and the capacitance C_1. I_{01} and C_1 can be obtained from spectroscopy measurements and they determine a unique Hamiltonian which can then be used to calculate the matrix elements $\left|\langle i \,|\, \hat{\gamma} \,|\, j\rangle\right|^2$.

If I_{01} and C_1 are known, the escape rates Γ_i from each levels can be found from Eq. 4.5 (see Chapter 4) [23, 24]. By plugging in estimates for T_1 and T, I can then solve the master equation in Eq. 5.32 and calculate the total escape rate from

$$\Gamma_{tot} = -\frac{1}{\rho_{tot}} \frac{d\rho_{tot}}{dt} \tag{5.37}$$

where $\rho_{tot} = \sum_i \rho_i$ is the total population that remained in the metastable wells which have not tunneled yet at time t. Γ_{tot} can be written as

$$\Gamma_{tot} = -\frac{1}{\rho_{tot}} \sum_i \frac{d\rho_i}{dt} = \frac{1}{\rho_{tot}} \sum_i \rho_i \Gamma_i = \sum_i \frac{\rho_i}{\rho_{tot}} \Gamma_i = \sum_i P_i \Gamma_i \tag{5.38}$$

where $P_i = \rho_i/\rho_{tot}$ and ρ_i are obtained from the master equation simulation.

I vary T and T_1 to get the best fit of the calculated Γ_{tot} to a measured data

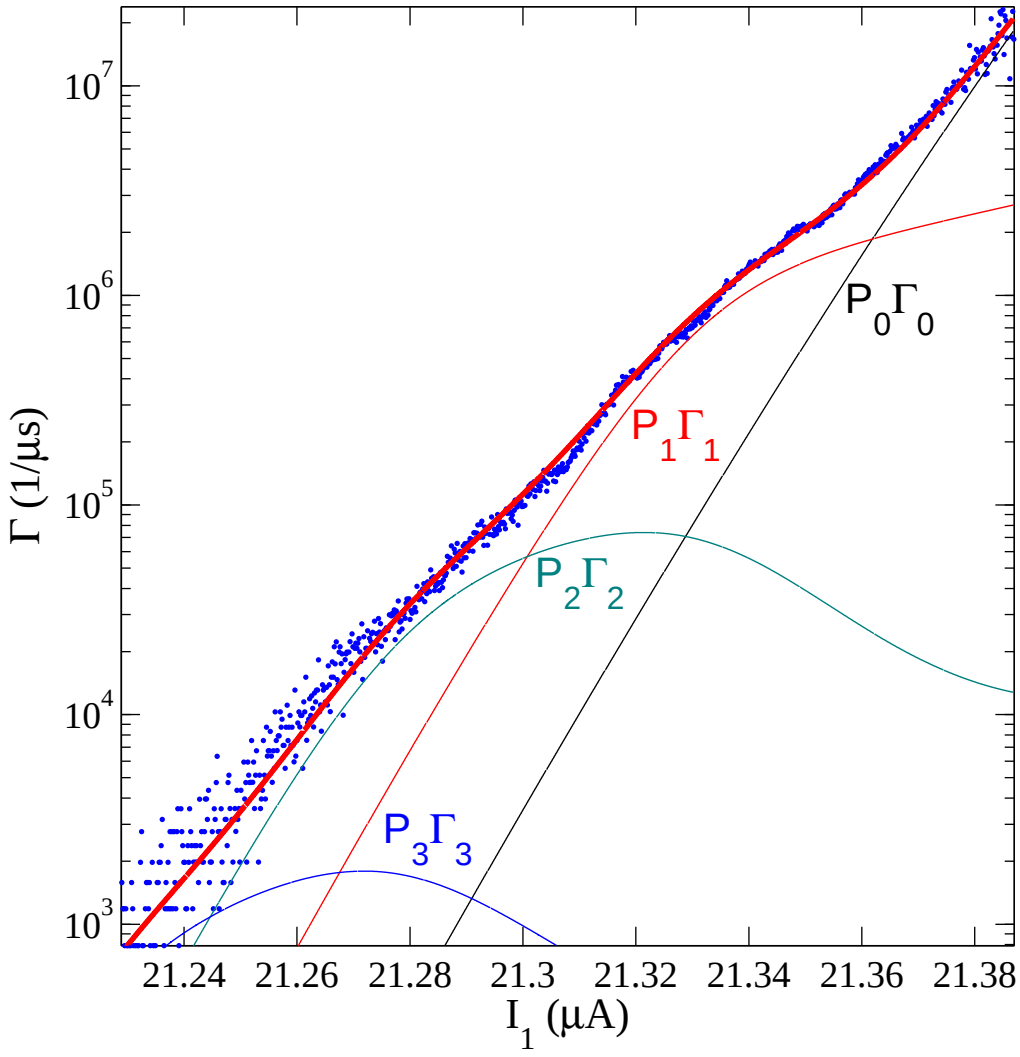

Figure 5.6: Total escape rate Γ versus current I_1 for qubit AL1. The points were measured at 80 mK. The red curve is from a 4-level master equation simulation. The thin solid curves show the components of the total escape rate $P_i\Gamma_i$. The simulation parameters are $T_1 = 17$ ns and T = 88 mK.

set. For example, Fig. 5.6 shows the total escape rate Γ_{tot} measured in device AL1 at 80 mK (blue dots), Γ_{tot} from a 4-level master equation simulation (red curve) and the components of the simulated Γ_{tot} due to each level. The best fit occurs for T_1 = 17 ns and T = 88 mK (I used the junction parameters listed in Table. 5.1.). Since the experiment was measured at relatively high temperature, $P_1\Gamma_1$ and $P_2\Gamma_2$ give large contributions. Note that $P_1\Gamma_1$ and $P_2\Gamma_2$ cause smooth bump-like features in the total escape rate. The starting position of the broad bump at high current is determined by $T_1 \cong 1/\Gamma_{10}$ and this relation can be used to obtain T_1 directly without fitting the entire curve [89]. I found that using the 4-level master equation simulation, the main features of Γ_{tot} in this device are well-explained, provided the device was well-isolated.

It turns out that under typical conditions, the analysis can be greatly simplified. If the speed of current bias ramp is slow enough, I can set the time derivative of P_i to be zero in Eq. 5.32. This produces a "stationary" solution where the normalized populations are kept constant in time. In my measurement, $(dln\Gamma/dt)^{-1} \approx$ 3.5 μs, which is much slower than $T_1 \approx$ 50 ns. The stationary solutions obtained by setting $dP_i/dt = 0$ provides an alternative approach to fit data to theory.

Figure 5.7 shows the discrepancy between the stationary and non-stationary solutions; I calculated Γ_{tot} from the master equation without using the stationary condition (Γ_{ME}) and with stationary solution (Γ_{SME}). I plotted $(\Gamma_{ME}-\Gamma_{SME})/\Gamma_{SME}$ versus current. Here I used T_1 = 17 ns and T = 88 mK. The other parameters are for device AL1 listed in Table 5.1. I note that fig. 5.7 shows there is less than 1 % difference between the stationary solution and the non-stationary solution for these parameters. Based on this close agreement, I used the stationary master equation solutions to fit my data from this point on in the thesis. The stationary solutions can be obtained by solving a single matrix equation based on Eq. 5.32 with dρ_i/dt = 0(see Appendix A.).

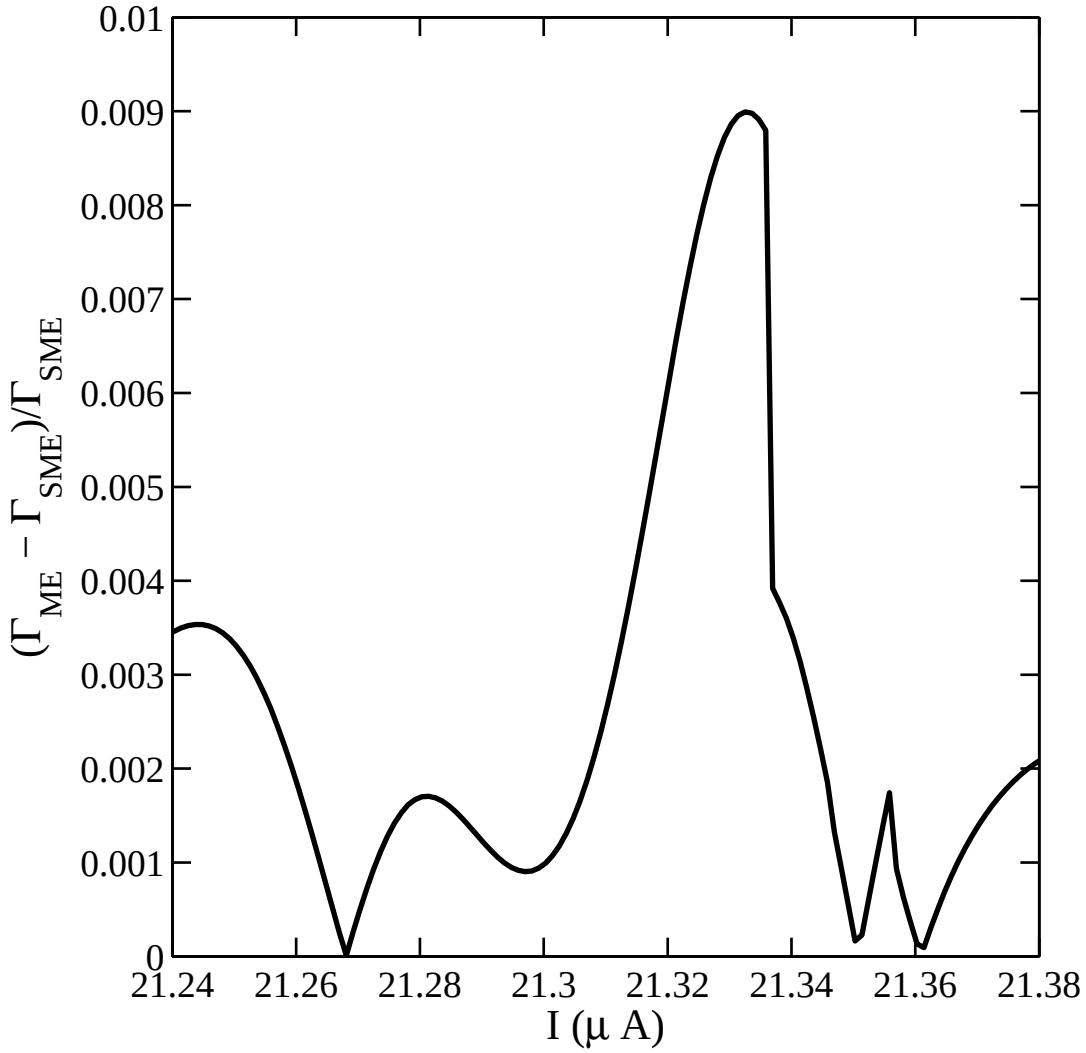

Figure 5.7: Plots of $(\Gamma_{ME} - \Gamma_{SME})/\Gamma_{SME}$ versus current. Here Γ_{ME} is the escape rate versus current from the non-stationary master equation simulation and Γ_{SME} is the stationary solution. For this curve, T_1 is 17 and T = 88 mK. The calculation covers the same current range as in Fig. 5.6.

5.4 Measuring the effect of isolation on an Al dc SQUID phase qubit

In this section, I discuss my measurements of the effect of the isolation factor on the thin-film dc SQUID qubit AL1 (see Ch. 4). I present results on the thermal noise induced escape rate and T_1 and compare my results with the theory discussed in the previous section.

5.4.1 dc SQUID phase qubit parameters; fit to spectroscopy and I - Φ curves

To be able to compare the observed behavior of the device with simulations, I need to know the device parameters, including the inductances L_1 and L_2, the critical currents and the capacitance of the junctions. The critical current I_{01} and the capacitance C_1 of the qubit junction J1 can be obtained from spectroscopy (see Chapter 4). Accordingly, I measured the qubit junction spectrum from 6 GHz to 8 GHz as a function of the current I_1. As I_1 increases, the energy levels of the qubit decrease. Well-defined peaks in the escape rate occur at currents where the microwave frequency is in resonance with an allowed transition.

Figure 5.8 shows an example of escape rates I measured in qubit AL1 at 80 mK (also shown in Chapter 4) at a sweep rate of about 30 mA/s. The black dotted curve shows the escape rate with 6.9 GHz microwave drive and the blue curve shows the corresponding measurement with no microwaves applied. Two clear resonance peaks appear in the escape rate and they correspond to the $|0\rangle \rightarrow |1\rangle$ transition (at about 22.02 μA) and the $|1\rangle \rightarrow |2\rangle$ transition (at about 21.97 μA). The red curve is the calculated escape rate Γ_0 from $|0\rangle$. I found this curve by fitting the total measured escape rate using the non-stationary 4-level master equation simulation discussed in the previous section. Comparing Γ to the Γ_0 curve, I see that there are many escape events from higher levels.

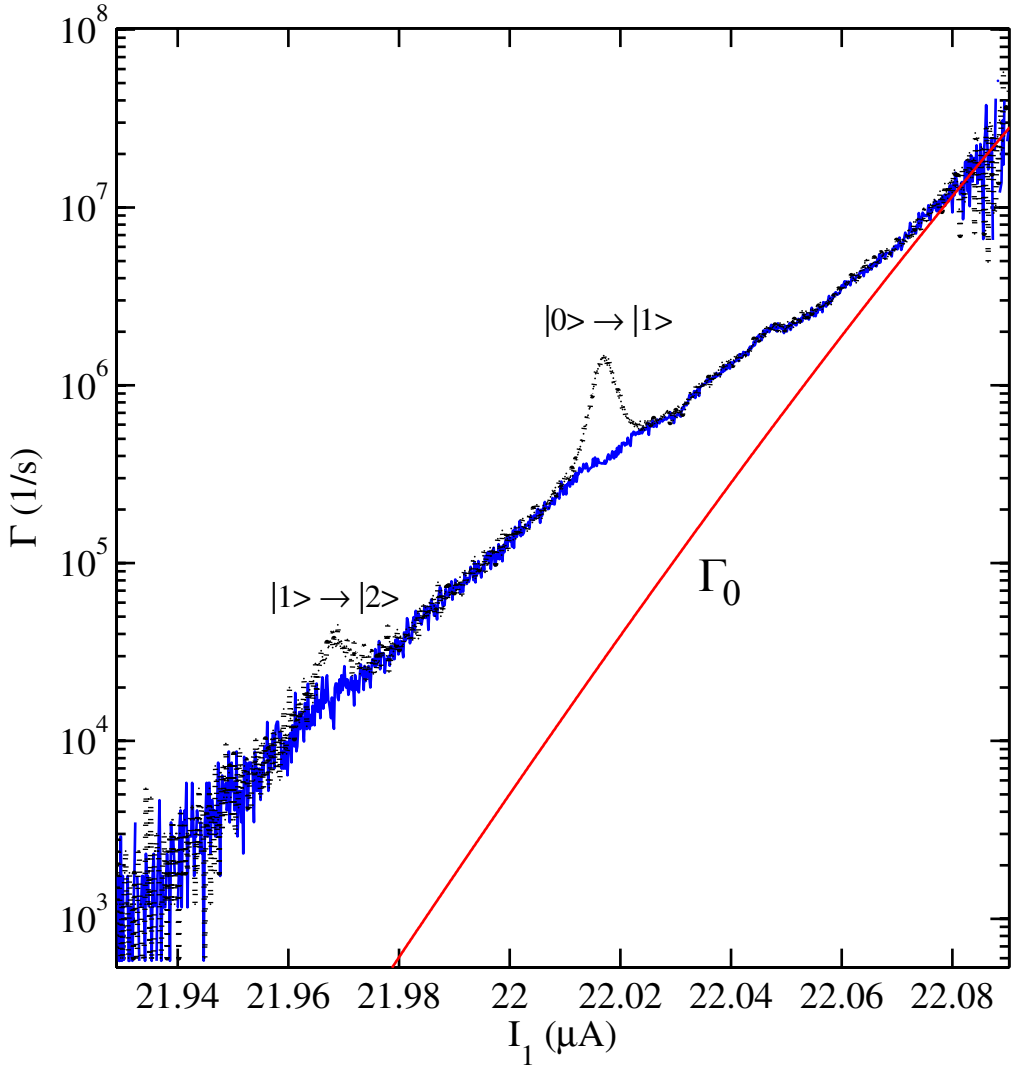

Figure 5.8: Escape rate of dc SQUID phase qubit AL1 at 80 mK with 6.9 GHz microwaves applied (black dotted curve) and without microwaves (blue solid curve). The red solid curve shows Γ_0 from the non-stationary master equation simulation of a single Josephson junction spectrum using parameters in Table 5.1.

To obtain the full spectrum of AL1, I measured a series of escape rates for different applied microwave frequency. As discussed in Chapter 4, This measurement was performed with simultaneous ramping of current and flux so that the current going through the isolation junction I_2 was kept at zero and the qubit junction was most isolated. Figure 5.9 shows the resulting spectrum of resonant frequency versus current for the qubit junction in AL1. I fit the spectrum to a simulation of a single Josephson junction (see Eq. 4.7) with two free parameters, the critical current I_{01} and the capacitance C_1 [23]. I obtained $I_{01} = 22.2138\ \mu A$ and $C_1 = 4.078$ pF. The two solid curves in fig. 5.9 show the simulation results of the energy level spacings between $|0\rangle$ and $|1\rangle$ (solid curve on the right) and $|1\rangle$ and $|2\rangle$ (solid curve on the left) calculated using these parameters. For comparison, from a separate fitting, I obtained $I_{01} = 22.2143\ \mu A$. I note that the minimum change in the resonance current that is caused by a change in the microwave frequency of 1 GHz was 3.8 nA. Given this data, this implies that I_{01} could be found to six significant figures. Using a similar analysis, C_1 could be found to four significant figures. However, since calculations of the energy level spacings are complicated, it is not easy to completely propagate the errors.

To find L_1, L_2, I_{02} and M, I measured the SQUID's current-flux characteristic curve (see Fig. 5.10). For this measurement, I initialized the SQUID in the zero trapped flux state using flux shaking [86] and applied a small dc flux to the SQUID loop. If a small offset flux Φ is applied, this produces a small I_2, *i.e.* it generates a bias current through the isolation junction. I then applied simultaneous flux and current ramps so that the current through the isolation junction was kept approximately fixed at the initial starting value (thereby fixing r_I), while I_1 was steadily increased. The current and flux at which the device escaped was recorded and this procedure was repeated about 10^5 times for each value of the initial offset flux. I fit the resulting $I - \Phi$ curves using the method by Tsang *et al.* (see Ch. 2) [37, 35]

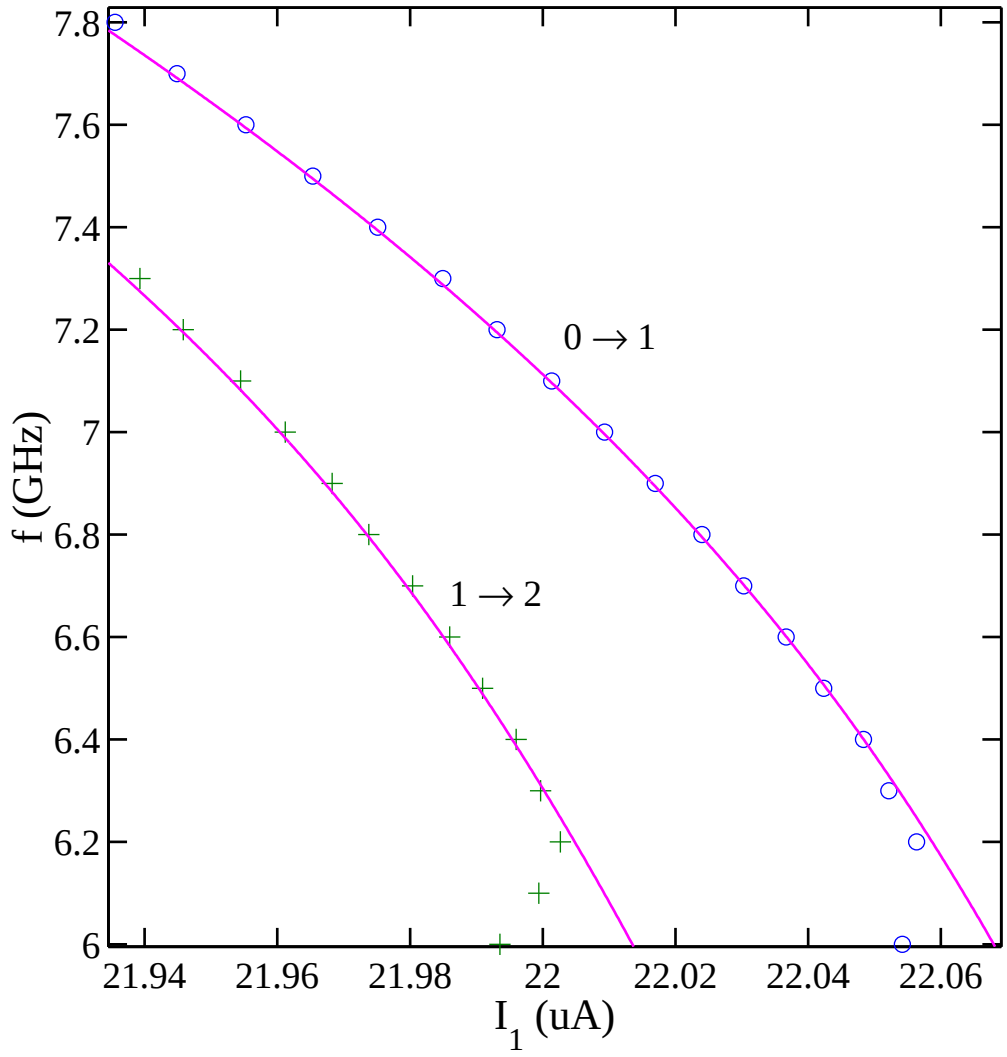

Figure 5.9: Transition spectrum of dc SQUID phase qubit AL1. Circles indicate $|0\rangle \rightarrow |1\rangle$ transitions and crosses are $|1\rangle \rightarrow |2\rangle$ transitions measured at 80mK. Solid curves are simulation fits to a single Josephson junction spectrum.

Table 5.2: Parameters of dc SQUID phase qubit AL1 from spectroscopy and current-flux map.

Parameters	I_{01} (μA)	C_1 (pF)	I_{02} (μA)	L_1 (pH)	L_2 (pH)	M (pH)
I - Φ	21.401	-	9.445	1236	5	15
Spectroscopy	22.2138	4.078	-	-	-	-

with L_1, L_2, I_{01}, I_{02} and M as free parameters.

From the fitted L_1, L_2, I_{01}, I_{02} and M, I obtained the estimated isolation factors [see Fig. 5.10(b)] as a function of I_2. The largest isolation was $r_I = 1000$ and the lowest isolation I operated at was $r_I \simeq 100$. The device parameters I obtained from spectroscopy and the $I - \Phi$ curve are listed in Table 5.2.

I note that the I_{01} value I found from spectroscopy disagree significantly from what I obtained by fitting the $I - \Phi$ curve (see Table 5.2). There are a few possible reasons for this. For example, we do not know I_1 precisely because it has to be inferred from the applied current I, flux ramps, and the device parameters. Also the fit to the $I - \Phi$ curves uses a classical picture of the SQUID. Since this picture does not account for quantum mechanical tunneling, it should result in an underestimate of the true critical current. However, the observed differences appear to be too large to be accounted for solely by this effect. Another problem is that the fit to the $I - \Phi$ curves is somewhat crude, especially near the minimum critical current, and this could be a cause for disagreements. Fortunately, I usually do not need to know the current I_1 with perfect accuracy. It is sufficient in many cases to have a set of I_{01} and C_1 from the spectroscopy data consistent with the frequency of the resonance peaks. For the master equation simulations of AL1 in this thesis, I used $I_{01} = 22.2138\ \mu A$ and $C_1 = 4.078$ pF from spectroscopy.

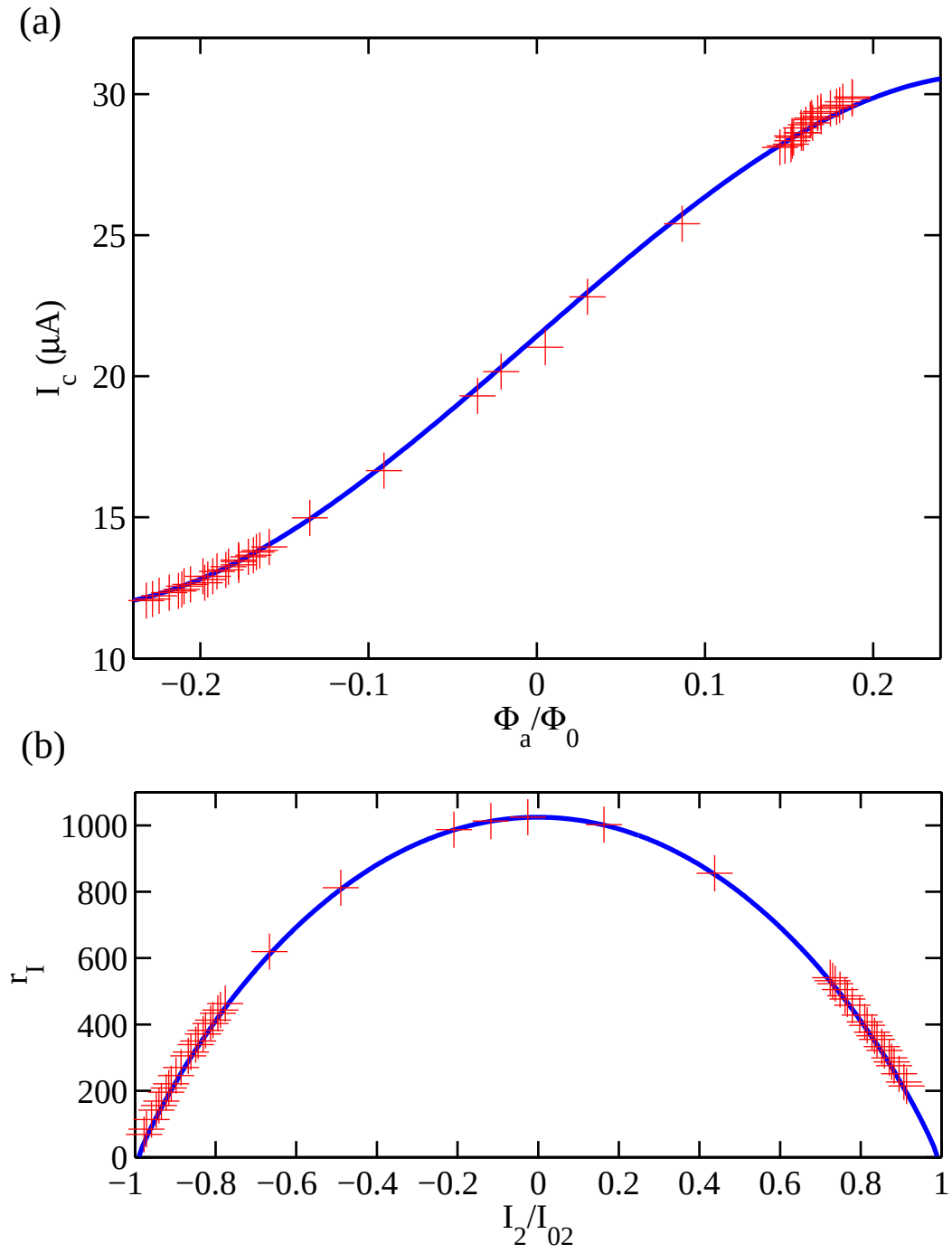

Figure 5.10: Current-flux characteristic curve of dc SQUID phase qubit AL1 measured at 80 mK. (a) Switching current versus normalized applied flux. Crosses are experimental data after flux shuffling to zero flux state and solid curve is a fit using Tsang's method discussed in Ch. 2. (b) Corresponding isolation factor r_I for each data points versus normalized current I_2.

5.4.2 Observing noise induced transitions.

One of the most surprising things I found in my measurements of AL1 was that noise induced transition peaks were clearly visible in the background escape rates when the device was poorly isolated (see Fig. 5.11 to 5.13). For these background measurements, I simultaneously ramped the current bias and flux bias so that the current going through the isolation junction I_2 was kept constant. For the most isolated case, I made the current bias and the flux bias cancel out at the isolation junction; *i.e.* where $I_2 = 0$ so that the measured bias current I is the same as I_1. Applying I_2 changes the isolation factor r_I and shifts the zero point of I_1. As a result, the measured switching current of SQUID I will be shifted by the applied I_2.

To keep track of shifts in I, I also measured the escape rates while applying 7.45 GHz microwaves (green curves in Figs. 5.11, 5.12, 5.13). I first set the offset flux to zero to get the most isolated escape rate and $I \simeq I_1$. Next I applied offset flux and measured how much the 7.45 GHz resonance peak shifted in current compared to the 7.45 GHz resonance peak for the most isolated case. By measuring how much the resonance peak was shifted along the current axis I, I could obtain I_2 from $I_2 = I - I_1$. It is important to remark that even for zero applied dc flux, there typically is always stray magnetic field coupled to the SQUID so that the current axes for the most isolated cases varied for different measurements.

Figure 5.11 shows the measured background escape rate (without microwaves) versus current for device AL1 at 80 mK for r = 1000 (blue curve) and the simulated background escape rate from a stationary 4-level master equation (red dashed curve) described in section [89, 23] with $T_1 = 20$ ns and T = 89 mK. I find a good overall agreement between the best fit and the data although some small deviations are evident.

Figure 5.12 shows escape rates for the case when the isolation factor r = 270. Again the measured background escape rate (without microwaves) versus current is

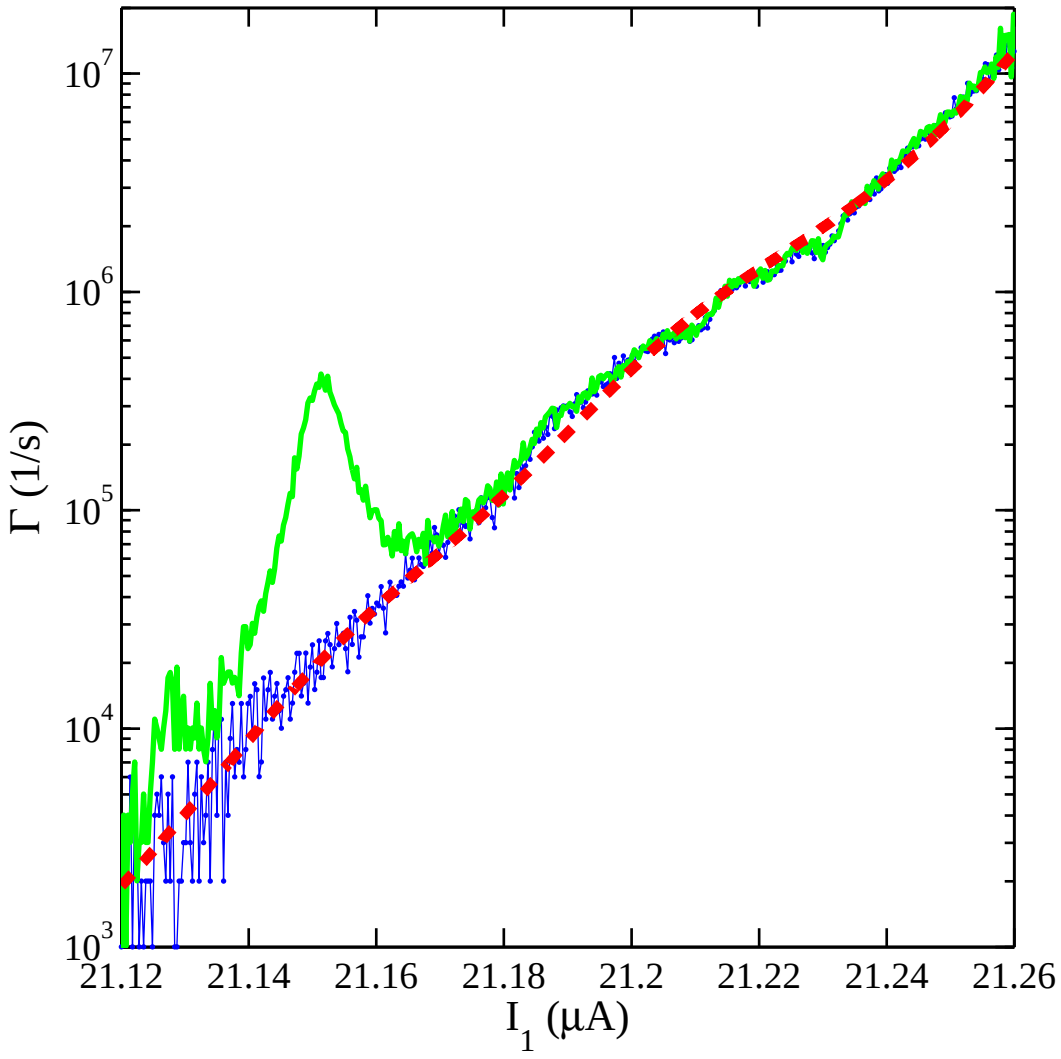

Figure 5.11: Escape rate versus current when the qubit is most isolated ($r_I = 1000$). The blue curve is the background escape rate (without microwaves) and the green curve is the escape rate with 7.45 GHz microwaves applied. The red dashed curve is the total escape rate from a stationary 4-level master equation simulation when the qubit is most isolated. The simulation parameters are $T_1 = 20$ ns and T = 89 mK.

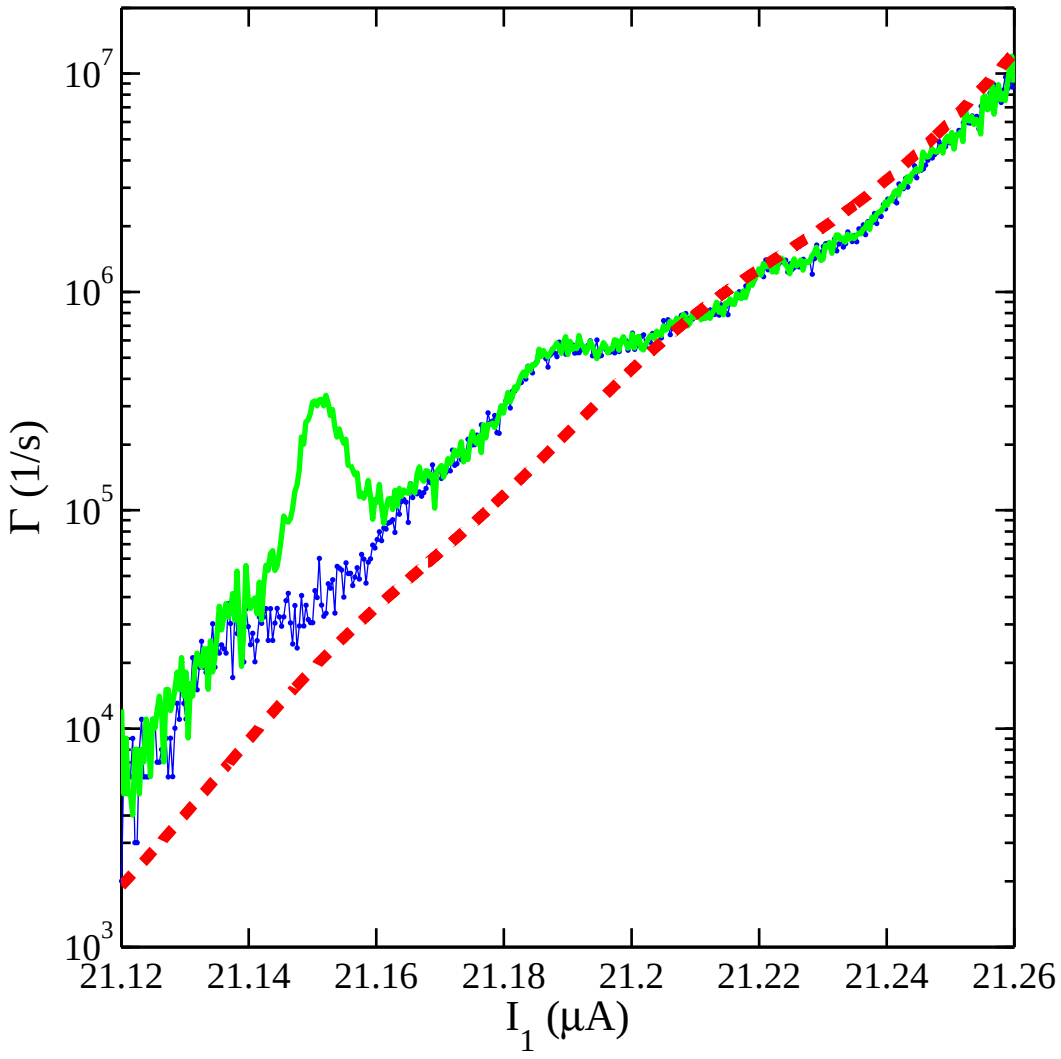

Figure 5.12: Escape rate versus current when the qubit is poorly isolated ($r_I = 270$). The blue curve is the background escape rate (without microwaves) and the green curve is the escape rate with 7.45 GHz microwaves applied. The red dashed curve is the total escape rate from a stationary 4-level master equation simulation when the qubit is most isolated. The simulation parameters are $T_1 = 20$ ns and T = 89 mK.

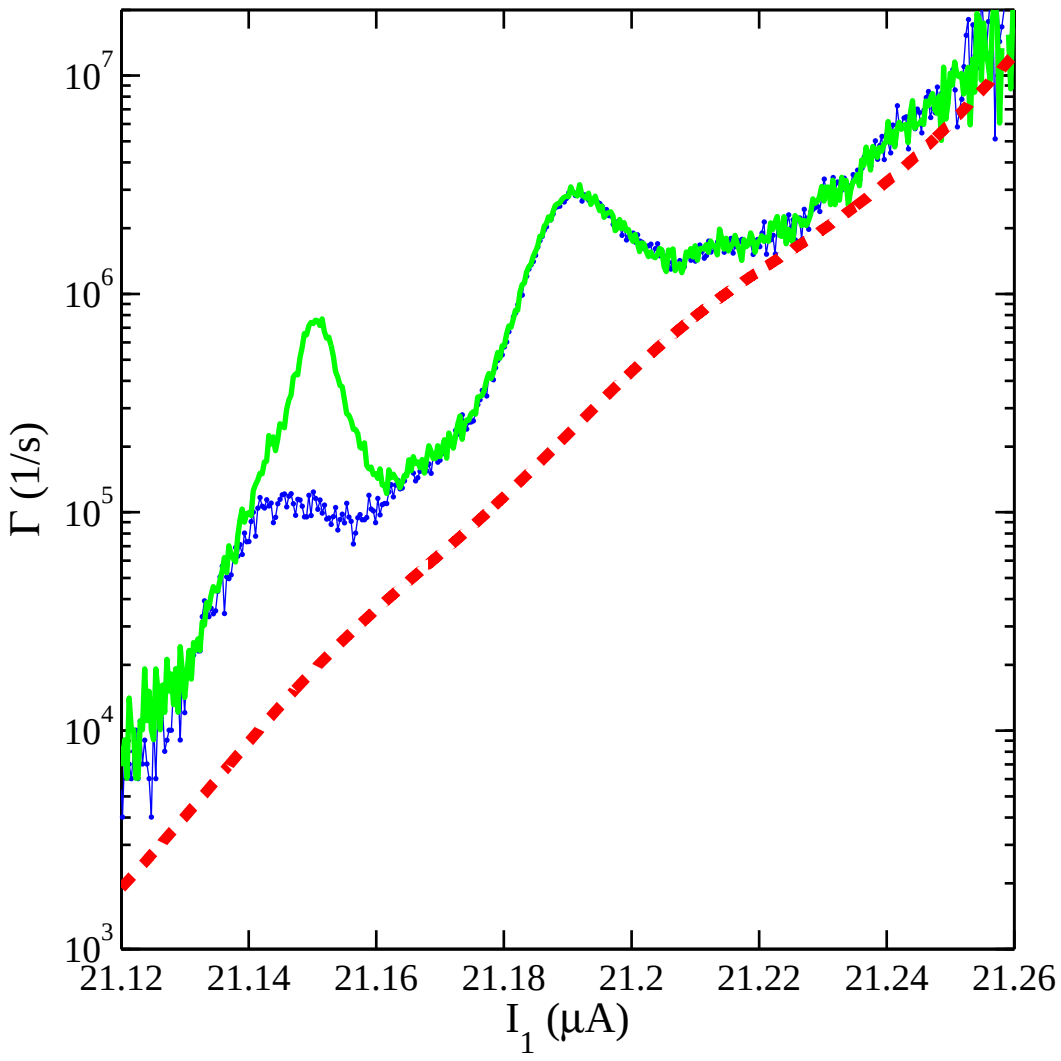

Figure 5.13: Escape rate versus current when the qubit is more poorly isolated (r_I = 220). The blue curve is the background escape rate (without microwaves) and the green curve is the escape rate with 7.45 GHz microwaves applied. The red dashed curve is the total escape rate from a stationary 4-level master equation simulation when the qubit is most isolated. The simulation parameters are T_1 = 20 ns and T = 89 mK.

shown as a blue curve. For comparison, I also show again the simulated background escape rate from a stationary 4-level master equation for the most isolated case as a red dashed curve; the simulation parameters are the same as in Figure 5.11, T_1 = 20 ns and T = 89 mK. In this figure, there is a large disagreement between the simulation and the data and it is not just because I did not use the best fit curve. In particular, there are two broad peaks in the background escape rate at low current that will not occur in this master equation simulation for any choice of T and fixed T_1.

As I decrease the isolation factor further to r = 220, two separate peaks become more apparent and their location shifts on the current axis (see Fig. 5.13). The simulated escape rate for the most isolated situation (red dashed curve in Fig. 5.13) clearly does a very poor job of representing the background escape rate, suggesting that the peaks are not caused by thermal excitations from a frequency independent R_{eff}.

The likely cause of the peaks is resonant transitions induced by high frequency components of current noise on the bias leads. Figure 5.14 is a false color plot that summarizes the somewhat complicated dependence of the noise induced peaks on the isolation when both I_1 and I_2 are swept smoothly in device AL1. The x-axis is the reduced current I_2/I_{02} through the isolation junction and the y-axis is the reduced current I_1/I_{02} through the qubit junction. Note that the y-axis (I_1) uses a backwards going current scale so that high frequency (low current) is at the top of the y-axis. The color scale corresponds to the enhancement G which is

$$G' = \frac{\Gamma_{tot} - \Gamma_{r=1000}}{\Gamma_{r=1000}} \tag{5.39}$$

where Γ_{tot} is the measured total escape rate and $\Gamma_{r=1000}$ is the measured total escape rate with r = 1000 (most isolated). I am using G' instead of G defined in Eq.

8.19 because Γ_{tot} involves contributions from several levels, not just two levels. By plotting G', I can concentrate on the behavior of the noise peaks for different I_1 and I_2. In this color-scale images, large G' is red and small G' is blue. The data in Fig. 5.14 covers a range of r_I from 70 to 400.

In Fig. 5.14, two broad peaks (indicated as red) are seen at each value of the applied I_2. The curves in Fig. 5.14 reveals the cause of the enhancement peaks; the solid yellow curve shows the locus of currents I_1 and I_2 for which the plasma frequency of the isolation junction ω_{p2} is equal to the $|0\rangle \rightarrow |2\rangle$ transition frequency ω_{02} of the qubit. Noise peaks along this curve would be due to current noise passing through the isolation junction at its resonance and driving the qubit into its second excited state. Since population in $|2\rangle$ tunnels very rapidly, even a small amount of noise induced transitions could produce substantial enhancements.

Similarly, the dashed yellow curve in Fig. 5.14 shows the locus of currents I_1 and I_2 for which $\omega_{p2} = \omega_{13}$, *i.e.* along this curve the resonant frequency of the isolation junction ω_{p2} equals the transition frequency ω_{13} between $|1\rangle$ and $|3\rangle$ in the qubit.

It is interesting that the two peaks in the background escape rate vary their location smoothly as a function of I_2 but seem to disappear on the right half of the figure. We note the peaks from $\omega_{p2} = \omega_{02}$ disappear at $I_1/I_{01} \cong 0.9911$ ($I_1 = 21.21$ μA) and the peaks $\omega_{p2} = \omega_{13}$ disappear at $I_1/I_{01} \cong 0.9892$ ($I_1 = 21.17$ μA) (see Fig. 5.14).

This behavior may be due to the $|2\rangle$ and $|3\rangle$ levels exiting the top of the well and merging with the continuum of levels above the barrier. Once $|3\rangle$ exits the well, the ω_{13} feature should disappear, for example. A more detailed of the situation suggests this explanation. Figure 5.15 shows a simulation of the energy levels for a Josephson junction done by solving Schrödinger's equation numerically using the AL1 parameters in Table 5.1 [23] (see Appendix A for the MATLAB routine I used).

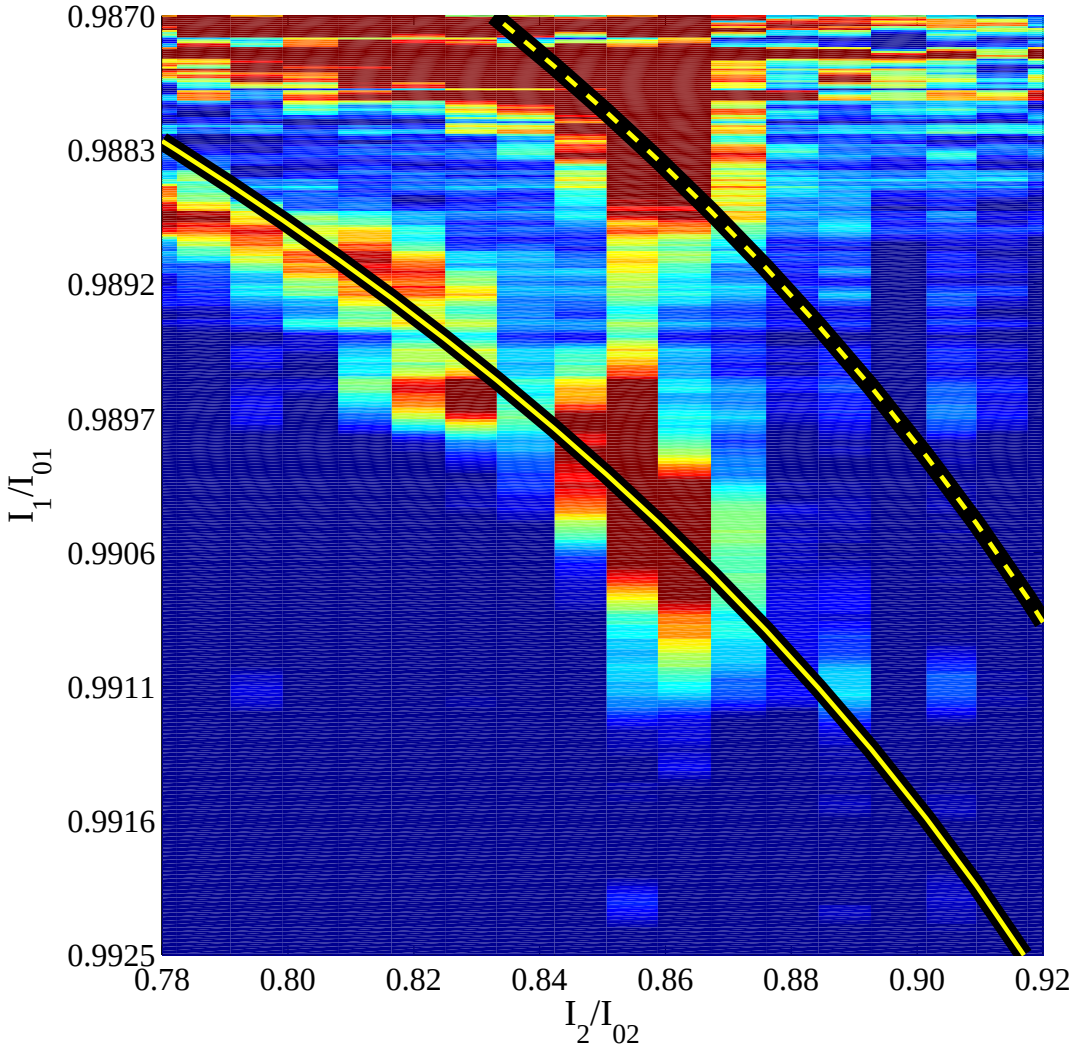

Figure 5.14: 3-D false color plot of the noise-induced transition peaks in the background escape rate enhancement G' in device AL1. Red indicates high G' and blue indicates low G'. The lower yellow-black solid curve is locus of points where the isolation junction plasma frequency ω_{p2} is equal to ω_{02} of the qubit junction. The upper yellow-black dashed curve is locus of points where the isolation junction plasma frequency ω_{p2} is equal to ω_{13} of the qubit junction.

The dashed curve ΔU is the height of the barrier in the tilted washboard potential. I note that at around $I_1/I_{01} = 0.9911$ where the $|0\rangle \rightarrow |2\rangle$ noise transition peak disappears, ΔU crosses with the second energy level E_2. Similarly, at around $I_1/I_{01} = 0.9892$ where the $|1\rangle \rightarrow |3\rangle$ noise transition peak disappears, ΔU crosses the second energy level E_3.

As mentioned above, the $|2\rangle$ and $|3\rangle$ levels have escape rates that are of order $(500)^2 \approx 10^5$ times and $(500)^2 \approx 10^7$ greater than the ground state, respectively, and thus even a very small probability of occupying $|2\rangle$ and $|3\rangle$ can cause a substantial enhancement in total escape rate. In particular, a population of about 10^{-4} in $|2\rangle$ or 10^{-6} in $|3\rangle$ would increase the escape rate by about an order of magnitude above that from $|0\rangle$. This would correspond to about the level of the enhancement above Γ_0 we see in the most isolated case for AL1. I note that these populations are so small that they are unlikely to produce significant effects in most qubit experiments. In fact, we have found that when Rabi oscillations are generated in this system, the time constant for the decay envelope does not appear to change significantly with the isolation r_I, even though the oscillations are taken with the device biased on top of a noise peak in the escape rate. The behavior of Rabi oscillations in AL1 are discussed in detail in Chapter 6.

5.4.3 T_1 measurements using relaxation

I measured T_1 using two methods. The first method involved measuring relaxation from $|1\rangle$ to $|0\rangle$. For this technique, I prepared the qubit in a mixed state of $|1\rangle$ and $|0\rangle$ by driving the qubit resonantly with microwaves and then shutting off the microwaves. The resulting state decays to $|0\rangle$ exponentially with a decay time constant T_1. There are a few problems that can arise with this technique, including (i) the need for the microwaves to shut off sharply at the qubit, (ii) the fact that we will get some population in $|2\rangle$ so that the relaxation process involves higher states

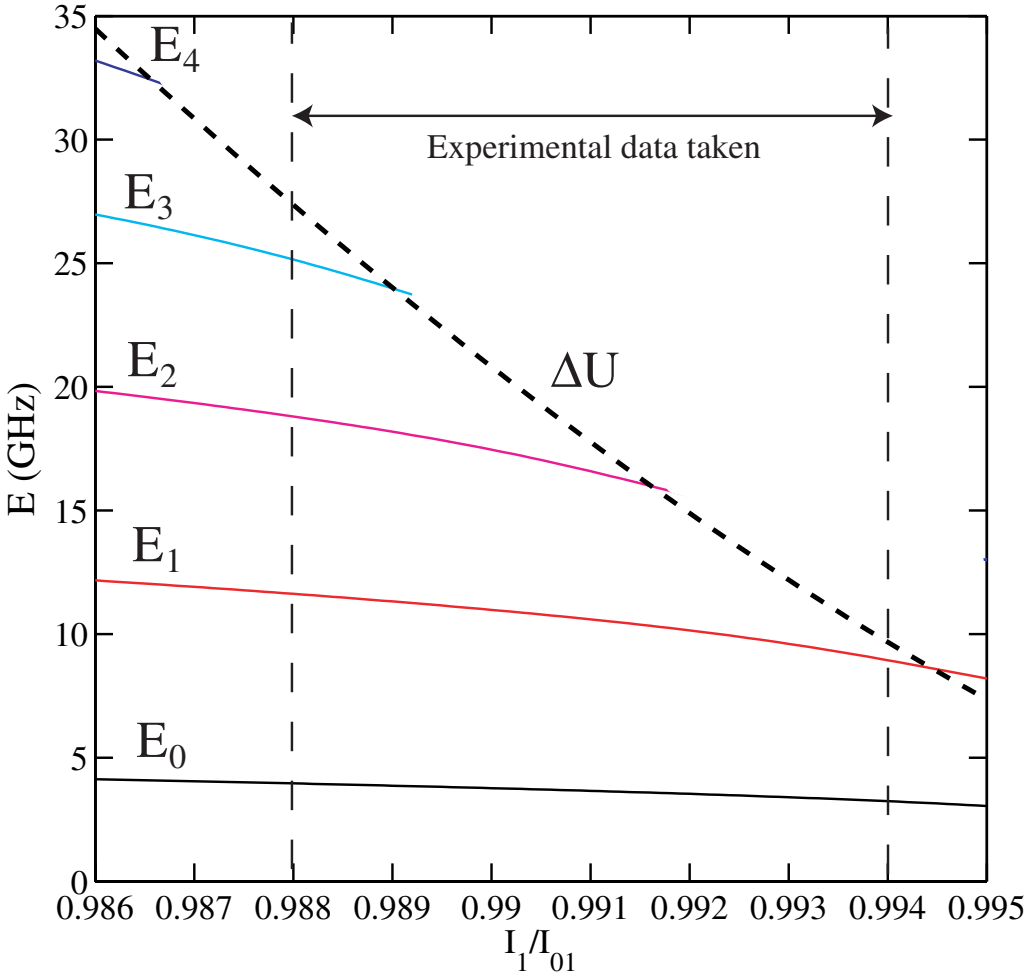

Figure 5.15: Energy levels of Josephson junction phase qubit using parameters for AL1 in Table 5.1. Energy levels were obtained by solving the Schrödinger equation numerically (see Appendix A). The dashed curve is the barrier height ΔU of the washboard potential.

and (iii) that the population in $|0\rangle$ increases as $|1\rangle$ decays. Due to population in $|2\rangle$ and escape from $|0\rangle$ as well as $|1\rangle$, multiple decay constants are observed in the relaxation measurement.

Figure 5.16 shows a measurement of relaxation in the escape rate in AL1 for $r_I = 1000$, when the qubit is most isolated. I drove the qubit junction at 7 GHz and measured the escape rate after the power was turned off. When the $|0\rangle \rightarrow |1\rangle$ transition frequency is resonant with the microwave drive, the escape rate is enhanced due to escape from high levels. I shut off the microwave at the peak of the microwave resonance and observed the subsequent escape rate versus time. The black dots are for the case when the microwave power was P = - 10 dBm and the blue dots are for the case when the microwave power was P = - 20 dBm. The data taken with a higher microwave power (P = - 10 dBm) has a weak oscillatory feature on top of an overall decay.

I used a χ^2 method to fit the decay in the relaxing escape rate to the following function

$$f(t) = A\exp[-t/t_0] + B\exp[-t/t_1] + C\exp[-t/t_2]. \tag{5.40}$$

(see smooth red curves in Fig. 5.16). The best fit parameters are listed in Table 5.3. The term with time constant $t_0 = 188.1$ μs is essentially an time constant due to the overall background escape rates. The decay time constant $t_2 \sim 5$ ns for all my data sets. This term is from a fast decay occurring at the beginning of the relaxation. S. K. Dutta found that the HP (Agilent) 83732B microwave generator I used for this measurement had a shut-off time of $\sim$ 5 ns [23] and I suspect that t_2 was caused at least partly by this. Dutta also observed short decay times from higher energy levels in his relaxation measurements [23], but in my case, I did not observe any decay times shorter than 5 ns, probably due to the limited time resolution (about 4 ns) in my setup (see Ch. 4). This leaves the time constant t_1, which represents the time constant for relaxation from $|1\rangle$ to $|0\rangle$. For the P = - 10 dBm data, the

relevant time constant is $T_1 \approx t_1 = 61$ ns and for P = - 20 dBm data, $T_1 \approx t_1 = 52$ ns. Thus the relaxation times for the most isolated case appears to be $T_1 = 50$ to 60 ns for AL1.

I also measured relaxation when the qubit junction was poorly isolated, with $r_I = 220$. In this case, I measured Rabi oscillation with a high power microwave drive (P = 17 dBm) and shut off the microwave power after 50 ns to observe decay in the escape rate. I fit the decay to Eq. 5.40 and found an initial decay time of about 5 ns, similar to the most isolated case with low power microwaves. For this data, the decay time constant $T_1 = t_1 = 59$ ns (see Fig. 5.17).

If the dissipation was due to the impedance of the bias leads, I would expect to observe the relaxation decay constant change with r_I. To calculate R_{iso}, I measured all device parameters using I - Φ fit and the spectroscopy (see Table 5.2) except R_1. Thus I calculated R_1 reversely from $T_1 = 55$ ns with $I_2 = 0$ ($r_I = 1000$, most isolated) measured from the relaxation measurement. When T_1 is 55 ns, R_{eff} is 13.5 kΩ. With known R_{iso}, I obtained $R_1 = 20$ kΩ. Using $R_1 = 20$ kΩ, I calculated T_1 for $r_I = 220$; If T_1 is 55 ns for $r_I = 1000$ and if T_1 is due to the bias leads, for $r_I = 220$ T_1 should be 19 ns.

However, as Fig. 5.17 and Table 5.3 show, the experimental results revealed no significant difference in T_1 and no systematic dependence on r_I. T_1 for all three relaxation curves were 50 ns to 60 ns; t_0 and t_2 also showed no systematic dependence on r_I.

5.4.4 T_1 measurements from the thermally induced escape rate

Dutta *et al.* showed that T_1 can also be obtained from measurements of the thermally populated background escape rates [23, 89]. I applied this method to find a separate estimate for T_1 in device AL1. Figure 5.18 shows experimental data (blue dots) for the escape rate in device AL1 obtained at 80 mK with $r_I = 1000$ (most

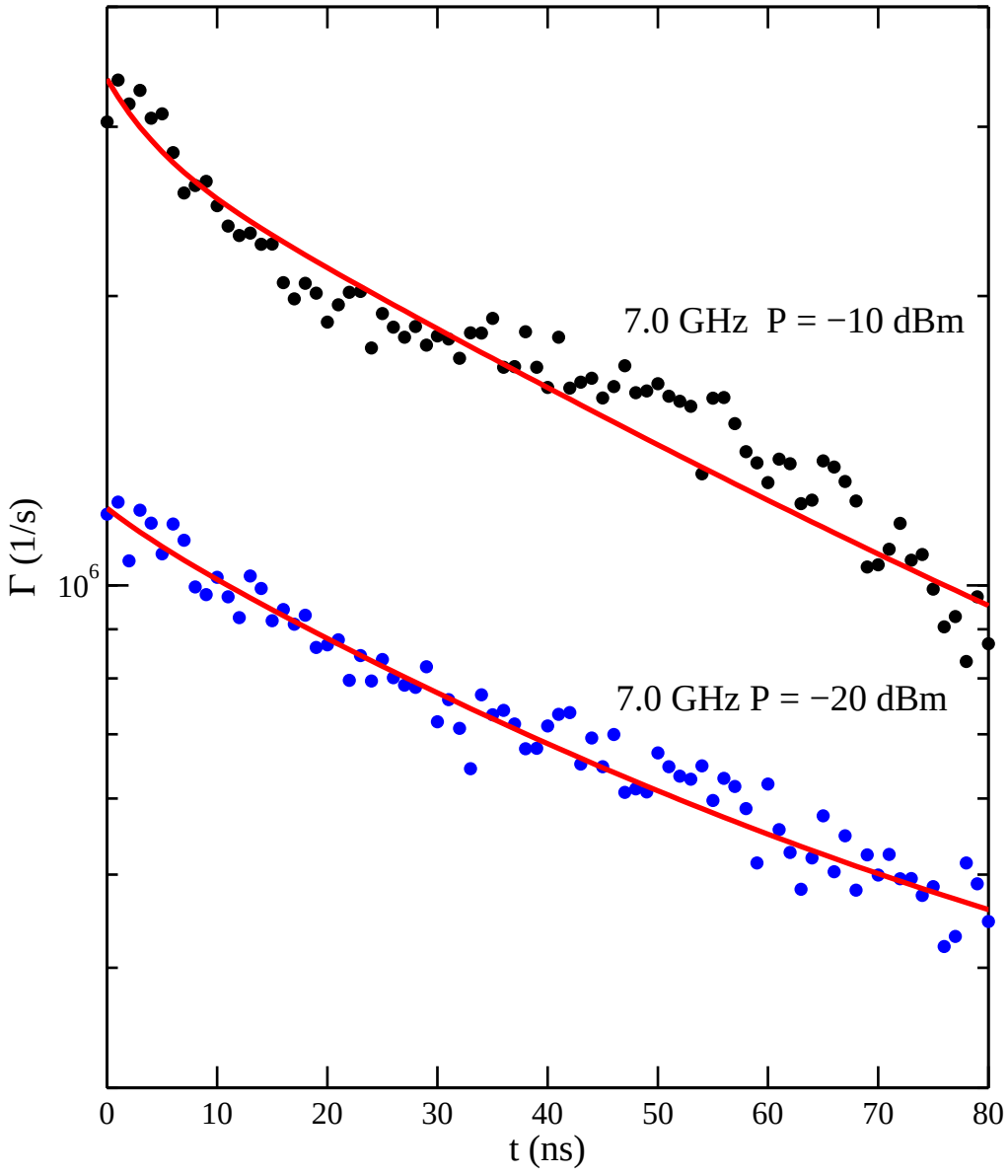

Figure 5.16: Observed relaxation in the escape rate for $r_I = 1000$ (most isolated) at 80 mK for two different microwave powers at 7.0 GHz. Solid curves are the χ^2 fits to Eq. 5.40. Upper dots are for microwave power P = -10 dBm and lower dots are for P = -20 dBm.

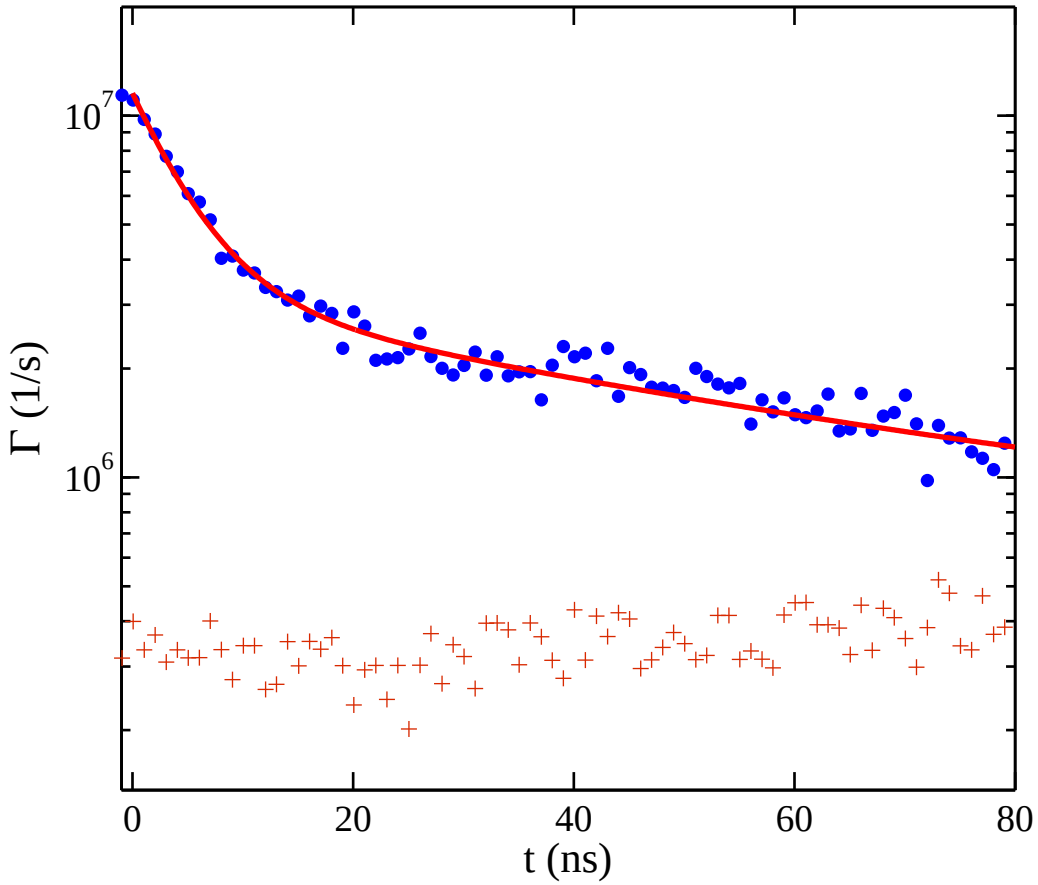

Figure 5.17: Observed relaxation in the escape rate for $r_I = 220$ (poorly isolated) at 80 mK in device AL1. Solid points are measured escape rates and the solid curve is the χ^2 fits to Eq. 5.40. This relaxation measurement was done with high power microwaves (P = 17 dBm) after measuring Rabi oscillations. Crosses are the measured background escape rate with no microwave power applied.

Table 5.3: Decay parameters that produced that best fit of Eq. 5.40 to the data in Fig. 5.16 and Fig. 5.17.

Parameters	A $(1/\mu s)$	B $(1/\mu s)$	C $(1/\mu s)$	t_0 (μ s)	t_1 (ns)	t_2 (ns)
$r_I = 1000$, P = -20 dBm	0.264	0.902	0.037	188.1	52.34	5.002
$r_I = 1000$, P = -10 dBm	0.252	2.617	0.494	188.1	60.71	4.544
$r_I = 220$, P = 12 dBm	0.519	2.661	8.355	188.1	59.29	5.004

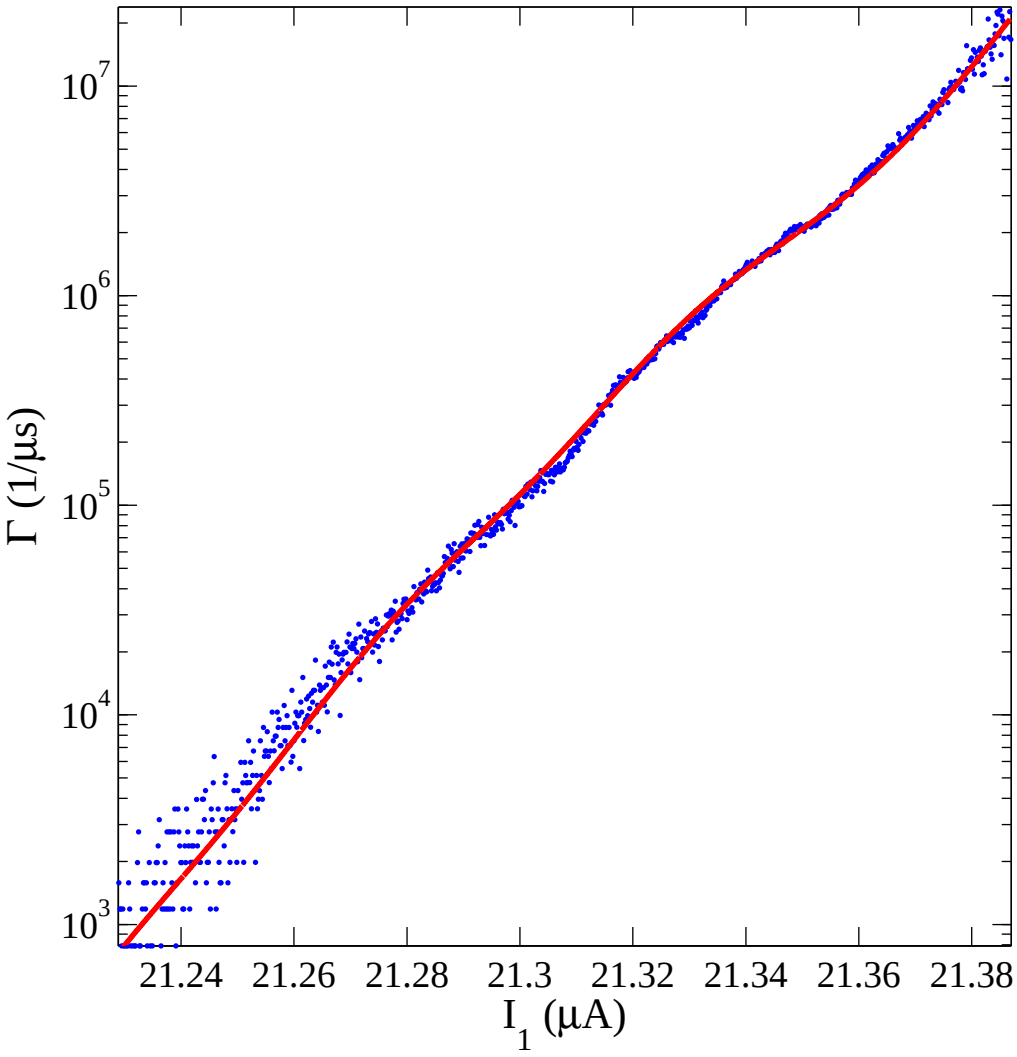

Figure 5.18: Total escape rate Γ versus current I_1 for qubit AL1 at $r_I = 1000$. The points are measured at 80 mK. The red curve is from a stationary 4-level master equation simulation with $T_1 = 17$ ns and T = 88 mK.

isolated). For comparison, the solid curve shows results from a stationary 4-level master equation simulation. The simulation parameters are $T_1 = 17$ ns, T = 88 mK and the qubit junction parameters $I_{01} = 22.2138\ \mu A$ and $C_1 = 4.078$ pF.

I performed a χ^2 fit of the experimental Γ_{tot} shown in Fig. 5.18 to find best fit parameters. Figure 5.19 shows a χ^2 map where χ^2 is obtained from

$$\chi^2 = \sum_{i=1}^{888} \left| \frac{\Gamma_{tot}(I_i) - \Gamma_{SME}(I_i)}{\sigma_{\Gamma_{tot}}(I_i)} \right|^2 \tag{5.41}$$

where $\Gamma_{tot}(I_i)$ is the experimental total escape rate at current I_i, $\Gamma_{SME}(I_i)$ is the calculated escape rate from a stationary 4-level master equation simulation at current I_i, and $\sigma_{\Gamma_{tot}}(I_i)$ is the uncertainty in Γ_{tot} at current I_i (from Eq. 4.3). I used 888 points in the measured escape rate, from $I_1 = 21.232\ \mu A$ to $21.387\ \mu A$. In the color scale of Fig. 5.19, red means that Γ_{SME} is far from Γ_{tot} and blue means that the calculated Γ_{SME} is close to Γ_{tot}. For this particular set, T_1 and T varied from 12 ns at 82 mK to 17 ns at 87 mK. This case was for r = 1000 (most isolated).

From Fig. 5.19, we can see that there is a relatively wide range of parameters that yield good fits to the data. Moreover the total escape rates measured in the experiments are not as smooth as the calculated escape rate, although Γ_{tot} for the most isolated case ($r_I = 1000$) is smoother than Γ_{tot} for the poorly isolated cases.

However, to see if T_1 is affected by r_I, we need to fit the poorly isolated data also. Unfortunately, as I discussed in sec.5.4.2, noise-induced peaks appear in Γ_{tot} when the qubit is poorly isolated. Thus fitting Γ_{tot} to a master equation simulation is problematic for poorly isolated data.

An alternative approach is to find T_1 for each current that reproduces the experimental total escape rate. In this analysis approach, I assumed that T_1 is a function of the qubit current I_1, not a constant as in the thermal model described in sec. 5.3.3. $T_1(I_1)$ incorporates the noise induced transition at each current by

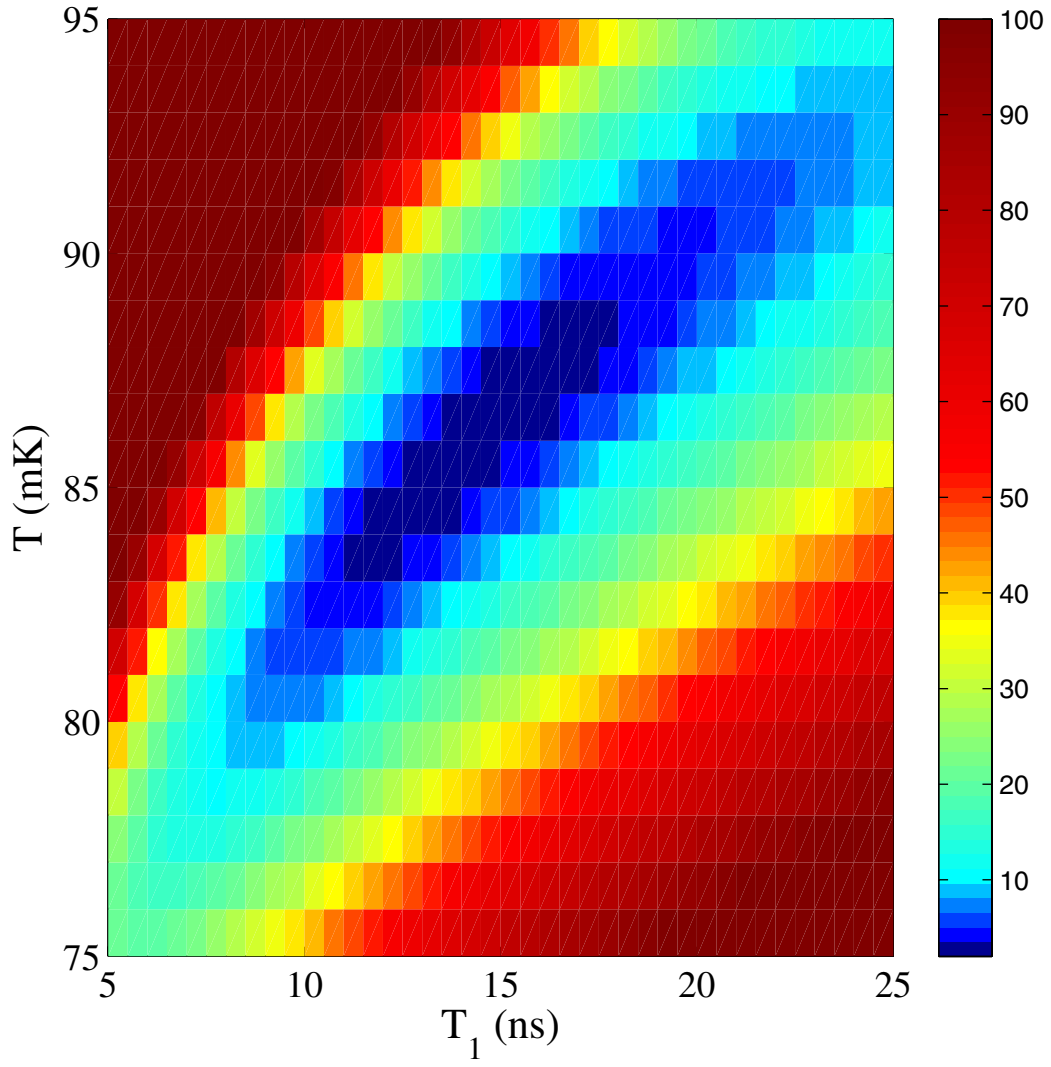

Figure 5.19: χ^2 map for parameters T_1 and T. χ^2 is calculated from the experimental Γ_{tot} and the calculated escape rate from the master equation simulation.

assuming the effective resistance R_{eff} is frequency dependent. In this approach, the thermal transition rate Eq. 5.35 becomes

$$W_{ij}^{st} = \frac{\hbar\omega_{ij}}{2R_{eff}(I_1, r_I)e^2} \frac{|\langle i \,|\, \hat{\gamma} \,|\, j\rangle|^2}{\exp\left(\hbar\omega_{ij}/k_B T\right) - 1} \tag{5.42}$$

where r_I is the isolation factor and I_1 is related to frequency through the corresponding energy level spacing.

Figure 5.20 shows the escape rate Γ from the experiment (blue dots) and a calculated escape rate Γ_{SME} (magenta curve) versus current I_1 for qubit AL1 at r_I = 1000. Γ_{SME} was obtained from a stationary 4-level master equation simulation by finding $T_1(I_1)$ that satisfied $|\Gamma - \Gamma_{SME}| = 0$ with a current dependent $T_1(I_1)$ where Γ is the escape rate data from Fig. 5.18. I assumed $C_1 = 4$ pF and T = 88 mK. For comparison, the black curve shows Γ_{SME} from a stationary 4-level master equation using a constant $T_1 = 17$ ns.

Figure 5.21 shows a plot of T_1 versus current that I found by analyzing the data in Fig. 5.20 using the stationary 4-level master equation solution. The simulation parameters are T = 88 mK, $I_{01} = 22.2138\ \mu A$ and $C_1 = 4.078$ pF. T_1 has maximums and minimums. On average, T_1 is roughly 15 ns but depending on current, T_1 can be as high as 23 ns or as low as 5 ns. The maximum T_1 is about 23 ns at $I_1 = 21.31\ \mu A$.

Using this method, I was able to calculate T_1 versus current I_1 for two different isolations, $r_I = 1000$ and $r_I = 400$. Figure 5.22 shows the calculated T_1 versus normalized current I_1/I_{01} for these two cases. The black curve shows T_1 for the most isolated case ($r_I = 1000$) and the blue curve shows T_1 for the poorly isolated case ($r_I = 400$). I note that the T_1 curves in Fig. 5.22 are different from the T_1 curve measured two months earlier shown in Fig. 5.21, suggesting that the device or external noise changed over a two month period.

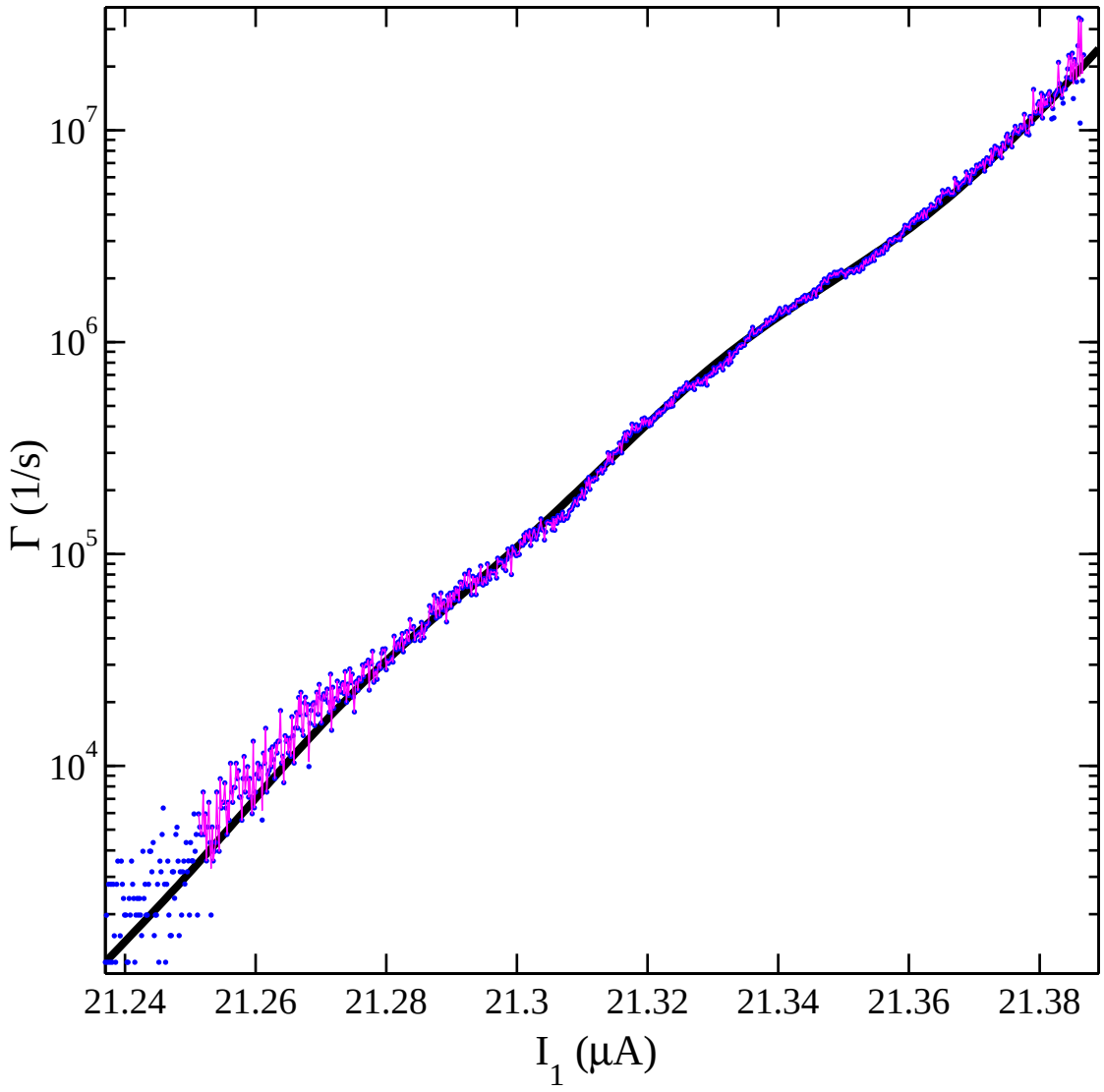

Figure 5.20: Experimental Γ (blue dots) and calculated Γ_{SME} (magenta line) versus current I_1 for qubit AL1 for $r_I = 1000$. Γ is the escape rate data from Fig. 5.18. For the calculation, I assumed $C_1 = 4$ pF and T = 88 mK. The black curve shows Γ_{SME} from a stationary 4-level master equation using a constant $T_1 = 17$ ns.

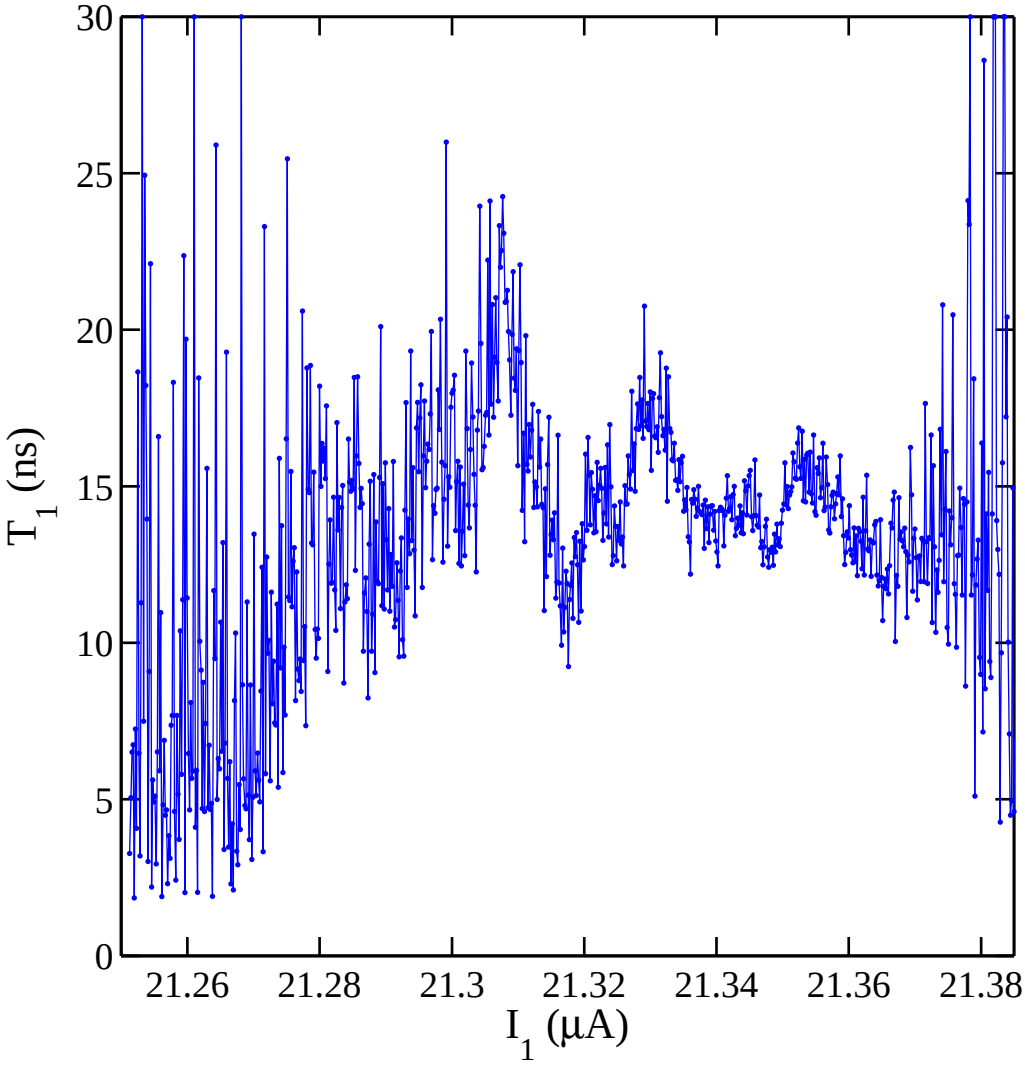

Figure 5.21: Calculated T_1 versus current I_1 for qubit AL1 at $r_I = 1000$ using escape rate data from Fig. 5.18, assuming $C_1 = 4$ pF and T = 88 mK. This data was taken on 01/23/05.

In Fig. 5.22, T_1 appears to depend on r_I, but not over the whole range of current I_1/I_{01}. For I_1/I_{01} less than about 0.992, $T_1(I_1)$ for $r_I = 1000$ is virtually the same as $T_1(I_1)$ for $r_I = 400$. However, below $I_1/I_{01} = 0.992$, T_1 scales as the isolation. For comparison, the red curve shows T_1 for $r_I = 400$ multiplied by the isolation factor ratio 1000/400. For $I_1/I_{01} < 0.992$, the red curve matches with T_1 for $r_I = 1000$ (black curve).

Fig. 5.22 suggests that both relaxation and noise induced transitions are occurring in the device. Low T_1 indicates high Γ_+ and a fast relaxation rate. Therefore, when I decrease the isolation factor r_I from 1000 to 400, the measured T_1 should decrease. This phenomena only happen below $I_1/I_{01} = 0.992$ near where $|2\rangle$ leaves the well, which suggests that Γ_+ involves $|2\rangle$ states, not $|1\rangle$.

I note that the T_1 values in Fig. 5.21 or Fig. 5.22 are very different from $T_1 \simeq 50$ ns obtained from the relaxation measurements. This raises several important questions, in particular, what is causing the enhancement evidenced in Fig. 5.16 and Fig. 5.17. Spurious two-level systems coupled to the qubit junction is a possible answer. The existence of two level systems coupled to phase qubits has been observed by several groups [90, 49, 23]. The idea is that microwaves can drive the system into a state in which the two level fluctuator is entangled with the qubit. If the fluctuator has a long relaxation time constant (say 50 ns) then the resulting entangled system can show a components with corresponding long relaxation time [55]. Another possibility is that the thermal rate estimation for T_1 is incorrect because of the presence of high frequency, non-thermal noise. Only thermal noise was included in this model, and the presence of a non-thermal source would produce an apparently smaller T_1 in Fig. 5.21 or Fig. 5.22. Further experiments and analysis will be needed to distinguish these possibilities.

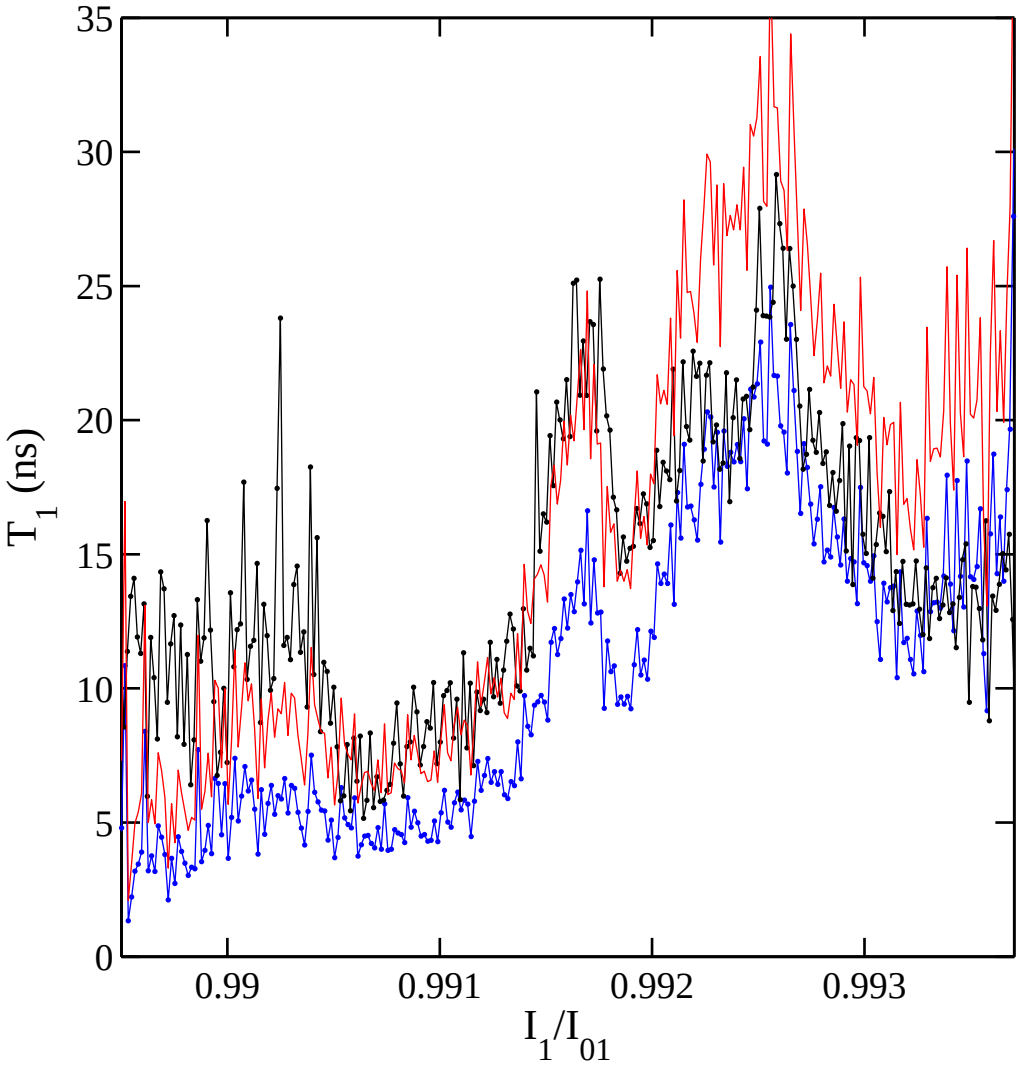

Figure 5.22: Comparison of results for T_1 vs I_1/I_{01} with $r_I = 1000$ (black curve) and for the escape rate with $r_I = 400$ (blue curve). I_{01} is 22.2138 μA. For comparison, the red points are T_1 for $r_I = 400$ multiplied by the isolation ratio 1000/400. This data was taken on 03/30/05.

5.5 Conclusions

In conclusion, I have shown how the isolation between the qubit junction and its bias leads can be varied *in situ* by applying current to the isolation junction in a dc SQUID phase qubit. I found that the isolation fails when the resonance frequency of the isolation junction matches a qubit transition frequency. This leads to prominent peaks in the escape rate when the $|0\rangle$ to $|2\rangle$ or $|1\rangle$ to $|3\rangle$ transition frequencies of the qubit matches with the plasma frequency of the isolation junction. Fortunately, the noise generates only very small population in the upper levels and this does not appear to significantly degrade the performance of the devices. Nevertheless, this behavior is undesirable, and could become an issue if the coherence times become significantly longer. Additional high frequency filtering and redesign of the isolation junction parameters will be needed to suppress the effect.

I measured T_1 of AL1 using a relaxation measurement technique and by measuring the thermally induced escape rate. The T_1 results are summarized in Table. 5.4 and they differ significantly. Since there have been several reports showing that the phase qubit can be coupled to spurious two level systems in nearby dielectrics [90, 49], it is possible that the larger value of T_1 from the relaxation measurement could be due to two level systems. It is unclear why I did not observe the same long T_1 from the thermally induced background escape rate fits. However, T_1 from the escape rates showed some dependence on the isolation factor which the relaxation measurements did not. This suggests that the escape rate estimates for T_1 may be contaminated by high frequency non-thermal noise. In the next chapter, I will generally assume $T_1 \sim 20$ ns which is what I obtained from the thermal escape rate measurements at large values of I_1.

Table 5.4: T_1 estimates for qubit AL1

Method	Isolation r_I	Frequency	Power	T_1 (ns)
Relaxation	1000	7 GHz	20 dBm	52.34
Relaxation	1000	7 GHz	-10 dBm	60.71
Relaxation	220	7 GHz	17 dBm	59.29
Thermal escape rate	1000	$\Delta E_{01}/h = 7$ GHz		25
Thermal escape rate	400	$\Delta E_{01}/h = 7$ GHz		15

Chapter 6

Measurements of coherence times in dc SQUID phase qubits

6.1 Overview

Superconducting circuits containing Josephson junctions are examples of relatively large systems that display quantum behavior [38, 41, 45, 47, 91, 92, 93]. In particular, it has been shown experimentally that Josephson junction can be placed into superpositions of quantum states as well as entangled quantum states [48, 94]. In these measurements, the junctions, although cooled to millikelvin temperatures, were attached to room-temperature amplifiers through thermally-anchored, low-pass-filtered wire leads. Such connections between a quantum system and a noisy environment will in general lead to decoherence of the quantum system.

In this chapter, I show results of Rabi oscillation measurements on a dc SQUID phase qubit with $Al/AlO_x/Al$ junctions. I was able to change the isolation of the qubit *in situ* and examined the effect of isolation on the Rabi oscillations and the spectroscopic coherence times. I also show Rabi oscillation data on a niobium SQUID from S. K. Dutta [23] for comparison with the aluminum device. I begin by reviewing the isolation scheme of the dc SQUID phase qubit and show how the isolation factor influences the decay time constant T' of the Rabi oscillations and the spectroscopic coherence time T_2^*.

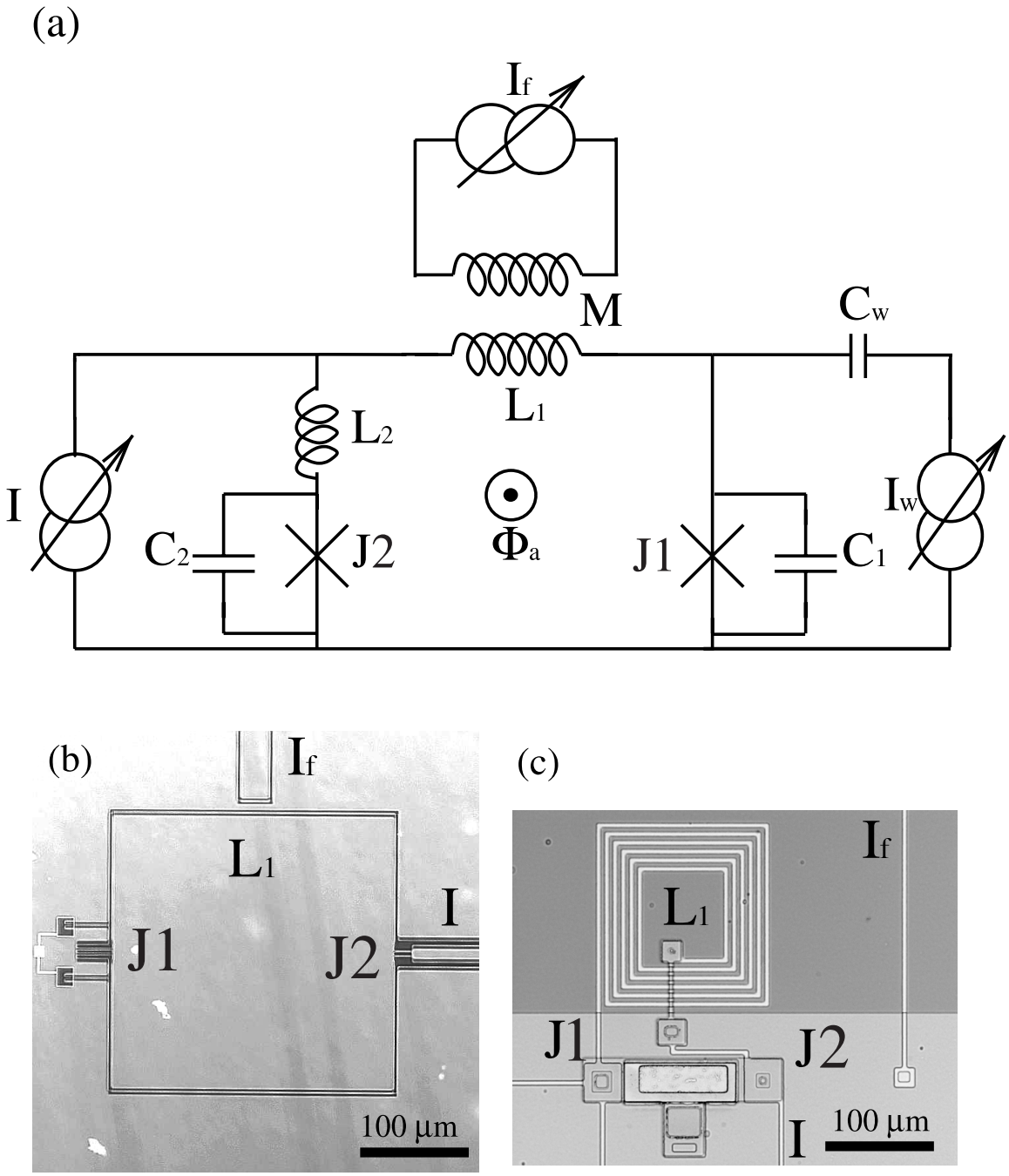

Figure 6.1: (a) Schematic of dc SQUID phase qubit. I is the bias current, I_f is current for the flux bias, M is mutual inductance between the flux bias coil and the SQUID loop and Φ_a is flux applied to the SQUID loop. C_1 and C_2 are the capacitances of the qubit junction J1 and the isolation junction J2, respectively. Microwave source I_w is coupled to J1 through capacitor C_w. Photographs of (b) single-turn aluminum SQUID magnetometer AL1 and (c) 6-turn niobium SQUID magnetometer NB1.

6.2 Current noise, isolation and coherence times in the dc SQUID phase qubit

In a dc SQUID phase qubit [see Fig. 6.1(a)], junction J1 acts as a phase qubit [12] and the rest of the SQUID serves as an inductive isolation network that filters out noise from the bias leads [47]. The isolation network consists of a fixed inductor L_1, an isolation junction J2 and a parasitic inductance L_2. When the applied flux Φ_a is held constant, a small fluctuation ΔI in the bias current I leads to a change ΔI_1 in the current I_1 flowing through junction J1. The current noise power isolation factor, r_I is given by

$$r_I = \left(\frac{\Delta I}{\Delta I_1}\right)^2 = \left(\frac{L_1 + L_{J1} + L_2 + L_{J2}}{L_{J2} + L_2}\right)^2 \approx \left(\frac{L_1 + L_2 + L_{J2}}{L_{J2}(I_2) + L_2}\right)^2. \tag{6.1}$$

as defined in Chapter 5 where I have assumed $L_1 \gg L_{J1}$ and neglected M_I, the mutual inductance between the current bias line and the SQUID loop. Hence

$$L_{Ji}(I_i) = \frac{\Phi_0}{2\pi} \frac{1}{I_{0i}\sqrt{1 - (I_i/I_{0i})^2}} \tag{6.2}$$

is the Josephson inductance of the i-th junction (i = 1 or 2) and I_{0i} is the critical current of the i-th junction. Since L_{J2} depends on I_2, the isolation is a function of I_2.

If the current on the leads has a noise power spectral density $S_I(f)$, then the current noise power spectral density $S_{I_1}(f)$ which reaches the qubit junction J1 is

$$S_{I1}(f) = \frac{S_I(f)}{r} \approx S_I(f)\left(\frac{L_{J2} + L_2}{L_1 + L_2 + L_{J2}}\right)^2. \tag{6.3}$$

Thus $S_{I_1}(f)$ can be varied *in situ* because L_{J2} can be changed by varying the current I_2 through the isolation junction (see Eq. 2). Good isolation can be achieved by

choosing $L_{J2} \ll L_1$. The best current bias isolation occurs at $I_2 = 0$ where L_{J2} is a minimum (see Chapter 5). The implication of Eq. 6.3 is that the current noise power from the bias leads is reduced by factor of r_I before it reaches the qubit junction. Equation 6.3 is valid if the fluctuation frequency f is much less than the plasma frequency f_{p2} of the isolation junction.

Current noise $S_{I_1}(f)$ can cause excitation, dissipation, decoherence and inhomogeneous broadening in the qubit. Which effect dominates a measurement depends on the nature of the measurement and the frequency range of the noise [25, 61]. For example, a flat noise spectrum (white noise) with a bandwidth that extends up to and beyond $1/T_1$ leads to pure dephasing or decoherence that cannot be removed using a spin-echo technique.

Decoherence, dissipation, power broadening and inhomogeneous broadening all contribute to the measured spectroscopic resonance widths. H. Xu showed that if the noise power is constant below a cut-off frequency $f_c \ll 1/T_1$, then inhomogeneous broadening dominates the spectroscopic coherence time T_2^* where

$$T_2^* = \frac{1}{2\pi\Delta f_{HWHM}} \tag{6.4}$$

and Δf_{HWHM} is the half-line width at half maximum (defined in Chapters 3 and 4) of the $|0\rangle$ to $|1\rangle$ transition peak at the transition frequency f_{01} [25, 95]. Given the relationship between I and I_1, Xu's analysis implies that in this case,

$$T_2^* = \left(1.65 \cdot 2\pi\sigma_{I1}\left|\frac{\partial f_{01}}{\partial I_1}\right|\right)^{-1} = \sqrt{r_I}\left(1.65 \cdot 2\pi\ \sqrt{S_I(0)f_c}\left|\frac{\partial f_{01}}{\partial I_1}\right|\right)^{-1} \tag{6.5}$$

where σ_{I1} is the rms current noise in I_1, S_I is the current noise power in I and I have assumed that the spectrum is measured in the low-power limit. Thus for low frequency noise, T_2^* scales with $\sqrt{r_I}$.

On the other hand, if the noise has a cutoff frequency $f_c \gg 1/T_1$, the effect is

to produce pure dephasing, and Xu's analysis implies that T_2^* is given by [25, 95]:

$$T_2^* = \left[\pi^2 S_{I1}(0)(\frac{\partial f_{01}}{\partial I_1})^2\right]^{-1} = r_I \left[\pi^2 S_I(0)(\frac{\partial f_{01}}{\partial I_1})^2\right]^{-1} \tag{6.6}$$

Thus T_2^* should scale linearly with r_I in this limit. Of course if current noise is not dominating the decoherence, T_2^* would likely be independent of r_I.

The decay time constant T' of the envelope of the Rabi oscillations is sensitive to noise at the Rabi frequency, while the shape of the envelope is affected by inhomogeneous broadening caused by low frequency noise [61]. If both decoherence and dissipation are present, the Rabi decay constant T' is related to the dephasing time T_2 and the relaxation time T_1 by

$$\frac{1}{T'} = \frac{1}{2T_1} + \frac{1}{2T_2} \tag{6.7}$$

when there is zero detuning (see Chapter 3) [25, 64]. Here I use the homogeneous coherence time T_2 as defined in Ch. 3. Although Eq. 6.7 was derived for two-level Rabi oscillations, it will still be applicable to a multi-level phase qubit if the higher-level occupations are small. The idea is that by measuring T', I can obtain information about T_2 and the amount of current noise at the Rabi frequency. I also expect T' will scale with isolation factor r_I if the bias current leads are the dominant source of decoherence and dissipation.

6.3 Effect of current noise on Rabi oscillations

I measured Rabi oscillations by driving resonant $|0\rangle \rightarrow |1\rangle$ transitions using a 7 GHz microwave drive. I obtained data for the most isolated case ($r_I = 1000$) and a poorly isolated case ($r_I = 200$). For these measurements, I first initialized the SQUID in the zero flux state, corresponding to no circulating current in the SQUID

loop. I then applied a small static offset flux to the SQUID to induce circulating current, thereby producing a fixed current I_2 (see Ch. 5).

Figure 6.2 shows the escape rate versus current I_1 for device AL1 measured at 80 mK when $r_I = 1000$ (black curve), $r_I = 200$ (red dotted curve) and with 7 GHz microwave applied at $r_I = 1000$. The escape rate with $r_I = 1000$ is in reasonable agreement with a stationary four-level master equation simulation with thermal population for T = 88 mK and $T_1 = 17$ ns, as discussed in Chapter 5. Reducing r_I by a factor of 5, an overall enhancement in the escape rate ($r_I = 200$, red crosses) was observed with two broad peaks at 21.02 μA and 21.08 μA. As discussed in Chapter 5, I found that these broad peaks in the background Γ are due to noise induced populations in $|2\rangle$ and $|3\rangle$. The dashed curve in Fig. 6.2 shows the escape rate when an f = 7.00 GHz microwave is turned on at the $|0\rangle \rightarrow |1\rangle$ transition resonance. The resulting resonance peak is very wide due to power broadening. Note that for $r_I = 200$, a large noise-induced transition peak already exists at the current where Rabi oscillations were measured (see crosses in Fig. 6.2).

Figure 6.4 shows Rabi oscillations in device AL1 for the most isolated case, $r_I = 1000$, measured with microwave powers from 6 dBm to 17 dBm, referred to the output of the microwave source at room temperature. The Rabi frequency increased as the microwave power increased, as expected for Rabi oscillations. Figure 6.3(a) show a plot of Rabi frequency squared vs. the microwave power in mW when $r_I = 1000$. A linear χ^2 fit is drawn as a red line. This fit gives a slope of 2.6×10^4 $(\text{MHz})^2/\text{mW}$ and a y-intercept of 2.0×10^3 $(\text{MHz})^2$. I note that power in dBm is related to power in mW by $P_{mW} = 10^{P_{dBm}/10}$ so 10 dBm is 10 mW.

Examination of Fig. 6.4 shows that for powers of 13 dBm and above, the oscillation amplitude gets progressively washed away. This may be because the Rabi frequency becomes smaller than the time resolution of my measurement system. The limited time resolution occurs because the voltage signal from the qubit switching

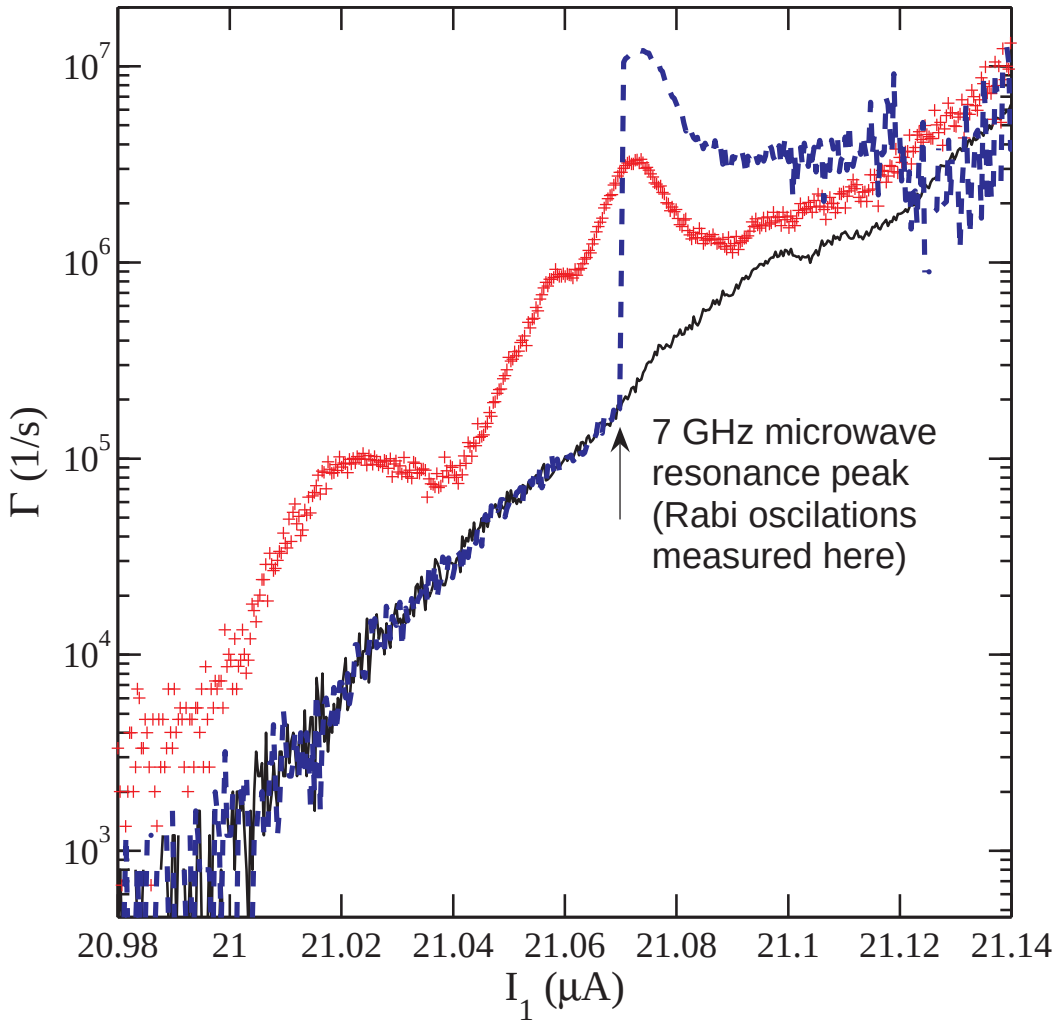

Figure 6.2: Escape rates of device AL1 at $r_I = 1000$ (solid curve), $r_I = 200$ (crosses) and with 7 GHz microwaves (dashed curve) at $r_I = 1000$.

has a finite slope with respect to time. With added noise, one gets jitter in the determination of the switching time. From the Rabi oscillation plots, I estimate that the time resolution is about 4.5 ns.

To extract the decay time constant of the envelope of the Rabi oscillations, I fit the oscillation curves to a phenomenological model for a decaying oscillation,

$$\Gamma_{fit} = g_0 + g_1(1 - e^{-(t-t_0)/T'}\cos(\Omega\{t - t_0\})) + g_2(1 - e^{-(t-t_0)/T_{back}}) \tag{6.8}$$

where the fitting parameter T′ gives the decay time constant of the Rabi oscillations. Here Ω is the Rabi frequency and t_0 is the microwave starting time. The first term, g_0, accounts for the initial escape from Γ_0 and any thermally induced population in upper levels at time t = t_0; i.e. $\Gamma(t = t_0) = g_0$. The second term accounts for the Rabi oscillation with frequency Ω and decay envelope time constant T'. The third term involving g_2 and T_{back} accounts for the finite rise time of the microwave pulse and changes in population in $|2\rangle$ caused by the drive (see Chapter 5). Note that $\Gamma_{fit}(t = \infty) = g_0 + g_1 + g_2$. I found that g_0, g_1, g_2, T_{back}, Ω and t_0 do not have much effect on the Rabi decay time fitting parameter T′, but improve the overall fit.

Figures. 6.5 and 6.6 show plots of Rabi oscillations in device AL1 at 80 mK with $r_I = 1000$ (grey open circles) and the best fit curves (black solid curves). I did a χ^2 fit and found the best fit parameters shown in Table 6.1. The smooth turn-on of the Rabi oscillations is due to the rise time of the microwave pulse as mentioned above, and the finite time resolution in my experiment. These effects are only roughly accounted for in Eq. 6.8. Nevertheless the fitted curves show reasonably good agreement overall, except near t = 0. Since it was difficult to get good fits for t < 5 ns, I performed the fitting for $r_I = 1000$ starting from t = 5 ns. For the data in Figs. 6.5 and 6.6, the average Rabi decay time T′ is 23.2 ns and there is some variation, as can be seen by examination of Table 6.1.

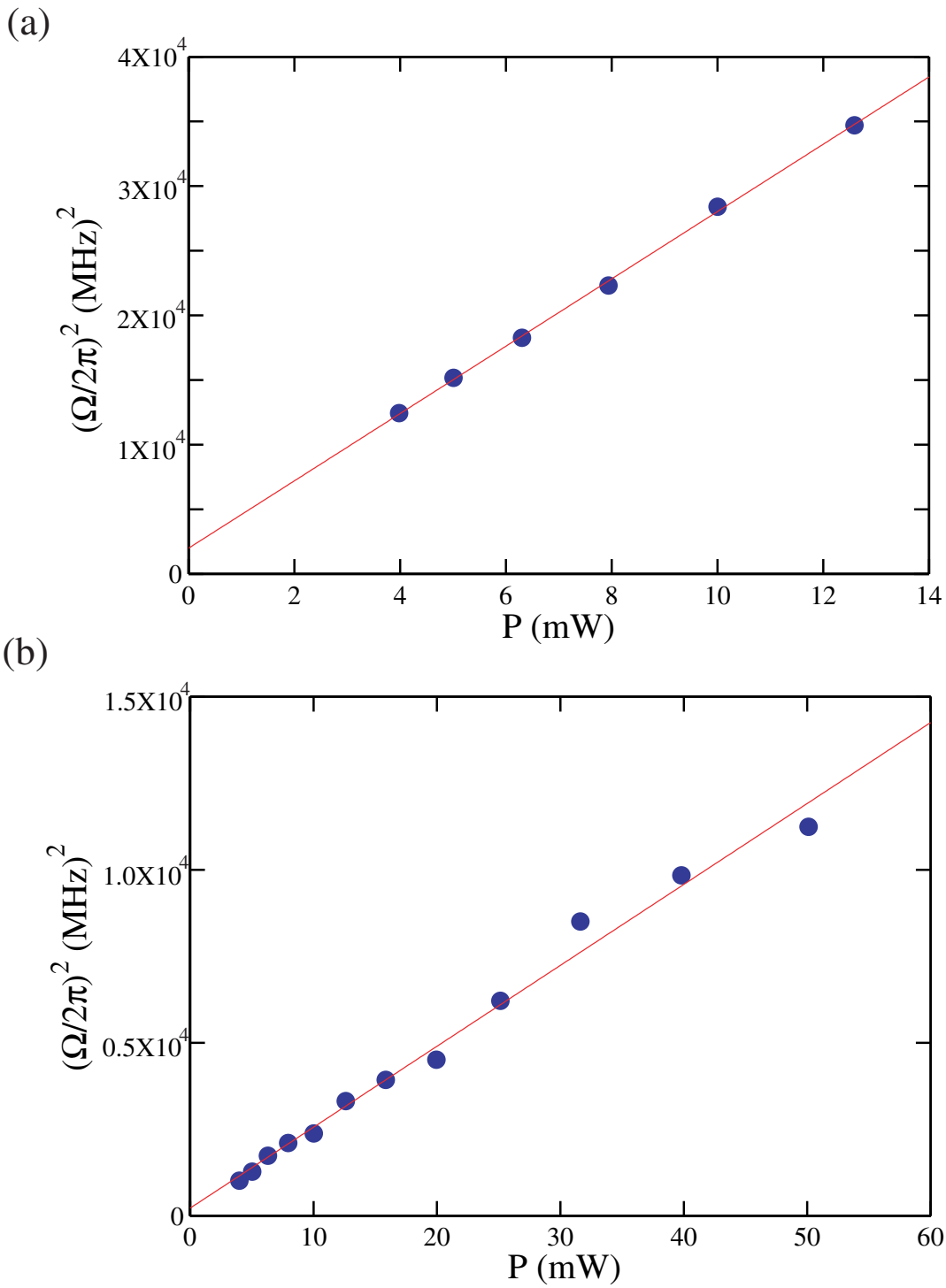

Figure 6.3: Square of the Rabi frequency vs. microwave power (a) for the most isolated case $r_I = 1000$ (filled dots) and (b) the poorly isolated case $r_I = 200$ (filled dots). The red lines in each plot are from a linear χ^2 fit.

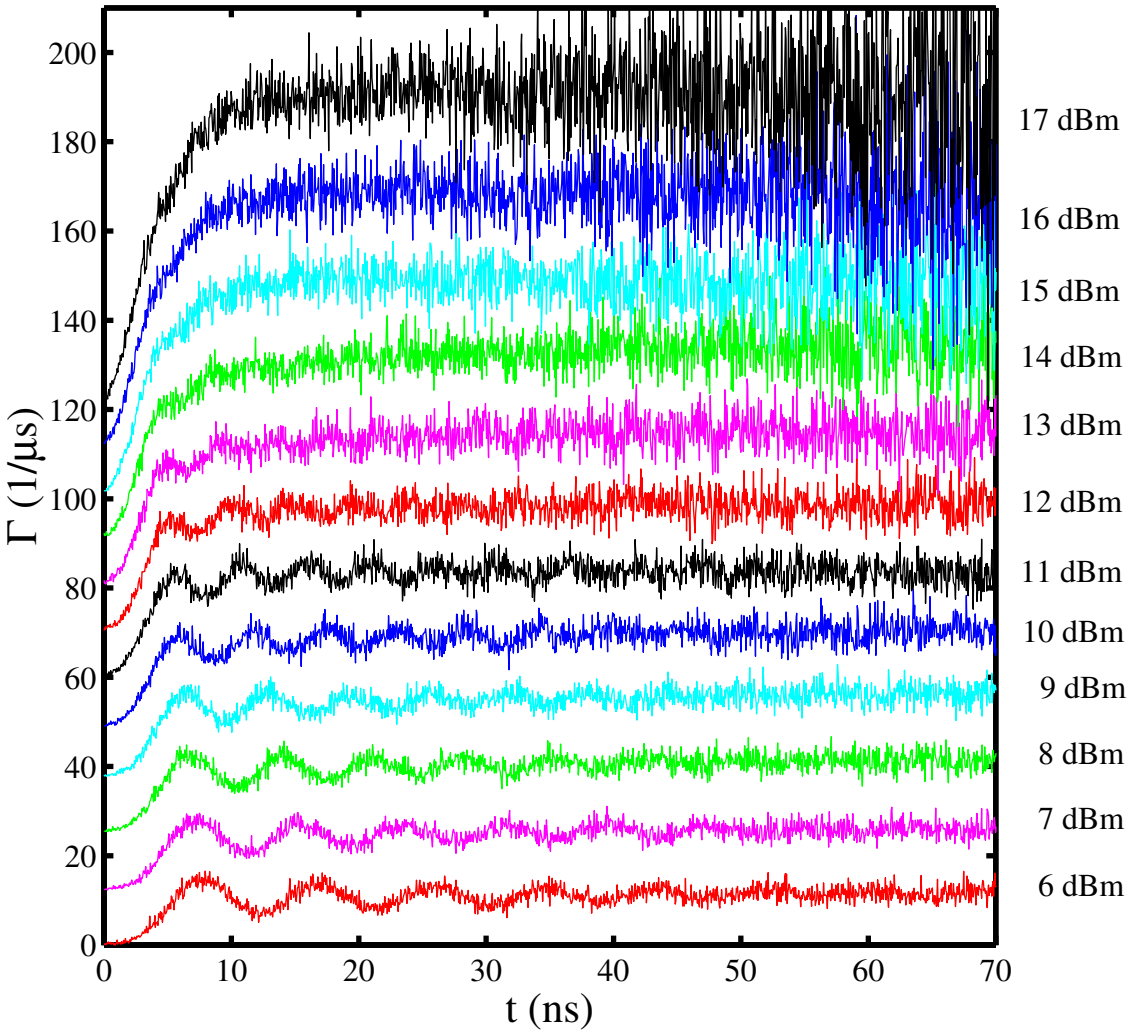

Figure 6.4: Rabi oscillations measured for r = 1000 in device AL1 at 80 mK. Each curve was taken with 7 GHz microwaves, with the power varying from 6 dBm to 17 dBm. Each successive curve was offset vertically by $10/\mu s$.

Table 6.1: Summary of fitting parameters for Rabi oscillations in device AL1 at 80 mK with $r_I = 1000$. The microwave was at 7.0 GHz.

	6 dBm	7 dBm	8 dBm	9 dBm	10 dBm	11 dBm
t_0 (ns)	1.83	1.71	2.42	2.34	2.47	2.57
g_0 $(1/\mu s)$	2.82	3.14	3.40	3.89	4.25	6.52
g_1 $(1/\mu s)$	4.89	4.56	4.57	4.59	4.21	3.95
$\Omega/2\pi$ (MHz)	111	123	136	151	168	188
T′(ns)	28.2	27.4	24.5	18.8	18.8	21.9
g_2 $(1/\mu s)$	3.12	4.89	6.80	8.52	11.7	13.1
T_{back}(ns)	1.70	2.21	2.60	2.69	3.16	2.81

Figure 6.7 shows Rabi oscillations for the poorly isolated case, $r_I = 200$, measured for microwave powers from 6 dBm to 17 dBm. The most obvious difference from Fig 6.4 is that Rabi frequencies are much lower for the same microwave power applied at the top of the refrigerator. This suggests the microwave coupling to the sample has decreased compared to when $r_I = 1000$. This was unexpected and suggests the microwaves are coupling through the current bias line. Figure 6.3(b) shows that the square of the Rabi frequency varies linearly with microwave power, as expected. A linear χ^2 fit to this data [red line in Figure 6.3(b)] gives a slope of 2800 $(\text{MHz})^2/\text{mW}$ and a y-intercept of 3300 $(\text{MHz})^2$; the slope is almost 10 times less than for $r_I = 1000$ while the intercepts are comparable.

I fit the oscillation curves in Fig. 6.7 to Eq. 6.8 to extract the decay times of the Rabi oscillation for $r_I = 200$. The solid curves in Figs. 6.8, 6.9, 6.10 and 6.11 show the resulting fits to the Rabi oscillations for $r_I = 200$. The best fit parameters are shown in Tables 6.2 and 6.3.

For $r_I = 200$, the escape rates clearly do not start from $\Gamma_{tot} = 0$ at t = 0, and from this, we can see that noise was exciting the system while we were measuring Rabi oscillations; the escape rate was already high at t = 0 mainly due to escapes

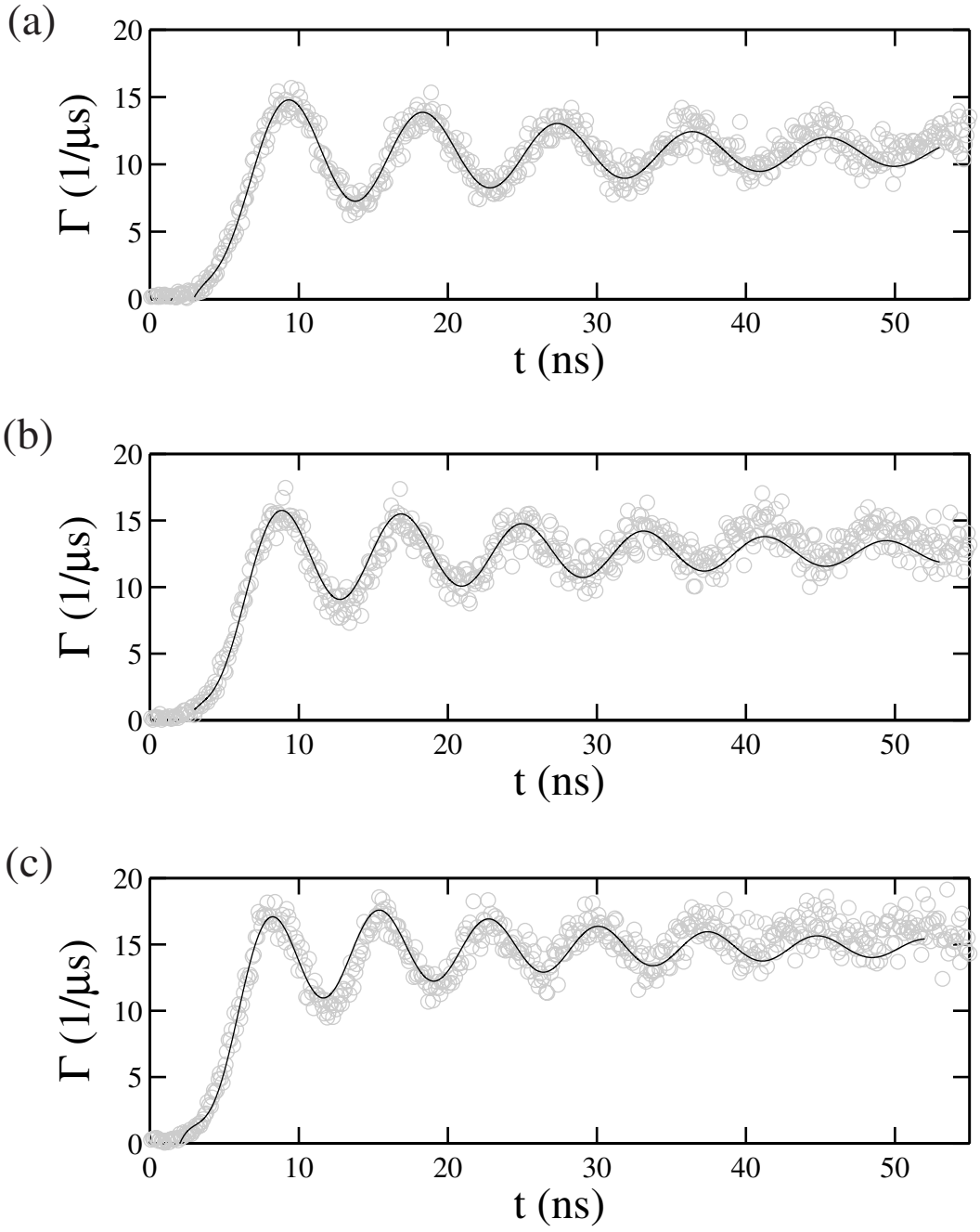

Figure 6.5: Rabi oscillations in the escape rate for device AL1 at 80 mK with $r_I = 1000$ (open circles). Solid curves show best fit to Eq. 6.8 for 7 GHz microwaves with power (a) P = 6 dBm, (b) P = 7 dBm, and (c) P = 8 dBm. Fitting parameters are listed in Table 6.1.

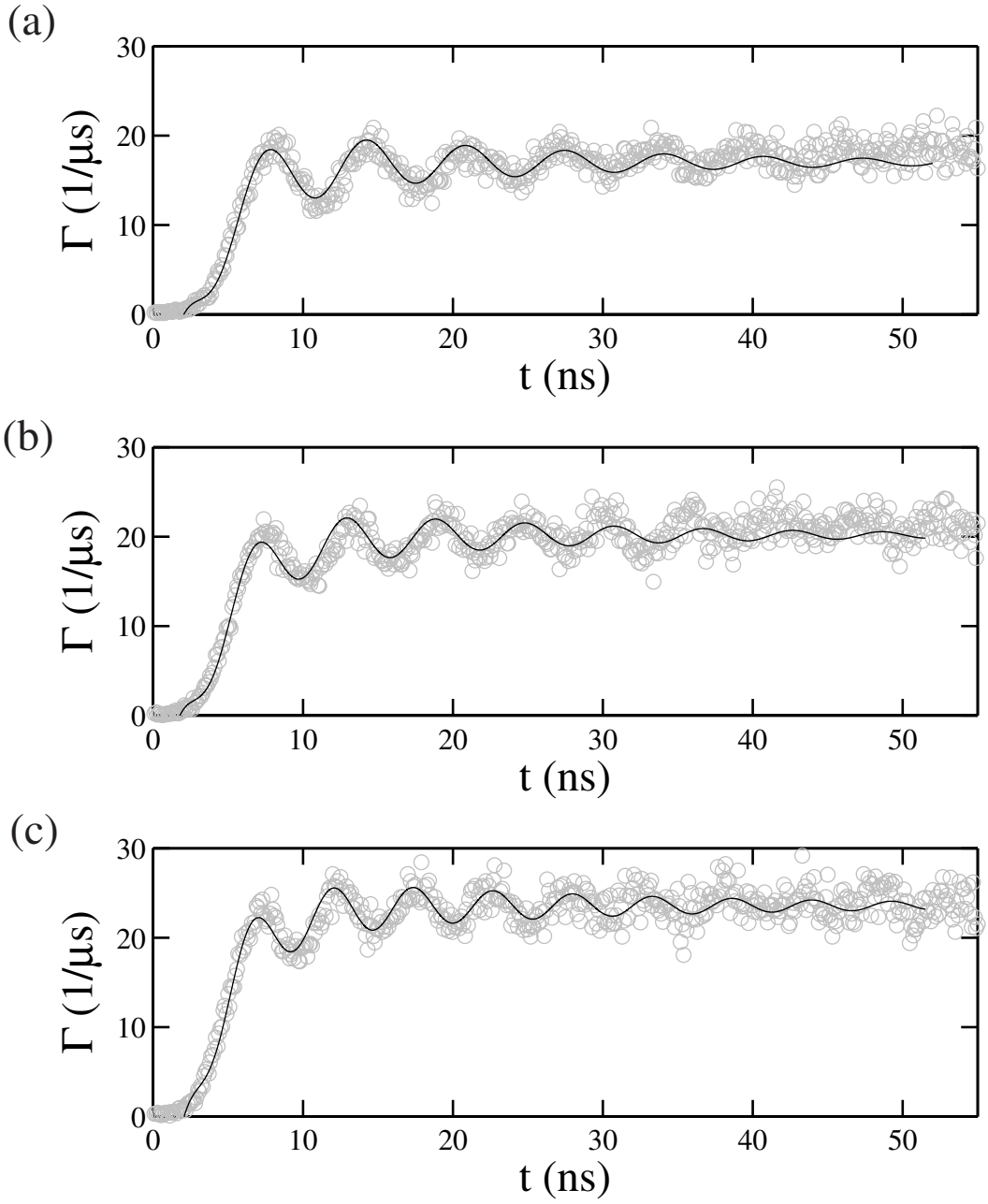

Figure 6.6: Rabi oscillations in the escape rate for device AL1 at 80 mK with $r_I = 1000$ (open circles). Solid curves show best fit to Eq. 6.8 for 7 GHz microwaves with power (a) P = 9 dBm, (b) P = 10 dBm, and (c) P = 11 dBm. Fitting parameters are listed in Table 6.1

Table 6.2: Summary of fitting parameters for Rabi oscillations in device AL1 at 80 mK with $r_I = 200$. The microwave power varies from 6 dBm to 11 dBm.

	6 dBm	7 dBm	8 dBm	9 dBm	10 dBm	11 dBm
t_0 (ns)	2.65	2.32	2.86	2.18	2.07	2.75
g_0 ($1/\mu$s)	3.31	3.13	3.28	3.31	3.31	3.89
g_1 ($1/\mu$s)	2.21	2.38	2.23	2.44	3.03	2.44
$\Omega/2\pi$ (MHz)	33.2	37.6	45.0	48.3	51.9	61.0
T′(ns)	26.9	27.2	32.5	32.3	23.0	25.3
g_2 ($1/\mu$s)	1.32	1.91	2.02	2.23	2.32	2.29
T_{back}(ns)	8.30	21.3	11.8	14.2	18.1	4.98

from $|2\rangle$ which was populated by noise-induced transitions. Since the escape rate from the second level is $\sim 10^3$ times higher than the escape level from the first level, even though $|2\rangle$ has less than 1 % population, its contribution to the total escape rate is significant. Inspection of Figs. 6.8, 6.9, 6.10 and 6.11 shows that the phenomenological function fits the data fairly well although these are obvious disagreements evident in Fig. 6.10. To obtain the best fit, I averaged the data over 200 ns for the P = 15 dBm, 16 dBm and 17 dBm data set, while I averaged the data over 300 ns for the other data sets. Thus the curves For P = 15 dBm, 16 dBm and 17 dBm data look more noisy. From the fits for $r_I = 200$, I find the average $T' \simeq$ 27.4 ns, which is somewhat longer than the 25 ns I found for $r_I = 1000$.

To summarize the above results on the Al dc SQUID phase qubit AL1, Rabi oscillations were measured using a 7 GHz microwave drive tuned on resonance to the $|0\rangle$ to $|1\rangle$ transition while we continuously monitored the escape rate. For a direct comparison, Fig. 6.12 shows Rabi oscillations for device AL1 at 80 mK using a 7 GHz microwave drive for $r_I = 1000$ [Fig. 6.12(a)] and for $r_I = 200$ [Fig. 6.12(b)]. Despite the $r_I = 200$ curve being about 5 times less isolated from current noise power, its decay envelope time constant $T' \simeq 36$ ns while the data set for $r_I = 1000$

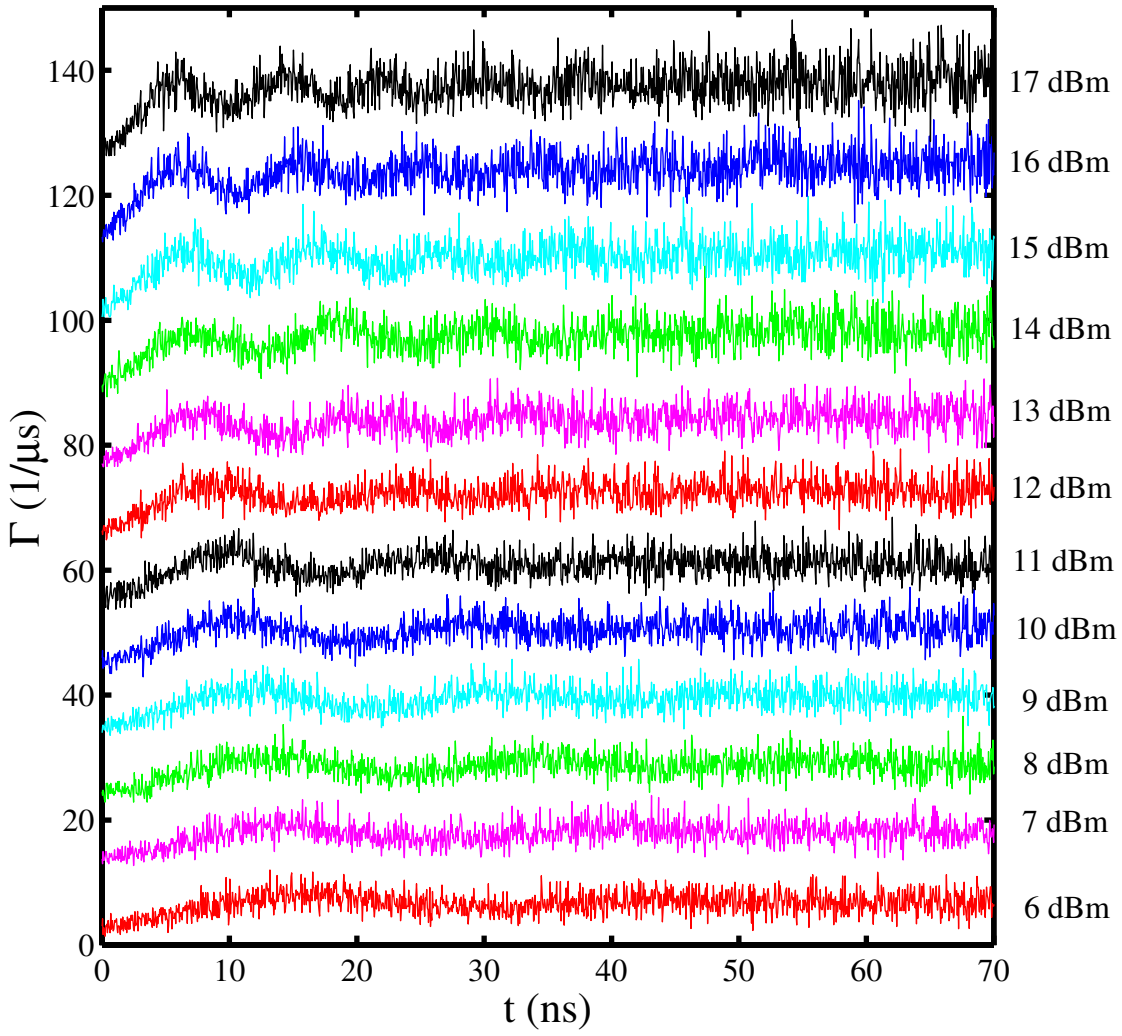

Figure 6.7: Rabi oscillations measured for the poorly isolated situation $r_I = 200$. Each Rabi oscillation curve was taken with 7 GHz microwaves applied, for power from 6 dBm to 17 dBm. Each successive curve was offset by about $10/\mu s$ for clarity.

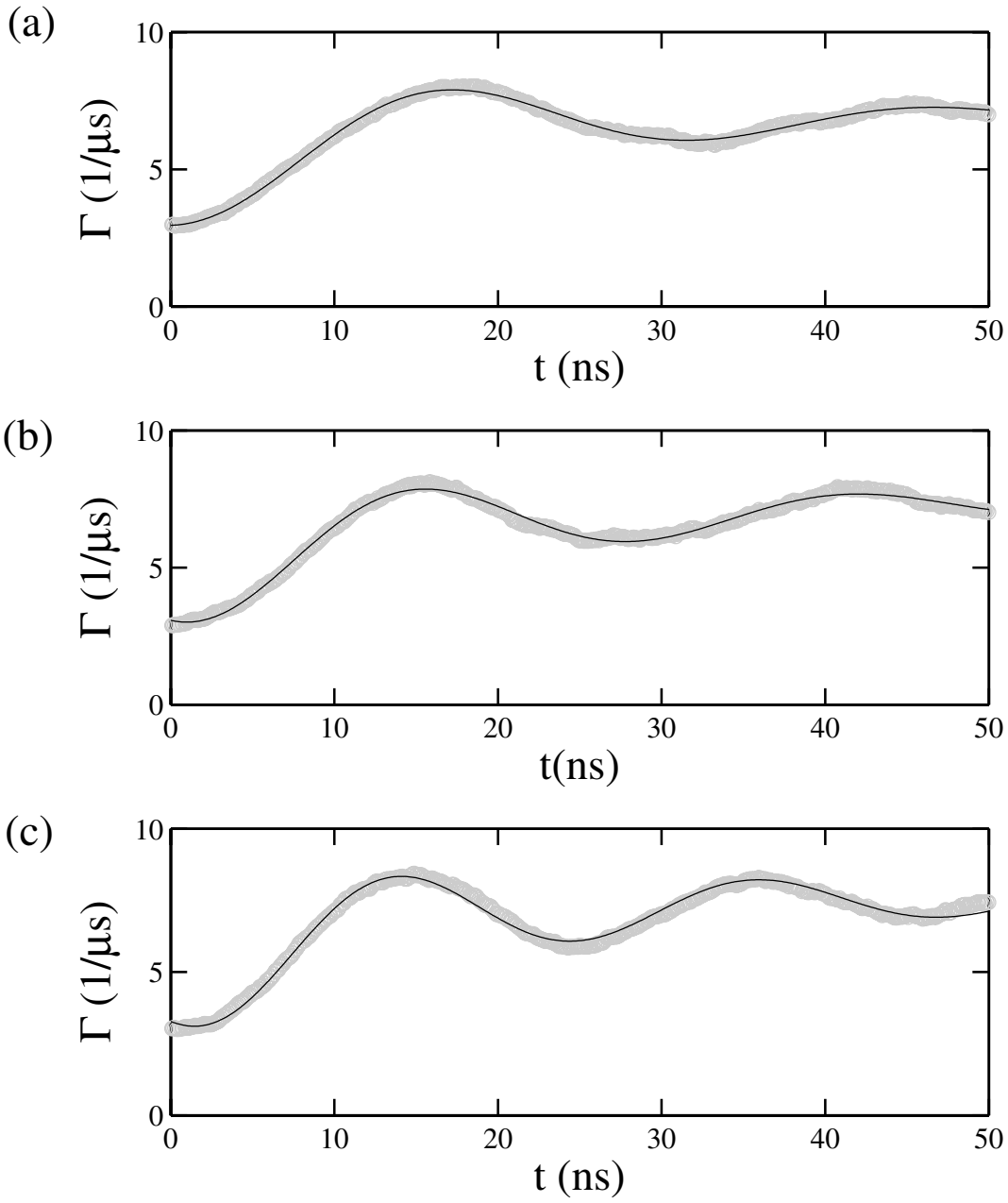

Figure 6.8: Rabi oscillations in the escape rate for device AL1 at 80 mK with $r_I = 200$ (open circles). Solid curves show best fit to Eq. 6.8 for 7 GHz microwave with power (a) P = 6 dBm, (b) P = 7 dBm, and (c) P = 8 dBm. Fitting parameters are listed in Table 6.2

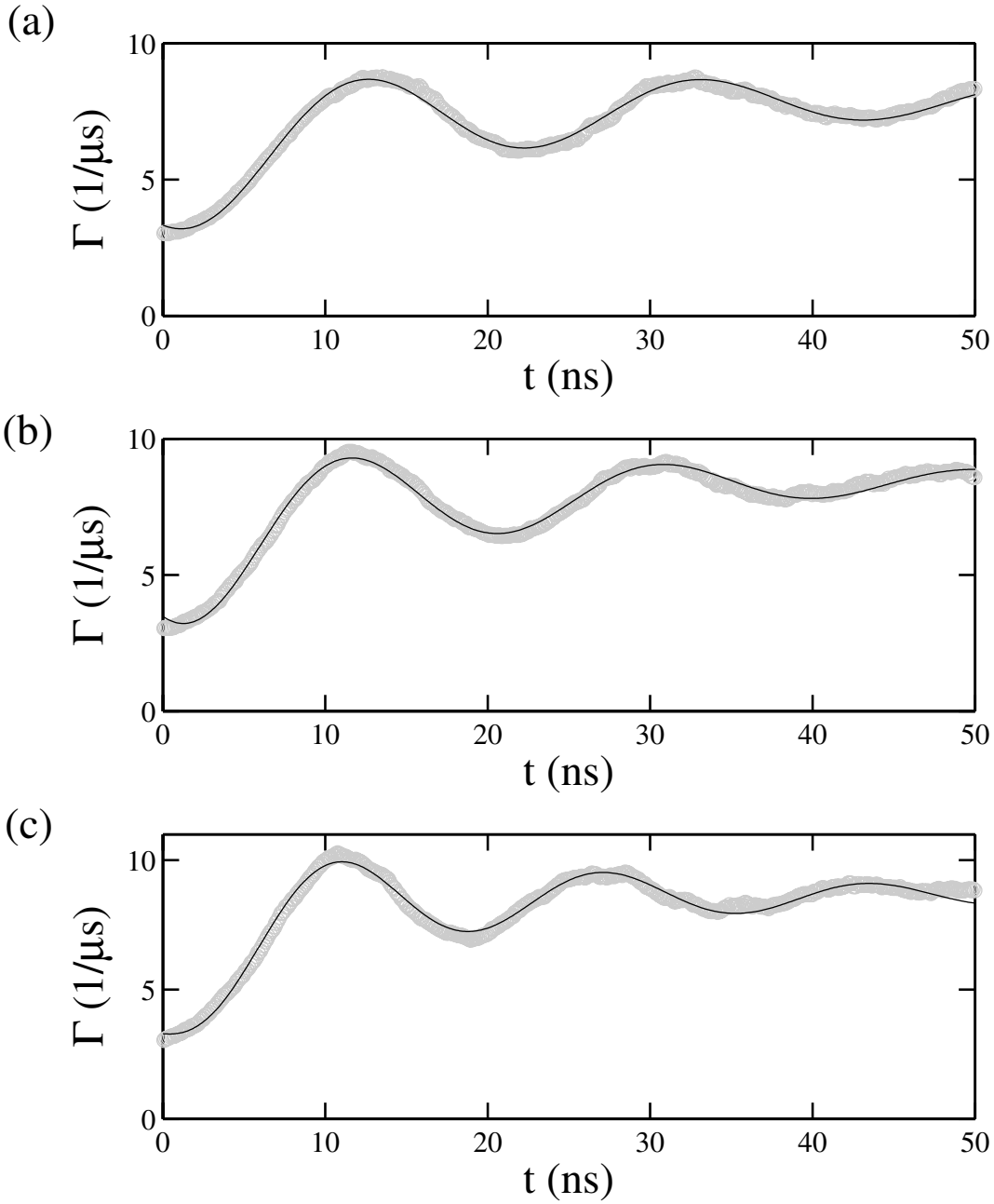

Figure 6.9: Rabi oscillations in the escape rate for device AL1 at 80 mK with $r_I = 200$ (open circles). Solid curves show best fit to Eq. 6.8 for 7 GHz microwave with power (a) P = 9 dBm, (b) P = 10 dBm, and (c) P = 11 dBm. Fitting parameters are listed in Table 6.2

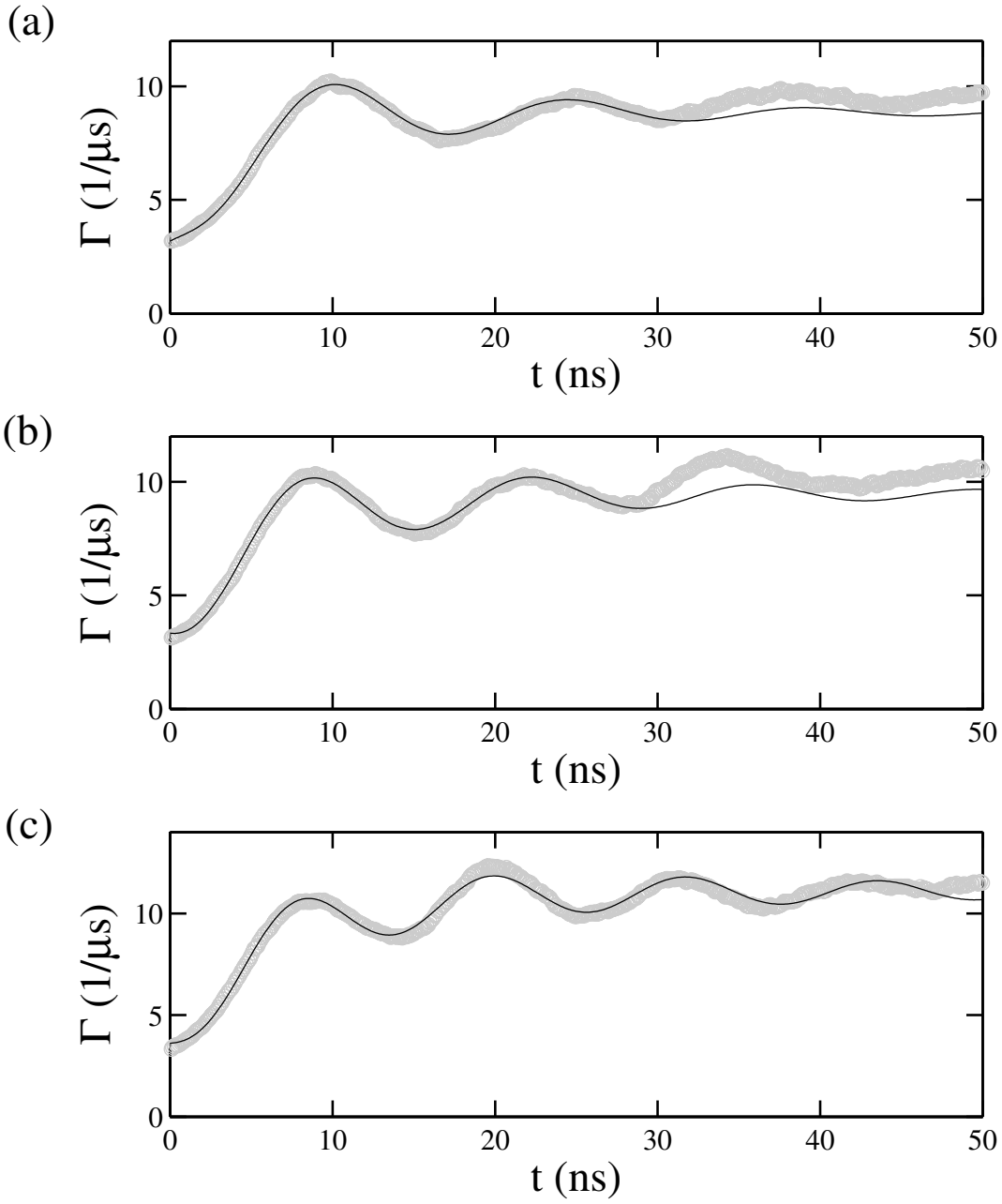

Figure 6.10: Rabi oscillations in the escape rate for device AL1 at 80 mK with $r_I = 200$ (open circles). Solid curves show best fit to Eq. 6.8 for 7 GHz microwave with power (a) P = 12 dBm, (b) P = 13 dBm, and (c) P = 14 dBm. Fitting parameters are listed in Table 6.3

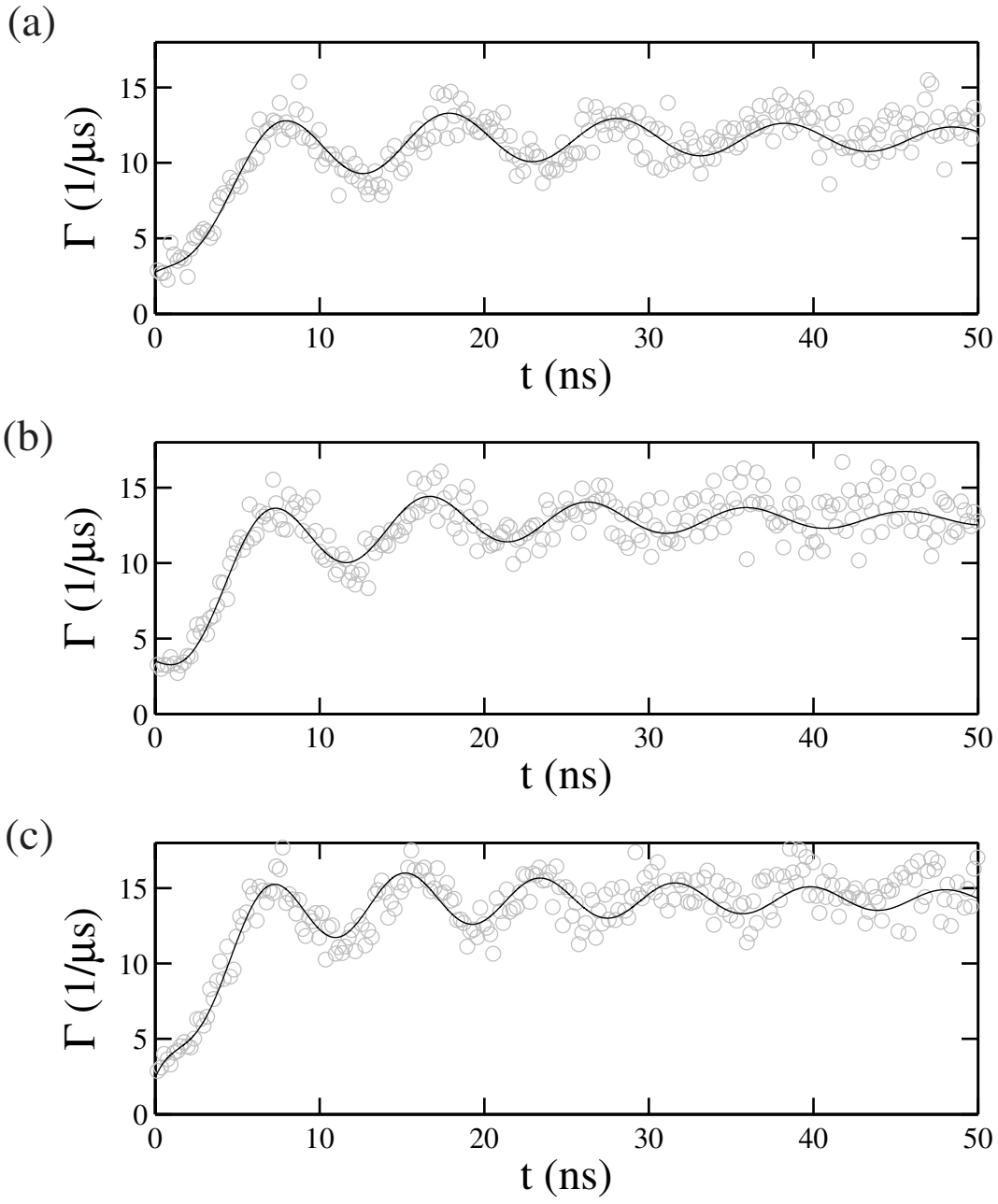

Figure 6.11: Rabi oscillations in the escape rate for device AL1 at 80 mK with $r_I = 200$ (open circles). Solid curves show best fit to Eq. 6.8 for 7 GHz microwave with power (a) P = 15 dBm, (b) P = 16 dBm, and (c) P = 17 dBm. Fitting parameters are listed in Table 6.3

Table 6.3: Summary of fitting parameters for Rabi oscillations in device AL1 at 80 mK with $r_I = 200$. The microwave power varies from 12 dBm to 17 dBm.

	12 dBm	13 dBm	14 dBm	15 dBm	16 dBm	17 dBm
t_0 (ns)	2.98	1.78	2.04	2.61	2.23	2.91
g_0 $(1/\mu s)$	4.55	3.82	4.39	4.45	4.08	6.08
g_1 $(1/\mu s)$	2.33	2.46	1.88	2.66	3.27	2.76
$\Omega/2\pi$ (MHz)	68.7	72.8	84.1	98.0	103	122
T′(ns)	15.5	19.3	32.2	36.4	23.1	30.9
g_2 $(1/\mu s)$	3.19	4.83	4.79	4.51	5.57	5.41
T_{back}(ns)	3.28	6.05	6.73	3.79	4.66	3.14

was fit using a decay envelope time constant $T' \simeq 28$ ns. Again, we see that the better isolated device did not have a larger Rabi decay time.

Figure 6.13 shows a summary of the analysis of my Rabi data, in which I plotted T′ vs. Rabi frequency for $r_I = 1000$ (crosses) and $r_I = 200$ (filled circles). The Rabi frequency is proportional to the square root of the microwave power, and there seems to be a weak tendency for Rabi oscillations measured at lower power to have longer T′. The average T′ for $r_I = 1000$ is 23.3 ns and for $r_I = 200$ is 27.4 ns. Needless to say, this is not the behavior one would expect if T′ was being limited by the bias leads.

6.4 T′ - comparison with a Nb device

S. K. Dutta observed much the same behavior in the Nb dc SQUID phase qubit NB1 [23]. Figure 6.14 shows Rabi oscillations that Dutta measured in NB1 at 25 mK with a 7.6 GHz microwave drive for $r_I = 1300$ [Fig 5(a)] and $r_I = 450$ [Fig 6.14(b)]. Fitting to Eq. 6.8 yields T′ = 12 ns for $r_I = 1300$ and T′ = 15 ns for r_I = 450.

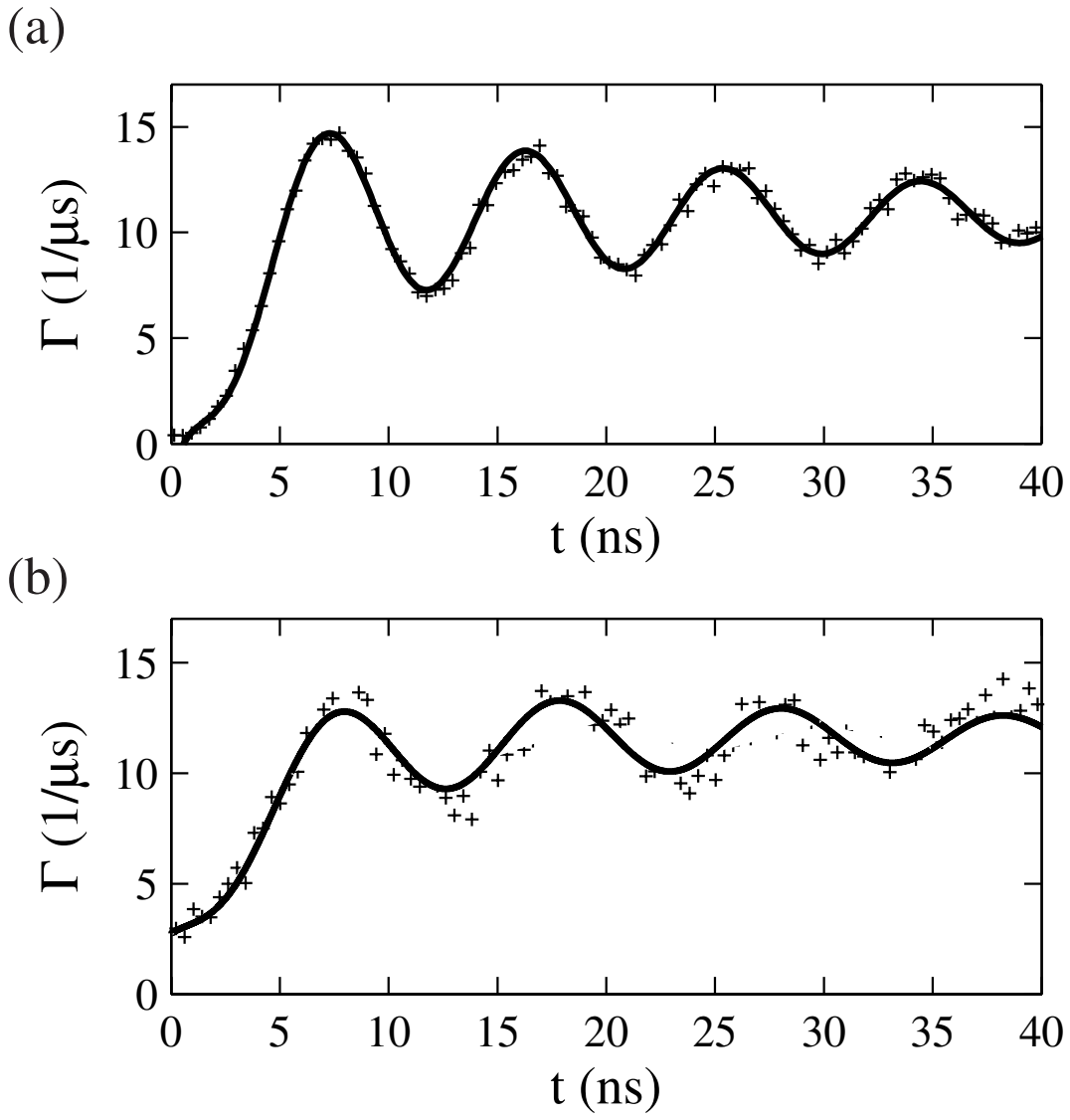

Figure 6.12: (a) Points show measured Rabi oscillations in device AL1 at 80 mK for $r_I(0)$ =1000, and (b) for $r_I(9.15\ \mu\text{A}) = 200$. Solid curves are phenomenological fits to the decay oscillation function shown in Eq. 6.8

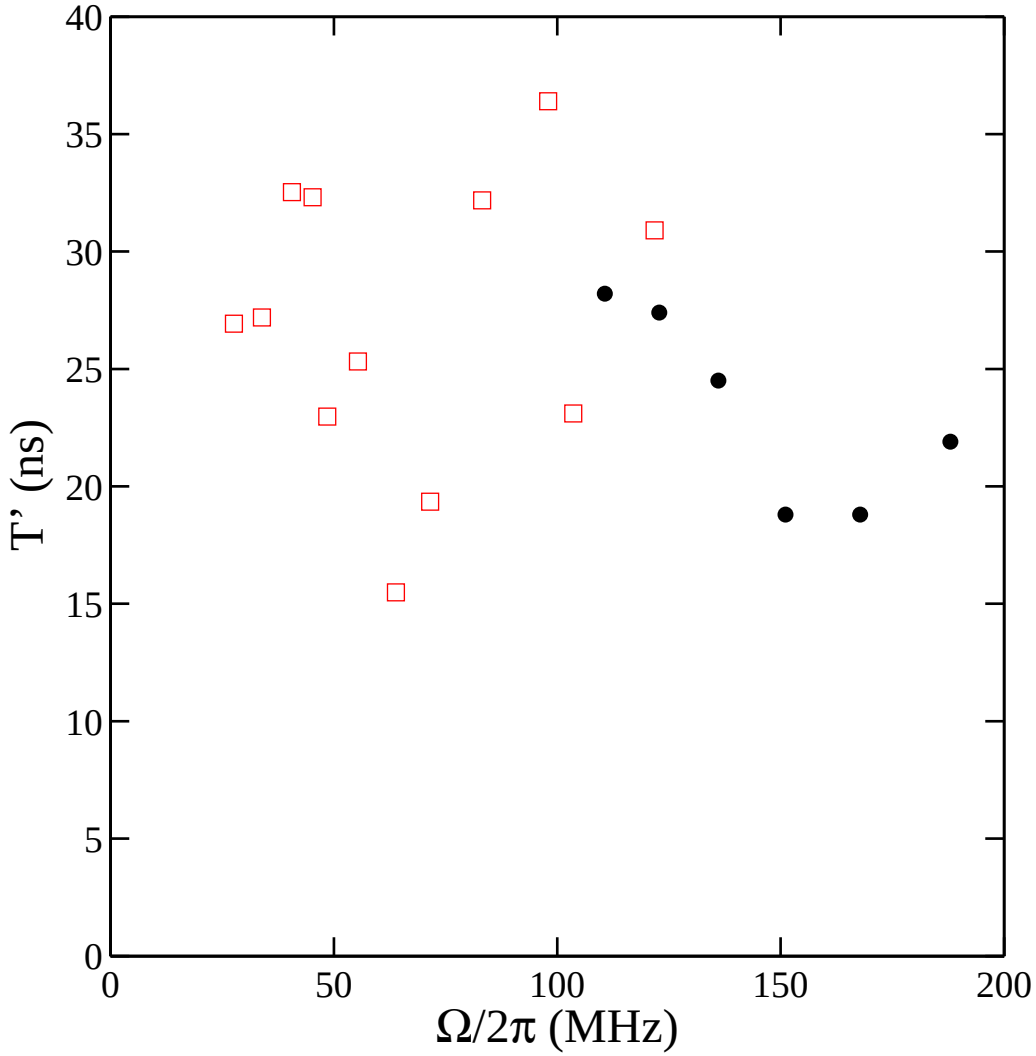

Figure 6.13: The decay time constant T' of Rabi oscillations vs. Rabi frequency $\Omega/2\pi$ of device AL1 measured at 80 mK at the most isolated biasing point, $r_I = 1000$ (filled circles) and at the poorly isolated biasing point (squares), $r_I = 200$.

Thus T' for this Nb device is also not scaling with isolation r_I. However, a remarkable fact here is that T' for AL1 was substantially longer than T' for NBl. This suggests that whatever was causing the decoherence may be dependent on materials used to build the device.

6.5 Spectroscopic coherence time T_2^* : comparison with a Nb device

I obtained the spectroscopic coherence time T_2^* from

$$T_2^* \equiv \frac{1}{2\pi\Delta f_{HWHM}} = \frac{dI}{df}\frac{1}{2\pi\Delta I_{HWHM}} \tag{6.9}$$

where (see also Chapter 4) ΔI_{HWHM} is the half width at half maximum of the $|0\rangle$ to $|1\rangle$ resonance peak, measured in the low power limit so that power-induced broadening was not apparent.

Figure 6.15 shows T_2^* in AL1 obtained from the spectroscopy data (see Fig. 4.19 in Chapter 4) at 80 mK. T_2^* varies from about 2 ns to 8 ns and the maximum T_2^* occurs at 7.3 GHz. The low values of T_2^* at 6.2 GHz to 6.7 GHz are likely due to tunneling [96] but the low values at 7.8 GHz were unexpected. Figure 6.16(a) shows T_2^* versus r_I for device AL1 at 80 mK with 7.45 GHz microwaves applied. T_2^* varies between a minimum of about 2.5 ns to a maximum of about 6.5 ns in an apparently random fashion with r_I. In particular, T_2^* does not show the systematic dependence on the isolation predicted in Eqs. 6.5 or 6.6. T_2^* versus r_I for device NB1 measured at 7.2, 7.3, 7.4, and 7.5 GHz at 25 mK, shows a similar random variation between about 3 and 6 ns [see Fig. 6.16(b)]. The average spectroscopic coherence time is about 4 ns for NB1. Also a closer look at Eq. 6.5 or 6.6 reveals that T_2^* should depend strongly on f_{01} if current or flux noise is the dominant factor. In contrast, the measured T_2^* does not show the expected strong dependence on frequency.

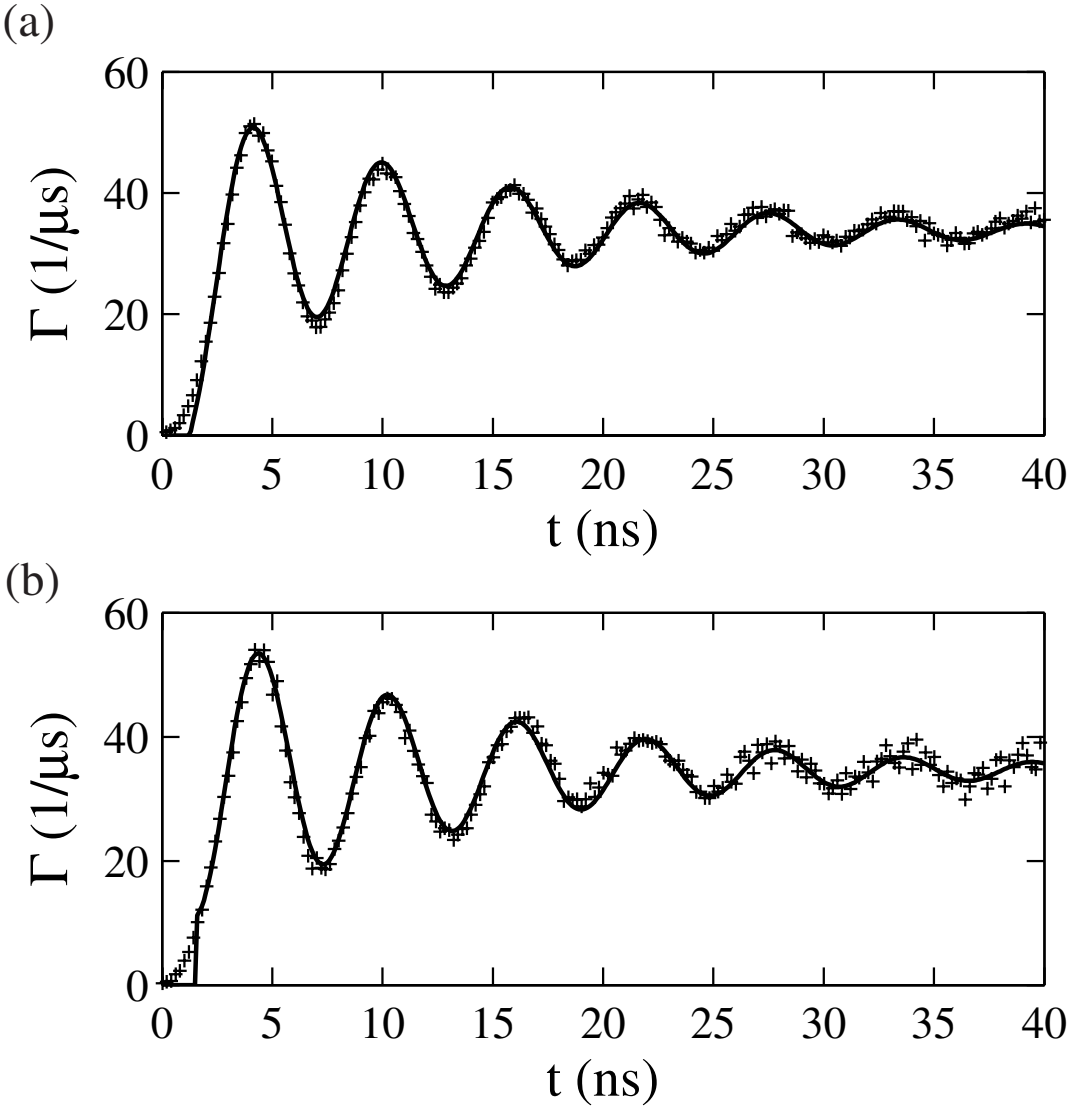

Figure 6.14: (a) Rabi oscillations in the escape rate Γ in device NB1 at 25 mK for (a) $r_I = 1300$ and (b) for $r_I = 450$ [23]. An 7.6 GHz drive was used.

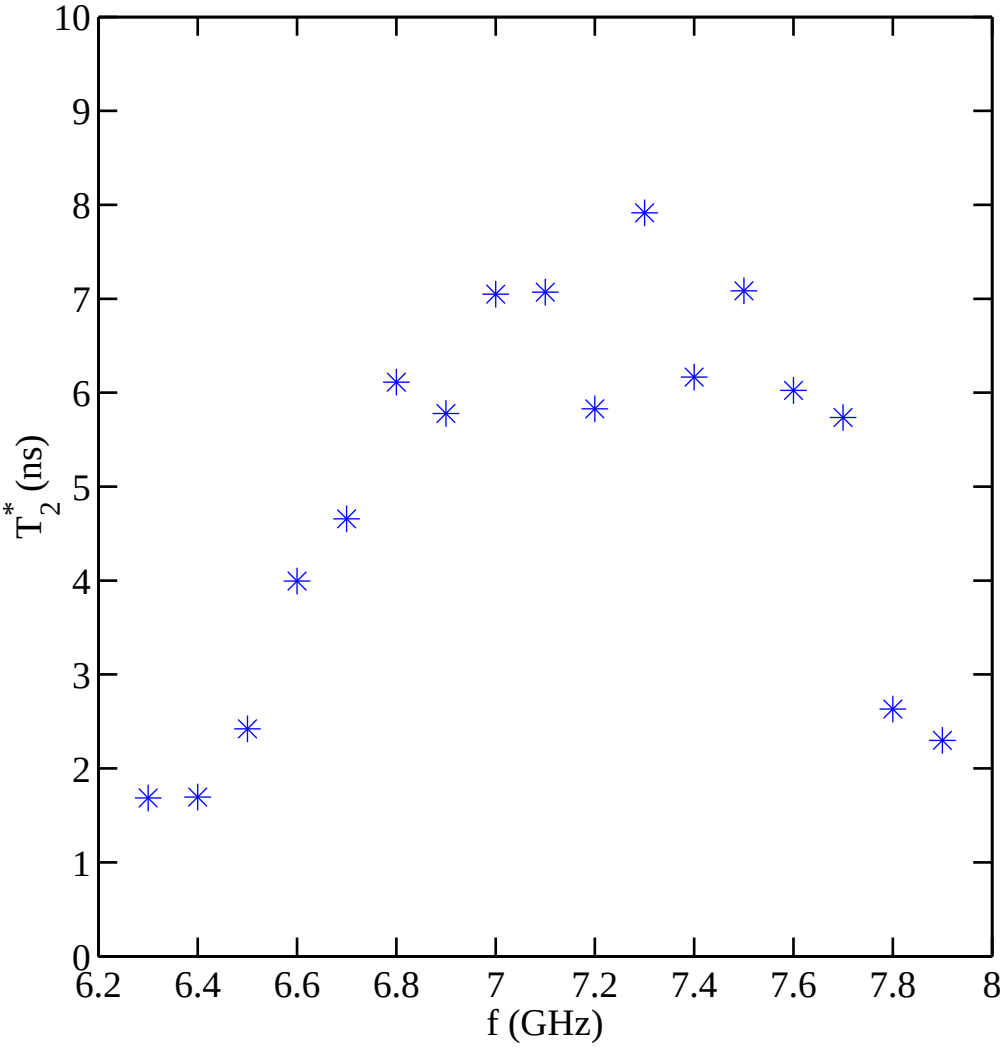

Figure 6.15: Spectroscopic coherence time T_2^* versus frequency for $r_I = 1000$ for device AL1 at 80 mK.

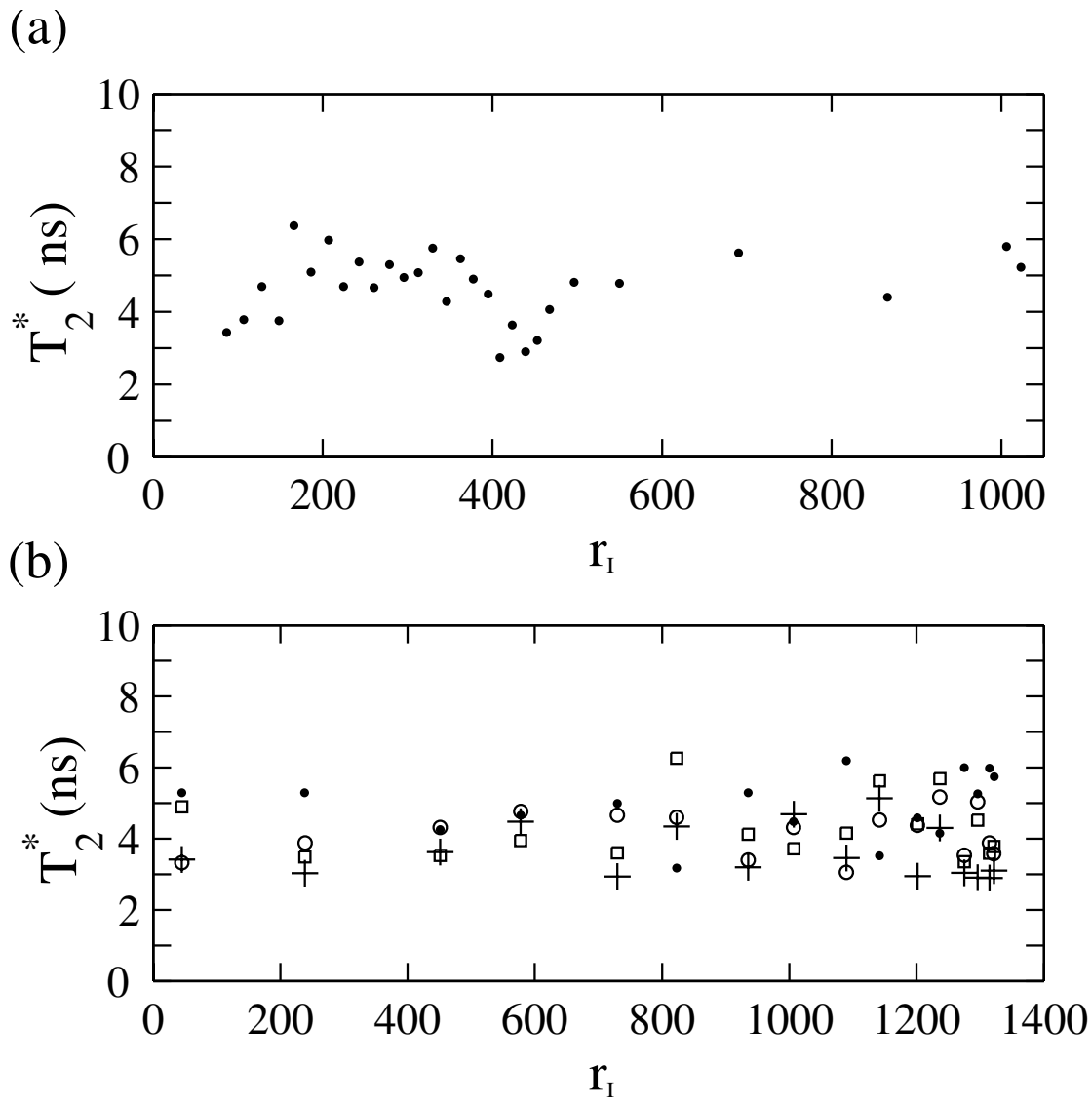

Figure 6.16: Spectroscopic coherence time T_2^* versus isolation factor r_I of (a) aluminum dc SQUID phase qubit AL1 measured at 7.45 GHz at 80 mK. (b) T_2^* for NB1 at 7.2 (crosses), 7.3 (open circles), 7.4 (squares) and 7.5 GHz (dots) at 25 mK.

6.6 Discussion

The fact that neither the spectroscopic coherence time nor the decay envelope of Rabi oscillations depends systematically on the isolation from the leads implies that the main source of decoherence is not current noise from the leads. It is also interesting that in both devices, T' is considerably larger than $2T_2^*$; For AL1, $T' = 27$ ns $> 2T_2^* \simeq 12$ ns and for NB1, $T' = 12$ to 15 ns $> 2T_2^* \simeq 8$ ns. This would be the case if we had significant inhomogeneous broadening of the spectrum caused by a local low-frequency noise source.

One possible source of decoherence in this system is spurious resonators or two-level fluctuators that reside in the substrate or dielectric layers [90, 49]. In particular, the fact that T' in AL1 was twice as long as in NB1 is consistent with the presence of two-level fluctuators in dielectric layers in NB1. AL1 had no insulation layers except for the thermally grown AlO_x tunnel barrier, native oxide on the exposed Al surfaces, and the thermally grown SiO_2 surface on the Si substrate, whereas NB1 had all of the above plus sputtered SiO_2 insulation layers. While we have not seen clear spurious resonator splittings (down to splittings of about 10 MHz) in spectroscopic data of AL1, S. K. Dutta found very small apparent splittings (10 MHz or less) in NB1 and other similar Nb SQUIDs from Hypres [23]. Another possible source of decoherence is local flux noise of unknown origin that has been found in other SQUIDs at millikelvin temperatures [97, 98]. However, this would have the same strong dependence on frequency as current noise. Since I did not find such a dependence, it suggests that flux noise is not the cause.

6.7 Conclusions

In conclusion, we have measured the spectroscopic coherence time T_2^* and the time constant T' for the decay of Rabi oscillations in dc SQUID phase qubits

with variable coupling to the leads. We found that varying the isolation by an order of magnitude produced no significant effect on either T_2^* or T'. However with comparable isolation, the aluminum qubit AL1 had a Rabi decay time that was two to three times longer than that of niobium device NB1 [23] with sputtered SiO_2 wiring layers. These results imply that the leads were not the dominant source for decoherence in these qubits. Instead, our data are consistent with a local source of decoherence.

Chapter 7

Comparison of coherence times in dc SQUID phase qubits

7.1 Introduction

Despite much recent progress in the use of superconducting devices for quantum computation [99], decoherence still presents a major challenge. Part of the problem is that there are many possible mechanisms that could cause decoherence and the picture of what is happening in real devices is still not entirely clear.

For Josephson phase qubits [47, 48, 89, 91, 100, 101, 102], Martinis *et al.* [49] have proposed that dielectric loss and two-level fluctuators in dielectrics are the primary cause of decoherence. They showed significant improvement could be obtained by replacing lossy dielectrics with lower-loss materials. This is now widely believed to be the dominant mechanism. Consistent with this, Van Harlingen *et al.* [103] argued that while critical current fluctuations would produce decoherence, the observed coherence times in flux and phase qubits were much shorter than would be expected from the level of critical current noise that has been typically observed in tunnel junctions [104, 105, 97]. Similarly, Martinis *et al.* [61] argued that charge noise should have a small impact on the coherence time of phase qubits due to their large junction capacitance. However in their dielectric loss paper [49], they argued that motion of charges was the dominant mechanism causing decoherence. In contrast, Bertet *et al.* reported that decoherence in their flux qubit came from the dc SQUID what was used to detect the flux state [46].

In principle, flux noise is another possible source of decoherence in phase qubits, as most are essentially rf or dc SQUIDs. In this chapter, I compare Rabi

oscillations and spectroscopic coherence times in three dc SQUID phase qubits. One device used a single-turn magnetometer configuration (AL1), the second had a multi-turn magnetometer configuration (NB1) and the third used a gradiometer configuration (NBG), respectively. Although we did not perform a direct test on the gradiometer balance, the counter-wound configuration should make it much less sensitive to spatially unform magnetic fields than either of the magnetometers.

7.2 dc SQUID phase qubits without and with gradiometer loops

Figure 7.1(a) shows a schematic of a dc SQUID phase qubit [47]. We refer to J1 as the qubit junction and J2 as the isolation junction. In this qubit design, junction J2 is needed to read out the state of J1 via tunneling to the voltage state [47]. J2 and inductor L_1 also inductively isolate the qubit from current noise on the bias leads. By choosing $L_1 \gg L_2 + L_{J2}$, where L_{J2} is the Josephson inductance of the isolation junction, current noise will be mainly diverted through the isolation junction J2 rather than the qubit junction J1.

Figures 7.1(b) and 7.1(c) show two of our SQUID phase qubits that have magnetometer loops. Device ALl is a single-turn dc SQUID magnetometer made from thin-film Al [see Fig. 7.1(b)]. We used photolithography and double-angle evaporation to form the loop and the Al/AlO_x/Al tunnel junctions (See Ch. 4). The qubit junction has an area of 80 μm^2. Other than AlO_x, no insulation layers were deposited on this device.

Device NB1 [see Fig. 7.1(c)] is a thin-film Nb magnetometer with a 6-turn loop. The device was made by Hypres, Inc., from a Nb/AlO_x/Nb trilayer using their 100 A/cm^2 process [78]. The qubit junction has an area of 100 μm^2 and was measured by S. K. dutta [23] *et al.*. He applied a small magnetic field in the plane of the junctions to reduce the critical current of the device to about 30 μA. Subsequent measurements on similar devices, which were not suppressed by

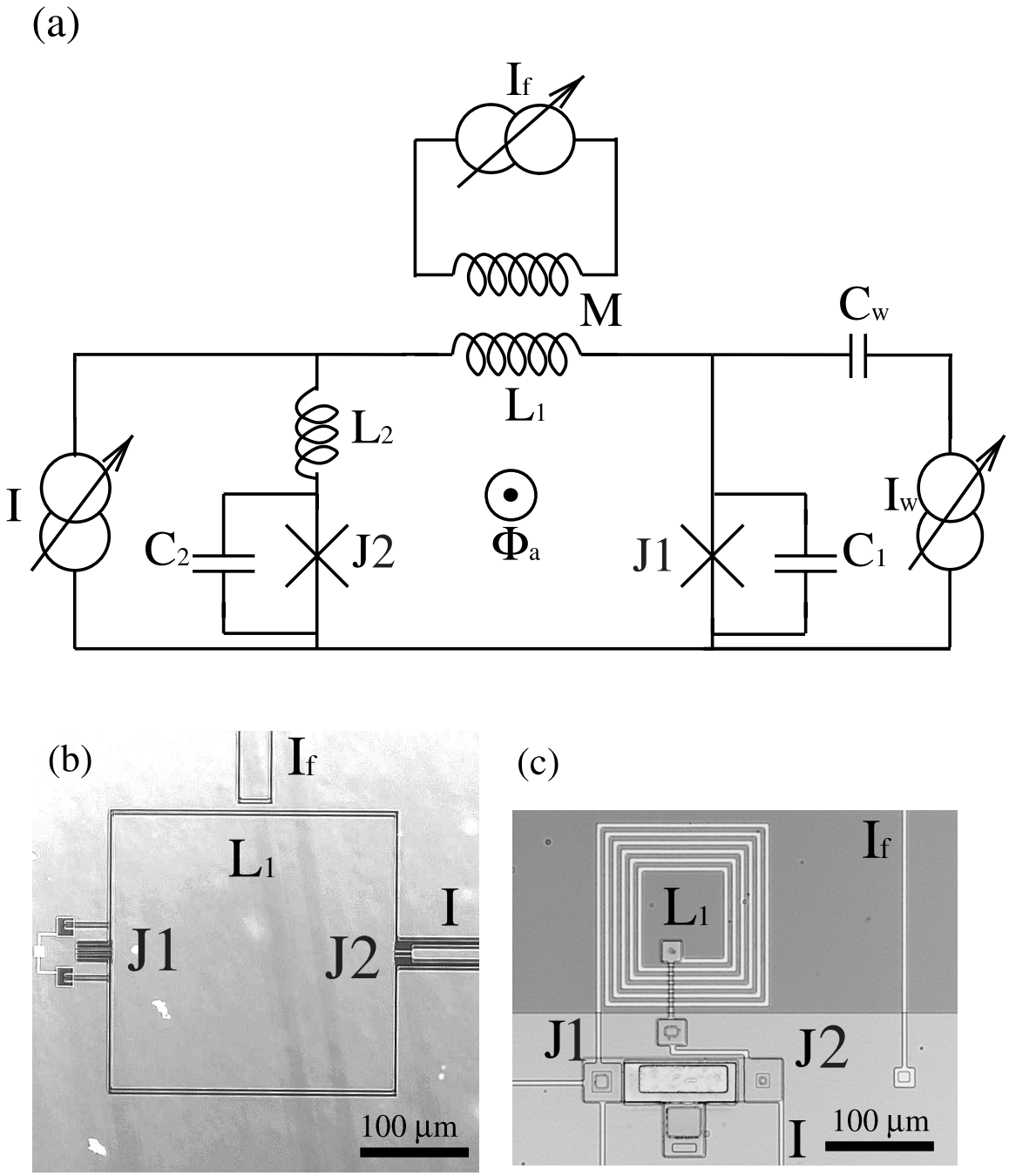

Figure 7.1: (a) Schematic of dc SQUID phase qubit. I is the bias current, I_f is current for the flux bias, M is mutual inductance between the flux bias coil and the SQUID loop and Φ_a is flux applied to the SQUID loop. C_1 and C_2 are the capacitances of the qubit junction J1 and the isolation junction J2, respectively. Microwave source I_w is coupled to J1 through capacitor C_w. Photographs of (b) single-turn aluminum SQUID magnetometer AL1 and (c) 6-turn niobium SQUID magnetometer NB1.

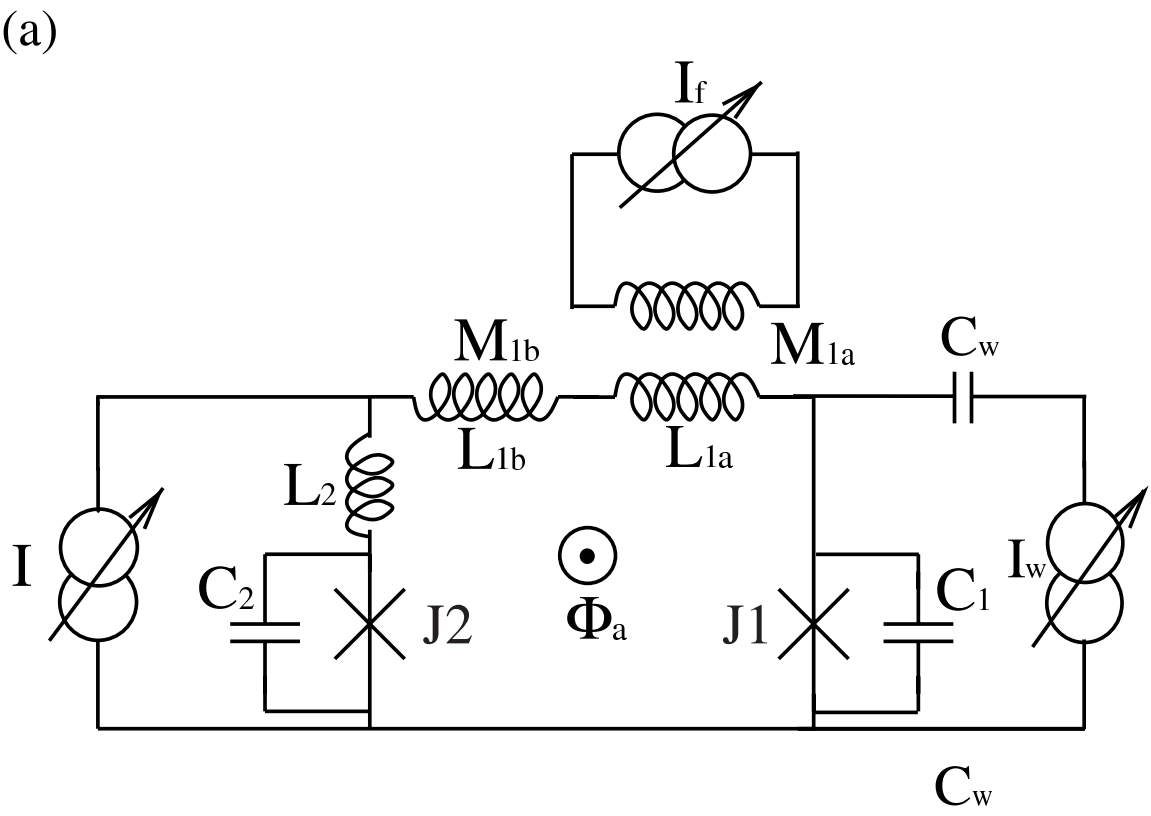

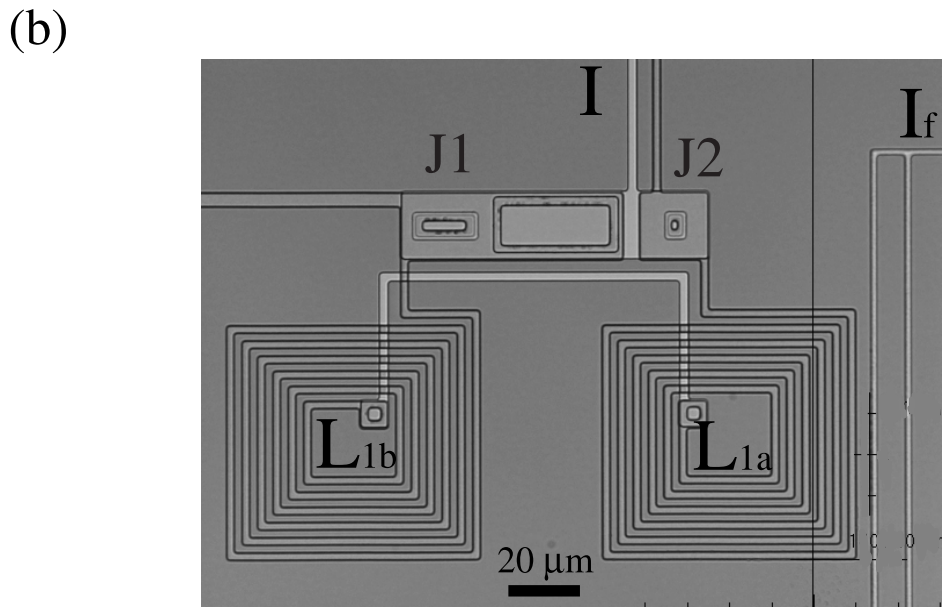

Figure 7.2: (a) Schematic of dc SQUID phase qubit with a gradiometer loop. I is the bias current, I_f is current for the flux bias, Φ_a is the applied flux in the SQUID loop. C_1 and C_2 are the capacitances of junctions J1 and J2. L_{1a} and L_{1b} are inductances of each coil of the gradiometer, M_{1a} and M_{1b} are mutual inductances between each coil, and the flux bias line. Microwave source I_w is coupled to J1 through capacitor C_w. (b) Photograph of dc SQUID phase qubit, gradiometer NBG.

Table 7.1: Parameters for SQUIDs NBG, NB1 and AL1. I_{01} and I_{02} are the critical currents of J1 and J2, respectively. $L_{j1}(0)$ and $L_{j2}(0)$ are the Josephson inductances of J1 and J2 when they are unbiased and $\beta = (I_{01} + I_{02})L/\Phi_0$, where $L = L_1 + L_2$ is the total inductance of the SQUID loop.

	gradiometer	magnetometer	magnetometer
Parameters	NBG	NB1	AL1
I_{01} (μA)	23.0	33.8	21.275
I_{02} (μA)	3.8	4.8	9.445
C_1 (pF)	4.1	4.4	4.1
C_2 (pF)	2.0	2.2	2.1
$L_{j1}(0)$ (pH)	13.9	9.7	13.2
$L_{j2}(0)$ (pH)	84.9	68	44.5
L_1 (pH)	4540	3530	1236
L_2 (pH)	12	20	5
β	34	66	19

magnetic field, yielded similar spectroscopic coherence times and Rabi decay times [23].

Device NBG (see Fig. 7.2) was made by Hypres from a Nb/AlO_x/Nb trilayer using their 30 A/cm^2 process. The qubit junction has an area of 100 μm^2. The SQUID has two 6-turn thin-film Nb coils wound in opposition to form a magnetic field gradiometer. To apply a net flux to the device, we placed a flux bias line on the right side of the device (closer to coil L_{1a} than to L_{1b} in Fig. 2). All three devices were made on silicon wafers with a layer of thermally grown silicon dioxide. Table 7.1 summarizes the devices parameters of AL1, NB1 and NBG.

7.3 Measurement of energy levels of NBG

The experimental procedures were discussed in Chapter 4 but here I review them again briefly. Before making any measurements on a SQUID, I used a flux

shaking technique to initialize the flux state [86]. I then applied a simultaneous flux and current ramp to bias the qubit junction with current, and not the isolation junction. With this biasing scheme, junction J1 acts as an ideal phase qubit with the two lowest levels in a well of the tilted washboard potential forming the qubit states $|0\rangle$ and $|1\rangle$.

I monitored the qubit state by measuring the rate at which the system tunnels to the voltage state [47]; the first excited state $|1\rangle$ typically tunnels about 500 times faster than the ground state $|0\rangle$. During the simultaneous current and flux ramp, I recorded the time at which the device escapes to the voltage state. I repeated this process on the order of 10^5 times to build up a histogram of escape events versus ramp time, which I then converted to escape rate versus current (for spectroscopy) or escape rate versus time (for Rabi oscillations).

As an example, Fig. 8.19 shows the total escape rate of the qubit junction in device NBG as a function of the bias current I, with and without application of 6.6 GHz microwaves. Sweeping current through the qubit changes the energy level spacing adiabatically. When the microwaves come into resonance with the energy level spacing, transitions to the excited state occur and we see enhancement in the total escape rate. In Fig 8.19, two clear resonance peaks are visible, at around 21.57 μA and 21.62 μA, corresponding to $|1\rangle \rightarrow |2\rangle$ and $|0\rangle \rightarrow |1\rangle$ transitions.

I measured the microwave response from 5.5 GHz to 8 GHz and fit the resonance peaks with a Lorentzian function to extract the peak locations and the half-widths. Figure 7.4 shows the spectrum of $|0\rangle$ to $|1\rangle$ transitions (circles), two-photon $|0\rangle$ to $|2\rangle$ transitions (squares) and $|1\rangle$ to $|2\rangle$ transitions (stars). I fit the spectra to a calculated single Josephson junction spectrum and found good agreement with data (see Fig. 7.4). The best fit to the spectrum yields the qubit junction critical current $I_{01} = 21.7969$ μA and the capacitance $C_1 = 4.18$ pF.

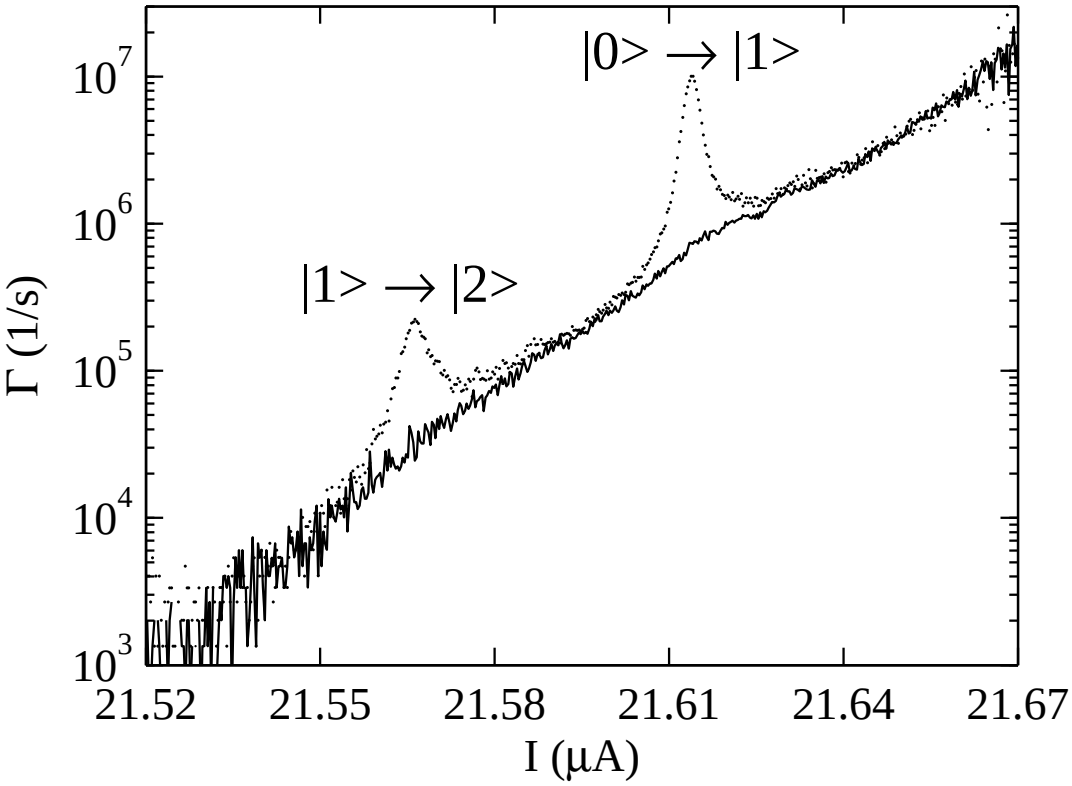

Figure 7.3: Total escape rate Γ vs. current I_1 for device NBG at 80 mK. Dotted line is when 6.6 GHz microwaves are applied to the qubit junction and solid line is without microwaves. Two prominent peaks are seen when microwaves are applied, corresponding to the $|0\rangle$ to $|1\rangle$ transition and the $|1\rangle$ to $|2\rangle$ transition.

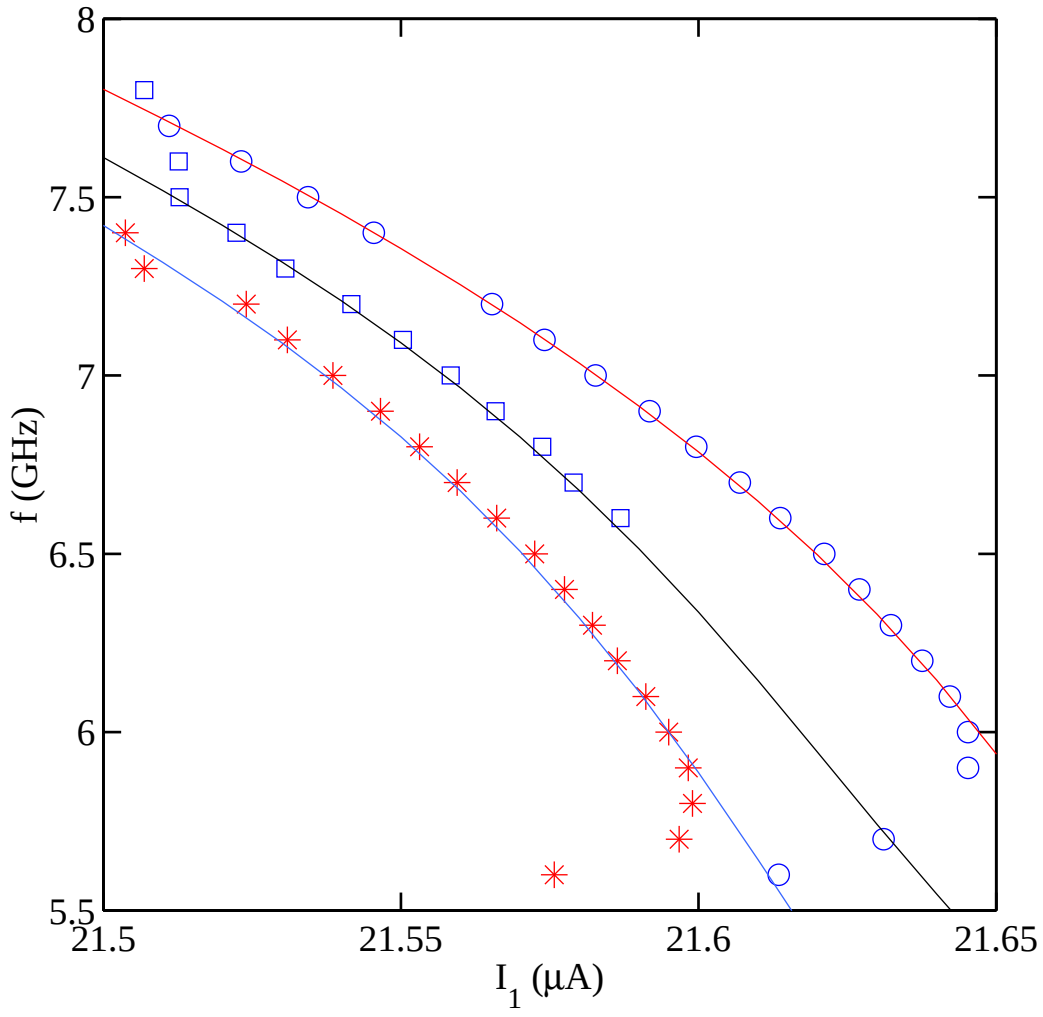

Figure 7.4: Resonance frequency vs. current for NBG at 80 mK. Circles are $|0\rangle$ to $|1\rangle$ transition data, squares are two-photon $|0\rangle$ to $|2\rangle$ transition data and stars are $|1\rangle$ to $|2\rangle$ transition data. Solid curves are from best fit to the energy spectrum of a single Josephson junction.

7.4 Measurement of T_1

To determine T_1 on the gradiometer dc SQUID qubit NBG, I performed a relaxation measurement. Figure 7.5 shows the decaying escape rate due to relaxation. For this measurement, I applied resonant 6.6 GHz microwaves and then shut off the microwaves while monitoring the escape rate. I fit the resulting escape rate data to a decaying exponential function (as discussed in Chapter 5):

$$f(t) = A\exp[-t/t_0] + B\exp[-t/t_1] + C\exp[-t/t_2]. \tag{7.1}$$

Using the χ^2 method, I obtained a best fit with $T_1 \sim t_1 = 62$ ns. The other fitting parameters are shown in Table 7.2. It is interesting that the fitting parameters were very similar to those of AL1 shown in Table 7.3, even though the two samples are quite different in their materials and design. This may support the possibility that the decay measured in this type of relaxation experiment may not be due to relaxation from $|1\rangle$ to $|0\rangle$ of the qubit junction, but instead by due to unrelated physical process. Or course both AL1 and NBG have $Al/AlO_x/Al$ tunnel barriers, and this may be what is determining the relaxation.

As a check on T_1, I also measured the thermally induced escape rate (See Fig. 7.6). To determine T_1, I fit the data using a stationary 4-level master equation simulation. The fitting was done with a χ^2 fit (described in Ch. 5), and the best fit parameters were $T_1 = 20$ ns and T = 85 mK. As I found for device AL1, $T_1 \simeq 20$ ns as determined from the escape rate'fit is significantly shorter than $T_1 \simeq 50$ ns from the relaxation measurement.

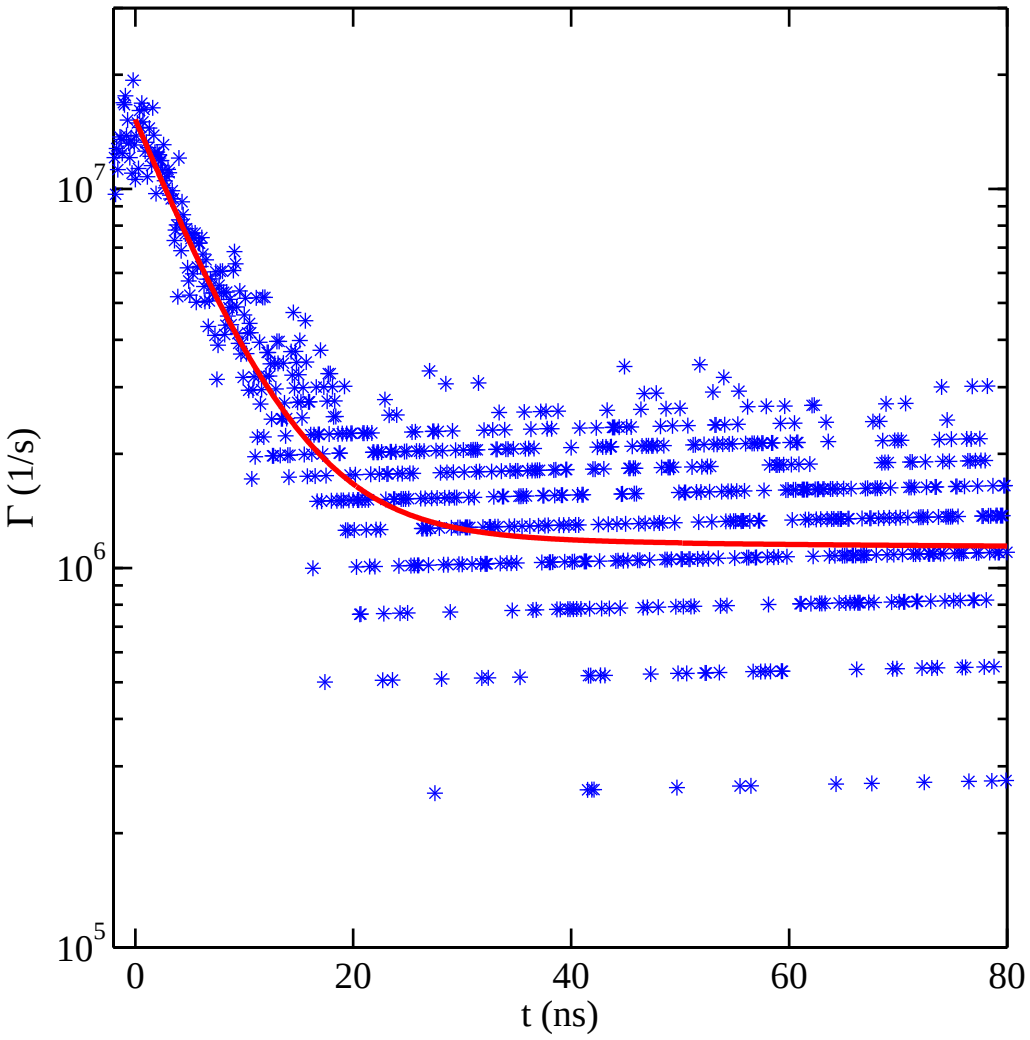

Figure 7.5: Observed relaxation in the escape rate for NBG at 80 mK. Asterisk points show measured escape rate. The solid curve is the χ^2 fits to the three exponential functions in Eq. 7.1. This relaxation measurement was done with 6.6 GHz high power microwaves (P = 12 dBm) after measuring Rabi oscillations.

Table 7.2: Parameters for best fit of Eq. 7.1 to the data in Fig. 7.5 for device NBG.

Parameters	A $(1/\mu s)$	B $(1/\mu s)$	C $(1/\mu s)$	t_0 (μ s)	t_1 (ns)	t_2 (ns)
6.6 GHz	1.114	0.104	14.03	188.1	62.1	5.908

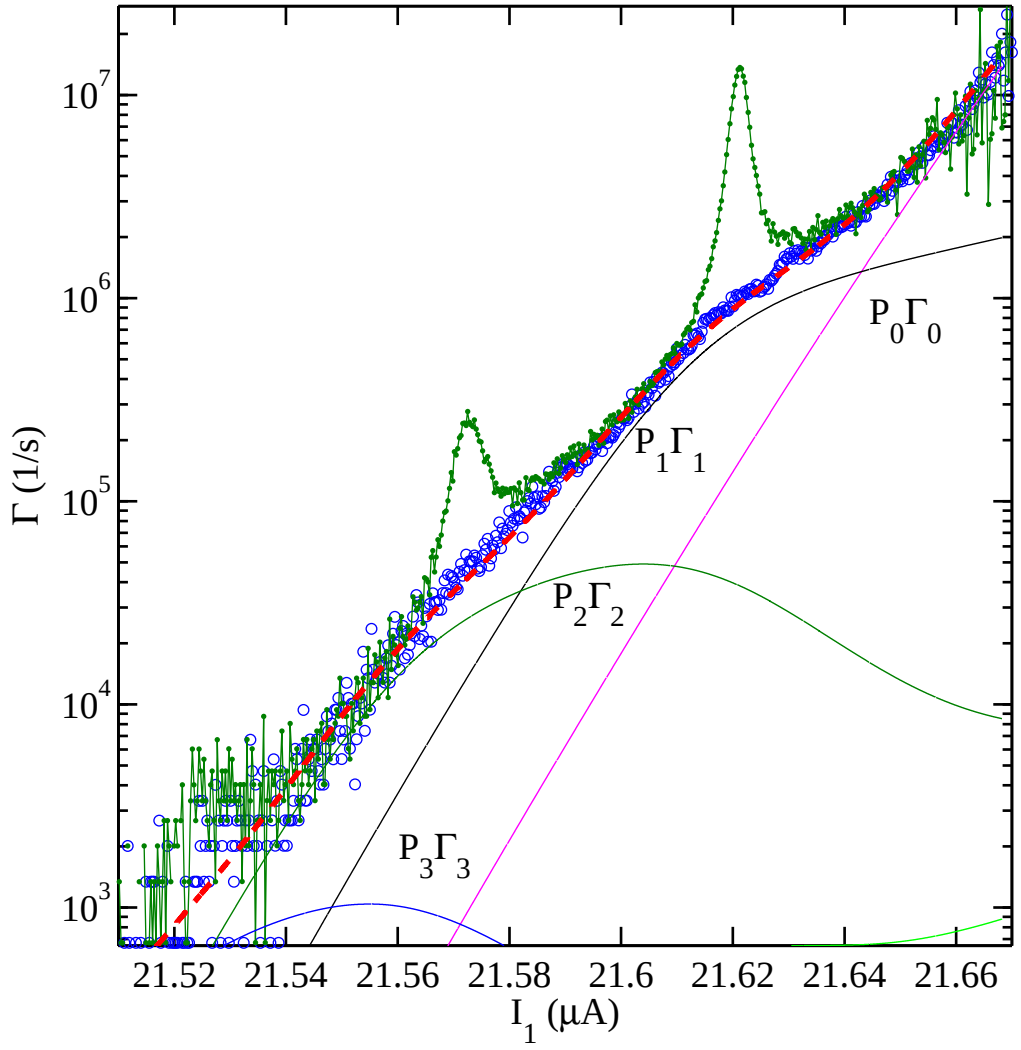

Figure 7.6: Total escape rate Γ versus current I_1 for qubit NBG at 80 mK. Crosses show the background escape rate and the solid curve with dots are the escape rate when 6.5 GHz microwaves are applied. Three peaks indicate $|0\rangle$ to $|1\rangle$ transition at I = 21.62 μA, $|1\rangle$ to $|2\rangle$ transition at I = 21.57 μA, and $|2\rangle$ to $|3\rangle$ transition at I = 21.52 μA. The dashed curve is from a stationary 4-level master equation simulation. The thin solid curves show the components of the total escape rates, $P_i\Gamma_i$, the probability of each level multiplied by the escape rate of the each level. The simulation parameters are T_1 = 20 ns and T = 85 mK.

Table 7.3: Parameters for best fit of Eq. 5.40 to the data in Fig. 5.16 and Fig. 5.17 for device AL1.

Parameters	A $(1/\mu s)$	B $(1/\mu s)$	C $(1/\mu s)$	t_0 (μ s)	t_1 (ns)	t_2 (ns)
r = 1000 P = -20 dBm	0.264	0.902	0.037	188.1	52.34	5.002
r = 1000 P = -10 dBm	0.252	2.617	0.494	188.1	60.71	4.544
r = 220 P = 12 dBm	0.519	2.661	8.355	188.1	59.29	5.004

7.5 Measurement of T_2^*

To determine the spectroscopic coherence time T_2^* [95] of the $|0\rangle \rightarrow |1\rangle$ transition, I obtained the low-power half-width at half-maximum ΔI of the resonance peak and recorded its location I(f_{01}). It is important to use low-power microwaves because of power broadening; the peak width increases steadily with power above a certain level determined by T_1, T_2 and inhomogeneous broadening. Repeating this procedure for a range of applied microwave frequencies yields f_{01} and ΔI_1 as a function of I_1. The spectroscopic coherence time as a function of the frequency was then found from (see Chapter 4)

$$T_2^* = \frac{dI_1}{df_{01}} \frac{1}{2\pi\Delta I_1}. \tag{7.2}$$

The half-width at half-maximum ΔI_1 can be obtained by fitting the resonance peaks with a Lorentzian function. With the measured df_{01}/dI_1 from spectroscopy, T_2^* can then be evaluated.

Figure 7.7 shows a plot of T_2^* versus microwave frequency for gradiometer NBG, measured at 100 mK. For frequencies in the 6.0 GHz to 7.2 GHz range, T_2^* varied between about 4 ns and 8 ns. Spectroscopic measurements on magnetometers NB1 and AL1 revealed comparable variations in T_2^*, from about 4 to 10 ns in the

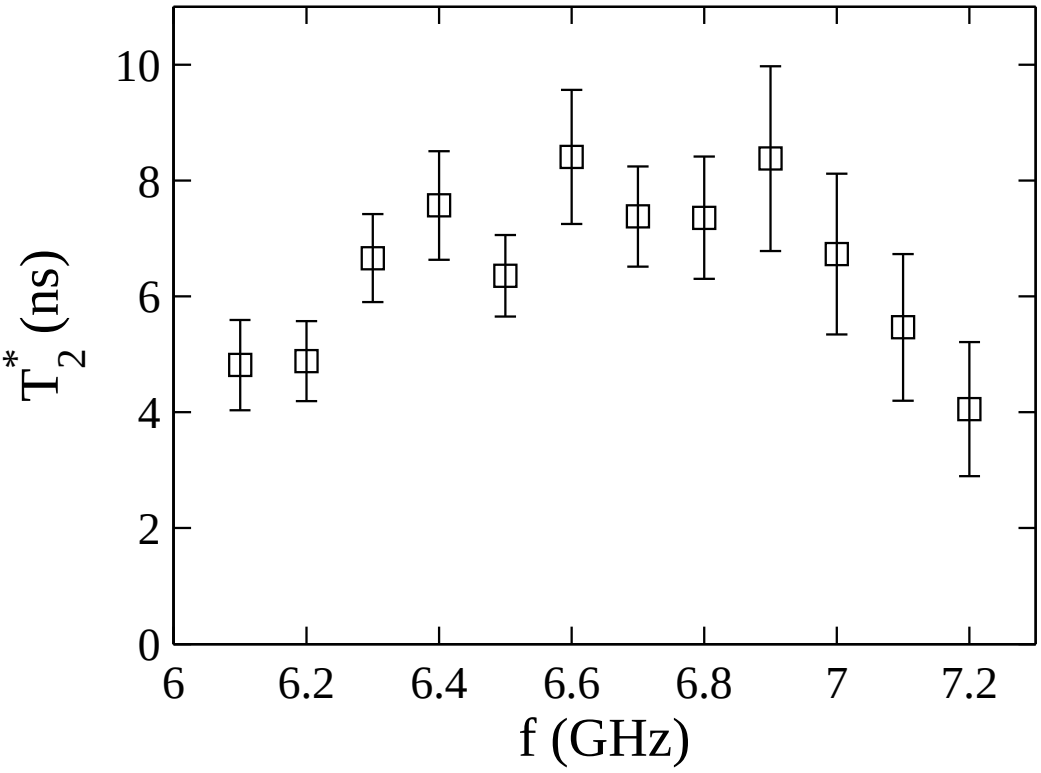

Figure 7.7: Spectroscopic coherence time T_2^* of the $|0\rangle$ to $|1\rangle$ transition versus frequency for SQUID gradiometer NBG measured at 80 mK.

same frequency range [23] (see Chapter 6). Since T_2^* is sensitive to low-frequency noise (inhomogeneous broadening), as well as pure dephasing and dissipation [95], we can conclude that the combined effect of low-frequency noise, pure dephasing and dissipation is comparable in the three devices.

7.6 Rabi oscillations in gradiometer NBG and comparison with magnetometers AL1 and NB1

I measured Rabi oscillations on resonance in NBG at 80 mK using microwaves with frequencies of 6.5 GHz, 6.6 GHz, 6.7 GHz, 6.8 GHz, and 6.9 GHz. Figure 7.8 shows the measured Rabi oscillations (dots) and the best fit curves (solid curves). I used a χ^2 fit to the decaying oscillation function given by (see Ch. 6)

$$\Gamma_{fit} = g_0 + g_1(1 - e^{-(t-t_0)/T'}\cos(\Omega\{1 - t_0\})) + g_2(1 - e^{-(t-t_0)/T_{back}}). \qquad (7.3)$$

My fits revealed that the decay time T' varied from 8 ns to 13 ns as I changed the microwave frequency. However, there was no systematic dependance on the microwave frequency. Table 7.4 summarizes the decay time constants from the χ^2 fits. The square of the Rabi frequency showed a linear dependence on the microwave power (see Fig. 7.9), as expected.

Measurements of Rabi oscillations allow one to distinguish the effects of low-frequency noise from dephasing processes. The idea is that the envelope decay time constant T' of a Rabi oscillation is sensitive to noise at the Rabi frequency while the main effect of noise at much lower frequencies (which acts like inhomogeneous broadening) is to change the shape of the envelope [61, 103]. This relative insensitivity of the Rabi oscillations to low-frequency noise is similar to the situation in a spin-echo measurement [61]. The envelope decay time constant T', the energy

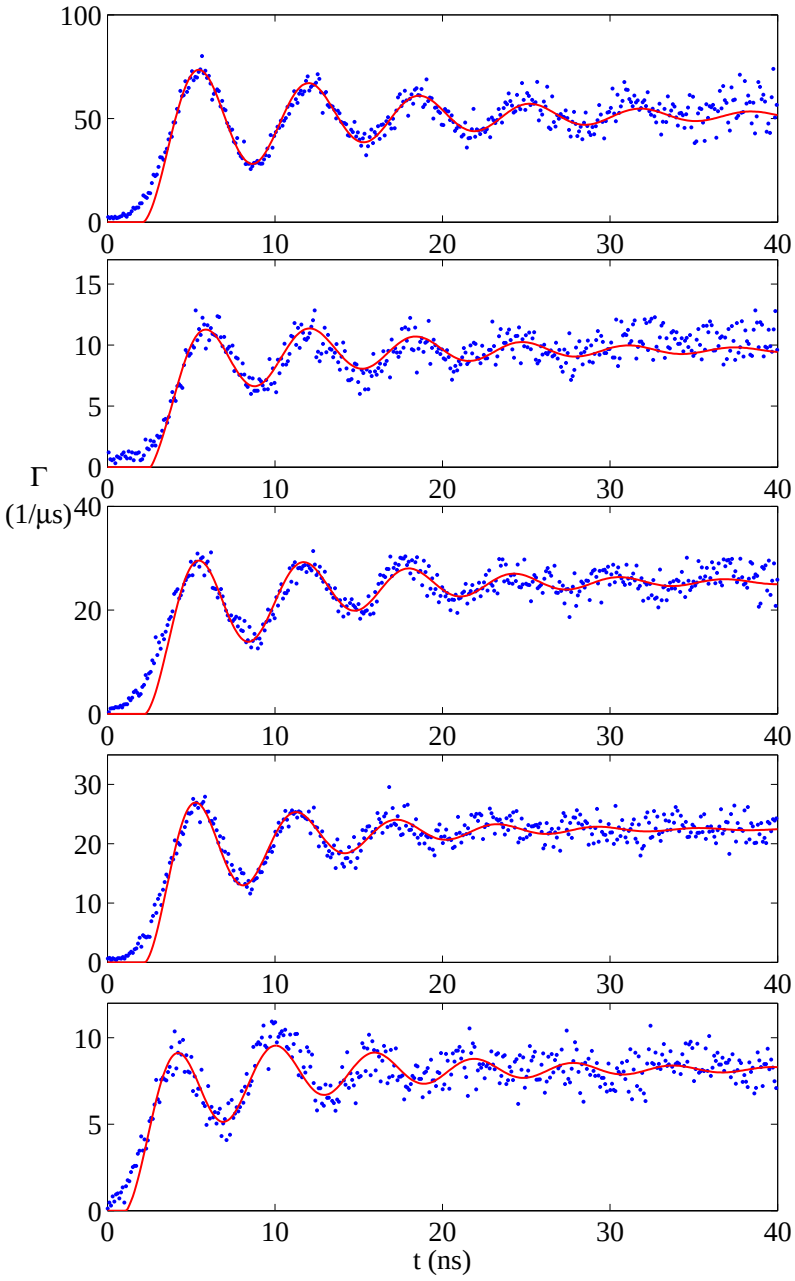

Figure 7.8: Measurements of Rabi oscillations in the escape rates in gradiometer NBG at 80 mK. In each case the solid curve is a least-square fit to Eq. 7.3. From the top, the plots are Rabi oscillation for microwave frequencies of 6.5 GHz, 6.6 GHz, 6.7 GHz, 6.8 GHz, and 6.9 GHz. The corresponding decay time constants T' are 12.6 ns, 12.2 ns, 10.7 ns, 8.1 ns and 11.8 ns.

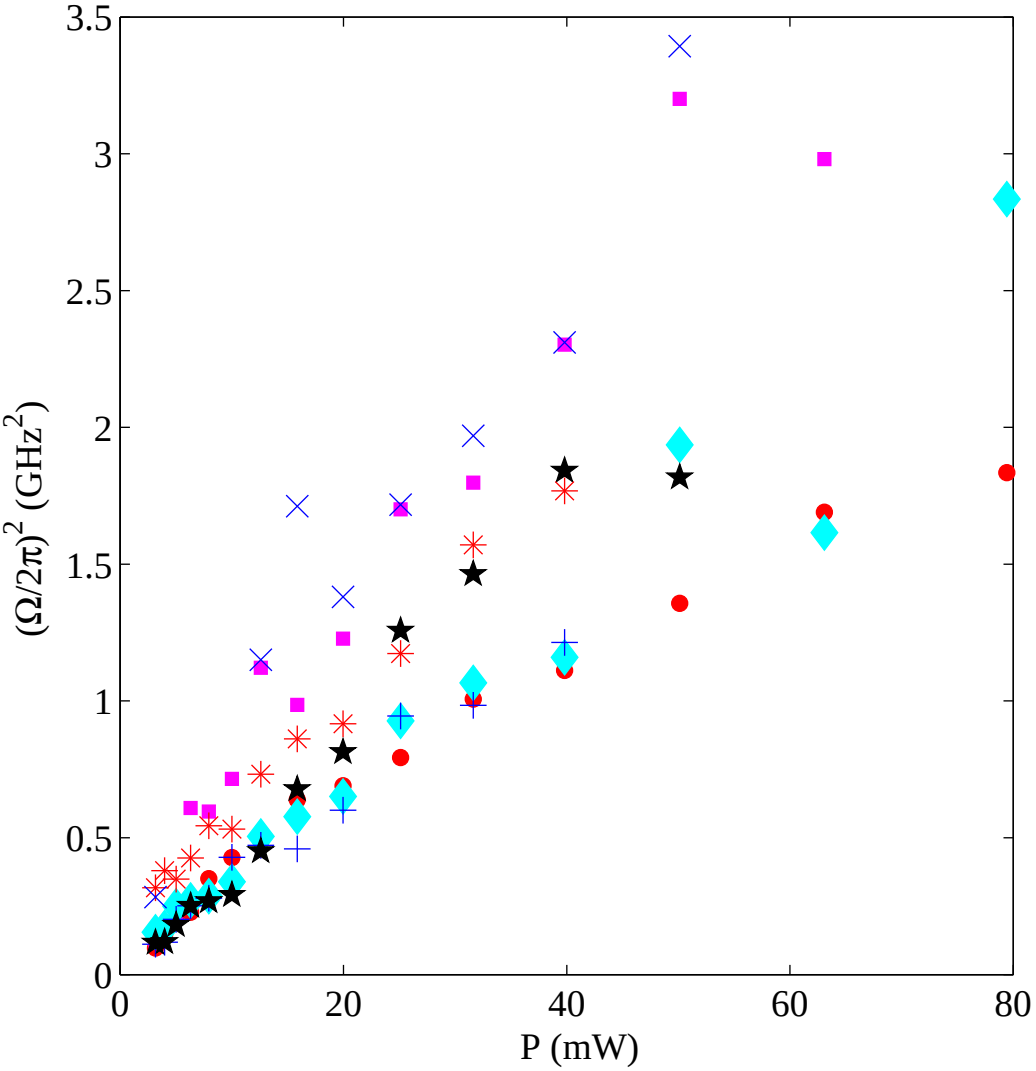

Figure 7.9: Square of the Rabi frequency in NBG vs. microwave power for microwaves with frequencies of 6.5 GHz (filled circles), 6.6 GHz (square), 6.7 GHz (diamonds), 6.8 GHz (crosses), 6.9 GHz (stars), 7.0 GHz (asterisks) and 7.1 GHz (tilted crosses). The data was measured at 80 mK.

relaxation time T_1, and the coherence time T_2 are related by [63]

$$\frac{1}{T'} = \frac{1}{2T_1} + \frac{1}{2T_2}, \tag{7.4}$$

when the Rabi oscillation is driven on resonance and inhomogeneous broadening can be neglected. Although spin-echo measurements are the best way to directly determine T_2 and distinguish pure dephasing from inhomogeneous broadening, we were not able to measure spin echoes in these devices due to their relatively short coherence times, and Rabi oscillations provided a good alternative.

Figure 7.10 shows typical examples of measured Rabi oscillations in the total escape rate for the three dc SQUID phase qubits. We applied microwave frequencies of 7.6 GHz for NB1 at 25 mK [see Fig. 4(a)], 7 GHz for AL1 at 80 mK [see Fig. 4(b)] and 6.5 GHz for NBG at 100 mK [see Fig. 4(c)]. The applied microwaves coupled capacitively to the qubit junction [See Fig. 1 and Fig. 2] and resonantly drove the qubit between $|0\rangle$ and $|1\rangle$. In each case, we observed clear oscillations in the escape rate. In these plots, t = 0 indicates when the microwaves were turned on. The solid curves in Fig. 7.10 are least-square fits to Eq. 7.3. From the fits, I found T′ for the gradiometer NBG was about 12 ns, while for magnetometers AL1 and NB1, it

Table 7.4: The decay time constant T' of Rabi oscillations in NBG measured at 80 mK for different microwave frequencies.

f (GHz)	T' (ns)
6.5	12.6
6.5	12.2
6.5	10.7
6.5	8.1
6.9	11.8

was about 27 ns and 12 ns, respectively (see Table 7.5). Density matrix simulations reveal that the escape rate we observe is dominated by a small population in $|2\rangle$ that escapes very rapidly ($\Gamma_2 \sim 10^{10}/\mathrm{s} \gg 1/\mathrm{T}'$), and this population is directly proportional to the occupancy of $|1\rangle$ which escapes much more slowly ($\Gamma_1 \sim 10^7/\mathrm{s}$). While tunneling contributes to spectroscopic broadening [95], measurements over a wide range of conditions with different escape rates did not appear to alter T' by more than about 30 % [23].

Figure 7.11 and Table 7.5 summarize T' values in devices AL1, NB1 and NBG. From the figure and table, we see that the single-turn aluminum magnetometer AL1 had a substantially longer envelope decay time T' than either the Nb magnetometer or the Nb gradiometer. I note that $T_2 < 2T_1$ in NB1 and NBG while in AL1 I see $T_2 \sim 2T_1$. This suggests that niobium qubits seem to have additional dephasing sources beyond just dissipation. Since NB1 and NBG have SiO_2/Si wiring dielectrics while AL1 has no wiring dielectrics and just SiO_2 as a substrate, the additional dephasing source could be from the wiring dielectrics in the niobium devices.

From this comparison, we can also safely conclude that T' in our dc SQUID phase qubits is not being limited by spatially uniform flux noise and the materials seem to play a role in decoherence. Finally, from $\mathrm{T}' \ll 2\mathrm{T}_2^*$ (see Table 7.5), this suggests low-frequency noise is causing significant inhomogeneous broadening of the resonance. In particular, tunneling could also cause $\mathrm{T}' \ll 2\mathrm{T}_2^*$ [96], but most of the data was taken deep in the well, so this is unlikely.

7.7 Conclusions

In conclusion, we have measured the spectroscopic coherence times and Rabi oscillations in three dc SQUID phase qubits. One device was a Nb gradiometer with 6-turn wound and counter-wound coils, the second was an Al magnetometer made with a single-turn loop, and the third was a Nb magnetometer with a 6-turn coil.

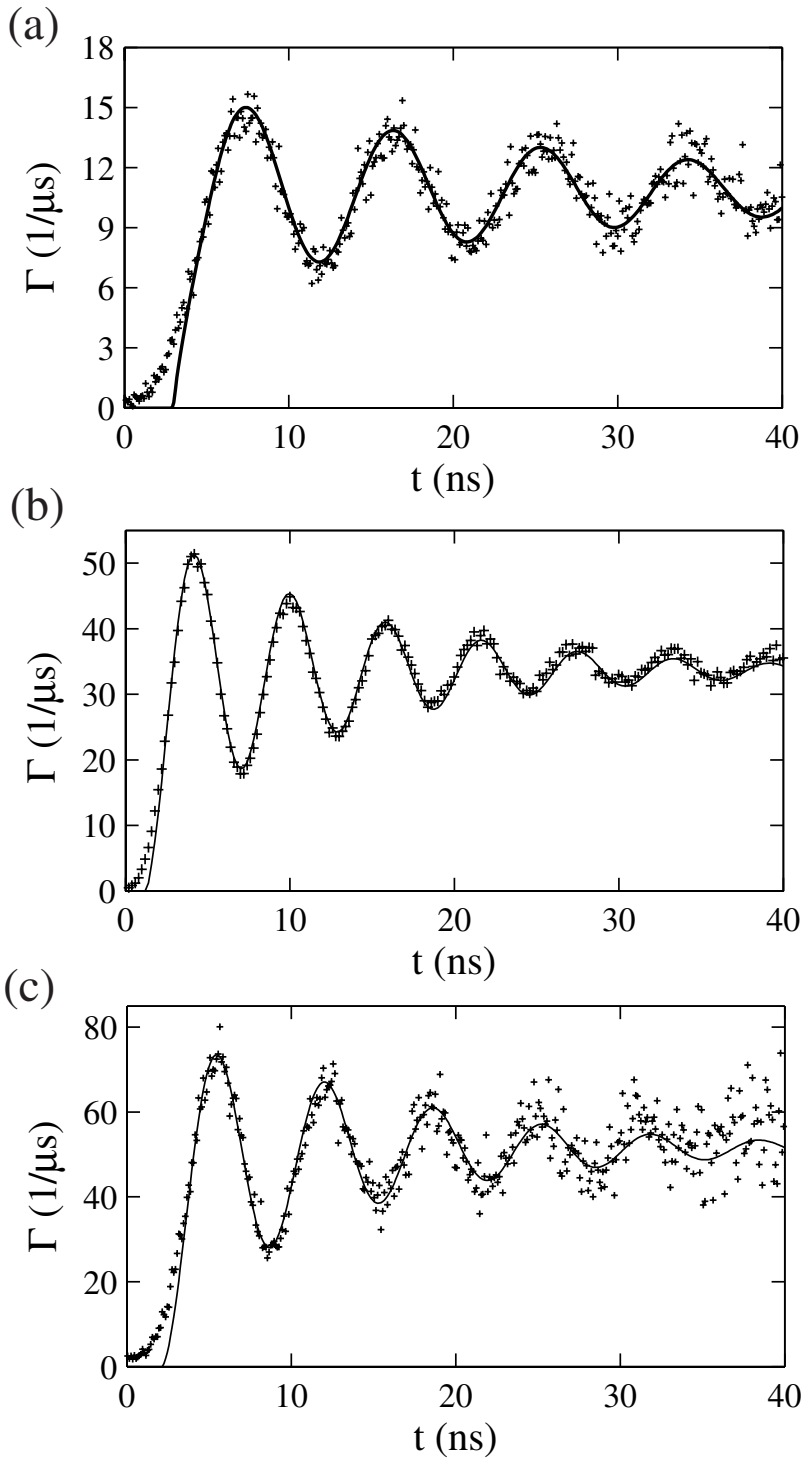

Figure 7.10: Measurements of Rabi oscillations in the escape rate in (a) single-turn magnetometer AL1 at 80 mK, (b) 6-turn magnetometer NB1 at 25 mK, (c) gradiometer NBG at 80 mK. In each case the solid curve is a χ^2 fit to Eq. 7.3.

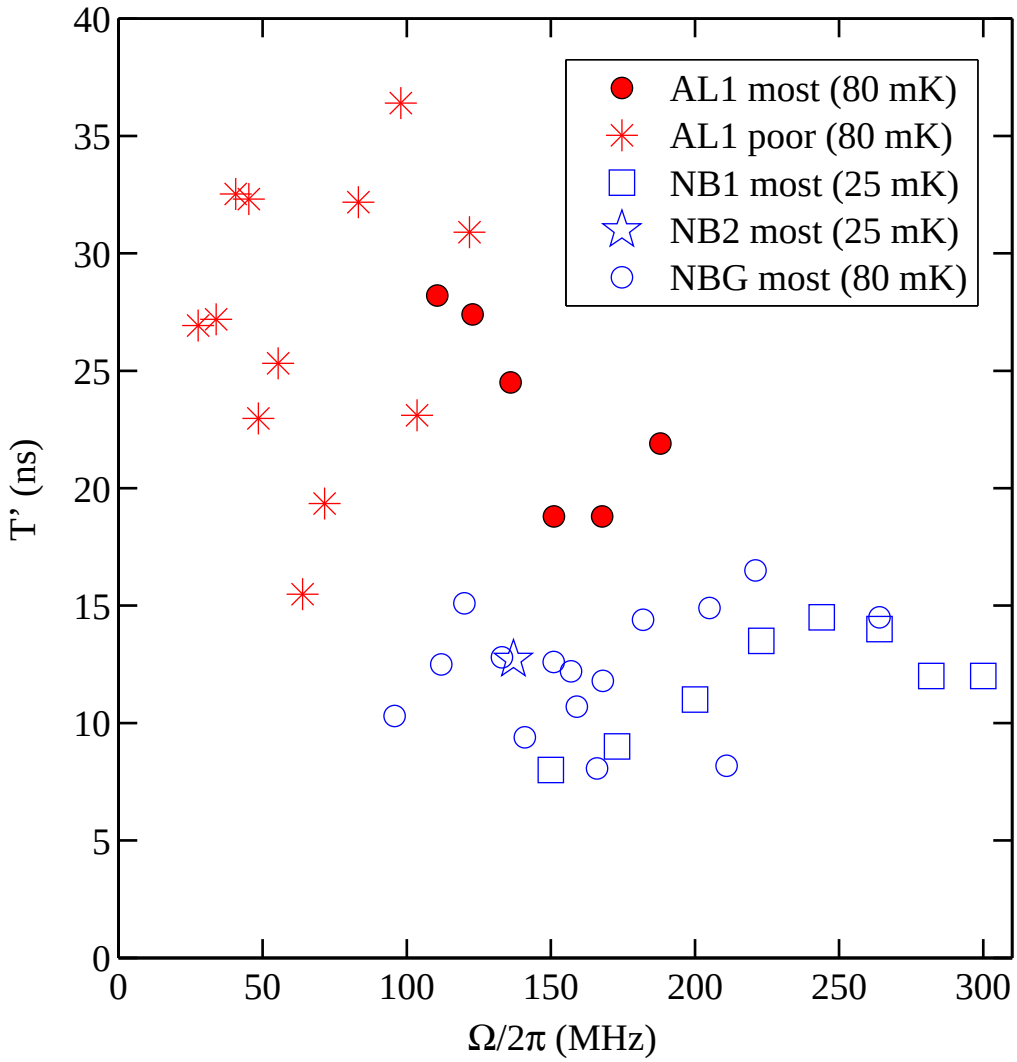

Figure 7.11: The decay time constant T' of Rabi oscillations vs. Rabi frequency $\Omega/2\pi$ of five devices. Filled circles are T' for AL1 measured at 80 mK at the most isolated biasing point, $r_I = 1000$ and asterisks are for AL1 at the poorly isolated biasing point, $r_I = 200$. Open circles are T' for NB1 measured at 25 mK at the most isolated point, Open squares are T' for NBG measured at 80 mK at the most isolated point and a star indicates T' for NB2 measured at 25 mK at the most isolated biasing point.

Table 7.5: Summary of spectroscopic coherence time T_2^*, time constant T' for decay of Rabi oscillation, relaxation time T_1 and estimated $T_1 = 3T'/4$ that would occur if all decoherence was due to dissipation.

	gradiometer NBG	magnetometer NB1	magnetometer AL1
T_2^*(ns)	4 - 8	4 - 10	4 - 10
T'(ns)	10 - 15	10 - 15	20 - 30
T_1(ns)	15	15	20
$T_1 = 3T'/4$(ns)	8 - 11	8 - 11	15 - 23

The gradiometer did not show significantly longer T' or T_2^* [79], and in fact the single-turn Al magnetometer showed a significantly longer T' than either the Nb gradiometer or Nb magnetometer. We conclude that spatially uniform flux noise is not a dominant source of decoherence in our phase qubits. There is a possibility of a local source of flux noise causing dephasing, which would not be nulled by a gradiometer. However, the observed dependence on frequency f_{01} of the either T' or T_2^* is not consistent with flux noise or critical current noise. I note that the results appear to be qualitatively consistent with a material-dependent decoherence mechanism such as dielectric loss from a distribution of 2-level charge fluctuators. In this picture, the longer T' and T_2^* of the Al device would be attributed to the absence of the thin-film lossy SiO_2 dielectrics layers. Since the coherence times are still quite short, such loss as remains is still quite significant. Since all three devices possess AlO_x tunnel barriers as well as thermally grown SiO_2 as the substrate, it is possible that these are the remaining sources of dissipation.

Chapter 8

The Cooper pair box as a coupling component in a quantum computer

8.1 Introduction: The Cooper pair box

A Cooper-pair box is a device that can store a well-defined integer number of Cooper pairs. It consists of a small superconducting island that is connected to ground via an ultra-small superconducting Josephson tunnel junction and to a gate voltage source via a capacitor [13] [see Fig. 8.1 (a)]. The phrase "ultra-small junction" refers to a junction with an area that is much less than 1 μm^2. When the total island capacitance is sufficiently small, the Coulomb energy associated with putting one pair on the island becomes big enough to suppress the tunneling. This suppression of tunneling due to an electrostatic energy barrier is called the Coulomb blockade effect [21]. The Coulomb blockade effect can be observed in both superconducting and normal ultra-small junctions. For normal junctions, the device is called a single-electron box.

The scale of the charging energy required to place one pair on the island is set by

$$E_c = \frac{(2e)^2}{2C_\Sigma} \tag{8.1}$$

where $\mathrm{C}_\Sigma = C_J + C_g$ is the total capacitance of the island, C_J is the capacitance of the ultra small junction, and C_g is the capacitance of the gate. C_Σ is typically in the femto farad range. For an island with $\mathrm{C}_\Sigma \simeq 2$ fF, the associated E_c is $\sim 1\mathrm{K}/k_B$. This implies that charge will not be very likely to tunnel through the junction if it is below about 1K, at least for certain values of gate voltage.

For a Cooper pair box, the energy associated with tunneling of Cooper pairs

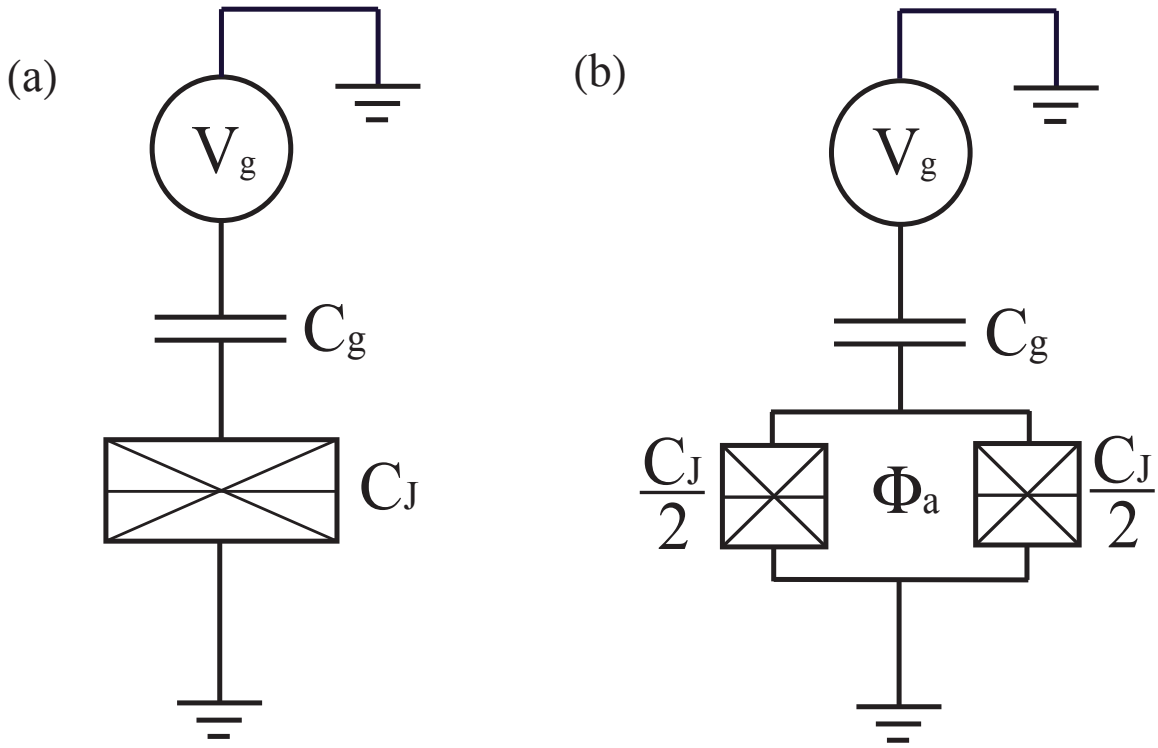

Figure 8.1: Cooper-pair box with (a) single ultra-small Josephson tunnel junction and (b) dc SQUID with two ultra-small junctions in parallel. C_J is the capacitance of the superconducting ultra-small junction, C_g is the gate capacitance, and V_g is the gate voltage. For the dc SQUID Cooper pair box, E_J of the SQUID can be tuned by applying a magnetic flux Φ_a to the loop.

through the ultra-small junction, the Josephson coupling energy must be included in the Hamiltonian in addition to the charging energy. The Josephson coupling energy can be found by calculating the power cost for supercurrent to tunnel through the junction [13]

$$P = IV = \left(I_c \sin\gamma \right) \left(\frac{\Phi_0}{2\pi} \frac{d\gamma}{dt} \right). \tag{8.2}$$

The Josephson coupling energy E is then:

$$\begin{aligned} E &= \int^t P dt \\ &= \int^t \left(I_c \sin\gamma \right) \left(\frac{\Phi_0}{2\pi} \frac{d\gamma}{dt} \right) dt \\ &= \frac{\Phi_0}{2\pi} I_c \int^\gamma \sin\gamma d\gamma \\ &= -E_J \cos\gamma \end{aligned} \tag{8.3}$$

where

$$E_J = \frac{\Phi_0}{2\pi} I_c \tag{8.4}$$

is the Josephson energy. The Josephson coupling energy shows how strongly the two superconducting wavefunctions on opposite sides of a tunnel junction are coupled to each other. Equation 8.4 reveals that Josephson energy E_J only depends on the critical current.

Figure 8.1(a) shows a schematic of the Cooper pair box. The small area between the ultra-small junction and the gate is the "island". The number of Cooper pairs on the island can be varied by applying a voltage bias to the gate. Fig. 8.1(b) shows a Cooper pair box with two ultra-small junctions in parallel. The design looks like there is a split in the junction so the device is also called a split Cooper pair box. The two junctions form a small SQUID and its critical current can be adjusted by applying a magnetic flux Φ_a to the loop. This enables us to tune the effective

Josephson energy, E_J of the split Cooper pair box :

$$E_J = \frac{\Phi_0}{2\pi} I_c = \frac{\Phi_0}{2\pi} 2I_0 \cos(\frac{\Phi_a}{\Phi_0}) \tag{8.5}$$

where Φ_0 is the flux quantum, Φ_a is the applied magnetic flux, I_c is the critical current of the SQUID when Φ_a is applied and $2I_0 = I_{01} + I_{02}$ is the maximum critical current of the SQUID. Since the Josephson energy affects the resonance frequency of the Cooper pair box, the frequency can be tuned to a limited extent by having a flux bias source.

The Cooper pair box has been used as a charge qubit [93, 106] and a tunable circuit element [107, 108]. Recently the Yale group [41] showed that a Cooper pair box that was biased at the degeneracy point ("sweet spot") and coupled to an LC resonator readout had a coherence time of 2 μs, one of the longest coherence times so far seen in any superconducting qubit.

The main application we envision here for a Cooper-pair box is as a switchable coupling element (variable capacitor) between two qubits in a quantum computer. To manipulate specific pairs of qubits or individual qubits, it's useful to be able to turn the coupling on and off. In this chapter, I introduce the basic physics of the Cooper pair box and examine how the Cooper pair box affects a phase qubit when they are coupled together.

8.2 Charging energy of a Cooper pair box with two voltage bias sources

Figure 8.2 shows a schematic of a Cooper pair box with two voltage sources; a voltage bias and a gate voltage source. This configuration differs from the conventional design where there is only a gate voltage. This configuration will be useful for finding the effective capacitance of the box with respect to the bias voltage, and

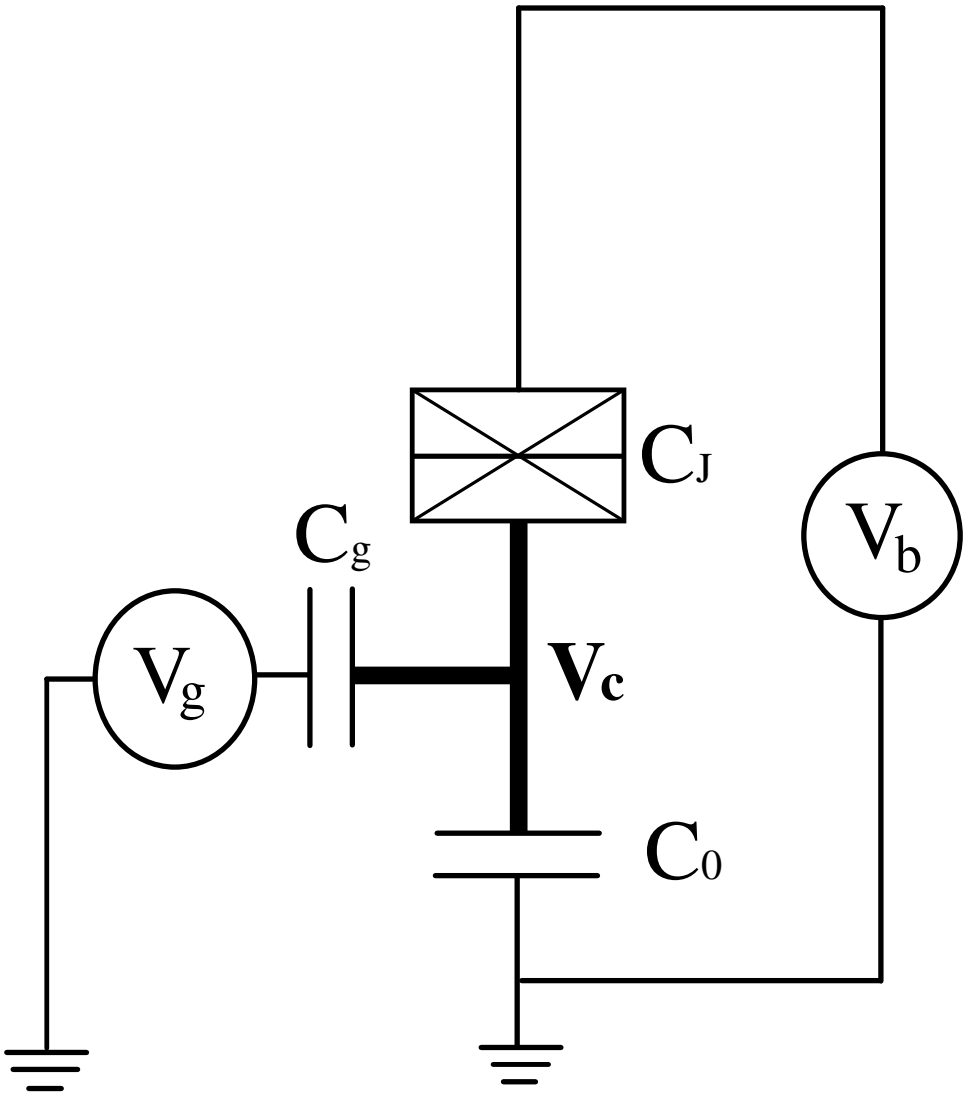

Figure 8.2: Cooper pair box with a voltage bias source V_b and a gate voltage source V_g. Note that V_b is connected the ultra-small junction directly. The box consists of one superconducting ultra-small junction with capacitance C_J and two capacitors C_0 and C_g. The energy of the system depends on V_b and V_g as well as the excess number of Cooper-pairs n on the box, where each pair has charge $-2|e|$. V_c is the island potential.

this will help us understand what happens when the box is coupled to a large-area Josephson junction phase qubit. In this case C_0 acts as a coupling element to the voltage source V_b, or ultimately the phase qubit. The derivation of the charging energy of a Cooper pair box can be found in Ref. [13]. Here I calculate the charging energy of the Cooper pair box with two voltage sources. The result reduces to the conventional Cooper pair box when the bias voltage V_b is zero.

To calculate the charging energy, we need to know the electrostatic potential V_c of the island. If the number of excess Cooper pairs on the island is n, the total of all the charges on each capacitor plate of the island must obey:

$$-2en = C_g(V_c - V_g) + C_J(V_c - V_b) + C_0 V_c \tag{8.6}$$

so that the electrostatic potential V_c of the island becomes

$$V_c = \frac{-2en + C_J V_b + C_g V_g}{C_\Sigma} \tag{8.7}$$

where $C_\Sigma = C_J + C_0 + C_g$, is the sum of all the capacitances linked to the island. Note that I use e as positive number: e = 1.6×10^{-19}C throughout the thesis so that the charge of a Cooper pair is -2e.

Excess charge appear on the island by tunneling through the ultra-small junction. Changes in n cause changes in the island potential, and the resulting charge is redistributed to each capacitor. The voltage sources have to do "work" during this charge transfer. From Eq. 8.7, the change in V_c when one Cooper pair is moved onto the island is,

$$\Delta V_c = -\frac{2e}{C_\Sigma}. \tag{8.8}$$

The work W done by a voltage source that moves a charge Q across voltage V is W = QV. The work δW_b done by the bias source V_b and the work δW_g done by V_g

when one excess Cooper pair oves onto the island is

$$\begin{aligned} \delta W_b &= (\Delta Q_j - 2e)V_b = (2e\frac{C_J}{C_\Sigma} - 2e)V_b \quad (8.9) \\ \delta W_g &= \Delta Q_g V_g = 2e\frac{C_g}{C_\Sigma}V_g \quad (8.10) \\ W &= \delta W_b + \delta W_g = 2e\left[\frac{C_g}{C_\Sigma}V_g + \left(\frac{C_J}{C_\Sigma} - 1\right)V_b\right] \quad (8.11) \end{aligned}$$

where ΔQ_b and ΔQ_g are charges that must be supplied by V_b and V_g, respectively when one Cooper pair is introduced on the island. For n excess Cooper pairs, the total work done by V_b and V_g is simply W_n which is

$$W_n = n \times W = 2en\left[\frac{C_g}{C_\Sigma}V_g + \left(\frac{C_J}{C_\Sigma} - 1\right)V_b\right]. \quad (8.12)$$

The electrostatic energy, U_E stored in the capacitors is

$$U_E = \frac{1}{2}[C_J(V_c - V_b)^2 + C_0{V_c}^2 + C_g(V_g - V_c)^2] + C_gC_J \quad (8.13)$$

The total electrostatic free energy of the island is the electrostatic energy stored in the capacitors minus the work done by the voltage sources. After some work, I find the n-dependent charging energy U

$$\begin{aligned} U &= U_E - nW \\ &= \frac{1}{2C_\Sigma}\left[4e^2n^2 + 4en((C_0 + C_g)V_b - C_gV_g) + C_gC_J(V_b - V_g)^2 + C_0(C_JV_b^2 + C_gV_g^2)\right] \end{aligned} \quad (8.14)$$

This can also be written in the form

$$\begin{aligned}
U =& \frac{1}{2C_\Sigma}\left[4e^2n^2 + 4en((C_0+C_g)V_b - C_gV_g) + C_gC_J(V_b-V_g)^2 + C_0(C_JV_b^2 + C_gV_g^2)\right] \\
&+ (C_0V_b + C_gV_b - C_gV_g)^2 - (C_0V_b + C_gV_b - C_gV_g)^2 \\
=& \frac{1}{2C_\Sigma}\left[2en + (C_0+C_g)V_b - C_gV_g\right]^2 + + G(V_b,V_g) \\
=& \frac{(2e)^2}{2C_\Sigma}\left[n + \frac{(C_0+C_g)V_b}{2e} - \frac{C_gV_g}{2e}\right]^2 + G(V_b,V_g) \\
=& E_c(n+n_b-n_g)^2 + G(V_b,V_g),
\end{aligned} \tag{8.15}$$

where I define,

$$n_g = \frac{C_gV_g}{2|e|} \tag{8.16}$$

$$n_b = \frac{(C_0+C_g)V_b}{2|e|} \tag{8.17}$$

$$E_c = \frac{4e^2}{2C_\Sigma} \tag{8.18}$$

and $G(V_b, V_g)$ is an n-independent energy term

$$G(V_b,V_g) = \frac{1}{2C_\Sigma}[(C_0V_b + C_g(V_b-V_g)^2 + C_gC_J(V_b-V_g)^2 + C_0(C_JV_b^2 + C_gV_g^2)] \tag{8.19}$$

which is a function of the bias voltage and the gate voltage. This term doesn't affect the average number of excess Cooper pairs $\langle n\rangle$ or any dynamics of the Cooper pair box.

Considering the above expression for U, I see that increasing V_g will cause Cooper pairs to be induced to tunnel onto the island (n increases), since this will lower the total energy. Similarly, when we increase V_b, Cooper pairs leave (n decreases) to lower the energy.

8.3 Hamiltonian and energy bands of the Cooper pair box

The total energy of a Cooper pair box with two voltage sources is the sum of the charging energy and the Josephson coupling energy, given by

$$H = E_c(n + n_b - n_g)^2 - E_J \cos\gamma \tag{8.20}$$

where the Josephson energy is

$$E_J = \frac{\Phi_0}{2\pi} I_c, \tag{8.21}$$

γ is the gauge invariant phase difference across the junction, $C_\Sigma = C_J + C_0 + C_g$, I_c is the critical current of the junction and I have dropped the term $G(V_b, V_g)$ since it is an independent of n. Here n and γ are dynamical variables. When we describe the Cooper pair box using quantum mechanics, H, n and γ become operators, and we can write the Hamiltonian as

$$\hat{H} = E_c(\hat{n} + n_b - n_g)^2 - E_J \cos\hat{\gamma}. \tag{8.22}$$

There are a few things that should be remembered at this point. First, Eq. 8.22 is a fairly general expression for the Hamiltonian of a Josephson junction with n_b and n_g terms added due to the extra capacitors. However, the Hamiltonian lacks a current bias term since there is no current source in this circuit. Second, the superconducting gap energy Δ is another important energy scale but it does not explicitly appear in the Hamiltonian. This happens because I assumed that $\Delta \gg E_c$ and that no quasiparticle are present. In this case, the tunneling processes only involve Cooper pairs and the dynamics of the system has periodicity 2e.

The dynamics of the Cooper pair box are largely determined by the relative sizes of the energies E_c and E_J. If the Josephson coupling energy dominates the Hamiltonian ($E_J \gg E_c$), the Josephson effect dominates and large currents can flow

through the junction. In this case, $\hat{N}$ is not a good quantum number but $\hat{\gamma}$ is. For $E_J \ll E_c$, the charging energy dominates the dynamics and $\hat{N}$ is a good quantum number. The Cooper pair box that I deal with in this chapter has $E_J \ll E_c$. So here I will describe the dynamics in terms of $\hat{N}$.

In the low temperature limit $k_B T << E_J << E_c$, the Cooper-pair box mostly stays in the two lowest energy states. If I restrict the gate voltage to the range $0 < V_g < e/C_g$, the Hamiltonian can then be represented by a 2×2 matrix

$$\langle 0|\widehat{H}|0\rangle = H_{00} \tag{8.23}$$

$$\langle 0|\widehat{H}|1\rangle = H_{01} \tag{8.24}$$

$$\langle 1|\widehat{H}|0\rangle = H_{10} \tag{8.25}$$

$$\langle 1|\widehat{H}|1\rangle = H_{11} \tag{8.26}$$

where $|0\rangle$ and $|1\rangle$ are number states corresponding to the number of Cooper pairs on the island being n = 0 and 1. Note that due to the Josephson coupling energy the number states are not exact eigenstates of the Hamiltonian anymore, i.e. $\hat{N}$ and $\hat{H}$ do not commute.

To express the Josephson coupling energy in the number basis, let's start with

$$cos\hat{\gamma} = \frac{e^{i\hat{\gamma}} + e^{-i\hat{\gamma}}}{2} \tag{8.27}$$

where $\hat{\gamma}$ satisfy the relations:

$$e^{i\hat{\gamma}}|N\rangle = |N-1\rangle \tag{8.28}$$

$$e^{-i\hat{\gamma}}|N\rangle = |N+1\rangle. \tag{8.29}$$

Thus $e^{i\hat{\gamma}}$ is a translation operator for $\hat{N}$, just as $e^{-ix\hat{p}/\hbar}$ is the translation operator for a free particle with momentum $\hat{p}$. This tells us that by changing γ, n can increase or

decrease. This makes sense intuitively since $\sin\gamma \simeq \gamma$ is current. Fundamentally, this occurs because the number of Cooper pairs in the island can change by Josephson tunneling. From Eqs. 8.27, 8.28 and 8.29, One sees that in the number basis, the Josephson coupling energy term introduces off-diagonal elements in the Hamiltonian. Combining the charging energy and the Josephson coupling energy, the Hamiltonian matrix in the number basis becomes

$$\hat{H} = \begin{pmatrix} E_c(0 + n_b - n_g)^2 & \frac{-E_J}{2} \\ \frac{-E_J}{2} & E_c(1 + n_b - n_g)^2 \end{pmatrix}. \tag{8.30}$$

By diagonalizing $\hat{H}$, we can obtain the energy eigenvalues and energy eigenstates as well as the average number $\langle N \rangle$ of Cooper pairs on the island. The number operator $\hat{N}$ is defined as

$$\hat{N}|N\rangle = n|N\rangle \tag{8.31}$$

where n is the excess number of Cooper pairs on the island. The energy eigenstates $|E_0\rangle$ and $|E_1\rangle$ in the number basis can be written as

$$|E_0\rangle = a_{11}|0\rangle + a_{21}|1\rangle \tag{8.32}$$

$$|E_1\rangle = a_{12}|0\rangle + a_{22}|1\rangle \tag{8.33}$$

The average number $\langle N \rangle$ of Cooper pairs is

$$\langle N \rangle = \langle \Psi | \widehat{N} | \Psi \rangle \tag{8.34}$$

where $|\Psi\rangle$ is a general wavefunction.

Figure 8.3 shows the calculated energy levels [Fig 8.3(a)] and the average number of Cooper pairs in the ground state of the box [Fig 8.3(b)]. Both curves are plotted with respect to the normalized gate charge n_g. The simulation parameters

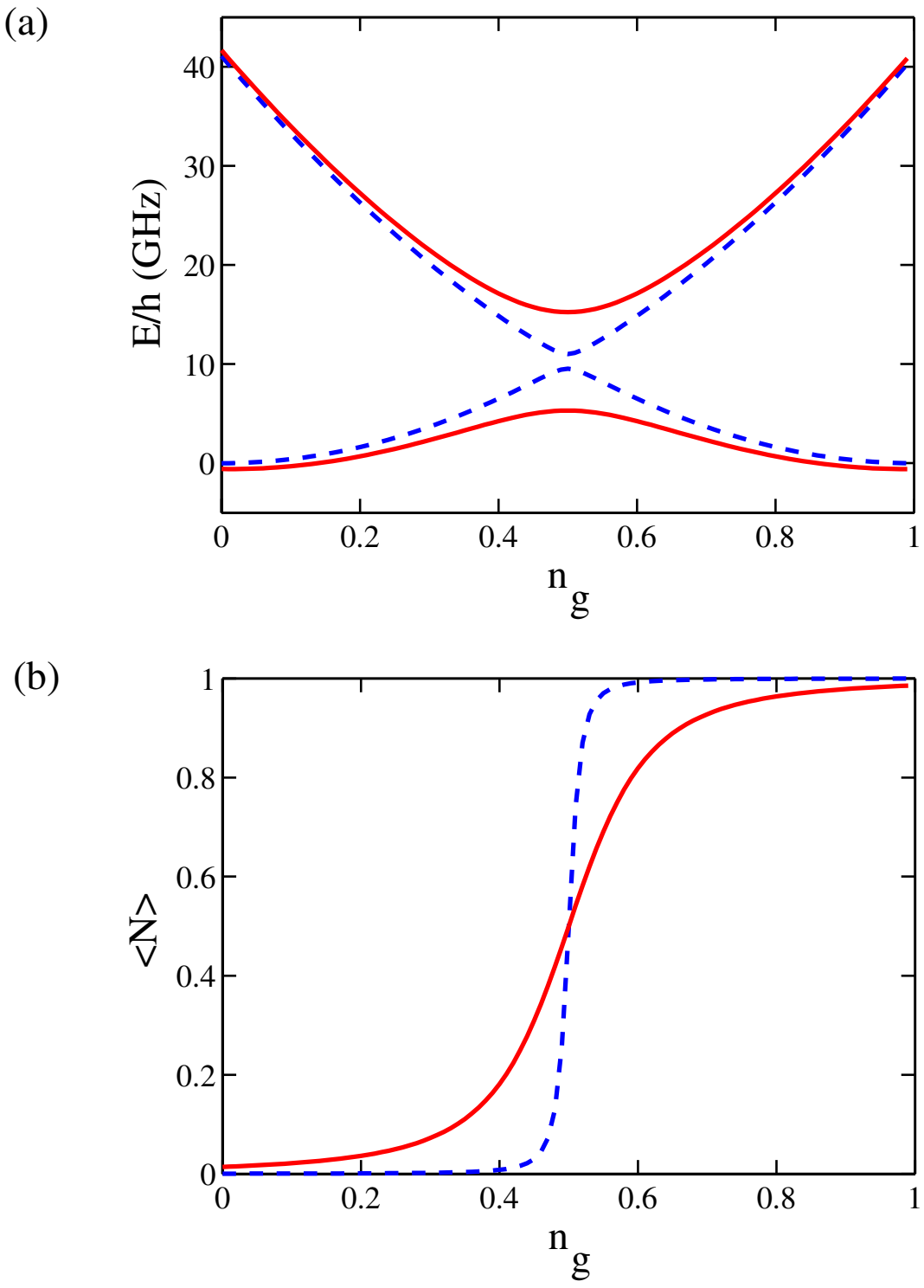

Figure 8.3: (a) Simulation of the energy vs. normalized gate charge n_g and (b) the average number $\langle 0|\widehat{N}|0\rangle$ of Cooper pairs in the ground state of the box for different E_J. In both figures, the dashed curve is for $E_c/E_J = 27$ and the solid curve is for $E_c/E_J = 4.1$. The simulation parameters are shown in Table 8.1

Table 8.1: Parameters of Cooper pair box for the simulation shown in Fig. 8.3.

Device	Blue dashed curve	Red solid curve
A (nm^2)	100×100	100×100
C_J (fF)	0.88	0.88
C_0 (fF)	1	1
C_g (fF)	0.001	0.001
C_s (fF)	0	0
E_c/h (GHz)	41	41
I_c (nA)	3	10
E_J/h (GHz)	1.5	10

are shown in Table 8.1. In Fig 8.3(a), the dashed curve is for $E_c/E_j = 27$, *i.e.* the charging energy dominates. In this case, the Josephson coupling energy acts as a small perturbation to the charging energy. Thus the energy E is nearly quadratic in n_g except for a small avoided crossing at $n_g = 0.5$. At $n_g = 0.5$, the energy gap between the ground state and the first excited state is a minimum and equals E_J. For this simulation with $E_c/E_j = 27$, $E_J/h = 1.5$ GHz. At $n_g = 0$ or 1, the gap is largest, and is given by $E_c/h = 41$ GHz. If I increase E_J/h to 10 GHz [solid curve in Fig. 8.3(a)], the gap at $n_g = 0.5$ opens up and the energy curves flatten.

Figure 8.3(b), shows the average number $\langle N \rangle$ of Cooper pairs on the island when the box is in its ground state for $E_J/h = 1.5$ GHz and $E_c/E_J = 27$ (dashed curve) and for $E_J/h = 10$ GHz and $E_c/E_j = 4.1$ (solid curve). When the charging energy dominates, *i.e.* $E_c/E_J = 27$, $\langle N \rangle$ (the dashed curve) varies more rapidly with n_g than when $E_c/E_j = 4.1$ (the solid curve). This is because when E_J is larger, N has a larger uncertainty.

In practice, a shunt capacitor can be added across the ultra-small junction to suppress the charging energy. This provides some additional ability to control E_c. Figure 8.4 shows results from a simulation for this situation; the dashed curve is

Table 8.2: Parameters of the Cooper pair box for simulation shown in Fig. 8.4

Device	Blue dashed curve	Red solid curve
A (nm^2)	100×100	100×100
C_J (fF)	0.88	0.88
C_0 (fF)	1	1
C_g (fF)	0.001	0.001
C_s (fF)	0	10
E_c/h (GHz)	41	1.5
I_c (nA)	3	3
E_J/h (GHz)	1.5	1.5

without a shunt capacitor and the solid curve is with an added a shunt capacitor C_s. This decreases E_c/E_j while keeping E_J fixed. Fig. 8.4(a) shows the total energy vs n_g. When the charging energy is reduced by adding C_s (solid curve), the gap at $n_g = 0.5$ stays the same but the curve becomes smoother. Figure 8.4(b) shows that the average number $\langle N \rangle$ of pairs in the ground state varies much more smoothly with n_g for the small E_c/E_j, as expected.

8.4 Calculation of effective capacitance

Here I propose a simple semi-classical way to calculate the effective capacitance of a Cooper-pair box and demonstrate that a Cooper-pair box can be used as a variable capacitor. One possible experiment to show that a box will work as a variable capacitor is to connect a phase qubit (large area Josephson junction) in parallel with a Cooper-pair box (see Fig. 8.5). The total capacitance across the junction determines the energy levels of the phase qubit. Thus changes in C_{eff} will shift the energy levels, which we can detect by microwave spectroscopy. In this section, I examine how the coupled Cooper pair box changes the energy levels of a

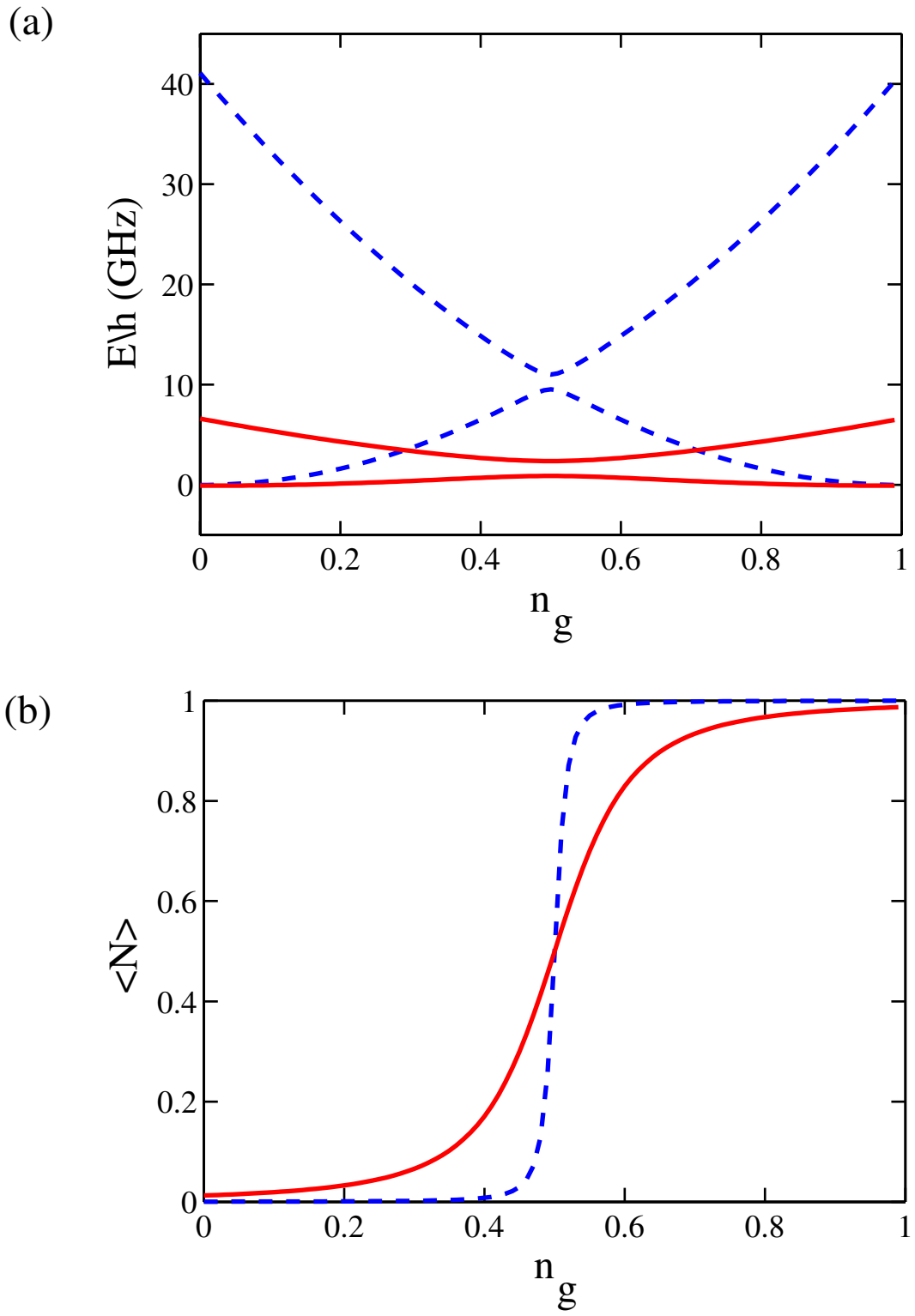

Figure 8.4: (a) Simulation of energy vs. normalized gate charge n_g and (b) average number $\langle N \rangle$ of Cooper pairs in the ground state with and without a 10 fF shunt capacitor. In both figures, the dashed curve is for $E_c/E_J = 27$ and the solid curve is for $E_c/E_J = 4.4$. The simulation parameters are shown in Table 8.2

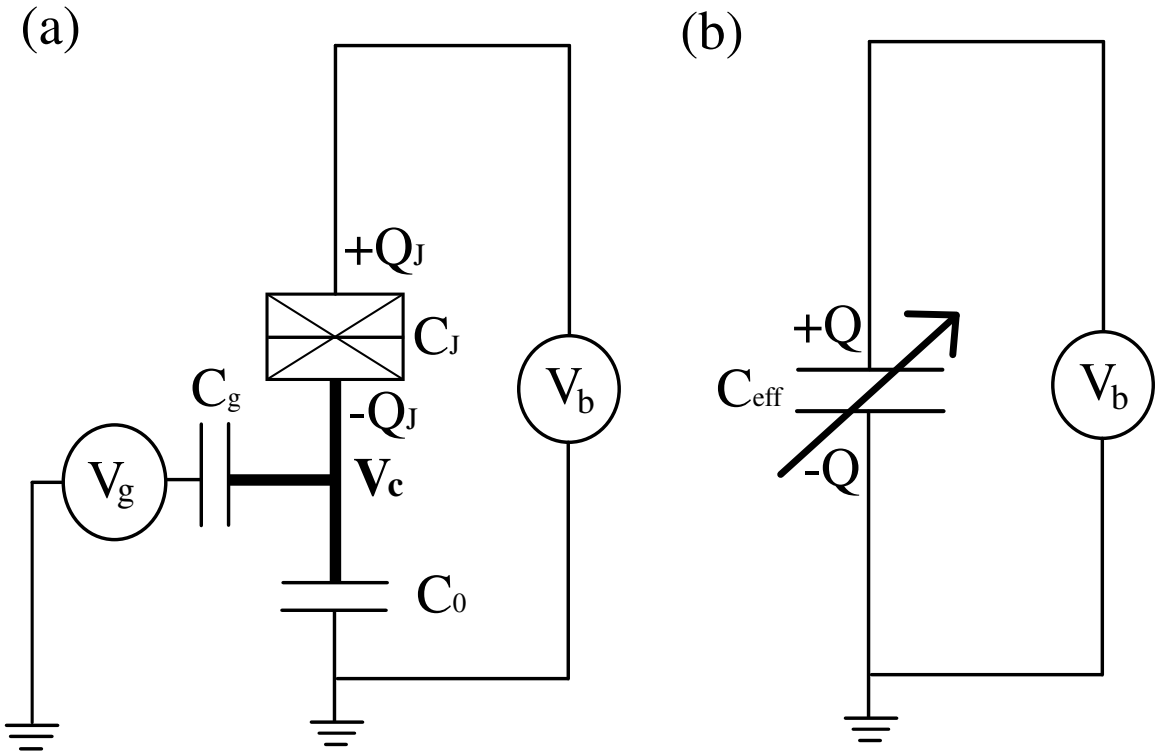

Figure 8.5: (a) A Cooper-pair box and an equivalent effective variable capacitor. C_J, C_0, C_g are capacitance of the superconducting small junction, coupling capacitance and gate capacitance, respectively. V_b and V_g are the bias voltage and the gate voltage, V_c is the island potential, and Q_J is the charge stored in the junction capacitance. (b) The equivalent variable effective capacitor C_{eff}.

phase qubit.

8.4.1 Effective capacitance: definition

A Cooper pair box with a bias voltage and a gate voltage can act as an effective capacitance which varies with the gate voltage. The ability to vary the effective capacitance of the box makes it potentially useful as a coupling element between superconducting qubits.

If a total charge Q is sent from the battery V_b into a Cooper pair box, the Q will be split. Some stays on the positive plate of the small junction and the rest tunnels through the junction and onto the island. We can define the effective differential capacitance of this system [see Fig 8.5(b)] as the rate at which charge Q changes with the bias voltage V_b,

$$C_{eff} = \frac{\delta\langle Q\rangle}{\delta V_b} \tag{8.35}$$

where V_g is fixed. In this expression $\langle Q\rangle$ is the charge transferred from the battery V_b. We can write

$$\langle Q\rangle = C_J\langle V_b - V_c\rangle - 2|e|\langle N\rangle \tag{8.36}$$

where V_c is the potential of the island. Thus $\langle Q\rangle$ is just the sum of the charge Q_j that is on the positive plate of the junction and the charge $-2|e|\langle N\rangle$ that tunneled through the junction onto the island. V_c is a function of V_g and V_b and depends on the average number of pairs $\langle N\rangle$ on the island. Examination of the circuit shows

$$\langle Q\rangle = \frac{C_J}{C_\Sigma}(2|e|\langle N\rangle + (C_0 + C_g)V_b + C_gV_g) - 2|e|\langle N\rangle. \tag{8.37}$$

Substituting Eq. 8.37 into Eq. 8.35, we find

$$C_{eff} = \frac{\partial\langle Q\rangle}{\partial V_b} \tag{8.38}$$

$$= \frac{(C_0+C_g)}{C_\Sigma}(C_J - 2|e|\frac{\partial\langle N\rangle}{\partial V_b}) \tag{8.39}$$

Note that since $\langle N\rangle$ depends on V_g and V_b, Eq. 8.39 gives a non-linear voltage dependance to C_{eff}. The maximum C_{eff} occurs at $n_g = 0.5$ when $V_b \simeq 0$, which is where $n = 0$ and $n = 1$ have the same energy.

8.4.2 Effective capacitance: simulation

To see how large the effective capacitance is under typical circumstances, I simulated a device with $C_0 = 10$ fF, $C_J = 0.57$ fF, $C_g = 1$ aF, $I_c = 0.64$ nA, and $E_c/E_j = 22.97$ at various temperatures. To use C_{eff} as a variable coupler, it is important to maximize C_{eff} and obtain a high on-off ratio. Since V_b and V_g both control the charge transfer through the junction, in principle we can make C_{eff} maximum or minimum by applying appropriate V_b and V_g or both. However, if we are going to use the box as a variable capacitor and couple it across a phase qubit, then we need to take $V_b = 0$; since no voltage will be present across the qubit.

Figure 8.6(a) shows a plot of $\langle N\rangle$ vs n_g at $V_b = 0$. At $V_b = 0$ the number of pairs changes sharply as a function of n_g near $n_g = 0.5$. If V_b increases, the maximum C_{eff} point moves to a different V_g point. Plotting $\langle N\rangle$ versus n_b yields a curve which is very similar to Fig. 8.6(a), except with opposite sign and slope.

Due to thermal excitation the excited state gets occupied and $\partial\langle N\rangle/\partial V_b$ becomes smaller at higher temperature. Figure 8.6(b) shows the temperature dependence of C_{eff} at 20 mK, 50 mK and 100 mK. The maximum capacitance change is 80 fF at 20 mK. In comparison, at zero temperature Averin *et al.* [107] showed that $|\partial\langle n\rangle/\partial n_b| \sim E_c/E_J$ at the degeneracy point. For our case $C_\Sigma/C_0 \sim 1$ and so from

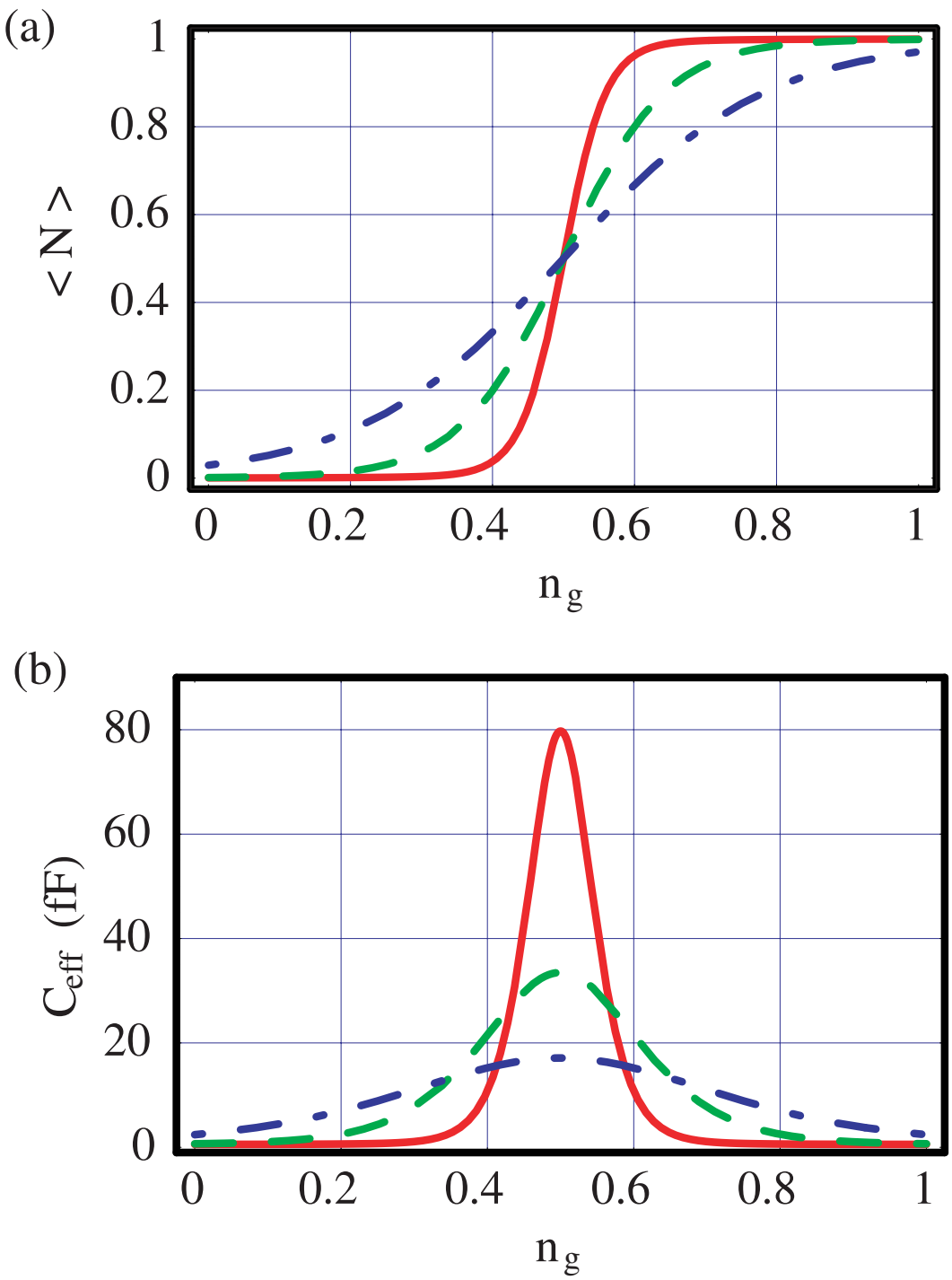

Figure 8.6: (a) Simulation of $< N >$ vs n_g at $V_b = 0$ at 20 mK (solid curve), 50 mK (dashed curve) and 100 mK (dashed-dot curve). Maximum tunneling of Cooper-pairs occurs at $n_g = 0.5$. (b) Simulation of the effective capacitance at 20 mK (solid curve), 50 mK (dashed curve) and 100 mK (dashed dot curve). The parameters are $C_J = 0.57$ fF, $C_g = 1$ aF, $C_0 = 10$ fF, the critical current of the ultrasmall junction $I_c = 0.64$ nA, and $E_c/E_j = 22.97$. The maximum C_{eff} is obtained at at $n_g = 0.5$ for $n_b = 0$.

Eq. 8.38 we find

$$\begin{aligned} C_{eff}|_{T\to 0} &\sim C_0 \frac{E_c}{E_J} \\ &\sim \frac{4\pi e^2}{\Phi_0}\frac{1}{I_0} \end{aligned} \tag{8.40}$$

which gives $C_{eff} \sim 200$ fF at $n_g = 0.5$. This equation tells us that C_{eff} will be maximized by making I_0 smaller. As we will see below, this is only part of the story, and in fact we will find that one should not make I_0 too small so that the energy level of the Cooper pair box is comparable to that of the phase qubit if the capacitance needs to work at high frequencies.

8.5 Cooper pair box coupled to a phase qubit

The motivation for this work was to use a Cooper pair box as a tunable coupling between two phase qubits. A Cooper-pair box coupled to a Josephson junction phase qubit can be thought about in a rather simple way. In the previous section, I showed that the Cooper pair box can change its effective capacitance. Once the Cooper pair box is connected as a variable capacitor to a Josephson junction phase qubit, it is possible to tune the energy levels of the Josephson junction, since the energy levels depend on the total capacitance of the junction.

It is important to see how the box behaves when it is coupled to the Josephson junction. In this section I show the result of energy level calculations and predict what we will expect from the spectroscopy experiment on the Josephson junction phase qubit. The derivation of the Hamiltonian and energy level calculations were initially done by Dr. Frederick W. Strauch and I will reproduce his calculations here.

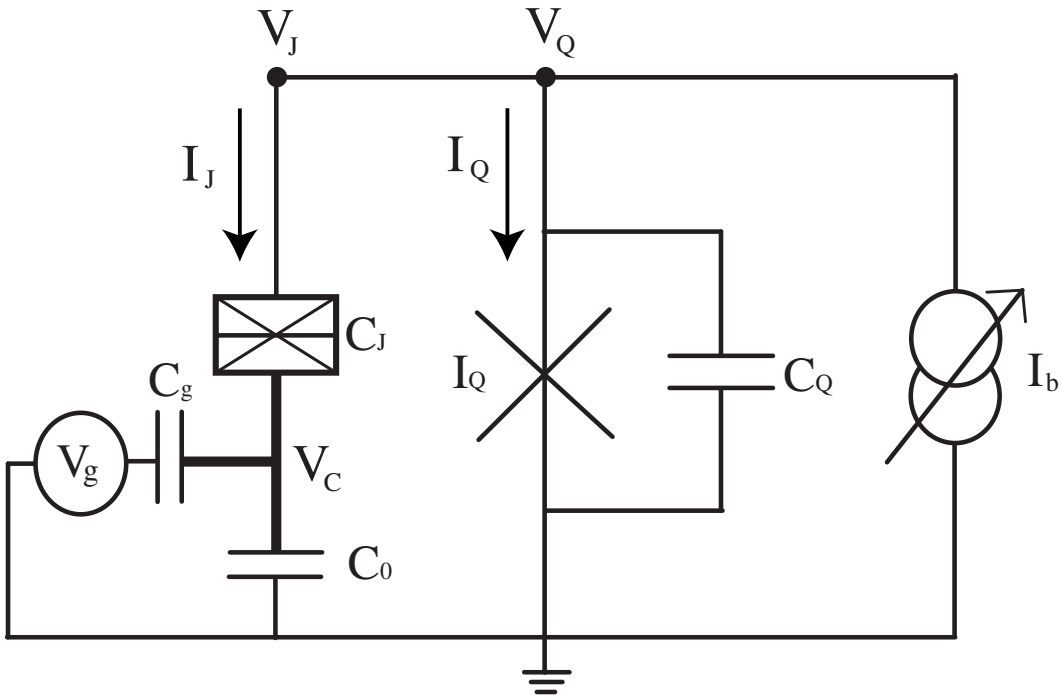

Figure 8.7: Circuit schematic of a Cooper pair box coupled to a Josephson junction.

8.5.1 Hamiltonian of the coupled box and junction

Figure 8.7 shows the circuit diagram of a Cooper box coupled to a Josephson junction. Index J indicates the small junction in the Cooper pair box and Q indicates the Josephson junction (qubit). Starting from the Josephson equations,

$$I = I_0 \cos\gamma \tag{8.41}$$

$$V = \frac{\Phi_0}{2\pi}\dot{\gamma}. \tag{8.42}$$

Note that V is the voltage **across** the junction. Applying Kirchhoff's laws at each node in the circuit of Fig. 8.7 gives current equations

$$I_b = I_J + I_Q \tag{8.43}$$

$$I_J = C_J(\dot{V}_J - \dot{V}_c) + I_{0J}\sin\gamma_J \tag{8.44}$$

$$I_Q = C_Q\dot{V}_Q + I_{0Q}\sin\gamma_Q \tag{8.45}$$

$$I_J = C_g(\dot{V}_c - \dot{V}_g) + C_0\dot{V}_c \tag{8.46}$$

and

$$V_J = V_Q. \tag{8.47}$$

I can also apply the ac Josephson relations and get

$$V_J - V_c = \frac{\Phi_0}{2\pi}\dot{\gamma}_J \tag{8.48}$$

$$V_Q = \frac{\Phi_0}{2\pi}\dot{\gamma}_Q \tag{8.49}$$

where $V_J - V_c$ is the voltage across the small junction, V_Q is the voltage across the qubit (large area Josephson) junction, and V_c is the voltage of the island. I_{0J} and I_{0Q} are the critical currents of the small junction in the Cooper pair box (indexed as J) and the qubit junction (indexed as Q). γ_J and γ_Q are the phase differences

associated with the small junction and the qubit junction, respectively. C_J, C_Q and C_g are the capacitance of the small junction, the qubit junction and the gate capacitor. I_b is the bias current.

Considering Eqs. 8.43 - 8.49, we find the equations of motion for γ_j and γ_Q :

$$C_J\frac{\Phi_0}{2\pi}\dot{\gamma_j} + I_{0J}\sin\gamma_j = \frac{\Phi_0}{2\pi}(C_g + C_0)(\ddot{\gamma_Q} - \ddot{\gamma_J}) - C_g\dot{V_g} \tag{8.50}$$

$$C_J\frac{\Phi_0}{2\pi}\dot{\gamma_Q} + I_{0Q}\sin\gamma_Q = I_b - \frac{\Phi_0}{2\pi}(C_g + C_0)(\ddot{\gamma_Q} - \ddot{\gamma_j}) + C_g\dot{V_g} \tag{8.51}$$

If we had the Lagrangian $\mathcal{L}$, we could have derived these equations of motion from Lagrange's equations

$$\frac{d}{dt}\frac{\partial\mathcal{L}}{\partial\dot{\gamma_J}} - \frac{\partial\mathcal{L}}{\partial\gamma_J} = 0 \tag{8.52}$$

$$\frac{d}{dt}\frac{\partial\mathcal{L}}{\partial\dot{\gamma_Q}} - \frac{\partial\mathcal{L}}{\partial\gamma_Q} = 0. \tag{8.53}$$

Comparing Eq. 8.50 to Eq. 8.52 and Eq. 8.51 to Eq. 8.53, we see that the following $\mathcal{L}$ works:

$$\begin{aligned}\mathcal{L} = \frac{1}{2}(\Phi_0)^2(C_{J\Sigma}\dot{\gamma_J}^2 + C_{Q\Sigma}\dot{\gamma_Q}^2 - 2C_{c\Sigma}\dot{\gamma_J}\dot{\gamma_Q}) \\ +\Phi_0 C_g V_g(\dot{\gamma_J} - \dot{\gamma_Q}) + E_{JJ}\cos\gamma_J + E_{JQ}\cos\gamma_Q + \frac{I_b}{I_{cQ}}\gamma_Q.\end{aligned} \tag{8.54}$$

where

$$C_{J\Sigma} = C_J + C_0 + C_g \tag{8.55}$$

$$C_{Q\Sigma} = C_Q + C_0 + C_g \tag{8.56}$$

$$C_{c\Sigma} = C_0 + C_g \tag{8.57}$$

$$E_{JJ} = \frac{\Phi_0}{2\pi}I_{cJ} \tag{8.58}$$

$$E_{JQ} = \frac{\Phi_0}{2\pi}I_{cQ} \tag{8.59}$$

I next introduce the generalized momenta $p_j = \partial\mathcal{L}/\partial\gamma_J$ and $p_Q = \partial\mathcal{L}/\partial\gamma_Q$. They have commutation relations with γ_J and γ_Q

$$[\gamma_J, p_J] = i\hbar \tag{8.60}$$

$$[\gamma_Q, p_Q] = i\hbar \tag{8.61}$$

We also can use number operators to describe the momenta:

$$p_J = \hbar n_J \tag{8.62}$$

$$p_Q = \hbar n_Q \tag{8.63}$$

where n_J and n_Q are number of Cooper pairs passing through the small junction in the box and the large area Josephson junction, respectively. Then from the Hamilton's equation $H = \sum_i p_i\gamma_i - \mathcal{L}$, the Hamiltonian of the coupled system becomes

$$\begin{aligned} H(n_J, n_Q, \gamma_J, \gamma_Q) = {} & 4E_{cJ}(n_J - n_g)^2 + 4E_{cQ}(n_Q + n_g)^2 + 8E_{cc}(n_J - n_g)(n_Q + n_g) \\ & - E_{JJ}\cos\gamma_J - E_{JQ}(\cos\gamma_Q + \frac{I_b}{I_{cQ}}\gamma_Q) \end{aligned} \tag{8.64}$$

where

$$E_{cJ} = \frac{e^2 C_{Q\Sigma}}{2(C_{J\Sigma}C_{Q\Sigma} - C_{c\Sigma}^2)} \tag{8.65}$$

$$E_{cQ} = \frac{e^2 C_{J\Sigma}}{2(C_{J\Sigma}C_{Q\Sigma} - C_{c\Sigma}^2)} \tag{8.66}$$

$$E_{cc} = \frac{e^2 C_{c\Sigma}}{2(C_{J\Sigma}C_{Q\Sigma} - C_{c\Sigma}^2)} \tag{8.67}$$

Again, the subscript Q indicates the current-biased Josephson junction. E_{cJ} and E_{cQ} are the charging energies of the small junction in the Cooper pair box and the Josephson junction qubit and E_{cc} is a coupling energy between the Josephson

junction and the Cooper-pair box associated with the capacitor C_0.

8.5.2 Solving the coupled Hamiltonian using the Jaynes-Cummings model.

With the Hamiltonian in Eq. 8.64, I can now find the energy spectrum of the coupled system. I will assume that I need only include the two lowest energy levels of the Cooper pair box. For the Josephson phase qubit, I will use the Harmonic oscillator approximation. In this case, the Hamiltonian in Eq. 8.64 can be shown to have a very similar form to the Jaynes-Cummings Hamiltonian [109, 110]

$$H = \frac{1}{2}\epsilon\sigma_z - \frac{1}{2}\Delta\sigma_x + \hbar\omega_0\left(a^\dagger a + \frac{1}{2}\right) + \lambda\sigma_z(\mathbf{a} + \mathbf{a}^\dagger). \tag{8.68}$$

where σ_x, σ_y and σ_z are the Pauli matrices for the Cooper pair box and a and $a^\dagger$ are the annihilation and creation operators for the Josephson phase qubit.

To get Eq. 8.68, I rewrite the Hamiltonian given by Eq. 8.64 using a new set of conjugate variables, x and p for the Josephson junction and the Pauli matrices for the Cooper pair box. I use the following transformation,

$$n_J = \frac{1}{2}(1 - \sigma_z) \tag{8.69}$$

$$\cos\gamma_J = \frac{1}{2}\sigma_x. \tag{8.70}$$

for the Cooper pair box. For the Josephson phase qubit, I transform n_Q and γ_Q into x and p given by

$$x = \gamma_Q - \sin^{-1}\frac{I_b}{I_{cQ}} = -i\left(\frac{4E_{cQ}}{\hbar\omega_0}\right)^{1/2}(\mathbf{a} - \mathbf{a}^\dagger) \tag{8.71}$$

$$p = n_Q + n_g + \frac{E_{cc}}{E_{cQ}}\left(\frac{1}{2} - n_g\right) = -\left(\frac{\hbar\omega_0}{16E_{cQ}}\right)^{1/2}(\mathbf{a} + \mathbf{a}^\dagger). \tag{8.72}$$

Using a harmonic approximation for the washboard potential of the Josephson junction qubit

$$-\cos\gamma_Q - \frac{I_b}{I_{cQ}}\gamma_Q \simeq \frac{1}{2}\sqrt{1-\left(\frac{I_b}{I_{cQ}}\right)^2}(\gamma_Q - \sin^{-1}\frac{I_b}{I_{cQ}})^2. \tag{8.73}$$

Substituting Eqs. 8.69, 8.70, 8.71, 8.72 and 8.73 into Eq. 8.64, I obtain

$$H = 4E_{cJ}\left(n_g - \frac{1}{2}\right)\sigma_z - \frac{1}{2}E_{JJ}\sigma_x + \hbar\omega_0\left(\mathbf{a}^\dagger\mathbf{a} + \frac{1}{2}\right) + 4E_{cc}\sqrt{\frac{\hbar\omega_0}{16E_{cQ}}}\sigma_z(\mathbf{a} - \mathbf{a}^\dagger). \tag{8.74}$$

Comparing 8.74 to Eq. 8.68, I can identify:

$$\epsilon = 8\left(E_{cJ} + \frac{E_{cc}^2}{E_{cQ}}\right)\left(n_g - \frac{1}{2}\right) \tag{8.75}$$

$$\Delta = E_{JJ} \tag{8.76}$$

$$\lambda = E_{cc}(\hbar\omega_0/E_{cQ})^{1/2}. \tag{8.77}$$

The first two terms in Eq. 8.74 correspond to the Hamiltonian of the Cooper pair box. The third term $\hbar\omega_0(a^\dagger a + \frac{1}{2})$ corresponds to the Hamiltonian of the Josephson phase qubit in the harmonic approximation. Here, the plasma frequency ω_0 is given by

$$\omega_0 = \frac{\sqrt{8E_{cQ}E_{JQ}}}{\hbar}\left[1 - \left(\frac{I_b}{I_{cQ}}\right)\right]^{1/4} \tag{8.78}$$

The last term, $\lambda\sigma_z(a + a^\dagger)$, is the coupling energy term between the Cooper pair box and the Josephson phase qubit. From Eqs. 8.57, 8.67 and 8.77, we see that for $C_g \ll C_0 \ll C_J$, the coupling energy is determined by C_0/C_J; big C_0 gives strong coupling.

8.5.3 Calculating the energy levels of the coupled Hamiltonian using perturbation theory.

The coupling energy term can be treated as a perturbation if it is much smaller than the energy of the uncoupled Cooper pair box or the uncoupled Josephson phase qubit, which is the case of interest here. Thus the Hamiltonian in Eq. 8.68 can be viewed as

$$H = H_0 + H' \tag{8.79}$$

where H_0 is a sum of the uncoupled Hamiltonians of the Cooper pair box and the Josephson phase qubit

$$H_0 = \frac{1}{2}\epsilon\sigma_z - \frac{1}{2}\Delta\sigma_x + \hbar\omega_0\left(\mathbf{a}^\dagger\mathbf{a} + \frac{1}{2}\right) \tag{8.80}$$

and H' is the perturbation,

$$H' = \lambda\sigma_z(\mathbf{a} + \mathbf{a}^\dagger). \tag{8.81}$$

The eigenstates of the unperturbed Hamiltonian H_0 are

$$|n,+\rangle = |n\rangle(\cos\theta|0\rangle + \sin\theta|1\rangle) \tag{8.82}$$

$$|n,-\rangle = |n\rangle(-\sin\theta|0\rangle + \cos\theta|1\rangle) \tag{8.83}$$

where $|n\rangle$ is the n-th harmonic oscillator state of the phase qubit, $|0\rangle$ and $|1\rangle$ are the two number states of the Cooper pair box, and θ is [109]

$$\tan\theta = \frac{\epsilon - \sqrt{\epsilon^2 + \Delta^2}}{\Delta}. \tag{8.84}$$

Using the eigenstates shown in Eqs. 8.82 and 8.83, I calculate the energy shift due to the perturbation. The unperturbed (zeroth order) energy eigenstates are

given by

$$E_{n,\pm}^{(0)} = \pm\frac{1}{2}\sqrt{\epsilon^2+\Delta^2} + \hbar\omega_0\left(n+\frac{1}{2}\right). \tag{8.85}$$

And the first order energy shift yields zero

$$E_{n,\pm}^{(1)} = \langle n,\pm|\lambda\sigma_z(\mathbf{a}+\mathbf{a}^\dagger)|n,\pm\rangle = 0 \tag{8.86}$$

since $\langle n,\pm|a+a^\dagger|n,\pm\rangle = 0$. The second order energy shift is given by

$$E_{n,\pm}^{(2)} = \lambda^2 \sum_{i,j\neq n,\pm} \frac{|\langle n,\pm|\lambda\sigma_z(\mathbf{a}+\mathbf{a}^\dagger)|i,j\rangle|^2}{E_{n,\pm}^{(0)} - E_{i,j}^{(0)}}. \tag{8.87}$$

The matrix elements are

$$\langle l|(\mathbf{a}+\mathbf{a}^\dagger)|m\rangle = \sqrt{m}\delta_{l,m-1} + \sqrt{m+1}\delta_{l,m+1} \tag{8.88}$$

and

$$\langle +|\sigma_z|+\rangle = -\langle -|\sigma_z|-\rangle = (\cos^2\theta - \sin^2\theta) \tag{8.89}$$

$$\langle +|\sigma_z|-\rangle = -2\sin\theta\cos\theta. \tag{8.90}$$

The second order energy shift is then:

$$E_{n,\pm}^{(2)} = \lambda^2\left(4\sin^2\theta\cos^2\theta\frac{\hbar\omega_0 \pm (2n+1)\sqrt{\epsilon^2+\Delta^2}}{\epsilon^2+\Delta^2-(\hbar\omega_0)^2} - \frac{\sin^2\theta-\cos^2\theta}{\hbar\omega_0}\right). \tag{8.91}$$

8.5.4 Energy level spacings

I can now calculate the energy level spacing between the shifted Josephson phase qubit $|0\rangle$ state and $|1\rangle$ from

$$\hbar\omega_{01,\pm} = (E_{1,\pm}^{(0)} + E_{1,\pm}^{(2)}) - (E_{0,\pm}^{(0)} + E_{0,\pm}^{(2)}) \tag{8.92}$$

which yields

$$\hbar\omega_{01,\pm} = \hbar\omega_0 \pm 8\lambda^2 \sin^2\theta \cos^2\theta \frac{\sqrt{\epsilon^2+\Delta^2}}{\epsilon^2+\Delta^2-(\hbar\omega_0)^2} \tag{8.93}$$

I can now use the trigonometric relations

$$\sin 2\theta = \frac{2\tan\theta}{1+\tan^2\theta} \tag{8.94}$$

and

$$\cos 2\theta = \frac{1-\tan^2\theta}{1+\tan^2\theta} \tag{8.95}$$

along with

$$\tan\theta = \frac{\epsilon - \sqrt{\epsilon^2+\Delta^2}}{\Delta}. \tag{8.96}$$

to express all θ terms in Eq. 8.93 in terms of ϵ and Δ. I obtain the energy level spacing $\hbar\omega_{01,\pm}$ as

$$\hbar\omega_{01,\pm} = \hbar\omega_0 \pm \frac{2\Delta^2\sqrt{\epsilon^2+\Delta^2}}{(\epsilon^2+\Delta^2)(\epsilon^2+\Delta^2-(\hbar\omega_0)^2)}. \tag{8.97}$$

8.5.5 Energy level spacings: degenerate case.

For the case $\hbar\omega_0 = \sqrt{\epsilon^2+\Delta^2}$, I have to use degenerate perturbation theory. When $\hbar\omega_0 = \sqrt{\epsilon^2+\Delta^2}$, I find

$$E^{(0)}_{n,+} = \frac{1}{2}\sqrt{\epsilon^2+\Delta^2} + \hbar\omega_0\left(n+\frac{1}{2}\right) = (n+1)\hbar\omega_0 \tag{8.98}$$

and

$$E^{(0)}_{n+1,-} = -\frac{1}{2}\sqrt{\epsilon^2+\Delta^2} + \hbar\omega_0\left(n+1+\frac{1}{2}\right) = (n+1)\hbar\omega_0 \tag{8.99}$$

which makes $|n,+\rangle$ and $|n+1,-\rangle$ degenerate. The perturbation Hamiltonian H' removes the degeneracy. To calculate the splitting, I span the perturbation Hamil-

Table 8.3: Parameters for energy level simulation of a Cooper pair box coupled to a Josephson junction phase qubit.

C_J	10 fF
C_Q	4.078 PF
C_0	10 fF
I_{0J}	10 nA
I_{0Q}	22.213 μA
E_{cJ}	0.95 GHz
E_{cQ}	0.0048 GHz
E_{cc}	0.0024 GHz

tonian H' with the degenerate states $|n,+\rangle$ and $|n+1,-\rangle$ yielding

$$H' \simeq \begin{pmatrix} E^{(0)}_{n,+} & \lambda\Delta/\sqrt{\epsilon^2+\Delta^2} \\ \lambda\Delta/\sqrt{\epsilon^2+\Delta^2} & E^{(0)}_{n+1,-} \end{pmatrix} \tag{8.100}$$

where

$$\langle n,+|H'|n+1,-\rangle = -2\sqrt{n+1}\sin\theta\cos\theta = \frac{\lambda\Delta}{\sqrt{\epsilon^2+\Delta^2}}. \tag{8.101}$$

Diagonalizing Eq. 8.100, I obtain the energy splitting

$$E'_{\pm} = \frac{1}{2}\left(E^{(0)}_{n,+} + E^{(0)}_{n+1,-} \pm \sqrt{(E^{(0)}_{n,+} - E^{(0)}_{n+1,-})^2 + \frac{4\lambda^2\Delta^2}{\epsilon^2+\Delta^2}}\right). \tag{8.102}$$

From Eq. 8.102, for the lowest two states, the energy level spacing becomes

$$\hbar\omega_{\pm} = E'_{\pm} - E^{(0)}_{0,-} = \frac{1}{2}\hbar\omega + \frac{1}{2}\sqrt{\epsilon^2+\Delta^2} \pm \frac{1}{2}\left((\hbar\omega - \sqrt{\epsilon^2+\Delta^2})^2 + \sqrt{\frac{4\lambda^2\Delta^2}{\epsilon^2+\Delta^2}}\right). \tag{8.103}$$

The energy level spacing due to the degenerate energy splitting in Eq. 8.103 can also be applied to the near-resonant case where $\hbar\omega_0 \simeq \sqrt{\epsilon^2+\Delta^2}$.

Figures 8.8 and 8.9 show energy level spacings calculated from Eq. 8.103. Figure 8.8 shows energy level spacings and splittings at the bias current $I_b = 0.989 I_{0Q}$. Figure 8.8 shows energy level spacings and splitting at the bias current $I_b = 0.991 I_{0Q}$. Note that the energy level spacing of the Josephson phase qubit decreased as I_b increased; as expected. Comparing Fig. 8.9 to Fig. 8.10, I notice that the phase qubit energy has been shifted more in Fig. 8.10 at around $n_g = 0.5$. This is because $\hbar\omega_0$ in simulation in fig. 8.10 is more close to E_{cJ} and E_{JJ} of the Cooper pair box. The effective capacitance model would apply for $E_{cJ} > \hbar\omega_0$ where the Cooper pair box adds an effective capacitance to the phase qubit. This results in decreasing the plasma frequency of the phase qubit. In fig. 8.9 and Fig. 8.10, the effective capacitance of the Cooper pair box increased the plasma frequency of the phase qubit at $n_g = 0.5$ when $E_{cJ} < \hbar\omega_0$. I expect the maximum effect of the effective capacitance would occur if $E_{cJ}, E_{JJ} \sim \hbar\omega_0$.

These results are very similar to those from the Yale group where they coupled the box to an LC resonator [41]. The difference is that in this case the box is coupled to the Josephson phase qubit which is a non-linear resonator so that the energy levels of the Josephson phase qubit are distinguishable. The energy level spacings of the Josephson phase qubit can be measured in principle using the spectroscopic measurement.

I also compared this result to that from a full numerical calculation (solving the eigenvalues of Eq. 8.100 with cubic approximation for a Josephson phase qubit) [109]. The numerical simulation yielded almost the same result as the harmonic approximation.

8.6 Conclusions

In this chapter, I analyzed the Cooper-pair box and showed that it acts as a variable capacitor. The effective capacitance of the Cooper-pair box depends on the

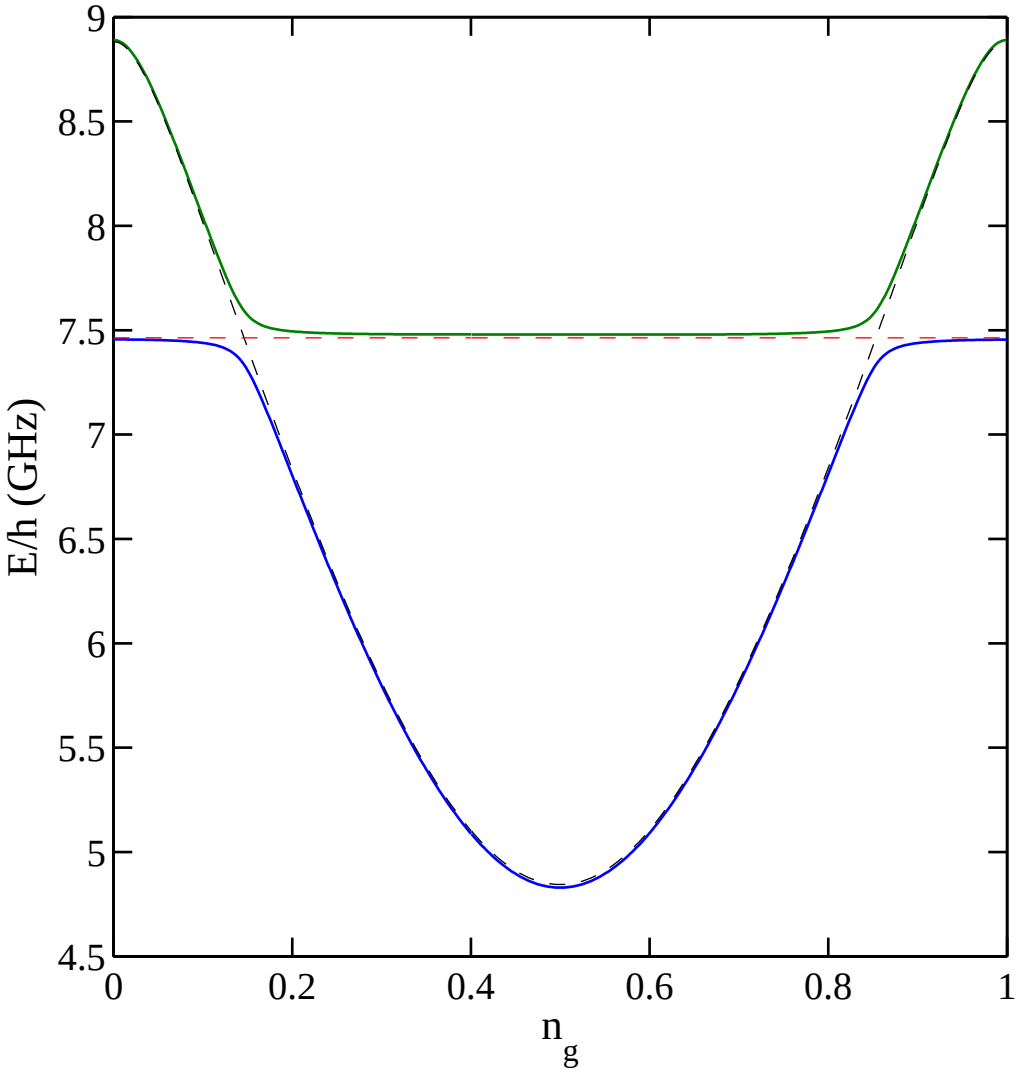

Figure 8.8: Simulated energy level spacings for a Cooper pair box coupled to a Josephson phase qubit for $I_b = 0.989\ I_{cQ}$ (solid curves). The simulation parameters are given in Table. 8.3. The dashed horizontal line is the uncoupled energy level spacing $\hbar\omega_{01}$ of the Josephson phase qubit and the dashed parabola is the uncoupled energy level spacing of the Cooper pair box.

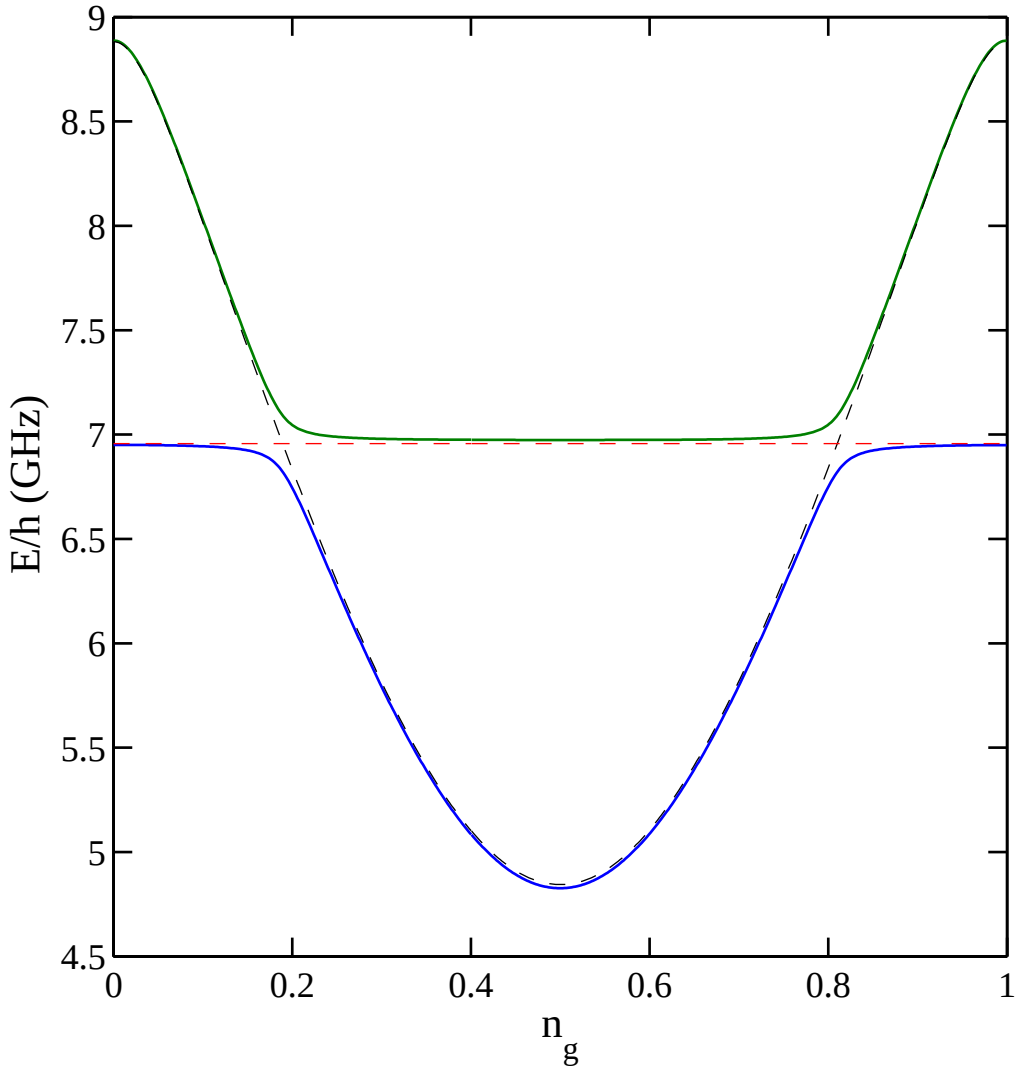

Figure 8.9: Simulated energy level spacings for a Cooper pair box coupled to a Josephson phase qubit for $I_b = 0.991\ I_{cQ}$ (solid curves). The simulation parameters are given in Table. 8.3. The dashed horizontal line is the uncoupled energy level spacing $\hbar\omega_{01}$ of the Josephson phase qubit and the dashed parabola is the uncoupled energy level spacing of the Cooper pair box.

gate voltage and the bias voltage applied. I have proposed a technique to measure the effective capacitance at high frequency by coupling the box to a Josephson junction and showed simulation results for the coupled system. Finally I attempted to build and measure these coupled devices (see Fig. 4.6 in Chapter 4) but I did not get a working Cooper pair box.

Chapter 9
Conclusions

In this thesis, I discussed the effect of isolation on escape rate, dissipation, and coherence in the aluminum dc SQUID phase qubit AL1 and the niobium dc SQUID phase qubit NBG which had a gradiometer loop. The main purpose of my experiments was to find out what was limiting the coherence times of our phase qubits.

In Chapters 2 to 4, I reviewed the basic physics of two level systems, described our dc SQUID phase qubit and reported my qubit fabrication technique. The fabrication techniques involved double-angle evaporation through a photolithographic bridge, and yielded devices with no oxide layers other than native AlO_x.

In Ch. 5, I discussed the inductive isolation scheme used in the dc SQUID phase qubit. I calculated the isolation factor r_I and the effective resistance R_{eff} from the qubit circuit. I also showed that the isolation factor and its effect on the qubit could be changed *in situ*. I measured the state of the qubit AL1 through the total escape rate while varying the isolation factor r_I and observed high frequency noise induced transitions in AL1; I found prominent peaks when the qubit junction $|0\rangle$ to $|2\rangle$ transition matched the isolation junction $|0\rangle$ to $|1\rangle$ transition, and at the resonance between the qubit junction $|1\rangle$ to $|3\rangle$ transition and the isolation junction $|0\rangle$ to $|1\rangle$ transition. These noise induced transitions moved in frequency as I changed the current I_2 through the isolation juction.

Second, I obtained T_1 using two techniques: Relaxation measurements and a thermal escape rate technique. I found that the two techniques yielded quite different values for T_1. For AL1, the relaxation measurement yielded $T_1 \simeq 50$ ns to 60 ns for all isolations, which the thermal escape rate technique yielded $T_1 \simeq 20$ ns. I observed that T_1 obtained from the thermal escape rate measurements showed some

dependence on the isolation factor r_I for certain range of I_1, and this dependence suggested that low T_1 values inferred by the escape technique may be an artifact of high frequency noise in the bias leads.

In Ch. 6, I showed experimental results on Rabi oscillations and spectroscopic coherence times in AL1 for different isolations from the current bias leads. The decay time constant T' of Rabi oscillations showed no dependence on the isolation r_I, suggesting that T' is not limited by noise or loss from the current bias leads. In particular, I found that $T' \simeq 20$ ns to 30 ns independent of the isolation for device AL1. This was 2 to 4 times longer than we have found in our Nb phase qubits, suggesting that materials may be playing an important role in the decoherence.

In Ch. 7, I discussed my experimental results on Rabi oscillations and spectroscopic coherence time T_2^* in a niobium dc SQUID phase qubit with a gradiometer loop, device NBG. If uniform magnetic field noise were the main source of decoherence, one would expect to find a longer T' in NBG. However, I found that NBG did not show a longer T' or T_2^* than the magnetometer dc SQUID qubits. I also discovered that AL1 had the longest T' and T_2, while T_1 from all three devices were similar.

From the measurement of the energy relaxation time T_1, decay time constant T' of Rabi oscillations and the spectroscopic coherence time T_2^* with varying current isolation, I concluded that the current noise was not a major limiting factor for the coherence times in our SQUID phase qubits. Low frequency, flux and critical current noise can also be ruled out because our coherence times and relaxation time showed no significant dependence on frequency.

Finally, in Ch. 8, I discussed using a Cooper pair box as a coupling element between phase qubits and examined the coupling between a Cooper pair box and a Josephson junction phase qubit.

9.1 Current status of superconducting quantum computing and future plans

To increase the coherence times, many superconducting quantum computing groups [40, 49, 46, 90, 111] have been putting tremendous effort into decoherence studies for past few years. Still, it is not entirely clear what exactly limits the coherence time, especially in phase qubits. Groups at NIST and UCSB found out that lossy dielectrics and two level fluctuators from electric dipoles embedded in the dielectrics are the main factor of imiting T_2 in phase qubits [49, 90, 112, 113].

However, recent reports on a charge-phase hybrid qubit (the "transmon") [43] have claimed very long coherence times with minimal changes in materials. The transmon is an ultra-small Josephson junction with an added shunt capacitor. Although the junction area is small, the transmon is effectively a phase qubit where the Josephson energy dominates. Having an ultra-small junction area minimizes decoherence from the junction materials. Also using a large shunt capacitor and large E_J/E_c ratio, the device becomes relatively insensitive to charge fluctuations, which produces an improved "sweet spot". Another important factor was they read out the transmon using a non-demolition method, through a LC resonator, that was capacitively coupled to the transmon.

The future will almost certainly see more study of ideal qubit materials and searching for better qubit read-out methods. Currently many researchers are making a good progress on quantum computation including our UMD group. Perhaps it will not be too many years before we hear someone factored 21 using a superconducting quantum computer.

Appendix A

MATLAB Code

Here I introduce MATLAB codes that I used for the data analysis in this thesis. Sudeep K. Dutta [23] made or refurbished all the codes that I used. The first section is the code for a single Josephson junction spectrum calculation which is Appendix B of Sudeep's thesis [23]. The second and third section has codes for the non-stationary and stationary master equation simulation also made by Sudeep [23].

A.1 Solution of the Junction Hamiltonian

Here is the first section of Appendix B of S. K. Dutta's thesis [23].

The following programs calculate the eigenfunctions, energy levels, and tunneling rates of a single current-biased junction and two capacitively coupled junctions[1]. The heart of the algorithms was written by Huizhong Xu; see §2.4 and §3.3.2 of Ref. [25]. The programs in this section solve the Hamiltonian for a current-biased junction in the absence of dissipation, given in Eq. (2.23). The nature of these solutions is discussed in §2.3.3. `jjspectrum` is the main driver that just collects the solutions returned by `jjeigentbc`, given below. The `diary` command creates a file of everything that is dumped to the screen, which I found useful for debugging.

```
function [stuff,wavefn] = ...
  jjspectrum(Io, Cj, Iri, Irf, dIr, levelmaxIr, E0, psi0)
```

[1]The two coupled junction solution code is not included in this thesis.

```
% [stuff, wavefn] =
%   jjspectrum(Io, Cj, Iri, Irf, dIr, levelmaxIr, E0, psi0)
% This calculates all the energies and wavefunctions for a single
% junction with critical current 'Io' (Amps), junction capacitance
% 'Cj' (Farads), from reduced bias current 'Iri' to 'Irf', in 'dIr'
% steps.  'levelmaxIr' sets the number of levels to calculate; it's
% defined in 'keeplevels'.  'E0' and 'psi0' are optional -- they
% specify the initial guesses for all the levels.  Everything sent
% back in a big structure.
% calls: hbar, keeplevels, jjeigentbc, wp, plotlevels, xaxis

more off
diary on
global hbar;

stuff.params.Io = Io;
stuff.params.Cj = Cj;
stuff.params.Iri = Iri;
stuff.params.Ifr = Irf;
stuff.params.dIr = dIr;
stuff.params.levelmaxIr = levelmaxIr;
stuff.params.start = clock;

NIr = floor( (Irf - Iri) / dIr ) + 1;

for Ircount = 1 : NIr
  Ir = Iri + (Ircount-1) * dIr;
  stuff.Ir(Ircount) = Ir;
  disp(['Reduced current ' num2str(Ir)]);

% After the first current, use the previous wavefunction as the
% initial guess.  Use the same n, which (at a higher current) will
% give a lower initial guess for the energy.

  for levelcount = keeplevels(levelmaxIr, Ir)
    disp(['Level ' num2str(levelcount)]);

    if Ircount == 1
      if nargin == 8
        % User supplied energy and wavefunction
        solution = jjeigentbc(Ir*Io, Io, Cj, length(levelmaxIr)-1,...
          E0(levelcount+1)/hbar/wp(Ir*Io, Io, Cj) - 0.5, ...
          psi0(levelcount+1,:));

      elseif nargin == 7
```

```
        % User supplied energy -- use a random initial wavefunction
        solution = jjeigentbc(Ir*Io, Io, Cj, length(levelmaxIr)-1,...
          E0(levelcount+1)/hbar/wp(Ir*Io, Io, Cj) - 0.5);

      else
        % User didn't give you anything.  Guess the energy and use a
        % random psi.
        corr = 0.15 - 5 * (1 - Ir - 0.005);
        solution = jjeigentbc(Ir*Io, Io, Cj, length(levelmaxIr)-1,...
                              levelcount*(1-corr));
      end

      stuff.params.xleft = solution.x(1);
      stuff.params.dx = solution.dx;
      stuff.params.Ngrid = length(solution.x);

    else
      solution = jjeigentbc(Ir*Io, Io, Cj, length(levelmaxIr)-1, ...
                            n0(levelcount+1), psi(levelcount+1,:));
    end

    energy = real(solution.E);
    gamma = -imag(solution.E) / (hbar/2);

    psi(levelcount+1,:) = solution.wavefn;
    n0(levelcount+1) = energy / hbar / wp(Ir*Io, Io, Cj) - 0.5;

    levstr = num2str(levelcount);
    Irstr = num2str(Ircount);
    eval(['stuff.energy' levstr '(' Irstr ') = energy;']);
    eval(['stuff.gamma' levstr '(' Irstr ') = gamma;']);
    eval(['wavefn.level' levstr '(' Irstr ',:) = solution.wavefn;']);
  end

  if Ircount == 1
    Eplot = figure;
  end

  figure(Eplot);
  plotlevels(stuff);
  xaxis([stuff.Ir(1) 1]);
  shg;
end

stuff.params.stop = clock;
```

```
more on
diary off
```

This is the primary routine that calculates the solutions for a single value of the bias current, using transmission boundary conditions.

```
function solution = jjeigentbc(Ib, Io, Cj, nmax, n0, psi0)

% solution = jjeigentbc(Ib, Io, Cj, nmax, n0, psi0)
% Calculates the energy, potential, and wavefunction (on a grid x,
% with steps dx) for bias current 'Ib', critical current 'Io',
% capacitance 'Cj', maximum number of levels 'nmax', and current
% level 'n0' (or the best guess of what it is).  'psi0' is the
% (optional) inital guess for the wavefunction.  Uses transmission
% boundary conditions.  Results sent back in a structure.
% calls: mj, wp, hbar, jjeigengrid

% Some constants
global hbar;

% Set up a grid to solve Schrodinger's eq.
[xleft, dx, Ngrid] = jjeigengrid(0.97, 0.999, Io, Cj, nmax);

disp(['xleft = ' num2str(xleft) '  dx = ' num2str(dx) '  ...
      Ngrid = ' num2str(Ngrid)]);

% This constant is in front of d2(psi)/dx2.  Multiply it over to
% V and E and call them Vp and Ep (p for prime)

m = mj(Cj);
a = 2 * m * (dx / hbar)^2;

Umin = twb(Ib, Io, asin(Ib/Io));

for i = 1 : Ngrid
  x(i) = xleft + dx * (i-1);
  Utwb(i) = twb(Ib, Io, x(i)) - Umin;
end

Uleft = Utwb(1);
Uright = Utwb(Ngrid);
```

```
% The matrix is N-2 x N-2, because the boundary conditions are
% evaluated in the 2 and N-1 equations.  Set up H*psi = E*psi.

A(1 : Ngrid-2) = -1;
C(1 : Ngrid-2) = -1;

for i = 1 : Ngrid-2
  B(i) = 2 + Utwb(i+1) * a;
end

% Here's the first guess at the eigenvalue.  Start with a random
% wavefunction (if one isn't provided) and use inverse iteration
% (Numerical Recipes 11.7) to improve it.

Ep = (n0 + 0.5) * hbar * wp(Ib, Io, Cj) * a;

if nargin == 6
  newpsi = psi0(2:end-1);
else
% This is the MATLAB R12 command
%  newpsi = random('unif', 0, 1, 1, Ngrid-2);

% This is the MATLAB R14 command
  newpsi = rand(1, Ngrid-2);
end

newpsi = newpsi / sqrt(sum(newpsi.^2));

% Boundary conditions for first go round.

Btbc = B;
Kleft = sqrt(2 * m * (Uleft - Ep/a)) / hbar;
Btbc(1) = B(1) - exp(-1 * Kleft * dx);
Kright = sqrt(2 * m * (Ep/a - Uright)) / hbar;
Btbc(Ngrid-2) = B(Ngrid-2) - exp(sqrt(-1) * Kright * dx);

% First iterate a couple times, without updating the eigenvalue.
diff = 2; err = 0;

count1 = 0;
while (diff > 1e-6) & (err == 0)
  oldpsi = newpsi;
  [temppsi, err] = tridiag(A, Btbc - Ep, C, oldpsi);
  newpsi = temppsi / sqrt( sum(abs(temppsi).^2) );
  diff = max(abs( (abs(newpsi)./abs(oldpsi)).^2 - 1 ));
```

```
  count1 = count1 + 1;
end

% Now update the energy too
oldEp = Ep;
newEp = oldEp + sum( conj(temppsi) .* oldpsi ) ...
          / sum(abs(temppsi).^2);
diff = 1;

count2 = 0;
while((diff > 1e-7) ...
    | max(abs( imag(newEp)/imag(oldEp) - 1 )) > 1e-7) & err==0
  oldpsi = newpsi;
  oldEp = newEp;

  Kleft = sqrt(2 * m * (Uleft - oldEp/a)) / hbar;
  Btbc(1) = B(1) - exp(-1 * Kleft * dx);
  Kright = sqrt(2 * m * (oldEp/a - Uright)) / hbar;
  Btbc(Ngrid-2) = B(Ngrid-2) - exp(sqrt(-1) * Kright * dx);

  [temppsi, err] = tridiag(A, Btbc - oldEp, C, oldpsi);
  newpsi = temppsi / sqrt( sum(abs(temppsi).^2) );
  diff = max(abs( (abs(newpsi)./abs(oldpsi)).^2 - 1 ));
  newEp = oldEp + sum( conj(temppsi) .* oldpsi ) ...
            / sum(abs(temppsi).^2);

  count2 = count2 + 1;
end

% So far, have been normalizing the vector psi.  But to make it
% a 'continuous' function on x, do a Riemann sum.

newpsi = -sqrt(-1) * newpsi / sqrt(dx);
wavefn = [newpsi(1)*exp(-1 * Kleft * dx) newpsi ...
          newpsi(Ngrid-2)*exp(sqrt(-1) * Kright * dx)];
wavefn = wavefn / sqrt( sum(abs(wavefn).^2) ) / sqrt(dx);

solution.E = newEp/a;
solution.x = x;
solution.Utwb = Utwb;
solution.wavefn = wavefn;
solution.dx = dx;

disp([num2str(count1) ' iterations of first loop; ' ...
```

```
      num2str(count2) ' iterations of second']);
```

This sets up the grid on which the solution is calculated.

```
function [xleft, dx, Ngrid] = jjeigengrid(Irmin, Irmax, Io, Cj, nmax)

% [xleft, dx, Ngrid] = jjeigengrid(Irmin, Irmax, Io, Cj, nmax)
% This calculates a grid for jjeigentbc.  It should select the
% smallest grid compatible for currents between 'Irmin' and 'Irmax',
% critical current 'Io', capacitance 'Cj', and maximum quantum level
% 'nmax'.  If everything is done on the same grid, then you can take
% inner products and stuff with the wavefunctions later.
% calls: mj, wp, hbar, twb

% Some constants
global hbar;
m = mj(Cj);

% Ideally, you would use the smallest range for a given Irmin/max and
% Cj.  However, this is complicated.

% First, you need to find the values of the phase, where the
% washboard hits (again) the local max (to the left) and min (to the
% right) of the first well.  The widest range of phase occurs for the
% smallest bias current.  Just pick a fixed [0.8, 2.3], which should
% cover down to Ir = 0.95.

% Then, you want enough phase outside of this to capture some
% oscillations (to the right of the well) and the decay (to the
% left).  This is set by the constant alpha below.  The longest
% spatial scale occurs at the highest current, opposite of the
% previous paragraph -- ignore this.  Don't really know how many of
% these spatial constants to keep.  This should be optimized.

wpmin = wp(Irmax*Io, Io, Cj);
alphamin = sqrt(m*wpmin/hbar);
wpmax = wp(Irmin*Io, Io, Cj);
alphamax = sqrt(m*wpmax/hbar);

xleft = 0.8 - 4/alphamin;
xright = 2.3 + 4/alphamin;

% Next get the step size, which is based on the oscillations of the
```

```
% highest energy you plan to calculate.  These should be evaluated at
% the highest current, where the potential is steep and the energy
% differences are large.

xmin = asin(Irmax);
Umin = twb(Irmax*Io, Io, xmin);
Uleft = twb(Irmax*Io, Io, xleft) - Umin;
Uright = twb(Irmax*Io, Io, xright) - Umin;

Emax = (nmax + 0.5) * hbar * wpmax;

lambdal = sqrt(2*m * (Uleft - Emax)) / hbar;
lambdar = sqrt(2*m * (Emax - Uright)) / hbar;
dx = 1 / max([alphamax lambdal lambdar]) / 10;

Ngrid = floor((xright - xleft) / dx) + 1;
```

The main M-files above call several simple routines, given below. In addition, global variables called `hbar` and `Phio` (which, not surprisingly, are equal to $\hbar$ and Φ_0) should be defined in the workspace.

```
function levels = keeplevels(levelmaxIr, Ir)

% levels = keeplevels(levelmaxIr, Ir)
% This returns a vector of the levels to keep at a given reduced bias
% current, 'Ir'.  'levelmaxIr'(i) gives the reduced current where the
% (i-1)th state leaves the well (or least where you don't want it
% anymore).  If you should keep it, i-1 is included in 'levels'.
% 0 is the ground state.  The number of elements in 'levelmaxIr' sets
% the maximum number of levels to keep.

levels = [];
for i = 1 : length(levelmaxIr)
  if Ir <= levelmaxIr(i)
    levels = [levels i-1];
  end
end



function omegap = wp(Ib, Io, C);
```

```
% wp(Ib, Io, C) gives the plasma frequency of a junction

global Phio;
omegap = sqrt(2*pi*Io/C/Phio) .* (1-(Ib./Io).^2).^(1/4);
```

`plotlevels` plots the energy levels as the solutions are calculated. Running the program for a large number of bias currents can be time-taking, so this is a useful way of spotting trouble early.

```
function plotlevels(eigenstuff)

% plotlevels(eigenstuff)
% This assumes 'eigenstuff' has fields named Ir and energy0, energy1.

colors = 'bgrcmy';
plotcnt = 0;

fields = fieldnames(eigenstuff);

for i = 1 : length(fields)
  if strncmp(fields(i), 'energy', 6) == 1
    data = getfield(eigenstuff, char(fields(i)));
    plot(eigenstuff.Ir(1:length(data)), data, ...
      colors(mod(plotcnt, 6) + 1));
    hold on
    plotcnt = plotcnt + 1;
  end
end
```

```
function xaxis(xbounds)

% xaxis([xmin xmax])
% This replots the current graph, using new x bounds.

graphaxes = axis;
graphaxes(1) = xbounds(1);
graphaxes(2) = xbounds(2);
axis(graphaxes);
```

```
function mass = mj(Cj);

% mass = mj(Cj) returns the phase particle mass, given the junction
% capacitance.
% calls: Phio

global Phio;
mass = Cj * (Phio/2/pi)^2;
```

```
function U = twb(Ib, Io, gamma);

% U = twb(Ib, Io, gamma) returns the tilted washboard potential.
% calls: Phio

global Phio;
U = -Phio/2/pi * (Io * cos(gamma) + Ib * gamma);
```

A.2 Non-stationary Master equation solution

Here is the MATLAB code for solving a non-stationary master equation for a single Josephson junction that I used to calculate the escape rate versus current. The free parameters are T_1 and temperature T. By comparing this to measurements of Γ versus current, I could extract T_1 [23].

```
function result = ME(mode, stepper, dtsave, dtupdate, ti, tf, Gi,
fj, T1, T, Ni0, minN, varargin)

% result = ME(mode, stepper, dtsave, dtupdate, ti, tf, Gi, fj, T1, T,
%             Ni0, minN, modeAparams, modeBparams, ...)
% This calculates the populations and escape rates under the master
% equation, between times 'ti' and 'tf' (in seconds).  Escape rates
% and energy levels are directly specified.  Results are sent back
% in a structure.
%
% 'mode' is a vector that selects the type of simulation.  It is
% unused at the moment.
%
```

```
% A little note about indices: the levels in well are labelled 0,
% 1, 2, ...
%
% Results are saved roughly at intervals 'dtsave'.
%
% 'dtupdate' sets how often to update parameters that are time-
% dependent (as described below); if it is 0, then they are updated
% on every iterate if needed.
%
% 'fj' is the energy level vector, in Hertz.
%
% 'T1' gives all the energy dissipation times, in seconds.
%
% 'T' is the temperature in Kelvin.
%
% calls: ensurerow, ensurecolumn, calcG1nm
% created 11/1/05    modified 12/19/05

more off;

dt = dtsave; t = ti;

diffmax = stepper(1); dtdec = stepper(2); diffmin = stepper(3);
dtinc = stepper(4);


result.params.start = clock; result.params.mode = mode;
result.params.stepper = stepper; result.params.dtsave = dtsave;
result.params.dtupdate = dtupdate; result.params.ti = ti;
result.params.tf = tf;

if (isa(Gi, 'function_handle') == 1) | (isa(Gi, 'inline') == 1)
  FGi = Gi;
else
  FGi = inline(['repmat(' mat2str(ensurecolumn(Gi)) ', 1, ...
  length(t))'], 't');
end result.params.Gi = Gi; result.params.FGi = FGi;

if (isa(fj, 'function_handle') == 1) | (isa(fj, 'inline') == 1)
  Ffj = fj;
else
  Ffj = inline(mat2str(ensurerow(fj)));
end result.params.fj = fj; result.params.Ffj = Ffj;

if (isa(T1, 'function_handle') == 1) | (isa(T1, 'inline') == 1)
```

```
  FT1 = T1;
else
  FT1 = inline(mat2str(ensurerow(T1)));
end result.params.T1 = T1; result.params.FT1 = FT1;

if (isa(T, 'function_handle') == 1) | (isa(T, 'inline') == 1)
  FT = T;
else
  FT = inline(mat2str(T));
end result.params.T = T; result.params.FT = FT;

result.params.Ni0 = Ni0; Nlevel = length(Ni0); Ni =
ensurecolumn(Ni0);

result.params.minN = minN;

result.time(1) = t; result.level(1) = Nlevel; Nisave = Ni;
lastsave = t; lastupdate = t; savecnt = 2;

Gi = feval(FGi, t); fj = feval(Ffj, t); T1 = feval(FT1, t); T =
feval(FT, t);

if length(Gi) ~= Nlevel
  disp('Gi is the wrong size');
  return;
end

if length(fj) ~= Nlevel-1
  disp('fj is the wrong size');
  return;
end

if length(T1) ~= (Nlevel-1) * Nlevel / 2
  disp('T1 is the wrong size');
  return;
end


D = calcG1nm(T1, T, fj); G = diag(Gi);

P = D - G; expPdt = expm(P * dt);

while t <= tf

  newNi = expPdt * Ni;
```

```
diff = max( abs((newNi - Ni) ./ (newNi + 0.05)) );

while diff > diffmax
  dt = dt / dtdec;
  disp(['Step size decreased to ' num2str(dt) ' at
         t = ' num2str(t) ' with
         ' num2str(length(Ni)) ' levels']);
  expPdt = expm(P * dt);
  newNi = expPdt * Ni;
  diff = max( abs((newNi - Ni) ./ (newNi + 0.05)) );
end

Ni = newNi;
t = t + dt;

if (t - lastsave) >= dtsave
  result.time(savecnt) = t;
  result.level(savecnt) = Nlevel;

  % Pad the populations if needed

  if length(Ni) < length(Ni0)
    Nipad = [Ni; zeros(length(Ni0)-length(Ni), 1)];
  else
    Nipad = Ni;
  end

  Nisave = [Nisave Nipad];

  savecnt = savecnt + 1;
  lastsave = t;

  % Print an update every once in a while
  if mod(savecnt, 25) == 0
    disp(['Time = ' num2str(t)]);
  end
end

updateP = 0;

if diff < diffmin
  dttemp = dt * dtinc;
  if dttemp <= dtsave
    dt = dttemp;
    disp(['Step size increased to ' num2str(dt) '
```

```
      at t = ' num2str(t) ' with
      ' num2str(length(Ni)) ' levels']);
      updateP = 1;
    end
  end

  if (t - lastupdate) >= dtupdate
    lastupdate = t;

    Ginew = feval(FGi, t);
    fjnew = feval(Ffj, t);
    T1new = feval(FT1, t);
    Tnew = feval(FT, t);

    if ~isequal(Ginew, Gi)
      Gi = Ginew;
      G = diag(Gi(1:Nlevel));
      updateP = 1;
    end

    if ~isequal(fjnew, fj) | ~isequal(T1new, T1) | ~isequal(Tnew, T)
      fj = fjnew;
      T1 = T1new;
      T = Tnew;
      D = calcG1nm(T1, T, fj, Nlevel);
      updateP = 1;
    end
  end

  if length(Ni) > 2 & Ni(end) < minN
    Ni = Ni(1 : end-1);
    Nlevel = length(Ni);
    G = diag(Gi(1:Nlevel));
    D = calcG1nm(T1, T, fj, Nlevel);
    disp(['Number of levels decreased to ' num2str(length(Ni)) ...
          ' at t = ' num2str(t)]);
    updateP = 1;
  end

  if updateP == 1
    P = D - G;
    expPdt = expm(P * dt);
  end
end
```

```
for j = 0 : length(Ni0)-1
  eval(['result.N' num2str(j) ' = Nisave(' num2str(j+1) ', :);']);
end

result.params.stop = clock; more on;
```

A.3 Stationary Master equation solution

Here is the MATLAB code for solving a stationary master equation for a single Josephson junction. I used this program to calculate the escape rate versus time. By comparing this to measurements of Γ versus time, I could extract T_1 [23]. The free parameters are T_1 and temperature T.

```
function result = SME(mode, tlist, Gi, fj, T1, T, varargin)

% result = SME(mode, tlist, Gi, fj, T1, T, ...
% modeAparams, modeBparams, ...)
% This calculates the populations of the master equation under
% stationary conditions.  The idea is that the relevant transitions
% are directly specified, with no mention of junction parameters
% (Io, Cj, etc.).  Populations are calculated at each of the times
% specified by the vector 'tlist' independently (i.e. this does no
% evolution).  Of course, there is no time-dependence in the equations.
% In this case, time is only used as a parameter that controls the
% values of the other arguments, as described below.  For example,
% the "time" could just be the bias current.  Results are sent back
% in a structure.
%
% 'mode' is a vector that selects the type of simulation.
%
% A little note about indices: the levels in well are labeled
% 0, 1, 2, ...
%
% If 'Gi' is a vector, then its ith element gives the escape
% rate out of the (i-1) level (so the first element is for the ground
% state) in inverse seconds.
%
% 'fj' is the energy level vector, in Hertz.
%
% 'T1' gives all the energy dissipation times, in seconds.
```

```
%
% 'T' is the temperature in Kelvin.
%
% calls: Boltzdist, SMEPi, calcG1nm, ensurerow, ensurecolumn
% created 3/31/04    modified 11/8/05

more off

result.params.start = clock; result.params.mode = mode; result.time
= tlist;

if (isa(Gi, 'function_handle') == 1) | (isa(Gi, 'inline') == 1)
  FGi = Gi;
else
  FGi = inline(['repmat(' mat2str(ensurecolumn(Gi)) ',
  1, length(t))'], 't');
end result.params.Gi = Gi; result.params.FGi = FGi;

if (isa(fj, 'function_handle') == 1) | (isa(fj, 'inline') == 1)
  Ffj = fj;
else
  Ffj = inline(mat2str(ensurerow(fj)));
end result.params.fj = fj; result.params.Ffj = Ffj;

if (isa(T1, 'function_handle') == 1) | (isa(T1, 'inline') == 1)
  FT1 = T1;
else
  FT1 = inline(mat2str(ensurerow(T1)));
end result.params.T1 = T1; result.params.FT1 = FT1;

if (isa(T, 'function_handle') == 1) | (isa(T, 'inline') == 1)
  FT = T;
else
  FT = inline(mat2str(T));
end result.params.T = T; result.params.FT = FT;

Gi = feval(FGi, tlist(1)); fj = feval(Ffj, tlist(1)); T1 =
feval(FT1, tlist(1)); T = feval(FT, tlist(1));

Nlevel = length(Gi);

if length(fj) ~= Nlevel-1
  disp('fj is the wrong size');
  return;
end
```

```
if length(T1) ~= (Nlevel-1) * Nlevel / 2
  disp('T1 is the wrong size');
  return;
end


Pi = Boltzdist(fj, T);


for tcount = 1 : length(tlist)
  t = tlist(tcount);
  Gi = feval(FGi, t);
  fj = feval(Ffj, t);
  T1 = feval(FT1, t);
  T = feval(FT, t);

  D = calcG1nm(T1, T, fj);
  G = diag(Gi);
  MEP = D - G;


  Pi = SMEPi(MEP, Gi, Pi);

  for j = 1 : length(Pi)
    eval(['result.P' num2str(j-1) '(' num2str(tcount) ') = Pi(j);']);
  end
end

result.params.stop = clock; more on
```

Bibliography

[1] *Quantum Computer* (Encyclopædia Britannica Online, 2007), URL `http://www.search.eb.com/eb/article-9343823`.

[2] R. P. Feynman, "Simulating Physics with Computers," Int. J. Theor. Phys. **21**(6/7), 467 (1982).

[3] D. Deutsch, "Quantum theory, the Church-Turing principle and the universal quantum computer," Proc. R. Soc. Lond. A **400**(1818), 97 (1985).

[4] B. Schumacher, "Quantum coding," Phys. Rev. A **51**(4), 2738 (1995).

[5] R. L. Rivest, A. Shamir, and L. Adleman, "A method for obtaining digital signatures and public-key cryptosystems," Communications of the ACM **21**(2), 120 (1978).

[6] M. A. Nielsen and I. L. Chuang, *Quantum Computation and Quantum Information* (Cambridge University Press, Cambridge, 2000).

[7] L. M. K. Vandersypen, M. Steffen, G. Breyta, C. S. Yannoni, M. H. Sherwood, and I. L. Chuang, "Experimental realization of Shor's quantum factoring algorithm using nuclear magnetic resonance," Nature **414**(6866), 883 (2001).

[8] J. Preskill, "Lecture notes on Quantum computation class," URL `http://www.theory.caltech.edu/people/preskill/ph229/index.html`.

[9] D. P. DiVincenzo, "Topics in Quantum Computers," in *Mesoscopic Electron Transport*, edited by G. Schön (Kluwer, 1997), available as cond-mat/9612126.

[10] A. J. Leggett, "Macroscopic Quantum Systems and the Quantum Theory of Measurement," Prog. Theor. Phys. (Suppl.) **69**, 80 (1980).

[11] J. Clarke, A. N. Cleland, M. H. Devoret, D. Esteve, and J. Martinis, "Quantum mechanics of a macroscopic variable - The phase difference of a Josephson junction," Science **239**(4843), 992 (1988).

[12] R. C. Ramos, M. A. Gubrud, A. J. Berkley, J. R. Anderson, C. J. Lobb, and F. C. Wellstood, "Design for Effective Thermalization of Junctions for Quantum Coherence," IEEE Trans. Appl. Supercond. **11**(1), 998 (2001).

[13] M. Tinkham, *Introduction to Superconductivity*, 2nd ed. (McGraw-Hill, New York, 1996).

[14] "Nobel Lecture by Onnes in 1913." URL `http://nobelprize.org/nobel_prizes/physics/laureates/1913/`.

[15] J. Bardeen, L. N. Cooper, and J. R. Schrieffer, "Theory of Superconductivity," Phy. Rev. **108**(5), 1175 (1957).

[16] T. P. Orlando and K. A. Delin, *Foundations of Applied Superconductivity*, 1st ed. (Addison-Wesley, Reading, MA, 1991).

[17] C. P. Poole, H. A. Farach, and R. J. Creswick, *Superconductivity*, 1st ed. (Academic Press, London, 1995).

[18] B. D. Josephson, "Possible new effects in superconductive tunnelling," Phys. Lett. **1**(7), 251 (1962).

[19] J. M. Rowell, "Magnetic Field Dependence of the Josephson Tunnel Current," Phys. Rev. Lett. **11**(5), 200 (1963).

[20] "Nobel Lecture by Josephson and Giaever in 1973." URL `http://nobelprize.org/nobel_prizes/physics/laureates/1973/`.

[21] T. A. Fulton and G. J. Dolan, "Observation of single-electron charging effects in small tunnel junctions," Phys. Rev. Lett. **59**(1), 109 (1987).

[22] D. B. Sullivan and J. E. Zimmerman, "Mechanical Analogs of Time Dependent Josephson Phenomena," Am. J. Phys. **39**(12), 1504 (1971).

[23] S. K. Dutta, *Characterization of Josephson Devices For Use In Quantum Computation*, Ph.D. thesis, University of Maryland (2006).

[24] F. W. Strauch, *Theory of Superconducting Phase Qubits*, Ph.D. thesis, University of Maryland, College Park (2004).

[25] H. Xu, *Quantum Computing with Josephson Junction Circuits*, Ph.D. thesis, University of Maryland, College Park (2004).

[26] J. M. Martinis, M. H. Devoret, and J. Clarke, "Experimental tests for the quantum behavior of a macroscopic degree of freedom: The phase difference across a Josephson junction," Phys. Rev. B **35**(10), 4682 (1987).

[27] J. M. Martinis, M. H. Devoret, and J. Clarke, "Energy-Level Quantization in the Zero-Voltage State of a Current-Biased Josephson Junction," Phys. Rev. Lett. **55**(15), 1543 (1985).

[28] A. O. Caldeira and A. J. Leggett, "Influence of Dissipation on Quantum Tunneling in Macroscopic Systems," Phys. Rev. Lett. **46**(4), 211 (1981).

[29] R. S. Newrock, C. J. Lobb, U. Geigenmüller, and M. Octavio, *Solid State Physics*, vol. 54 (Academic Press, San Diego, 2000).

[30] J. J. Sakurai and S. F. Tuan (Editor), *Modern Quantum Mechanics*, rev. ed. (Addison-Wesley, Reading, MA, 1994).

[31] A. Silver, "How the SQUID was born," Supercond. Sci. Technol **19**(5), S173 (2006).

[32] R. L. Kautz, "Jim Zimmerman and the SQUID," IEEE Trans. Appl. Supercond. **11**(1), 1026 (2001).

[33] J. Clarke and R. H. Koch, "The Impact of High-Temperature Superconductivity on SQUID Magnetometers," Science **242**(4876), 217 (1988).

[34] F. C. Wellstood, Y. Gim, A. Amar, R. C. Black, and A. Mathai, "Magnetic Microscopy using SQUID," IEEE Trans. Appl. Supercond. **7**(2), 3134 (1997).

[35] C. D. Tesche and J. Clarke, "dc SQUID: Noise and Optimization," J. Low Temp. Phys. **29**(3/4), 301 (1977).

[36] C. D. Tesche, *Noise and Optimization of the dc SQUID*, Ph.D. thesis, University of California (1978).

[37] W.-T. Tsang and T. Van Duzer, "dc analysis of parallel arrays of two and three Josephson junctions," J. Appl. Phys. **46**(10), 4573 (1975).

[38] Y. Nakamura, Yu. A. Pashkin, and J. S. Tsai, "Coherent control of macroscopic quantum states in a single-Cooper-pair box," Nature **398**(6730), 786 (1999).

[39] A. Wallraff, D. I. Schuster, A. Blais, L. Frunzio, J. Majer, M. H. Devoret, S. M. Girvin, and R. J. Schoelkopf, "Approaching Unit Visibility for Control of a Superconducting Qubit with Dispersive Readout," Phys. Rev. Lett. **95**(6), 060501 (2005).

[40] I. Siddiqi, R. Vijay, M. Metcalfe, E. Boaknin, L. Frunzio, R. J. Schoelkopf, and M. H. Devoret, "Dispersive measurements of superconducting qubit coherence with a fast latching readout," Phys. Rev. B **73**(5), 054510 (2006).

[41] A. Wallraff, A. Lukashenko, C. Coqui, A. Kemp, T. Duty, and A. V. Ustinov, "Strong coupling of a single photon to a superconducting qubit using circuit quantum electrodynamics," Nature **431**(7005), 162 (2004).

[42] I. Siddiqi, R. Vijay, F. Pierre, C. M. Wilson, L. Frunzio, M. Metcalfe, C. Rigetti, R. J. Schoelkopf, M. H. Devoret, D. Vion, and D. Esteve, "Direct Observation of Dynamical Bifurcation between Two Driven Oscillation States of a Josephson Junction," Phys. Rev. Lett. **94**(2), 027005 (2005).

[43] J. Koch, T. M. Yu, J. Gambetta, A. A. Houck, D. I. Schuster, J. Majer, A. Blais, M. H. Devoret, S. M. Girvin, and R. J. Schoelkopf, "Introducing the Transmon: a new superconducting qubit from optimizing the Cooper Pair Box," ArXiv Condensed Matter e-prints (2007), `cond-mat/0703002`.

[44] T. P. Orlando, J. E. Mooij, L. Tian, C. H. van der Wal, L. S. Levitov, S. Lloyd, and J. J. Mazo, "Superconducting persistent-current qubit," Phys. Rev. B **60**(22), 15398 (1999).

[45] J. R. Friedman, V. Patel, W. Chen, S. K. Tolpygo, and J. E. Lukens, "Quantum superposition of distinct macroscopic states," Nature **406**(6791), 43 (2000).

[46] P. Bertet, I. Chiorescu, G. Burkard, K. Semba, C. J. P. M. Harmans, D. P. DiVincenzo, and J. E. Mooij, "Dephasing of a Superconducting Qubit Induced by Photon Noise," Phys. Rev. Lett. **95**(25), 257002 (2005).

[47] J. M. Martinis, S. Nam, J. Aumentado, and C. Urbina, "Rabi Oscillations in a Large Josephson-Junction Qubit," Phys. Rev. Lett. **89**(11), 117901 (2002).

[48] A. J. Berkley, H. Xu, R. C. Ramos, M. A. Gubrud, F. W. Strauch, P. R. Johnson, J. R. Anderson, A. J. Dragt, C. J. Lobb, and F. C. Wellstood, "Entangled Macroscopic Quantum States in Two Superconducting Qubits," Science **300**(5625), 1548 (2003), comment, **301**(5637), 1183 (2003).

[49] J. M. Martinis, K. B. Cooper, R. McDermott, M. Steffe, M. Ansmann, K. D. Osborn, K. Cicak, S. Oh, D. Pappas, R. Simmonds, and C. C. Yu, "Decoherence in Josephson Qubits from Dielectric Loss," Phys. Rev. Lett. **95**(21), 210503 (2005).

[50] I. I. Rabi, J. R. Zacharias, S. Millman, and P. Kusch, "A New Method of Measuring Nuclear Magnetic Moment," Phys. Rev. **53**(4), 318 (1938).

[51] E. M. Purcell, H. C. Torrey, and R. V. Pound, "Resonance Absorption by Nuclear Magnetic Moments in a Solid," Phys./ Rev. **69**(1-2), 37 (1946).

[52] F. Bloch, "Nuclear Induction," Phys. Rev. **70**(7 and 8), 460 (1946).

[53] F. Bloch, W. W. Hansen, and M. Packard, "The Nuclear Induction Experiment," Phys. Rev. **70**(7 and 8), 474 (1946).

[54] L. Allen and J. H. Eberly, *Optical Resonance and Two-Level Atoms* (Dover, New York, 1987).

[55] F. C. Wellstood, (unpublished).

[56] A. Abragam, *The Principles of Nuclear Magnetism* (Oxford, London, 1961).

[57] C. Cohen-Tannoudji, J. Dupont-Roc, and G. Grynberg, *Atom-Photon Interactions: Basic Processes and Applications* (Wiley, New York, 1992).

[58] J. B. Marion and S. T. Thornton, *Classical Dynamics of Particles and Systems*, 3rd ed. (Harcourt Brace Jovanovich, Inc, Orlando, FL, 1988).

[59] I. I. Rabi, N. F. Ramsey, and J. Schwinger, "Use of Rotating Coordinates in Magnetic Resonance Problems," Rev. Mod. Phys. **26**(2), 167 (1954).

[60] A. O. Caldeira and A. J. Leggett, "Quantum Tunnelling in a Dissipative System," Ann. Phys. **149**(2), 374 (1983).

[61] J. M. Martinis, S. Nam, J. Aumentado, K. M. Lang, and C. Urbina, "Decoherence of a superconducting qubit due to bias noise," Phys. Rev. B **67**(9), 094510 (2003).

[62] D. J. Diestler and R. S. Wilson, "Quantum Dynamics of Vibrational Relaxation in Condensed Media," J. Chem. Phys. **62**(4), 1572 (1975).

[63] H. C. Torrey, "Transient Nutation in Nuclear Magnetic Resonance," Phys. Rev. **76**(8), 1059 (1949).

[64] R. A. Smith, "Excitation of transitions between atomic or molecular energy levels by monochromatic laser radiation," Proc. R. Soc. Lond. A **362**(1708), 1 (1978).

[65] M. Steffen, M. Ansmann, R. C. Bialczak, N. Katz, E. Lucero, R. McDermott, M. Neeley, E. M. Weig, A. N. Cleland, and J. M. Martinis, "Measurement of the Entanglement of Two Superconducting Qubits via State Tomography," Science **313**(5792), 1423 (2006).

[66] MicroChem Corp., 1254 Chestnut Street, Newton, MA 02464. http://www.microchem.com.

[67] Berkeley Microlab, University of California, CA. http://microlab.berkeley.edu.

[68] Alfa Aesar, 26 Parkridge Road, Ward Hill, MA 01835. http://www.alfa.com.

[69] R. D. Mathis, P.O BOX 92916, Long Beach, Ca 90809-2916. http://www.rdmathis.com/.

[70] IC Editor, Inc., I heard a rumor that this company is currently (Sep. 2007) out of business and ICED is now a freeware. Please check. http://www.iceditors.com/.

[71] Chemical Products R. Borghgraef S.A.-N.V., Rue Bollinckx 271 - 273, 1190 Brussels, Belgium. http://www.rbs-cp.be/.

[72] SUSS MicroTec, Schleißheimer Str. 90, D 85748 Garching, Germany. http://www.suss.com/.

[73] JC Nabity Lithography Systems, P.O. Box 5354, Bozeman, MT 59717. http://www.jcnabity.com/.

[74] IMSI, 100 Rowland Way, 3rd floor, Novato, CA 94945 . http://www.imsisoft.com.

[75] P. G. Gloersen, "Ion-beam etching," J. Vac. Sci. Technol. **12**(1), 28 (1975).

[76] H. R. Kaufman, J. J. Cuomo, and J. M. E. Harper, "Technology and applications of broad-beam ion sources used in sputtering. Part I. Ion source technology," J. Vac. Sci. Technol. **21**(3), 725 (1982).

[77] J. M. E. Harper, J. J. Cuomo, and H. R. Kaufman, "Technology and applications of broad-beam ion sources used in sputtering. Part II. Applications," J. Vac. Sci. Technol. **21**(3), 737 (1982).

[78] Hypres Inc., 175 Clearbrook Road, Elmsford, NY 10523. http://www.hypres.com.

[79] H. Paik, B. K. Cooper, S. K. Dutta, R. M. Lewis, , R. C. Ramos, T. A. Palomaki, A. J. Przybysz, A. J. Dragt, J. R. Anderson, C. J. Lobb, and F. C. Wellstood, "Measurements of Decoherence in Three dc SQUID Phase Qubits," IEEE Trans. Appl. Supercond. **17**(2), 120 (2007).

[80] T. A. Palomaki, S. K. Dutta, R. M. Lewis, H. Paik, , K. Mitra, B. K. Cooper, A. J. Przybysz, A. J. Dragt, J. R. Anderson, C. J. Lobb, and F. C. Wellstood, "Pulse Current Measurements and Rabi Oscillations in a dc SQUID Phase Qubit," IEEE Trans. Appl. Supercond. **17**(2), 162 (2007).

[81] Oxford Instruments, 300 Baker Avenue, Suite 150, Concord, MA 01742. http://www.oxinst.com/.

[82] THERMOCOAX SAS, BP 26, 61438 FLERS CEDEX, France http://www.thermocoax.com/.

[83] A. B. Zorin, "The thermocoax cable as the microwave frequency filter for single electron circuits," Rev. Sci. Instrum. **66**(8), 4296 (1995).

[84] K. Bladh, D. Gunnarsson, E. Hürfeld, S. Devi, C. Kristoffersson, B. Smålander, S. Pehrson, T. Claeson, P. Delsing, and M. Taslakov, "Comparison of cryogenic filters for use in single electronics experiments," Rev. Sci. Instrum. **74**(3), 1323 (2003).

[85] V. Lefevre-Seguin, E. Turlot, C. Urbina, D. Esteve, and M. H. Devoret, "Thermal activation of a hysteretic dc superconducting quantum interference device from its different zero-voltage states," Phys. Rev. B **46**(9), 5507 (1992).

[86] T. A. Palomaki, S. K. Dutta, H. Paik, H. Xu, J. Matthews, R. M. Lewis, R. C. Ramos, K. Mitra, P. R. Johnson, F. W. Strauch, A. J. Dragt, C. J. Lobb, J. R. Anderson, and F. C. Wellstood, "Initializing the flux state of multiwell inductively isolated Josephson junction qubits," Phys. Rev. B **73**(1), 014520 (2006).

[87] J. M. Martinis, *Macroscopic Quantum Tunneling and Energy-Level Quantization in the Zero Voltage State of the Current-Biased Josephson Junction*, Ph.D. thesis, University of California (1985).

[88] H. Xu, F. W. Strauch, S. K. Dutta, P. R. Johnson, R. C. Ramos, A. J. Berkley, H. Paik, J. R. Anderson, A. J. Dragt, C. J. Lobb, and F. C. Wellstood, "Spectroscopy of Three-Particle Entanglement in a Macroscopic Superconducting Circuit," Phys. Rev. Lett. **94**(2), 027003 (2005).

[89] S. K. Dutta, H. Xu, A. J. Berkley, R. C. Ramos, M. A. Gubrud, J. R. Anderson, C. J. Lobb, and F. C. Wellstood, "Determination of relaxation time of a Josephson junction qubit," Phys. Rev. B **70**(14), 140502(R) (2004).

[90] R. W. Simmonds, K. M. Lang, D. A. Hite, S. Nam, D. P. Pappas, and J. M. Martinis, "Decoherence in Josephson Phase Qubits from Junction Resonators," Phys. Rev. Lett. **93**(7), 077003 (2004).

[91] S. Han, Y. Yu, X. Chu, S. Chu, and Z. Wang, "Time-Resolved Measurement of Dissipation-Induced Decoherence in a Josephson Junction," Science **293**(5534), 1457 (2001).

[92] I. Chiorescu, Y. Nakamura, C. J. P. M. Harmans, and J. E. Mooij, "Coherent Quantum Dynamics of a Superconducting Flux Qubit," Science **299**(5614), 1869 (2003).

[93] D. Vion, A. Aassime, A. Cottet, P. Joyez, H. Pothier, C. Urbina, D. Esteve, and M. H. Devoret, "Manipulating the Quantum State of an Electrical Circuit," Science **296**(5569), 886 (2002).

[94] M. Steffen, M. Ansmann, R. McDermott, N. Katz, R. C. Bialczak, E. Lucero, M. Neeley, E. M. Weig, A. N. Cleland, and J. M. Martinis, "State Tomography of Capactively Shunted Phase Qubits with High Fidelity," Phys. Rev. Lett. **97**(5), 050502 (2006).

[95] H. Xu, A. J. Berkley, R. C. Ramos, M. A. Gubrud, P. R. Johnson, F. W. Strauch, A. J. Dragt, J. R. Anderson, C. J. Lobb, and F. C. Wellstood, "Spectroscopic resonance broadening in a Josephson junction qubit due to current noise," Phys. Rev. B **71**(6), 064512 (2005).

[96] A. J. Berkley, *A Josephson Junction Qubit*, Ph.D. thesis, University of Maryland, College Park (2003).

[97] F. C. Wellstood, C. Urbina, and J. Clarke, "Flicker $(1/f)$ Noise in the Critical Current of Josephson Junctions at 0.09-4.2 K," Appl. Phys. Lett. **85**(22), 5296 (2004).

[98] F. C. Wellstood, C. Urbina, and J. Clarke, "Low Frequency Noise in dc Superconducting Quantum Interference Devices Below 1K," Appl. Phys. Lett. **50**(12), 772 (1987).

[99] J. Q. You and F. Nori, "Superconducting Circuits and Quantum Information," Phys. Today **58**(11), 42 (2005).

[100] J. Claudon, F. Balestro, F. W. J. Hekking, and O. Buisson, "Coherent Oscillations in a Superconducting Multilevel Quantum System," Phys. Rev. Lett. **93**(18), 187003 (2004).

[101] K. B. Cooper, M. Steffen, R. McDermott, R. W. Simmonds, S. Oh, D. A. Hite, D. P. Pappas, and J. M. Martinis, "Observation of Quantum Oscillations between a Josephson Phase Qubit and a Microscopic Resonator Using Fast Readout," Phys. Rev. Lett. **93**(18), 180401 (2004).

[102] R. McDermott, R. W. Simmonds, M. Steffen, K. C. K. B. Cooper, K. D. Osborn, S. Oh, D. P. Pappas, and J. M. Martinis, "Simultaneous State Measurement of Coupled Josephson Phase Qubits," Science **307**(5713), 1299 (2005).

[103] D. J. Van Harlingen, T. L. Robertson, B. L. T. Plourde, P. A. Reichardt, T. A. Crane, and J. Clarke, "Decoherence in Josephson-junction qubits due to critical-current fluctuations," Phys. Rev. B **70**(6), 064517 (2004).

[104] B. Savo, F. C. Wellstood, , and J. Clarke, "Low-frequency Excess Noise in Nb-Al_2O_3-Nb Josephson Tunnel Junctions," Appl. Phys. Lett. **50**(24), 1757 (1987).

[105] R. T. Wakai and D. J. V. Harlingen, "Direct Lifetime Measurements and Interactions of Charged Defect States in Submicron Josephson Junctions," Phys. Rev. Lett. **58**(16), 1687 (1987).

[106] Yu. A. Pashkin, T. Yamamoto, O. Astafiev, Y. Nakamura, D. V. Averin, and J. S. Tsai, "Quantum oscillations in two coupled charge qubits," Nature **421**(6925), 823 (2003).

[107] D. Averin and C. Bruder, "Variable Electrostatic Transformer: Controllable Coupling of Two Charge Qubits," Phys. Rev. Lett. **91**(5), 057003 (2003).

[108] E. K. Irish and K. Schwab, "Quantum measurement of a coupled nanomechanical resonator Cooper-pair box system," Phys. Rev. B **68**(15), 155311 (2003).

[109] F. W. Strauch, (unpublished).

[110] E. T. Jaynes and F. W. Cummings, "Comparison of Quantum and Semiclassical Radiation Theories with Application to the Beam Maser," Proc. IEEE **51**(1), 89 (1963).

[111] F. Yoshihara, K. Harrabi, A. O. Niskanen, Y. Nakamura, and J. S. Tsai, "Decoherence of Flux Qubits due to $1/f$ Flux Noise," Phys. Rev. Lett. **97**(16), 167001 (2006).

[112] S. Oh, K. Cicak, R. McDermott, K. B. Cooper, K. D. Osborn, R. W. Simmonds, M. Steffen, J. M. Martinis, and D. P. Pappas, "Low-leakage superconducting tunnel junctions with a single-crystal Al_2O_3 barrier," Supercond. Sci. Technol. **18**(10), 1396 (2005).

[113] S. Oh, K. Cicak, J. S. Kline, M. A. Sillanpää, K. D. Osborn, J. D. Whittaker, R. W. Simmonds, and D. P. Pappas, "Elimination of two level fluctuators in superconducting quantum bits by an epitaxial tunnel barrier," Phys. Rev. B **74**(10), 100502(R) (2006).